mathematics

Mathematical Physics II

Edited by
Enrico De Micheli

Printed Edition of the Special Issue Published in *Mathematics*

www.mdpi.com/journal/mathematics

MDPI

Mathematical Physics II

Mathematical Physics II

Editor

Enrico De Micheli

MDPI • Basel • Beijing • Wuhan • Barcelona • Belgrade • Manchester • Tokyo • Cluj • Tianjin

Editor
Enrico De Micheli
Consiglio Nazionale delle Ricerche
Italy

Editorial Office
MDPI
St. Alban-Anlage 66
4052 Basel, Switzerland

This is a reprint of articles from the Special Issue published online in the open access journal *Mathematics* (ISSN 2227-7390) (available at: https://www.mdpi.com/journal/mathematics/special_issues/Mathematical_Physic_II).

For citation purposes, cite each article independently as indicated on the article page online and as indicated below:

LastName, A.A.; LastName, B.B.; LastName, C.C. Article Title. *Journal Name* **Year**, *Article Number*, Page Range.

ISBN 978-3-03943-495-4 (Hbk)
ISBN 978-3-03943-496-1 (PDF)

© 2020 by the authors. Articles in this book are Open Access and distributed under the Creative Commons Attribution (CC BY) license, which allows users to download, copy and build upon published articles, as long as the author and publisher are properly credited, which ensures maximum dissemination and a wider impact of our publications.
The book as a whole is distributed by MDPI under the terms and conditions of the Creative Commons license CC BY-NC-ND.

Contents

About the Editor

Enrico De Micheli is currently Senior Researcher at the National Research Council (CNR) of Italy and teaches Quantum Information Theory and Computation at the Information Technology Institute (ISICT) of the University of Genova (Italy). He received his degree in Theoretical Physics from the University of Genova in 1986. He worked as research fellow at the Institute for Scientific Research (IRST) of Trento. He has been visiting scientist at the University of British Columbia in Vancouver (Canada). He is reviewer of the AMS and Editor/Referee of several mathematical journals and has published some 60 papers in peer-reviewed journals. His research interests include Special Functions of Mathematical Physics, Potential Theory, Quantum Mechanics, Thermal Quantum Field Theory, Approximation Theory, Inverse Problems, and Computational Physics.

Preface to "Mathematical Physics II"

The mysterious charm of Mathematical Physics is beautifully represented in the celebrated 1960 paper of Eugene Wigner "The Unreasonable Effectiveness of Mathematics in the Natural Sciences." It is indeed hard for us to understand the astonishing appropriateness of the language of mathematics for the formulation of the laws of physics and its capability to do predictions, appropriateness that emerged immediately at the beginning of the scientific thought and was splendidly depicted by Galileo: "The grand book, the Universe, is written in the language of Mathematics." Paraphrasing the words of Bertrand Russell, in this marriage the supreme beauty, cold and austere, of Mathematics complements the supreme beauty, warm and engaging, of Physics. This book, which consists of nine articles, gives a flavor of this beauty and covers various topics related to physics and engineering. A brief outline of these topics is given hereafter.

The study of free probability in certain probability spaces induced by functions on p-adic number fields is here a very interesting example of the application of p-adic mathematical methods for modeling physical phenomena. Within the quantum information processing framework is presented the analysis of a non-commutative measure of quantum discord in the two-qubit case. The Riemann–Hilbert problem plays relevant but different roles in two papers. In one paper, the Riemann–Hilbert problem, formulated with respect to the spectral parameter, and the prolongation structure theory are used to analyze the modified nonlinear Schrödinger equation. In the other case, the Riemann–Hilbert structure emerges from the holomorphic extension of certain Legendre expansions, leading thus to an explicit connection between spherical Laplace transform and non-Euclidean Fourier transform. Remaining in the spectral analysis field, the study of a deformed wave equation, with the Laplacian being replaced by a differential-difference Dunkl operator, shows its relation with a generalized Fourier transform and the non-existence of the related Huygens principle. The Gibbs phenomenon is then the subject of a paper where the primary tool of analysis is the representation of suitable functions in terms of dual tight framelets. Finally, numerical analysis and optimization methods are the main mathematical devices used to study equations that are relevant in the study of material properties, such as thermomechanical performances, flaw dynamics, and bearing capacity of structures.

In conclusion, as Editor of this Special Issue, I wish to thank the authors of the articles for their valuable contributions, the referees for their precious reviews, and Ms. Julie Shi and Ms. Grace Wang of MDPI for their kind assistance.

Enrico De Micheli
Editor

mathematics

MDPI

Article

Primes in Intervals and Semicircular Elements Induced by p-Adic Number Fields $\mathbb{Q}_p$ over Primes p

Ilwoo Cho [1,*] and Palle Jorgensen [2]

[1] Department of Mathematics & Statistics, Saint Ambrose University, 421 Ambrose Hall, 518 W. Locust St., Davenport, IA 52803, USA

[2] Department of Mathematics, University of Iowa, 14 McLean Hall, Iowa City, IA 52242, USA; palle-jorgensen@uiowa.edu

* Correspondence: choilwoo@sau.edu

Received: 11 December 2018; Accepted: 15 February 2019; Published: 19 February 2019

Abstract: In this paper, we study free probability on (weighted-)semicircular elements in a certain Banach $*$-probability space $(\mathfrak{LS}, \tau^0)$ induced by measurable functions on p-adic number fields $\mathbb{Q}_p$ over primes p. In particular, we are interested in the cases where such free-probabilistic information is affected by primes in given closed intervals of the set $\mathbb{R}$ of real numbers by defining suitable "truncated" linear functionals on $\mathfrak{LS}$.

Keywords: free probability; primes; p-adic number fields; Banach $*$-probability spaces; weighted-semicircular elements; semicircular elements; truncated linear functionals

MSC: 05E15; 11G15; 11R47; 11R56; 46L10; 46L54; 47L30; 47L55

1. Introduction

In [1,2], we constructed-and-studied *weighted-semicircular elements* and *semicircular elements* induced by *p-adic number fields* $\mathbb{Q}_p$, for all $p \in \mathcal{P}$, where $\mathcal{P}$ is the set of all *primes* in the set $\mathbb{N}$ of all *natural numbers*. In this paper, we consider certain "truncated" free-probabilistic information of the weighted-semicircular laws and the semicircular law of [1]. In particular, we are interested in free distributions of certain free reduced words in our (weighted-)semicircular elements under conditions dictated by the primes p in a "suitable" *closed interval* $[t_1, t_2]$ of the set $\mathbb{R}$ of *real numbers*. Our results illustrate how the original (weighted-)semicircular law(s) of [1] is (resp., are) distorted by truncations on $\mathcal{P}$.

1.1. Preview and Motivation

Relations between *primes* and *operators* have been widely studied not only in mathematical fields (e.g., [3–6]), but also in other scientific fields (e.g., [7]). For instance, we studied how primes act on certain *von Neumann algebras* generated by p -adic and Adelic *measure spaces* in [8,9]. Meanwhile, in [10], primes are regarded as *linear functionals* acting on *arithmetic functions*, understood as *Krein-space operators* under the representation of [11]. Furthermore, in [12,13], free-probabilistic structures on *Hecke algebras* $\mathcal{H}\left(GL_2(\mathbb{Q}_p)\right)$ are studied for $p \in \mathcal{P}$. These series of works are motivated by number-theoretic results (e.g., [4,5,7]).

In [2], we constructed weighted-semicircular elements $\{Q_{p,j}\}_{j\in\mathbb{Z}}$ and corresponding semicircular elements $\{\Theta_{p,j}\}_{j\in\mathbb{Z}}$ in a certain Banach $*$-algebra $\mathfrak{LS}_p$ induced from the $*$-*algebra* $\mathcal{M}_p$ consisting of *measurable functions* on a p-adic number field $\mathbb{Q}_p$, for $p \in \mathcal{P}$. In [1], the *free product* Banach $*$-probability space $\left(\mathfrak{LS}, \tau^0\right)$ of the measure spaces $\{\mathfrak{LS}_p(j)\}_{p\in\mathcal{P}, j\in\mathbb{Z}}$ of [2] were constructed over both primes and integers, and weighted-semicircular elements $\{Q_{p,j}\}_{p\in\mathcal{P},\, j\in\mathbb{Z}}$ and semicircular elements $\{\Theta_{p,j}\}_{p\in\mathcal{P},\, j\in\mathbb{Z}}$ were studied in $\mathfrak{LS}$, as *free generators*.

In this paper, we are interested in the cases where the free product linear functional τ^0 of [1] on the Banach $*$-algebra $\mathfrak{LG}$ is truncated in $\mathcal{P}$. The distorted free-distributional data from such truncations are considered. The main results characterize how the original free distributions on $(\mathfrak{LG}, \tau^0)$ are affected by the given truncations on $\mathcal{P}$.

1.2. Overview

We briefly introduce the backgrounds of our works in Section 2. In the short Sections 3–8, we construct the Banach $*$-probability space $(\mathfrak{LG}, \tau^0)$ and study *weighted-semicircular elements* $Q_{p,j}$ and corresponding *semicircular elements* $\Theta_{p,j}$ in $(\mathfrak{LG}, \tau^0)$, for all $p \in \mathcal{P}$, $j \in \mathbb{Z}$.

In Section 9, we define a free-probabilistic sub-structure $\mathbb{LS} = (\mathbb{LS}, \tau^0)$ of the Banach $*$-probability space $(\mathfrak{LG}, \tau^0)$, having possible non-zero free distributions, and study free-probabilistic properties of $\mathbb{LS}$. Then, *truncated linear functionals of* τ^0 on $\mathbb{LS}$ and truncated free-probabilistic information on $\mathbb{LS}$ are studied. The main results illustrate how our truncations distort the original free distributions on $\mathbb{LS}$ (and hence, on $\mathfrak{LG}$).

In Section 10, we study *free sums* X of $\mathbb{LS}$ having their free distribution, the (weighted-)semicircular law(s), under truncation. Note that, in general, if free sums X have more than one summand as operators, then X cannot be (weighted-)semicircular in $\mathbb{LS}$. However, certain truncations make them be.

In Section 11, we investigate a type of truncation (compared with those of Sections 9 and 10). In particular, certain truncations inducing so-called *prime-neighborhoods* are considered. The *unions* of such prime-neighborhoods provide corresponding distorted free probability on $\mathbb{LS}$ (different from that of Sections 9 and 10).

2. Preliminaries

In this section, we briefly introduce the backgrounds of our proceeding works.

2.1. Free Probability

Readers can review *free probability theory* from [14,15] (and the cited papers therein). *Free probability* is understood as the noncommutative operator-algebraic version of classical *measure theory* and *statistics*. The classical *independence* is replaced by the *freeness*, by replacing *measures* on sets with *linear functionals* on noncommutative ($*$-)algebras. It has various applications not only in pure mathematics (e.g., [16–20]), but also in related topics (e.g., see [2,8–11]). Here, we will use the *combinatorial free probability theory* of *Speicher* (e.g., see [14]).

In the text, without introducing detailed definitions and combinatorial backgrounds, *free moments* and *free cumulants* of operators will be computed. Furthermore, the *free product of* $*$*-probability spaces in the sense of* [14,15] is considered without detailed introduction.

Note now that one of our main objects, the $*$-algebra $\mathcal{M}_p$ of Section 3, are commutative, and hence, (traditional, or usual "noncommutative") free probability theory is not needed for studying *functional analysis* or *operator algebra theory* on $\mathcal{M}_p$, because the freeness on this commutative structure is trivial. However, we are not interested in the free-probability-depending operator-algebraic structures of commutative algebras, but in statistical data of certain elements to establish (weighted-)semicircular elements. Such data are well explained by the free-probability-theoretic terminology and language. Therefore, as in [2], we use "free-probabilistic models" on $\mathcal{M}_p$ to construct and study our (weighted-)semicircularity by using concepts, tools, and techniques from free probability theory "non-traditionally." Note also that, in Section 8, we construct "traditional" free-probabilistic structures, as in [1], from our "non-traditional" free-probabilistic structures of Sections 3–7 (like the *free group factors*; see, e.g., [15,19]).

2.2. Analysis of $\mathbb{Q}_p$

For more about p-adic and Adelic analysis, see [7]. Let $p \in \mathcal{P}$, and let $\mathbb{Q}_p$ be the *p-adic number field*. Under the p-adic addition and the p-adic multiplication of [7], the set $\mathbb{Q}_p$ forms a *field* algebraically. It is equipped with the *non-Archimedean norm* $|.|_p$, which is the inherited *p-norm* on the set $\mathbb{Q}$ of all *rational numbers* defined by:

$$|x|_p = \left|p^k \frac{a}{b}\right|_p = \frac{1}{p^k},$$

whenever $x = p^k \frac{a}{b}$ in $\mathbb{Q}$, where k, $a \in \mathbb{Z}$, and $b \in \mathbb{Z} \setminus \{0\}$. For instance,

$$\left|\frac{8}{3}\right|_2 = \left|2^3 \times \frac{1}{3}\right|_2 = \frac{1}{2^3} = \frac{1}{8},$$

and:

$$\left|\frac{8}{3}\right|_3 = \left|3^{-1} \times 8\right|_3 = \frac{1}{3^{-1}} = 3,$$

and:

$$\left|\frac{8}{3}\right|_q = \frac{1}{q^0} = 1, \text{ whenever } q \in \mathcal{P} \setminus \{2, 3\}.$$

The *p-adic number field* $\mathbb{Q}_p$ is the maximal p-norm closure in $\mathbb{Q}$. Therefore, under norm topology, it forms a *Banach space* (e.g., [7]).

Let us understand the *Banach field* $\mathbb{Q}_p$ as a *measure space*,

$$\mathbb{Q}_p = \left(\mathbb{Q}_p,\ \sigma(\mathbb{Q}_p),\ \mu_p\right),$$

where $\sigma(\mathbb{Q}_p)$ is the *σ-algebra of $\mathbb{Q}_p$* consisting of all *μ_p-measurable subsets*, where μ_p is a left-and-right additive invariant *Haar measure* on $\mathbb{Q}_p$ satisfying:

$$\mu_p(\mathbb{Z}_p) = 1,$$

where $\mathbb{Z}_p$ is the *unit disk of* $\mathbb{Q}_p$, consisting of all *p-adic integers* x satisfying $|x|_p \leq 1$. Moreover, if we define:

$$U_k = p^k \mathbb{Z}_p = \{p^k x \in r\mathbb{Q}_p : x \in \mathbb{Z}_p\}, \tag{1}$$

for all $k \in \mathbb{Z}$ (with $U_0 = \mathbb{Z}_p$), then these μ_p-measurable subsets U_k's of (1) satisfy:

$$\mathbb{Q}_p = \underset{k \in \mathbb{Z}}{\cup} U_k,$$

and:

$$\mu_p\left(U_k\right) = \frac{1}{p^k} = \mu_p\left(x + U_k\right), \forall x \in \mathbb{Q}_p, \tag{2}$$

and:

$$\cdots \subset U_2 \subset U_1 \subset U_0 = \mathbb{Z}_p \subset U_{-1} \subset U_{-2} \subset \cdots.$$

In fact, the family $\{U_k\}_{k \in \mathbb{Z}}$ forms a *basis* of the Banach topology for $\mathbb{Q}_p$ (e.g., [7]).

Define now subsets ∂_k of $\mathbb{Q}_p$ by:

$$\partial_k = U_k \setminus U_{k+1}, for\ all k \in \mathbb{Z}. \tag{3}$$

We call such μ_p-measurable subsets ∂_k the k^{th} boundaries of U_k in $\mathbb{Q}_p$, for all $k \in \mathbb{Z}$. By (2) and (3), one obtains that:

$$\mathbb{Q}_p = \underset{k \in \mathbb{Z}}{\sqcup} \partial_k,$$

and:

$$\mu_p\left(\partial_k\right) = \mu_p\left(U_k\right) - \mu_p\left(U_{k+1}\right) = \frac{1}{p^k} - \frac{1}{p^{k+1}}, \tag{4}$$

and:

$$\partial_{k_1} \cap \partial_{k_2} = \begin{cases} \partial_{k_1} & \text{if } k_1 = k_2 \\ \varnothing & \text{otherwise,} \end{cases},$$

for all $k, k_1, k_2 \in \mathbb{Z}$, where $\sqcup$ is the *disjoint union* and $\varnothing$ is the *empty set*.

Now, let $\mathcal{M}_p$ be the algebra,

$$\mathcal{M}_p = \mathbb{C}\left[\{\chi_S : S \in \sigma(\mathbb{Q}_p)\}\right], \tag{5}$$

where χ_S are the usual *characteristic functions* of $S \in \sigma\left(\mathbb{Q}_p\right)$.

Then the algebra $\mathcal{M}_p$ of (5) forms a well-defined $*$-*algebra over* $\mathbb{C}$, with its *adjoint*,

$$\left(\sum_{S\in\sigma(G_p)} t_S\chi_S\right)^* \stackrel{def}{=} \sum_{S\in\sigma(G_p)} \overline{t_S}\,\chi_S,$$

where $t_S \in \mathbb{C}$, having their *conjugates* $\overline{t_S}$ in $\mathbb{C}$.

Let $\sum\limits_{S\in\sigma(G_p)} t_S\chi_S \in \mathcal{M}_p$. Then, one can define the *p-adic integral* by:

$$\int_{\mathbb{Q}_p} \left(\sum_{S\in\sigma(\mathbb{Q}_p)} t_S\chi_S\right) d\mu_p = \sum_{S\in\sigma(\mathbb{Q}_p)} t_S\mu_p(S). \tag{6}$$

Note that, by (4), if $S \in \sigma(\mathbb{Q}_p)$, then there exists a subset Λ_S of $\mathbb{Z}$, such that:

$$\Lambda_S = \{j \in \mathbb{Z} : S \cap \partial_j \neq \varnothing\}, \tag{7}$$

satisfying:

$$\begin{aligned} \int_{\mathbb{Q}_p} \chi_S\, d\mu_p &= \int_{\mathbb{Q}_p} \sum_{j\in\Lambda_S} \chi_{S\cap\partial_j}\, d\mu_p \\ &= \sum_{j\in\Lambda_S} \mu_p\left(S \cap \partial_j\right) \end{aligned}$$

by (6)

$$\leq \sum_{j\in\Lambda_S} \mu_p\left(\partial_j\right) = \sum_{j\in\Lambda_S} \left(\frac{1}{p^j} - \frac{1}{p^{j+1}}\right), \tag{8}$$

by (4), for all $S \in \sigma(\mathbb{Q}_p)$, where Λ_S is in the sense of (7).

Proposition 1. *Let $S \in \sigma(\mathbb{Q}_p)$, and let $\chi_S \in \mathcal{M}_p$. Then, there exist $r_j \in \mathbb{R}$, such that:*

$$0 \leq r_j \leq 1 in \mathbb{R}, for all j \in \Lambda_S, \tag{9}$$

and:

$$\int_{\mathbb{Q}_p} \chi_S\, d\mu_p = \sum_{j\in\Lambda_S} r_j \left(\tfrac{1}{p^j} - \tfrac{1}{p^{j+1}}\right).$$

Proof. The existence of $r_j = \frac{\mu_p\left(S\cap\partial_j\right)}{\mu_p\left(\partial_j\right)}$, for all $j \in \mathbb{Z}$, is guaranteed by (7) and (8). The p-adic integral in (9) is obtained by (8). □

3. Free-Probabilistic Model on $\mathcal{M}_p$

Throughout this section, fix a prime $p \in \mathcal{P}$, and let $\mathbb{Q}_p$ be the corresponding p-adic number field and $\mathcal{M}_p$ be the $*$-algebra (5) consisting of μ_p-measurable functions on $\mathbb{Q}_p$. Here, we establish a suitable (non-traditional) free-probabilistic model on $\mathcal{M}_p$ implying p-adic analytic data.

Let U_k be the basis elements (1) of the topology for $\mathbb{Q}_p$ with their boundaries ∂_k of (3), i.e.,

$$U_k = p^k \mathbb{Z}_p, for all k \in \mathbb{Z}, \tag{10}$$

and:

$$\partial_k = U_k \setminus U_{k+1}, \text{ for all } k \in \mathbb{Z}.$$

Define a linear functional $\varphi_p : \mathcal{M}_p \to \mathbb{C}$ by the p-adic integration (6),

$$\varphi_p(f) = \int_{\mathbb{Q}_p} f d\mu_p, for all f \in \mathcal{M}_p. \tag{11}$$

Then, by (9) and (11), one obtains:

$$\varphi_p\left(\chi_{U_j}\right) = \frac{1}{p^j} \text{ and } \varphi_p\left(\chi_{\partial_j}\right) = \frac{1}{p^j} - \frac{1}{p^{j+1}},$$

for all $j \in \mathbb{Z}$.

Definition 1. *We call the pair $\left(\mathcal{M}_p, \varphi_p\right)$ the p-adic (non-traditional) free probability space for $p \in \mathcal{P}$, where φ_p is the linear functional (11) on $\mathcal{M}_p$.*

Remark 1. *As we discussed in Section 2.1, we study the measure-theoretic structure $\left(\mathcal{M}_p, \varphi_p\right)$ as a free-probabilistic model on $\mathcal{M}_p$ for our purposes. Therefore, without loss of generality, we regard $\left(\mathcal{M}_p, \varphi_p\right)$ as a non-traditional free-probabilistic structure. In this sense, we call $\left(\mathcal{M}_p, \varphi_p\right)$ the p-adic free probability space for p. The readers can understand $\left(\mathcal{M}_p, \varphi_p\right)$ as the pair of a commutative $*$-algebra $\mathcal{M}_p$ and a linear functional φ_p, having as its name the p-adic free probability space.*

Let ∂_k be the k^{th} boundary $U_k \setminus U_{k+1}$ of U_k in $\mathbb{Q}_p$, for all $k \in \mathbb{Z}$. Then, for $k_1, k_2 \in \mathbb{Z}$, one obtains that:

$$\chi_{\partial_{k_1}} \chi_{\partial_{k_2}} = \chi_{\partial_{k_1} \cap \partial_{k_2}} = \delta_{k_1,k_2} \chi_{\partial_{k_1}},$$

by (4), and hence,

$$\begin{aligned} \varphi_p\left(\chi_{\partial_{k_1}} \chi_{\partial_{k_2}}\right) &= \delta_{k_1,k_2} \varphi_p\left(\chi_{\partial_{k_1}}\right) \\ &= \delta_{k_1,k_2}\left(\frac{1}{p^{k_1}} - \frac{1}{p^{k_1+1}}\right), \end{aligned} \tag{12}$$

where δ is the *Kronecker delta*.

Proposition 2. *Let $(j_1, ..., j_N) \in \mathbb{Z}^N$, for $N \in \mathbb{N}$. Then:*

$$\prod_{l=1}^{N} \chi_{\partial_{j_l}} = \delta_{(j_1,...,j_N)} \chi_{\partial_{j_1}} \text{ in } \mathcal{M}_p,$$

and hence,

$$\varphi_p\left(\prod_{l=1}^{N} \chi_{\partial_{j_l}}\right) = \delta_{(j_1,...,j_N)}\left(\frac{1}{p^{j_1}} - \frac{1}{p^{j_1+1}}\right), \tag{13}$$

where:

$$\delta_{(j_1,...,j_N)} = \left(\prod_{l=1}^{N-1} \delta_{j_l,j_{l+1}}\right)\left(\delta_{j_N,j_1}\right).$$

Proof. The proof of (13) is done by induction on (12). □

Thus, one can get that, for any $S \in \sigma\left(\mathbb{Q}_p\right)$,

$$\varphi_p(\chi_S) = \varphi_p\left(\sum_{j \in \Lambda_S} \chi_{S \cap \partial_j}\right) \tag{14}$$

where Λ_S is in the sense of (7).

$$\begin{aligned} &= \sum_{j\in\Lambda_S} \varphi_p\left(\chi_{S\cap\partial_j}\right) = \sum_{j\in\Lambda_S} \mu_p\left(S\cap\partial_j\right) \\ &= \sum_{j\in\Lambda_S} r_j\left(\frac{1}{p^j}-\frac{1}{p^{j+1}}\right), \end{aligned} \tag{15}$$

by (13), where $0 \leq r_j \leq 1$ are in the sense of (9) for all $j \in \Lambda_S$.

Furthermore, if $S_1, S_2 \in \sigma\left(\mathbb{Q}_p\right)$, then:

$$\begin{aligned} \chi_{S_1}\chi_{S_2} &= \left(\sum_{k\in\Lambda_{S_1}} \chi_{S_1\cap\partial_k}\right)\left(\sum_{j\in\Lambda_{S_2}} \chi_{S_2\cap\partial_j}\right) \\ &= \sum_{(k,j)\in\Lambda_{S_1}\times\Lambda_{S_2}} \delta_{k,j}\chi_{(S_1\cap S_2)\cap\partial_j} \\ &= \sum_{j\in\Lambda_{S_1,S_2}} \chi_{(S_1\cap S_2)\cap\partial_j}, \end{aligned} \tag{16}$$

where:

$$\Lambda_{S_1,S_2} = \Lambda_{S_1}\cap\Lambda_{S_2}.$$

Proposition 3. *Let $S_l \in \sigma(\mathbb{Q}_p)$, and let $\chi_{S_l} \in \left(\mathcal{M}_p,\ \varphi_p\right)$, for $l = 1, ..., N$, for $N \in \mathbb{N}$. Let:*

$$\Lambda_{S_1,...,S_N} = \bigcap_{l=1}^{N} \Lambda_{S_l} \text{ in } \mathbb{Z},$$

where Λ_{S_l} are in the sense of (7), for $l = 1, ..., N$. Then, there exist $r_j \in \mathbb{R}$, such that:

$$0 \leq r_j \leq 1 \text{ in } \mathbb{R}, \text{for } j \in \Lambda_{S_1,...,S_N},$$

and:

$$\varphi_p\left(\prod_{l=1}^{N}\chi_{S_l}\right) = \sum_{j\in\Lambda_{S_1,...,S_N}} r_j\left(\frac{1}{p^j}-\frac{1}{p^{j+1}}\right). \tag{17}$$

Proof. The proof of (17) is done by induction on (16) with the help of (15). □

4. Representations of $\left(\mathcal{M}_p,\ \varphi_p\right)$

Fix a prime p in $\mathcal{P}$, and let $\left(\mathcal{M}_p,\ \varphi_p\right)$ be the p-adic free probability space. By understanding $\mathbb{Q}_p$ as a measure space, construct the L^2-*space* H_p,

$$H_p \overset{def}{=} L^2\left(\mathbb{Q}_p,\ \sigma(\mathbb{Q}_p),\ \mu_p\right) = L^2\left(\mathbb{Q}_p\right), \tag{18}$$

over $\mathbb{C}$. Then, this L^2-space H_p of (18) is a well-defined *Hilbert space* equipped with its *inner product* $<,>_2$,

$$\langle h_1,\ h_2\rangle_2 \overset{def}{=} \int_{\mathbb{Q}_p} h_1 h_2^* d\mu_p, \tag{19}$$

for all $h_1, h_2 \in H_p$.

Definition 2. *We call the Hilbert space H_p of (18), the p-adic Hilbert space.*

By the definition (18) of the p-adic Hilbert space H_p, our $*$-algebra $\mathcal{M}_p$ acts on H_p, via an *algebra-action* α^p,

$$\alpha^p(f)(h) = fh, for all h \in H_p, \tag{20}$$

for all $f \in \mathcal{M}_p$.

Notation: Denote $\alpha^p(f)$ of (20) by α^p_f, for all $f \in \mathcal{M}_p$. Furthermore, for convenience, denote $\alpha^p_{\chi_S}$ simply by α^p_S, for all $S \in \sigma\left(\mathbb{Q}_p\right)$. □

By (20), the linear morphism α^p is indeed a well-determined $*$-algebra-action of $\mathcal{M}_p$ acting on H_p (equivalently, every α^p_f is a $*$-homomorphism from $\mathcal{M}_p$ into the operator algebra $B(H_p)$ of all bounded operators on H_p, for all $f \in \mathcal{M}_p$), since:

$$\begin{aligned}\alpha^p_{f_1f_2}(h) &= f_1f_2h = f_1\left(f_2h\right)\\ &= f_1\left(\alpha^p_{f_2}(h)\right) = \alpha^p_{f_1}\alpha^p_{f_2}(h),\end{aligned}$$

for all $h \in H_p$, implying that:

$$\alpha^p_{f_1f_2} = \alpha^p_{f_1}\alpha^p_{f_2}, \tag{21}$$

for all $f_1, f_2 \in \mathcal{M}_p$; and:

$$\begin{aligned}\left\langle \alpha^p_f(h_1),\ h_2\right\rangle_2 &= \langle fh_1,\ h_2\rangle_2 = \int_{\mathbb{Q}_p} fh_1h_2^*d\mu_p\\ &= \int_{\mathbb{Q}_p} h_1fh_2^*d\mu_p = \int_{\mathbb{Q}_p} h_1\left(h_2f^*\right)^*d\mu_p\\ &= \int_{\mathbb{Q}_p} h_1\left(f^*h_2\right)^*d\mu_p = \left\langle h_1,\ \alpha^p_{f^*}(h_2)\right\rangle_2,\end{aligned}$$

for all $h_1, h_2 \in H_p$, for all $f \in \mathcal{M}_p$, implying that:

$$\left(\alpha^p_f\right)^* = \alpha_{f^*}, for all f \in \mathcal{M}_p, \tag{22}$$

where $<,>_2$ is the inner product (19) on H_p.

Proposition 4. *The linear morphism α^p of (20) is a well-defined $*$-algebra-action of $\mathcal{M}_p$ acting on H_p. Equivalently, the pair $\left(H_p, \alpha^p\right)$ is a Hilbert-space representation of $\mathcal{M}_p$.*

Proof. The proof is done by (21) and (22). □

Definition 3. *The Hilbert-space representation $\left(H_p,\ \alpha^p\right)$ is said to be the p-adic representation of $\mathcal{M}_p$.*

Depending on the p-adic representation $\left(H_p, \alpha^p\right)$ of $\mathcal{M}_p$, one can construct the C^**-subalgebra* M_p of the operator algebra $B(H_p)$.

Definition 4. *Define the C^*-subalgebra M_p of the operator algebra $B(H_p)$ by:*

$$M_p \overset{def}{=} \overline{\alpha^p\left(\mathcal{M}_p\right)} = \overline{\mathbb{C}\left[\alpha^p_f\ : f \in \mathcal{M}_p\right]}, \tag{23}$$

where $\overline{X}$ mean the operator-norm closures of subsets X of $B(H_p)$. Then, this C^*-algebra M_p is called the p-adic C^*-algebra of the p-adic free probability space $\left(\mathcal{M}_p,\ \varphi_p\right)$.

5. Free-Probabilistic Models on M_p

Throughout this section, let us fix a prime $p \in \mathcal{P}$, and let $\left(\mathcal{M}_p,\ \varphi_p\right)$ be the corresponding p-adic free probability space. Let $\left(H_p,\ \alpha^p\right)$ be the p-adic representation of $\mathcal{M}_p$, and let M_p be the p-adic C^*-algebra (23) of $\left(\mathcal{M}_p,\ \varphi_p\right)$.

We here construct suitable free-probabilistic models on M_p. In particular, we are interested in a system $\{\varphi^p_j\}_{j\in\mathbb{Z}}$ of *linear functionals on* M_p, determined by the j^{th} boundaries $\{\partial_j\}_{j\in\mathbb{Z}}$ of $\mathbb{Q}_p$.

Define a linear functional $\varphi^p_j : M_p \to \mathbb{C}$ by a linear morphism,

$$\varphi^p_j(a) \overset{def}{=} \left\langle a\left(\chi_{\partial_j}\right),\ \chi_{\partial_j}\right\rangle_2, \tag{24}$$

for all $a \in M_p$, for all $j \in \mathbb{Z}$, where $<,>_2$ is the inner product (19) on the p-adic Hilbert space H_p of (18).

Remark that if $a \in M_p$, then:

$$a = \sum_{S \in \sigma(\mathbb{Q}_p)} t_S \, \alpha_S^p, \text{ in } M_p$$

(with $t_S \in \mathbb{C}$), where $\sum$ is a finite or infinite (i.e., limit of finite) sum(s) under the C^*-topology for M_p. Thus, the linear functionals φ_j^p of (24) are well defined on M_p, for all $j \in \mathbb{Z}$, i.e., for any fixed $j \in \mathbb{Z}$, one has that:

$$\begin{aligned} \left|\varphi_j^p(a)\right| &= \left| \sum_{S \in \sigma(\mathbb{Q}_p)} t_S \left\langle \chi_{S \cap \partial_j}, \chi_{\partial_j} \right\rangle_2 \right| \\ &= \left| \sum_{S \in \sigma(\mathbb{Q}_p)} t_S \mu_p \left(\chi_{S \cap \partial_j} \right) \right| \\ &\leq \mu_p\left(\partial_j\right) \left| \sum_{S \in \sigma(\mathbb{Q}_p)} t_S \right| \leq \left(\tfrac{1}{p^j} - \tfrac{1}{p^{j+1}} \right) \|a\|, \end{aligned} \tag{25}$$

where:

$$\|a\| = \sup \left\{ \|a(h)\|_2 : h \in H_p \text{ with } \|h\|_2 = 1 \right\}$$

is the C^*-norm on M_p (inherited by the operator norm on the operator algebra $B(H_p)$), and $\|.\|_2$ is the Hilbert-space norm,

$$\|f\|_2 = \sqrt{\langle f, f \rangle_2}, \forall f \in H_p,$$

induced by the inner product $<,>_2$ of (19). Therefore, for any fixed integer $j \in \mathbb{Z}$, the corresponding linear functional φ_j^p of (24) is bounded on M_p.

Definition 5. *Let $j \in \mathbb{Z}$, and let φ_j^p be the linear functional (24) on the p-adic C^*-algebra M_p. Then, the pair $\left(M_p, \varphi_j^p\right)$ is said to be the j^{th} p-adic (non-traditional) C^*-probability space.*

Remark 2. *As in Section 4, the readers can understand the pairs $\left(M_p, \varphi_j^p\right)$ simply as structures consisting of a commutative C^*-algebra M_p and linear functionals φ_j^p on M_p, whose names are j^{th} p-adic C^*-probability spaces for all $j \in \mathbb{Z}$, for $p \in \mathcal{P}$.*

Fix $j \in \mathbb{Z}$, and take the corresponding j^{th} p-adic C^*-probability space $\left(M_p, \varphi_j^p\right)$. For $S \in \sigma\left(\mathbb{Q}_p\right)$ and a generating operator α_S^p of M_p, one has that:

$$\begin{aligned} \varphi_j^p(\alpha_S^p) &= \left\langle \alpha_S^p(\chi_{\partial_j}), \chi_{\partial_j} \right\rangle_2 = \left\langle \chi_{S \cap \partial_j}, \chi_{\partial_j} \right\rangle_2 \\ &= \int_{\mathbb{Q}_p} \chi_{S \cap \partial_j} \chi_{\partial_j}^* d\mu_p = \int_{\mathbb{Q}_p} \chi_{S \cap \partial_j} \chi_{\partial_j} d\mu_p \end{aligned} \tag{26}$$

by (19)

$$\begin{aligned} &= \int_{\mathbb{Q}_p} \chi_{S \cap \partial_j} d\mu_p = \mu_p\left(S \cap \partial_j\right) \\ &= r_S \left(\tfrac{1}{p^j} - \tfrac{1}{p^{j+1}} \right), \end{aligned} \tag{27}$$

for some $0 \leq r_S \leq 1$ in $\mathbb{R}$, for $S \in \sigma\left(\mathbb{Q}_p\right)$.

Proposition 5. *Let $S \in \sigma\left(\mathbb{Q}_p\right)$ and $\alpha_S^p = \alpha_{\chi_S}^p \in \left(M_p, \varphi_j^p\right)$, for a fixed $j \in \mathbb{Z}$. Then, there exists $r_S \in \mathbb{R}$, such that:*

$$0 \leq r_S \leq 1 \text{ in } \mathbb{R},$$

and:

$$\varphi_j^p\left(\left(\alpha_S^p\right)^n\right) = r_S\left(\frac{1}{p^j} - \frac{1}{p^{j+1}}\right), \text{for all } n \in \mathbb{N}. \tag{28}$$

Proof. Remark that the generating operator α_S^p is a projection in M_p, in the sense that:

$$\left(\alpha_S^p\right)^* = \alpha_S^p = \left(\alpha_S^p\right)^2, \text{ in } M_p,$$

so,

$$\left(\alpha_S^p\right)^n = \alpha_S^p, \text{ for all } n \in \mathbb{N}.$$

Thus, for any $n \in \mathbb{N}$, we have:

$$\varphi_j^p\left(\left(\alpha_S^p\right)^n\right) = \varphi_j^p(\alpha_S^p) = r_S\left(\tfrac{1}{p^j} - \tfrac{1}{p^{j+1}}\right),$$

for some $0 \leq r_S \leq 1$ in $\mathbb{R}$, by (27). □

As a corollary of (28), one obtains the following corollary.

Corollary 1. *Let ∂_k be the k^{th} boundaries (10) of $\mathbb{Q}_p$, for all $k \in \mathbb{Z}$. Then:*

$$\varphi_j^p\left(\left(\alpha_{\partial_k}^p\right)^n\right) = \delta_{j,k}\left(\frac{1}{p^j} - \frac{1}{p^{j+1}}\right) \tag{29}$$

for all $n \in \mathbb{N}$, for all $j \in \mathbb{Z}$.

Proof. The formula (29) is shown by (28). □

6. Semigroup C^*-Subalgebras $\mathfrak{S}_p$ of M_p

Let M_p be the p-adic C^*-algebra (23) for an arbitrarily-fixed $p \in \mathcal{P}$. Take operators:

$$P_{p,j} = \alpha_{\partial_j}^p \in M_p, \tag{30}$$

where ∂_j are the j^{th} boundaries (10) of $\mathbb{Q}_p$, for the fixed prime p, for all $j \in \mathbb{Z}$.

Then, these operators $P_{p,j}$ of (30) are *projections* on the p-adic Hilbert space H_p in M_p, i.e.,

$$P_{p,j}^* = P_{p,j} = P_{p,j}^2,$$

for all $j \in \mathbb{Z}$. We now restrict our interest to these projections $P_{p,j}$ of (30).

Definition 6. *Fix $p \in \mathcal{P}$. Let $\mathfrak{S}_p$ be the C^*-subalgebra:*

$$\mathfrak{S}_p = C^*\left(\{P_{p,j}\}_{j\in\mathbb{Z}}\right) = \overline{\mathbb{C}\left[\{P_{p,j}\}_{j\in\mathbb{Z}}\right]} of M_p, \tag{31}$$

where $P_{p,j}$ are projections (30), for all $j \in \mathbb{Z}$. We call this C^*-subalgebra $\mathfrak{S}_p$ the p-adic boundary (C^*-)subalgebra of M_p.

The p-adic boundary subalgebra $\mathfrak{S}_p$ of the p-adic C^*-algebra M_p satisfies the following structure theorem.

Proposition 6. *Let $\mathfrak{S}_p$ be the p-adic boundary subalgebra (31) of the p-adic C^*-algebra M_p. Then:*

$$\mathfrak{S}_p \overset{*\text{-iso}}{=} \bigoplus_{j\in\mathbb{Z}} \left(\mathbb{C}\cdot P_{p,j}\right) \overset{*\text{-iso}}{=} \mathbb{C}^{\oplus|\mathbb{Z}|}, \tag{32}$$

in M_p.

Proof. The proof of (32) is done by the mutual orthogonality of the projections $\{P_{p,j}\}_{j\in\mathbb{Z}}$ in M_p. Indeed, one has:

$$P_{p,j_1}P_{p,j_2} = \alpha^p_{\partial_{j_1}}\alpha^p_{\partial_{j_2}} = \alpha^p_{\partial_{j_1}\cap\partial_{j_2}} = \delta_{j_1,j_2}P_{p,j_1},$$

in $\mathfrak{S}_p$, for all $j_1, j_2 \in \mathbb{Z}$. □

Define now linear functionals φ^p_j (for a fixed prime p) by:

$$\varphi^{(p)}_j = \varphi^p_j \,|_{\mathfrak{S}_p} \, on \mathfrak{S}_p, \tag{33}$$

where φ^p_j in the right-hand side of (33) are the linear functionals (24) on M_p, for all $j \in \mathbb{Z}$.

7. Weighted-Semicircular Elements

Let M_p be the p-adic C^*-algebra, and let $\mathfrak{S}_p$ be the p-adic boundary subalgebra (31) of M_p, satisfying the structure theorem (32). Fix $p \in \mathcal{P}$. Recall that the generating projections $P_{p,j}$ of $\mathfrak{S}_p$ satisfy:

$$\varphi^{(p)}_j\left(P_{p,j}\right) = \frac{1}{p^j} - \frac{1}{p^{j+1}}, \forall j \in \mathbb{Z}, \tag{34}$$

by (33) (also see (28) and (29)).

Now, let ϕ be the *Euler totient function*, an *arithmetic function:*

$$\phi : \mathbb{N} \to \mathbb{C},$$

defined by:

$$\phi(n) = \left|\{k \in \mathbb{N} : k \leq n, \ \gcd(n,k) = 1\}\right|, \tag{35}$$

for all $n \in \mathbb{N}$, where $|X|$ mean the cardinalities of sets X and gcd is the *greatest common divisor*.

It is well known that:

$$\phi(n) = n\left(\prod_{q\in\mathcal{P},\, q|n}\left(1-\tfrac{1}{q}\right)\right),$$

for all $n \in \mathbb{N}$, where "$q \mid n$" means "q divides n." For instance,

$$\phi(p) = p - 1 = p\left(1 - \frac{1}{p}\right), \forall p \in \mathcal{P}. \tag{36}$$

Thus:

$$\begin{aligned}\varphi^{(p)}_j\left(P_{p,j}\right) &= \left(\tfrac{1}{p^j} - \tfrac{1}{p^{j+1}}\right) = \tfrac{1}{p^j}\left(1-\tfrac{1}{p}\right)\\ &= \tfrac{p}{p^{j+1}}\left(1-\tfrac{1}{p}\right) = \tfrac{\phi(p)}{p^{j+1}},\end{aligned}$$

by (34), (35), and (36), for all $P_{p,j} \in \mathfrak{S}_p$. More generally,

$$\varphi^{(p)}_j\left(P_{p,k}\right) = \delta_{j,k}\left(\frac{\phi(p)}{p^{j+1}}\right), \forall p \in \mathcal{P}, k \in \mathbb{Z}. \tag{37}$$

Now, for a fixed prime p, define new linear functionals τ^p_j on $\mathfrak{S}_p$, by linear morphisms satisfying that:

$$\tau^p_j = \frac{1}{\phi(p)}\varphi^{(p)}_j, on \mathfrak{S}_p, \tag{38}$$

for all $j \in \mathbb{Z}$, where φ^p_j are in the sense of (33).

Then, one obtains new (non-traditional) C^*-probabilistic structures,

$$\{\mathfrak{S}_p(j) = \left(\mathfrak{S}_p,\ \tau_j^p\right) : p \in \mathcal{P}, j \in \mathbb{Z}\}, \tag{39}$$

where τ_j^p are in the sense of (38).

Proposition 7. *Let $\mathfrak{S}_p(j) = (\mathfrak{S}_p, \tau_j^p)$ be in the sense of (39), and let $P_{p,k}$ be generating operators of $\mathfrak{S}_p(j)$, for $p \in \mathcal{P}$, $j \in \mathbb{Z}$. Then:*

$$\tau_j^p\left(P_{p,k}^n\right) = \frac{\delta_{j,k}}{p^{j+1}}, for all n \in \mathbb{N}. \tag{40}$$

Proof. The formula (40) is proven by (37) and (38). Indeed, since $P_{p,k}$ are projections in $\mathfrak{S}_p(j)$,

$$\tau_j^p\left(P_{p,k}^n\right) = \tau_j^p\left(P_{p,k}\right) = \delta_{j,k}\left(\tfrac{1}{p^{j+1}}\right),$$

for all $n \in \mathbb{N}$, for all $p \in \mathcal{P}$, and $j, k \in \mathbb{Z}$. □

7.1. Semicircular and Weighted-Semicircular Elements

Let $(A,\ \varphi)$ be an arbitrary (traditional or non-traditional) *topological $*$-probability space* (C^*-probability space, or W^*-probability space, or Banach $*$-probability space, etc.), consisting of a (noncommutative, resp., commutative) topological $*$-algebra A (C^*-algebra, resp., W^*-algebra, resp., Banach $*$-algebra, etc.), and a (bounded or unbounded) linear functional φ on A.

Definition 7. *Let a be a self-adjoint element in $(A,\ \varphi)$. It is said to be even in $(A,\ \varphi)$, if all odd free moments of a vanish, i.e.,*

$$\varphi\left(a^{2n-1}\right) = 0, for all n \in \mathbb{N}. \tag{41}$$

Let a be a "self-adjoint," and "even" element of $(A,\ \varphi)$ satisfying (41). Then, it is said to be semicircular in $(A,\ \varphi)$, if:

$$\varphi(a^{2n}) = c_n, for all n \in \mathbb{N}, \tag{42}$$

where c_k are the k^{th} Catalan number,

$$c_k = \tfrac{1}{k+1}\begin{pmatrix} 2k \\ k \end{pmatrix} = \tfrac{1}{k+1}\tfrac{(2k)!}{(k!)^2} = \tfrac{(2k)!}{k!(k+1)!},$$

for all $k \in \mathbb{N}_0 = \mathbb{N} \cup \{0\}$.

It is well known that, if $k_n(...)$ is the *free cumulant on A in terms of a linear functional φ* (in the sense of [14]), then a self-adjoint element a is *semicircular* in $(A,\ \varphi)$, if and only if:

$$k_n\left(\underbrace{a,\ a,\ .....,\ a}_{n\text{-times}}\right) = \begin{cases} 1 & \text{if } n = 2 \\ 0 & \text{otherwise,} \end{cases} \tag{43}$$

for all $n \in \mathbb{N}$ (e.g., see [14]). The above equivalent free-distributional data (43) of the semicircularity (42) are obtained by the *Möbius inversion of* [14].

Motivated by (43), one can define the *weighted-semicircularity*.

Definition 8. *Let $a \in (A,\ \varphi)$ be a self-adjoint element. It is said to be weighted-semicircular in $(A,\ \varphi)$ with its weight t_0 (in short, t_0-semicircular), if there exists $t_0 \in \mathbb{C}^\times = \mathbb{C} \setminus \{0\}$, such that:*

$$k_n\left(\underbrace{a,\ a,\ ....,\ a}_{n\text{-times}}\right) = \begin{cases} t_0 & \text{if } n = 2 \\ 0 & \text{otherwise,} \end{cases} \tag{44}$$

for all $n \in \mathbb{N}$, where $k_n(...)$ is the free cumulant on A in terms of φ.

By the definition (44) and by the Möbius inversion of [14], one obtains the following free-moment characterization (45) of the weighted-semicircularity (44): A self-adjoint element a is t_0-*semicircular* in (A, φ), if and only if there exists $t_0 \in \mathbb{C}^{\times}$, such that:

$$\varphi(a^n) = \omega_n \, t_0^{\frac{n}{2}} c_{\frac{n}{2}},$$

where:

$$\omega_n = \begin{cases} 1 & \text{if } n \text{ is even} \\ 0 & \text{if } n \text{ is odd,} \end{cases} \tag{45}$$

for all $n \in \mathbb{N}$, where c_m are the m^{th} Catalan numbers for all $m \in \mathbb{N}_0$.

Thus, from below, we use the weighted-semicircularity (44) and its characterization (45) alternatively.

7.2. *Tensor Product Banach $*$-Algebra $\mathfrak{L}\mathfrak{S}_p$*

Let $\mathfrak{S}_p(k) = \left(\mathfrak{S}_p, \tau_k^p\right)$ be a (non-traditional) C^*-probability space (39), for $p \in \mathcal{P}$, $k \in \mathbb{Z}$. Define *bounded linear transformations* $\mathbf{c}_p$ and $\mathbf{a}_p$ "acting on the p-adic boundary subalgebra $\mathfrak{S}_p$ of M_p," by linear morphisms satisfying,

$$\mathbf{c}_p\left(P_{p,j}\right) = P_{p,j+1},$$

and:

$$\mathbf{a}_p\left(P_{p,j}\right) = P_{p,j-1}, \tag{46}$$

on $\mathfrak{S}_p$, for all $j \in \mathbb{Z}$.

By (46), these linear transformations $\mathbf{c}_p$ and $\mathbf{a}_p$ are bounded under the operator-norm induced by the C^*-norm on $\mathfrak{S}_p$. Therefore, the linear transformations $\mathbf{c}_p$ and $\mathbf{a}_p$ are regarded as Banach-space operators "acting on $\mathfrak{S}_p$," by regarding $\mathfrak{S}_p$ as a Banach space (under its C^*-norm). i.e., $\mathbf{c}_p$ and $\mathbf{a}_p$ are elements of the *operator space* $B\left(\mathfrak{S}_p\right)$ consisting of all bounded operators on the Banach space $\mathfrak{S}_p$.

Definition 9. *The Banach-space operators $\mathbf{c}_p$ and $\mathbf{a}_p$ of (46) are called the p-creation, respectively, the p-annihilation on $\mathfrak{S}_p$, for $p \in \mathcal{P}$. Define a new Banach-space operator $l_p \in B\left(\mathfrak{S}_p\right)$ by:*

$$l_p = \mathbf{c}_p + \mathbf{a}_p on \mathfrak{S}_p. \tag{47}$$

We call it the p-radial operator on $\mathfrak{S}_p$.

Let l_p be the p-radial operator $\mathbf{c}_p + \mathbf{a}_p$ of (47) on $\mathfrak{S}_p$. Construct a *closed subspace* $\mathfrak{L}_p$ of $B(\mathfrak{S}_p)$ by:

$$\mathfrak{L}_p = \overline{\mathbb{C}[l_p]} \subset B(\mathfrak{S}_p), \tag{48}$$

where $\overline{Y}$ means the operator-norm-topology closure of every subset Y of the operator space $B(\mathfrak{S}_p)$.

By the definition (48), $\mathfrak{L}_p$ is not only a closed subspace, but also a well-defined Banach algebra embedded in the vector space $B(\mathfrak{S}_p)$. On this Banach algebra $\mathfrak{L}_p$, define the adjoint $(*)$ by:

$$\sum_{k=0}^{\infty} s_k l_p^k \in \mathfrak{L}_p \longmapsto \sum_{k=0}^{\infty} \overline{s_k} l_p^k \in \mathfrak{L}_p, \tag{49}$$

where $s_k \in \mathbb{C}$ with their conjugates $\overline{s_k} \in \mathbb{C}$.

Then, equipped with the adjoint (49), this Banach algebra $\mathfrak{L}_p$ of (48) forms a *Banach $*$-algebra* inside $B(\mathfrak{S}_p)$.

Definition 10. *Let $\mathfrak{L}_p$ be a Banach $*$-algebra (48) in the operator space $B(\mathfrak{S}_p)$ for $p \in \mathcal{P}$. We call it the p-radial (Banach-$*$-)algebra on $\mathfrak{S}_p$.*

Let $\mathfrak{L}_p$ be the p-radial algebra (48) on $\mathfrak{S}_p$. Construct now the tensor product Banach $*$-algebra $\mathfrak{LS}_p$ by:

$$\mathfrak{LS}_p = \mathfrak{L}_p \otimes_{\mathbb{C}} \mathfrak{S}_p, \tag{50}$$

where $\otimes_{\mathbb{C}}$ is the *tensor product of Banach $*$-algebras* (Remark that $\mathfrak{S}_p$ is a C^*-algebra and $\mathfrak{L}_p$ is a Banach $*$-algebra; and hence, the tensor product Banach $*$-algebra $\mathfrak{LS}_p$ of (50) is well-defined.).

Take now a generating element $l_p^k \otimes P_{p,j}$, for some $k \in \mathbb{N}_0 = \mathbb{N} \cup \{0\}$, and $j \in \mathbb{Z}$, where $P_{p,j}$ is in the sense of (30) in $\mathfrak{S}_p$, with axiomatization:

$$l_p^0 = 1_{\mathfrak{S}_p}, \text{ the identity operator on } \mathfrak{S}_p,$$

in $B(\mathfrak{S}_p)$, satisfying:

$$1_{\mathfrak{S}_p}\left(P_{p,j}\right) = P_{p,j}, \text{ for all } P_{p,j} \in \mathfrak{S}_p,$$

for all $j \in \mathbb{Z}$.

By (50) and (32), the elements $l_p^k \otimes P_{p,j}$ indeed generate $\mathfrak{LS}_p$ under linearity, because:

$$\left(l_p \otimes P_{p,j}\right)^k = l_p^k \otimes P_{p,j},$$

for all $k \in \mathbb{N}_0$, and $j \in \mathbb{Z}$, for $p \in \mathcal{P}$, and their self-adjointness. We now focus on such generating operators of $\mathfrak{LS}_p$.

Define a linear morphism:

$$E_p : \mathfrak{LS}_p \to \mathfrak{S}_p$$

by a linear transformation satisfying that:

$$E_p\left(l_p^k \otimes P_{p,j}\right) = \frac{\left(p^{j+1}\right)^{k+1}}{[\frac{k}{2}]+1} l_p^k(P_{p,j}), \tag{51}$$

for all $k \in \mathbb{N}_0$, $j \in \mathbb{Z}$, where $\left[\frac{k}{2}\right]$ is the *minimal integer greater than or equal to* $\frac{k}{2}$, for all $k \in \mathbb{N}_0$; for example,

$$\left[\tfrac{3}{2}\right] = 2 = \left[\tfrac{4}{2}\right].$$

By the cyclicity (48) of the tensor factor $\mathfrak{L}_p$ of $\mathfrak{LS}_p$, and by the structure theorem (32) of the other tensor factor $\mathfrak{S}_p$ of $\mathfrak{LS}_p$, the above morphism E_p of (51) is a well-defined bounded surjective linear transformation.

Now, consider how our p-radial operator l_p of (47) works on $\mathfrak{S}_p$. Observe first that: if $\mathbf{c}_p$ and $\mathbf{a}_p$ are the p-creation, respectively, the p-annihilation on $\mathfrak{S}_p$, then:

$$\mathbf{c}_p\mathbf{a}_p\left(P_{p,j}\right) = P_{p,j} = \mathbf{a}_p\mathbf{c}_p\left(P_{p,j}\right),$$

for all $j \in \mathbb{Z}$, $p \in \mathcal{P}$, and hence:

$$\mathbf{c}_p\mathbf{a}_p = 1_{\mathfrak{S}_p} = \mathbf{a}_p\mathbf{c}_p on \mathfrak{S}_p. \tag{52}$$

Lemma 1. *Let $\mathbf{c}_p$, $\mathbf{a}_p$ be the p-creation, respectively, the p-annihilation on $\mathfrak{S}_p$. Then:*

$$\mathbf{c}_p^n\mathbf{a}_p^n = \left(\mathbf{c}_p\mathbf{a}_p\right)^n = 1_{\mathfrak{S}_p} = \left(\mathbf{a}_p\mathbf{c}_p\right)^n = \mathbf{a}_p\mathbf{c}_p,$$

and:

$$\mathbf{c}_p^{n_1}\mathbf{a}_p^{n_2} = \mathbf{a}_p^{n_2}\mathbf{c}_p^{n_1} on \mathfrak{S}_p, \tag{53}$$

for all n, n_1, $n_2 \in \mathbb{N}_0$.

Proof. The formula (53) holds by (52). □

By (53), one can get that:

$$l_p^n = \left(\mathbf{c}_p + \mathbf{a}_p\right)^n = \sum_{k=0}^n \begin{pmatrix} n \\ k \end{pmatrix} \mathbf{c}_p^k \mathbf{a}_p^{n-k} \text{ on } \mathfrak{S}_p,$$

with identities;

$$\mathbf{c}_p^0 = 1_{\mathfrak{S}_p} = \mathbf{a}_p^0, \tag{54}$$

for all $n \in \mathbb{N}$, where:

$$\begin{pmatrix} n \\ k \end{pmatrix} = \frac{n!}{k!(n-k)!}, \forall k \leq n \in \mathbb{N}_0.$$

Thus, one obtains the following proposition.

Proposition 8. *Let $l_p \in \mathfrak{L}_p$ be the p-radial operator on $\mathfrak{S}_p$. Then:*

$$l_p^{2m-1} \text{ does not contain } 1_{\mathfrak{S}_p} - \text{term, and} \tag{55}$$

$$l_p^{2m} \text{ contains its } 1_{\mathfrak{S}_p} - \text{term}, \begin{pmatrix} 2m \\ m \end{pmatrix} \cdot 1_{\mathfrak{S}_p}, \tag{56}$$

for all $m \in \mathbb{N}$.

Proof. The proofs of (55) and (56) are done by straightforward computations by (53) and (54). See [1] for more details. □

7.3. Weighted-Semicircular Elements $Q_{p,j}$ in $\mathfrak{LS}_p$

Fix $p \in \mathcal{P}$, and let $\mathfrak{LS}_p = \mathfrak{L}_p \otimes_{\mathbb{C}} \mathfrak{S}_p$ be the tensor product Banach $*$-algebra (50) and E_p be the linear transformation (51) from $\mathfrak{LS}_p$ onto $\mathfrak{S}_p$. Throughout this section, fix a generating element:

$$Q_{p,j} = l_p \otimes P_{p,j} of \mathfrak{LS}_p, \tag{57}$$

for $j \in \mathbb{Z}$, where $P_{p,j}$ is a projection (30) generating $\mathfrak{S}_p$. Observe that:

$$Q_{p,j}^n = \left(l_p \otimes P_{p,j}\right)^n = l_p^n \otimes P_{p,j}, \tag{58}$$

for all $n \in \mathbb{N}$, for all $j \in \mathbb{Z}$.

If $Q_{p,j} \in \mathfrak{LS}_p$ is in the sense of (57) for $j \in \mathbb{Z}$, then:

$$E_p\left(Q_{p,j}^n\right) = E_p\left(l_p^n \otimes P_{p,j}\right) = \frac{\left(p^{j+1}\right)^{n+1}}{\left[\frac{n}{2}\right]+1} l_p^n\left(P_{p,j}\right), \tag{59}$$

by (51) and (58), for all $n \in \mathbb{N}$.

Now, for a fixed $j \in \mathbb{Z}$, define a linear functional $\tau_{p,j}^0$ on $\mathfrak{LS}_p$ by:

$$\tau_{p,j}^0 = \tau_j^p \circ E_p on \mathfrak{LS}_p, \tag{60}$$

where $\tau_j^p = \frac{1}{\phi(p)} \varphi_j^{(p)}$ is the linear functional (38) on $\mathfrak{S}_p$.

By the bounded-linearity of both τ_j^p and E_p, the morphism $\tau_{p,j}^0$ of (60) is a bounded linear functional on $\mathfrak{LS}_p$.

By (59) and (60), if $Q_{p,j}$ is in the sense of (57), then:

$$\tau_{p,j}^0\left(Q_{p,j}^n\right) = \frac{\left(p^{j+1}\right)^{n+1}}{\left[\frac{n}{2}\right]+1} \tau_j^p\left(l_p^n(P_{p,j})\right), \tag{61}$$

for all $n \in \mathbb{N}$.

Theorem 1. *Let $Q_{p,j} = l_p \otimes P_{p,j} \in \left(\mathfrak{LS}_p, \tau^0_{p,j}\right)$, for a fixed $j \in \mathbb{Z}$. Then, $Q_{p,j}$ is $p^{2(j+1)}$-semicircular in $\left(\mathfrak{LS}_p,\ \tau^0_{p,j}\right)$. More precisely,*

$$\tau^0_{p,j}\left(Q^n_{p,j}\right) = \omega_n \left(p^{2(j+1)}\right)^{\frac{n}{2}} c_{\frac{n}{2}}, \tag{62}$$

for all $n \in \mathbb{N}$, where ω_n are in the sense of (45). Equivalently, if $k^{0,p,j}_n(...)$ is the free cumulant on $\mathfrak{LS}_p$ in terms of the linear functional $\tau^0_{p,j}$ of (61) on $\mathfrak{LS}_p$, then:

$$k^{0,p,j}_n\left(\underbrace{Q_{p,j},\ Q_{p,j},\ ...,\ Q_{p,j}}_{n\text{-times}}\right) = \begin{cases} p^{2(j+1)} & \text{if } n = 2 \\ 0 & \text{otherwise,} \end{cases} \tag{63}$$

for all $n \in \mathbb{N}$.

Proof. The free-moment formula (62) is obtained by (55), (56) and (61). The free-cumulant formula (63) is obtained by (62) under the Möbius inversion of [14]. See [1] for details. □

8. Semicircularity on $\mathfrak{LS}$

For all $p \in \mathcal{P}$, $j \in \mathbb{Z}$, let:

$$\mathfrak{LS}_p(j) = \left(\mathfrak{LS}_p,\ \tau^0_{p,j}\right) \tag{64}$$

be a Banach $*$-probabilistic model of the Banach $*$-algebra $\mathfrak{LS}_p$ of (50), where $\tau^0_{p,j}$ is the linear functional (60).

Definition 11. *We call the pairs $\mathfrak{LS}_p(j)$ of (64) the j^{textth} p-adic filters, for all $p \in \mathcal{P}$, $j \in \mathbb{Z}$.*

Let $Q_{p,k} = l_p \otimes P_{p,k}$ be the k^{th} generating elements of the j^{th} p-adic filter $\mathfrak{LS}_p(j)$ of (64), for all $k \in \mathbb{Z}$, for fixed $p \in \mathcal{P}$, $j \in \mathbb{Z}$. Then, the generating elements $\{Q_{p,k}\}_{k\in\mathbb{Z}}$ of the j^{th} p-adic filter $\mathfrak{LS}_p(j)$ satisfy that:

$$k^{0,p,j}_n\left(Q_{p,k},\ ...,\ Q_{p,k}\right) = \begin{cases} \delta_{j,k}\, p^{2(j+1)} & \text{if } n = 2 \\ 0 & \text{otherwise,} \end{cases}$$

and:

$$\tau^0_{p,j}\left(Q^n_{p,k}\right) = \delta_{j,k}\left(\omega_n \left(p^{2(j+1)}\right)^{\frac{n}{2}} c_{\frac{n}{2}}\right), \tag{65}$$

for all $p \in \mathcal{P}$, $j \in \mathbb{Z}$, for all $n \in \mathbb{N}$, by (62) and (63), where:

$$\omega_n = \begin{cases} 1 & \text{if } n \text{ is even} \\ 0 & \text{if } n \text{ is odd,} \end{cases}$$

for all $n \in \mathbb{N}$.

For the family:

$$\left\{\mathfrak{LS}_p(j) = \left(\mathfrak{LS}_p,\ \tau^0_{p,j}\right) : p \in \mathcal{P},\ j \in \mathbb{Z}\right\}$$

of j^{th} p-adic filters of (64), one can define the *free product Banach $*$-probability space*,

$$\mathfrak{LS} \overset{denote}{=} \left(\mathfrak{LS},\ \tau^0\right) \overset{def}{=} \underset{p\in\mathcal{P},\ j\in\mathbb{Z}}{\star} \mathfrak{LS}_p(j). \tag{66}$$

as in [14,15], with:

$$\mathfrak{LS} = \underset{p\in\mathcal{P},\, j\in\mathbb{Z}}{\star} \mathfrak{LS}_p, \text{ and } \tau^0 = \underset{p\in\mathcal{P},\, j\in\mathbb{Z}}{\star} \tau^0_{p,j}.$$

Note that the pair $\mathfrak{LS} = \left(\mathfrak{LS},\ \tau^0\right)$ of (66) is a well-defined "traditional or noncommutative" Banach $*$-probability space. For more about the (free-probabilistic) *free product* of free probability spaces, see [14,15].

Definition 12. *The Banach $*$-probability space $\mathfrak{LS} = \left(\mathfrak{LS},\ \tau^0\right)$ of (66) is called the free Adelic filtration.*

Let $\mathfrak{LS}$ be the free Adelic filtration (66). Then, by (65), one can take a subset:

$$\mathcal{Q} = \left\{Q_{p,j} = l_p \otimes P_{p,j} \in \mathfrak{LS}_p(j)\right\}_{p\in\mathcal{P},\, j\in\mathbb{Z}}$$

of $\mathfrak{LS}$, consisting of "j^{th}" generating elements $Q_{p,j}$ of the "j^{th}" p-adic filters $\mathfrak{LS}_p(j)$, which are the free blocks of $\mathfrak{LS}$, for all $j \in \mathbb{Z}$, for all $p \in \mathcal{P}$.

Lemma 2. *Let $\mathcal{Q}$ be the above family in the free Adelic filtration $\mathfrak{LS}$. Then, all elements $Q_{p,j}$ of $\mathcal{Q}$ are $p^{2(j+1)}$-semicircular in the free Adelic filtration $\mathfrak{LS}$.*

Proof. Since all self-adjoint elements $Q_{p,j}$ of the family $\mathcal{Q}$ are chosen from mutually-distinct *free blocks* $\mathfrak{LS}_p(j)$ of $\mathfrak{LS}$, they are $p^{2(j+1)}$-semicircular in $\mathfrak{LS}_p(j)$. Indeed, since every element $Q_{p,j} \in \mathcal{Q}$ is from a free block $\mathfrak{LS}_p(j)$, the powers $Q^n_{p,j}$ are free reduced words with their lengths-N in $\mathfrak{LS}_p(j)$ in $\mathfrak{LS}$. Therefore, each element $Q_{p,j} \in \mathcal{Q}$ satisfies that:

$$\tau^0\left(Q^n_{p,j}\right) = \tau^0_{p,j}\left(Q^n_{p,j}\right) = \omega_n p^{n(j+1)} c_{\frac{n}{2}},$$

equivalently,

$$\begin{aligned} k^0_n\left(Q_{p,j},\ ...,\ Q_{p,j}\right) &= k^{0,p,j}_n\left(Q_{p,j},\ ...,\ Q_{p,j}\right) \\ &= \begin{cases} p^{2(j+1)} & \text{if } n = 2 \\ 0 & \text{otherwise,} \end{cases} \end{aligned}$$

for all $n \in \mathbb{N}$, by (62) and (63), where $k^0_n(...)$ is the free cumulant on $\mathfrak{LS}$ in terms of τ^0. Therefore, all elements $Q_{p,j} \in \mathcal{Q}$ are $p^{2(j+1)}$-semicircular in $\mathfrak{LS}$, for all $p \in \mathcal{P}$, $j \in \mathbb{Z}$. □

Furthermore, since all $p^{2(j+1)}$-semicircular elements $Q_{p,j} \in \mathcal{Q}$ are taken from the mutually-distinct free blocks $\mathfrak{LS}_p(j)$ of $\mathfrak{LS}$, they are mutually free from each other in the free Adelic filtration $\mathfrak{LS}$ of (66), for all $p \in \mathcal{P}$, $j \in \mathbb{Z}$.

Recall that a subset $S = \{a_t\}_{t\in\Delta}$ of an arbitrary (topological or pure-algebraic) $*$-probability space $(A,\ \varphi)$ is said to be a *free family*, if, for any pair $(t_1,\ t_2) \in \Delta^2$ of $t_1 \neq t_2$ in a countable (finite or infinite) index set Δ, the corresponding free random variables a_{t_1} and a_{t_2} are free in $(A,\ \varphi)$ (e.g., [7,14]).

Definition 13. *Let $S = \{a_t\}_{t\in\Delta}$ be a free family in an arbitrary topological $*$-probability space $(A,\ \varphi)$. This family S is said to be a free (weighted-)semicircular family, if it is not only a free family, but also a set consisting of all (weighted-)semicircular elements a_t in $(A,\ \varphi)$, for all $t \in \Delta$.*

Therefore, by the construction (66) of the free Adelic filtration $\mathfrak{LS}$, we obtain the following result.

Theorem 2. *Let $\mathfrak{LS}$ be the free Adelic filtration (66), and let:*

$$\mathcal{Q} = \{Q_{p,j} \in \mathfrak{LS}_p(j)\}_{p\in\mathcal{P},\, j\in\mathbb{Z}} \subset \mathfrak{LS}, \tag{67}$$

where $\mathfrak{LS}_p(j)$ are the j^{th} p-adic filters, the free blocks of $\mathfrak{LS}$. Then, this family $\mathcal{Q}$ of (67) is a free weighted-semicircular family in $\mathfrak{LS}$.

Proof. Let $\mathcal{Q}$ be a subset (67) in $\mathfrak{LS}$. Then, all elements $Q_{p,j}$ of $\mathcal{Q}$ are $p^{2(j+1)}$-semicircular in $\mathfrak{LS}$ by the above lemma, for all $p \in \mathcal{P}$, $j \in \mathbb{Z}$. Furthermore, all elements $Q_{p,j}$ of $\mathcal{Q}$ are mutually free from each other in $\mathfrak{LS}$, because they are contained in the mutually-distinct free blocks $\mathfrak{LS}_p(j)$ of $\mathfrak{LS}$, for all $p \in \mathcal{P}$, $j \in \mathbb{Z}$. Therefore, the family $\mathcal{Q}$ of (67) is a free weighted-semicircular family in $\mathfrak{LS}$. □

Now, take elements:

$$\Theta_{p,j} \overset{def}{=} \frac{1}{p^{j+1}} Q_{p,j}, \forall p \in \mathcal{P}, j \in \mathbb{Z}, \tag{68}$$

in $\mathfrak{LS}$, where $Q_{p,j} \in \mathcal{Q}$, where $\mathcal{Q}$ is the free weighted-semicircular family (67) in the free Adelic filtration $\mathfrak{LS}$.

Then, by the self-adjointness of $Q_{p,j}$, these operators $\Theta_{p,j}$ of (68) are self-adjoint in $\mathfrak{LS}$, as well, because:

$$p^{j+1} \in \mathbb{Q} \subset \mathbb{R} \text{ in } \mathbb{C},$$

satisfying $\overline{p^{j+1}} = p^{j+1}$, for all $p \in \mathcal{P}$, $j \in \mathbb{Z}$.

Furthermore, one obtains the following free-cumulant computation; if $k_n^0(...)$ is the free cumulant on $\mathfrak{LS}$ in terms of τ^0, then:

$$\begin{array}{rcl} k_n^0\left(\Theta_{p,j}, ..., \Theta_{p,j}\right) & = & k_n^{0,p,j}\left(\frac{1}{p^{j+1}} Q_{p,j}, ..., \frac{1}{p^{j+1}} Q_{p,j}\right) \\ & = & \left(\frac{1}{p^{j+1}}\right)^n k_n^{0,p,j}\left(Q_{p,j}, ..., Q_{p,j}\right), \end{array} \tag{69}$$

by the *bimodule-map property* of the free cumulant (e.g., see [14]), for all $n \in \mathbb{N}$, where $k_n^{0,p,j}(...)$ are the free cumulants (63) on the free blocks $\mathfrak{LS}_p(j)$ in terms of the linear functionals $\tau_{p,j}^0$ of (60) on $\mathfrak{LS}_p$, for all $p \in \mathcal{P}$, $j \in \mathbb{Z}$.

Theorem 3. *Let $\Theta_{p,j} = \frac{1}{p^{j+1}} Q_{p,j}$ be free random variables (68) of the free Adelic filtration $\mathfrak{LS}$, for $Q_{p,j} \in \mathcal{Q}$. Then, the family:*

$$\Theta = \left\{\Theta_{p,j} \in \mathfrak{LS}_p(j) : p \in \mathcal{P},\ j \in \mathbb{Z}\right\} \tag{70}$$

forms a free semicircular family in $\mathfrak{LS}$.

Proof. Consider that:

$$\begin{array}{rcl} k_n^0\left(\Theta_{p,j}, ..., \Theta_{p,j}\right) & = & \left(\frac{1}{p^{j+1}}\right)^n k_n^{0,p,j}\left(Q_{p,j}, ..., Q_{p,j}\right) \text{ by (69)} \\ & = & \begin{cases} \left(\frac{1}{p^{j+1}}\right)^2 k_2^{0,p,j}\left(Q_{p,j}, Q_{p,j}\right) & \text{if } n = 2 \\ \left(\frac{1}{p^{j+1}}\right)^n k_n^{0,p,j}\left(Q_{p,j}, ..., Q_{p,j}\right) = 0 & \text{otherwise,} \end{cases} \end{array}$$

by the $p^{2(j+1)}$-semicircularity of $Q_{p,j} \in \mathcal{Q}$ in $\mathfrak{LS}$:

$$= \begin{cases} \left(\frac{1}{p^{j+1}}\right)^2 \left(p^{j+1}\right)^2 = 1 & \text{if } n = 2 \\ 0 & \text{otherwise,} \end{cases} \tag{71}$$

for all $n \in \mathbb{N}$.

By the free-cumulant computation (71), these self-adjoint free random variables $\Theta_{p,j} \in \mathfrak{LS}_p(j)$ are semicircular in $\mathfrak{LS}$ by (43), for all $p \in \mathcal{P}$, $j \in \mathbb{Z}$.

Furthermore, the family Θ of (70) forms a free family in $\mathfrak{LS}$, because all elements $\Theta_{p,j}$ are the scalar-multiples of $Q_{p,j} \in \mathcal{Q}$, contained in mutually-distinct free blocks $\mathfrak{LS}_p(j)$ of $\mathfrak{LS}$, for all $j \in \mathbb{Z}$, $p \in \mathcal{P}$.

Therefore, this family Θ of (70) is a free semicircular family in $\mathfrak{LS}$. □

Now, define a Banach $*$-subalgebra $\mathbb{LS}$ of $\mathfrak{LS}$ by:

$$\mathbb{LS} \stackrel{def}{=} \overline{\mathbb{C}[\mathcal{Q}]}in\mathfrak{LS}, \tag{72}$$

where $\mathcal{Q}$ is the free weighted-semicircular family (67) and $\overline{Y}$ means the Banach-topology closures of subsets Y of $\mathfrak{LS}$.

Then, one can obtain the following structure theorem for the Banach $*$-algebra $\mathbb{LS}$ of (72) in $\mathfrak{LS}$.

Theorem 4. *Let $\mathbb{LS}$ be the Banach $*$-subalgebra (72) of the free Adelic filtration $\mathfrak{LS}$ generated by the free weighted-semicircular family $\mathcal{Q}$ of (67). Then:*

$$\mathbb{LS} = \overline{\mathbb{C}[\Theta]}in\mathfrak{LS}, \tag{73}$$

where Θ is the free semicircular family (70) and where "$=$" means "being identically same as sets." Moreover,

$$\mathbb{LS} \stackrel{*\text{-}iso}{=} \underset{p\in\mathcal{P},\, j\in\mathbb{Z}}{\star} \overline{\mathbb{C}\left[\{Q_{p,j}\}\right]} \stackrel{*\text{-}iso}{=} \overline{\mathbb{C}\left[\underset{p\in\mathcal{P},\, j\in\mathbb{Z}}{\star}\{Q_{p,j}\}\right]}, \tag{74}$$

in $\mathfrak{LS}$, where "$\stackrel{*\text{-}iso}{=}$" means "being Banach-$*$-isomorphic," and:

$$\overline{\mathbb{C}\left[\{Q_{p,j}\}\right]} \text{ are Banach } *\text{-subalgebras of } \mathfrak{LS}_p(j),$$

for all $p \in \mathcal{P}$, $j \in \mathbb{Z}$, in $\mathfrak{LS}$.

Here, $(\star)$ in the first $*$-isomorphic relation of (74) is the (free-probability-theoretic) free product of [14,15], and $(\star)$ in the second $*$-isomorphic relation of (74) is the (pure-algebraic) free product (generating noncommutative algebraic free words in the family $\mathcal{Q}$).

Proof. Let $\mathbb{LS}$ be the Banach $*$-subalgebra (72) of $\mathfrak{LS}$. Then, all generating operators $Q_{p,j} \in \mathcal{Q}$ of $\mathbb{LS}$ are contained in mutually-distinct free blocks $\mathfrak{LS}_p(j)$ of $\mathfrak{LS}$, and hence, the Banach $*$-subalgebras $\overline{\mathbb{C}\left[\{Q_{p,j}\}\right]}$ of $\mathfrak{LS}$ are contained in the free blocks $\mathfrak{LS}_p(j)$, for all $p \in \mathcal{P}$, $j \in \mathbb{Z}$. Therefore, as embedded sub-structures of $\mathfrak{LS}$, they are free from each other. Equivalently,

$$\mathbb{LS} \stackrel{*\text{-iso}}{=} \underset{p\in\mathcal{P},\, j\in\mathbb{Z}}{\star} \overline{\mathbb{C}\left[\{Q_{p,j}\}\right]}in\mathfrak{LS}, \tag{75}$$

by (66).

Since every free block $\overline{\mathbb{C}\left[\{Q_{p,j}\}\right]}$ of the Banach $*$-algebra $\mathbb{LS}$ of (75) is generated by a single self-adjoint (weighted-semicircular) element, every operator T of $\mathbb{LS}$ is a limit of linear combinations of free words in the free family $\mathcal{Q}$ of (67), which form noncommutative free "reduced" words (in the sense of [14,15]), as operators in $\mathbb{LS}$ of (75). Note that every (pure-algebraic) free word in $\mathcal{Q}$ has a unique free reduced word in $\mathbb{LS}$, under operator-multiplication on $\mathfrak{LS}$ (and hence, on $\mathbb{LS}$). Therefore, the $*$-isomorphic relation (75) guarantees that:

$$\mathbb{LS} \stackrel{*\text{-iso}}{=} \overline{\mathbb{C}\left[\underset{p\in\mathcal{P},\, j\in\mathbb{Z}}{\star}\{Q_{p,j}\}\right]}, \tag{76}$$

where the free product $(\star)$ in (76) is pure-algebraic.

Remark that, indeed, the relation (76) holds well, because all weighted-semicircular elements of $\mathcal{Q}$ are self-adjoint; if:

$$T = \prod_{l=1}^{N} Q_{p_l,j_l}^{n_l} \in \mathbb{LS}$$

is a free (reduced) word (as an operator), then:

$$T^* = \prod_{l=1}^{N} Q_{p_{N-l+1}, j_{N-l+1}}^{n_{N-l+1}} \in \mathbb{LS}$$

is a free word of $\mathbb{LS}$ in $\mathcal{Q}$, as well. Therefore, by (75) and (76), the structure theorem (74) holds true.

Note now that $Q_{p,j} \in \mathcal{Q}$ satisfy:

$$Q_{p,j} = p^{j+1}\Theta_{p,j}, \text{ for all } p \in \mathcal{P}, j \in \mathbb{Z},$$

where $\Theta_{p,j}$ are semicircular elements in the family Θ of (70). Therefore, the free blocks of (75) satisfy that:

$$\overline{\mathbb{C}\left[\{Q_{p,j}\}\right]} = \overline{\mathbb{C}\left[\{p^{j+1}\Theta_{p,j}\}\right]} = \overline{\mathbb{C}\left[\{\Theta_{p,j}\}\right]}, \tag{77}$$

for all $p \in \mathcal{P}$, $j \in \mathbb{Z}$.

Thus, one can get that:

$$\mathbb{LS} \overset{*\text{-iso}}{=} \underset{p\in\mathcal{P},\, j\in\mathbb{Z}}{\star} \overline{\mathbb{C}\left[\{\Theta_{p,j}\}\right]}, \tag{78}$$

by (75) and (77).

With similar arguments of (75), we have:

$$\mathbb{LS} = \overline{\mathbb{C}[\Theta]}, set - theoretically, \tag{79}$$

by (78).

Therefore, the identity (73) holds true by (79). □

As a sub-structure, one can restrict the linear functional τ^0 of (66) on $\mathfrak{LS}$ to that on $\mathbb{LS}$, i.e., one can obtain the Banach $*$-probability space,

$$\left(\mathbb{LS},\ \tau^0 \overset{denote}{=} \tau^0\,|_{\mathbb{LC}}\right). \tag{80}$$

Definition 14. *Let* $(\mathbb{LS}, \tau^0)$ *be the Banach* $*$*-probability space* (80)*. Then, we call* $(\mathbb{LS}, \tau^0)$ *the semicircular (free Adelic sub-)filtration of* $\mathfrak{LS}$.

Note that, by (66), all elements of the semicircular filtration $(\mathbb{LS}, \tau^0)$ provide "possible" non-vanishing free distributions in the free Adelic filtration $\mathfrak{LS}$. Especially, all free reduced words of $\mathfrak{LS}$ in the generator set $\{Q_{p,j}\}_{p\in P, j\in\mathbb{Z}}$ have non-zero free distributions only if they are contained in $(\mathbb{LS}, \tau^0)$. Therefore, studying free-distributional data on $(\mathbb{LS}, \tau^0)$ is to study possible non-zero free-distributional data on $\mathfrak{LS}$.

9. Truncated Linear Functionals on $\mathbb{LS}$

In *number theory*, one of the most interesting, but difficult topics is to find a number of primes or a density of primes contained in closed intervals $[t_1, t_2]$ of the real numbers $\mathbb{R}$ (e.g., [3,6,21,22]). Since the theory is deep, we will not discuss more about it here. Hhowever, motivated by the theory, we consider certain "suitable" *truncated linear functionals* on our semicircular filtration $(\mathbb{LS}, \tau^0)$ of (80) in the free Adelic filtration $\mathfrak{LS}$ of (66).

Notation: From below, we will use the following notations to distinguish their structural differences;

$\mathbb{LS} \overset{denote}{=}$ the Banach $*$-subalgebra (72) of $\mathfrak{LS}$,

$\mathbb{LS}_0 \overset{denote}{=}$ the semicircular filtration $\left(\mathbb{LS},\ \tau^0\right)$ of (80).

□

9.1. Linear Functionals $\{\tau_{(t)}\}_{t\in\mathbb{R}}$ *on* $\mathbb{LS}$

Let $\mathbb{LS}_0$ be the semicircular filtration $(\mathbb{LS}, \tau^0)$ of the free Adelic filtration $\mathfrak{LS}$. Furthermore, let $\mathcal{Q}$ and Θ be the free weighted-semicircular family (67), respectively, the free semicircular family (70) of $\mathfrak{LS}$, generating $\mathbb{LS}$ by (73) and (74). We here truncate τ^0 on $\mathbb{LS}$ for a fixed real number $t \in \mathbb{R}$.

First, recall and remark that:

$$\tau^0 = \underset{p\in\mathcal{P},\, j\in\mathbb{Z}}{\star} \tau^0_{p,j} \text{ on } \mathbb{LS},$$

by (66) and (80). Therefore, one can sectionize τ^0 over $\mathcal{P}$, as follows;

$$\tau^0 = \underset{p\in\mathcal{P}}{\star} \tau^0_p \text{ on } \mathbb{LS},$$

with:

$$\tau^0_p = \underset{j\in\mathbb{Z}}{\star} \tau^0_{p,j} on \mathbb{LS}_p, forall p \in \mathcal{P}, \tag{81}$$

where:

$$\mathbb{LS}_p \overset{def}{=} \underset{j\in\mathbb{Z}}{\star} \overline{\mathbb{C}[\{\Theta_{p,j}\}]} \subset \mathbb{LS} \subset \mathfrak{LS}, \tag{82}$$

for each $p \in \mathcal{P}$, under (74).

From below, we understand the Banach $*$-subalgebras $\mathbb{LS}_p$ of $\mathbb{LS}$ as free-probabilistic sub-structures,

$$\mathbb{LS}_{(p)} \overset{denote}{=} \left(\mathbb{LS}_p,\ \tau^0_p\right), forall p \in \mathcal{P}. \tag{83}$$

Lemma 3. *Let* $\mathbb{LS}_{p_l}$ *be in the sense of* (82) *in the semicircular filtration* $\mathbb{LS}_0$*, for* $l = 1, 2$*. Then,* $\mathbb{LS}_{p_1}$ *and* $\mathbb{LS}_{p_2}$ *are free in* $\mathbb{LS}_0$*, if and only if* $p_1 \neq p_2$ *in* $\mathcal{P}$*.*

Proof. The proof is directly done by (81) and (82). Indeed,

$$\begin{aligned}\mathbb{LS} &= \underset{p\in\mathcal{P},\, j\in\mathbb{Z}}{\star} \overline{\mathbb{C}\left[\{\Theta_{p,j}\}\right]} \\ &= \underset{p\in\mathcal{P}}{\star} \left(\underset{j\in\mathbb{Z}}{\star} \overline{\mathbb{C}\left[\{\Theta_{p,j}\}\right]}\right) = \underset{p\in\mathcal{P}}{\star} \mathbb{LS}_p,\end{aligned}$$

by (80) and (82).

Therefore, $\mathbb{LS}_{p_1}$ and $\mathbb{LS}_{p_2}$ are free in $\mathbb{LS}_0$, if and only if $p_1 \neq p_2$ in $\mathcal{P}$. □

Fix now $t \in \mathbb{R}$, and define a new linear functional $\tau_{(t)}$ on $\mathbb{LS}$ by:

$$\tau_{(t)} \overset{def}{=} \begin{cases} \underset{p\leq t}{\star} \tau^0_p & \text{on } \underset{p\leq t}{\star} \mathbb{LS}_p \subset \mathbb{LS} \\ O & \text{on } \mathbb{LS} \setminus \left(\underset{p\leq t}{\star} \mathbb{LS}_p\right), \end{cases} \tag{84}$$

where τ^0_p are the linear functionals (81) on the Banach $*$-subalgebras $\mathbb{LS}_p$ of (82) in $\mathbb{LS}_0$, for all $p \in \mathcal{P}$, and O means the *zero linear functional* on $\mathbb{LS}$, satisfying that:

$$O(T) = 0, \text{ for all } T \in \mathbb{LS}.$$

For convenience, if there is no confusion, we simply write the definition (84) as:

$$\tau_{(t)} \overset{denote}{=} \underset{p\leq t}{\star} \tau^0_p. \tag{85}$$

By the definition (84) (with a simpler expression (85)), one can easily verify that, if $t < 2$ in $\mathbb{R}$, then the corresponding linear functional $\tau_{(t)}$ is identical to the zero linear functional O on $\mathbb{LS}$. To avoid such triviality, one may refine $\tau_{(t)}$ of (84) by:

$$\tau_{(t)} \stackrel{def}{=} \begin{cases} \tau_{(t)} \text{ of (84)} & \text{if } t \geq 2 \\ O & \text{if } t < 2, \end{cases} \tag{86}$$

for all $t \in \mathbb{R}$.

In the following text, $\tau_{(t)}$ mean the linear functionals in (86), satisfying (84) whenever $t \geq 2$, for all $t \in \mathbb{R}$. In fact, we are not interested in the cases where $t < 2$.

For example,

$$\tau_{(\frac{\sqrt{3}}{2})} = O, \tau_{(2.1003)} = \tau_2^0, and \tau_{(6)} = \tau_2^0 \star \tau_3^0 \star \tau_5^0,$$

on $\mathbb{LS}$, under (85), etc.

Theorem 5. *Let $Q_{p,j} \in \mathcal{Q}$ and $\Theta_{p,j} \in \Theta$ in the semicircular filtration $\mathbb{LS}_0$, for $p \in \mathcal{P}$, $j \in \mathbb{Z}$, and let $t \in \mathbb{R}$ and $\tau_{(t)}$, the corresponding linear functional (86) on $\mathbb{LS}$. Then:*

$$\tau_{(t)}\left(Q_{p,j}^n\right) = \begin{cases} \omega_n p^{2(j+1)} c_{\frac{n}{2}} & \text{if } t \geq p \\ 0 & \text{if } t < p, \end{cases}$$

and:

$$\tau_{(t)}\left(\Theta_{p,j}^n\right) = \begin{cases} \omega_n c_{\frac{n}{2}} & \text{if } t \geq p \\ 0 & \text{if } t < p, \end{cases} \tag{87}$$

for all $n \in \mathbb{N}$.

Proof. By the $p^{2(j+1)}$-semicircularity of $Q_{p,j} \in \mathcal{Q}$, the semicircularity of $\Theta_{p,j} \in \Theta$ in the semicircular filtration $\mathbb{LS}_0$, and by the definition (86), if $t \geq p$ in $\mathbb{R}$, then:

$$\begin{aligned} \tau_{(t)}\left(Q_{p,j}^n\right) &= \tau_p^0\left(Q_{p,j}^n\right) = \tau_{p,j}^0\left(Q_{p,j}^n\right) \\ &= \omega_n p^{2(j+1)} c_{\frac{n}{2}}, \end{aligned}$$

and:

$$\begin{aligned} \tau_{(t)}\left(\Theta_{p,j}^n\right) &= \tau_p^0\left(\Theta_{p,j}^n\right) = \tau_{p,j}^0\left(\Theta_{p,j}^n\right) \\ &= \omega_n c_{\frac{n}{2}}, \end{aligned}$$

by (62), (71), and (81), for all $n \in \mathbb{N}$.

If $t < p$, then:

$$\tau_{(t)} = \underset{2 \leq q < t < p \text{ in } \mathcal{P}}{\star} \tau_q^0 \text{ or } O, \text{ on } \mathbb{LS}.$$

Therefore, in such cases,

$$\tau_{(t)}\left(Q_{p,j}^n\right) = \tau_{(t)}\left(\Theta_{p,j}^n\right) = 0, \text{ for all } n \in \mathbb{N},$$

by (84), (85), and (86).

Therefore, the free-distributional data (87) for the linear functional $\tau_{(t)}$ hold on $\mathbb{LS}$. □

The above theorem shows how the original free-probabilistic information on the semicircular filtration $\mathbb{LS}_0$ is affected by the new free-probabilistic models on $\mathbb{LS}$, under "truncated" linear functionals $\tau_{(t)}$ of τ^0 on $\mathbb{LS}$, for $t \in \mathbb{R}$.

Definition 15. *Let $\tau_{(t)}$ be the linear functionals (86) on $\mathbb{LS}$, for $t \in \mathbb{R}$. Then, the corresponding new Banach $*$-probability spaces,*

$$\mathbb{LS}_{(t)} \overset{denote}{=} \left(\mathbb{LS},\ \tau_{(t)}\right), \tag{88}$$

are called the semicircular t-(truncated-)filtrations of $\mathbb{LS}$ (or, of $\mathbb{LS}_0$).

Note that if t is "suitable" in the sense that "$\tau_{(t)} \neq O$ on $\mathbb{LS}$," then the free-probabilistic structure $\mathbb{LS}_{(t)}$ of (88) is meaningful.

Notation and Assumption 9.1 (**NA 9.1**, from below): In the following, we will say "$t \in \mathbb{R}$ is suitable," if the semicircular t-filtration "$\mathbb{LS}_{(t)}$ of (88) is meaningful," in the sense that: $\tau_{(t)} \neq O$ fully on $\mathbb{LS}$. □

Now, let us consider the following concepts.

Definition 16. *Let (A_k, φ_k) be Banach $*$-probability spaces (or C^*-probability spaces, or W^*-probability spaces, etc.), for $k = 1, 2$. A Banach $*$-probability space (A_1, φ_1) is said to be free-homomorphic to a Banach $*$-probability space (A_2, φ_2), if there exists a bounded $*$-homomorphism:*

$$\Phi : A_1 \to A_2,$$

such that:

$$\varphi_2\left(\Phi(a)\right) = \varphi_1\left(a\right),$$

for all $a \in A_1$. Such a $*$-homomorphism Φ is called a free-homomorphism.

If Φ is both a $*$-isomorphism and a free-homomorphism, then Φ is said to be a free-isomorphism, and we say that (A_1, φ_1) and (A_2, φ_2) are free-isomorphic. Such a free-isomorphic relation is nothing but the equivalence in the sense of Voiculescu (e.g., [15]).

By (87), we obtain the following free-probabilistic-structural theorem.

Theorem 6. *Let $\mathbb{LS}_q = \underset{j\in\mathbb{Z}}{\star} \overline{\mathbb{C}\left[\{Q_{q,j}\}\right]}$ be Banach $*$-subalgebras (82) of $\mathbb{LS}$, for all $q \in \mathcal{P}$. Let $t \in \mathbb{R}$ be suitable in the sense of **NA 9.1** and $\mathbb{LS}_{(t)}$ be the corresponding semicircular t-filtration (88). Construct a Banach $*$-probability space $\mathbb{LS}^t$ by a Banach $*$-probabilistic sub-structure of the semicircular filtration $\mathbb{LS}_0$,*

$$\mathbb{LS}^t \overset{def}{=} \underset{p\leq t}{\star} \left(\mathbb{LS}_p,\ \tau_p^0\right) = \left(\underset{p\leq t}{\star} \mathbb{LS}_p,\ \underset{p\leq t}{\star} \tau_p^0\right), \tag{89}$$

where $\tau_p^0 = \underset{j\in\mathbb{Z}}{\star} \tau_{p,j}^0$ are in the sense of (81). Then:

$$\mathbb{LS}^t is free - homomorphic to \mathbb{LS}_{(t)}. \tag{90}$$

Proof. Let $\mathbb{LS}_{(t)}$ be the semicircular t-filtration (88) of $\mathbb{LS}$, and let $\mathbb{LS}^t$ be a Banach $*$-probability space (89), for a suitably fixed $t \in \mathbb{R}$.

Define a bounded linear morphism:

$$\Phi_t : \mathbb{LS}^t \to \mathbb{LS}_{(t)},$$

by the natural embedding map,

$$\Phi_t\left(T\right) = T in \mathbb{LS}_{(t)}, for\ all T \in \mathbb{LS}^t. \tag{91}$$

Then, this morphism Φ_t is an injective bounded $*$-homomorphism from $\mathbb{LS}^t$ into $\mathbb{LS}_{(t)}$, by (72), (75), (82), (89), and (91).

Therefore, one obtains that:

$$\tau_{(t)}\left(\Phi(T)\right) = \tau_{(t)}(T) = \left(\underset{p\leq t \text{ in } \mathcal{P}}{\star} \tau_p^0\right)(T) = \tau^t(T),$$

for all $T \in \mathbb{LS}^t$, by (87).

It shows that the Banach $*$-probability space $\mathbb{LS}^t$ of (89) is free-homomorphic to the semicircular t-filtration $\mathbb{LS}_{(t)}$ of (88). Therefore, the statement (90) holds under the free-homomorphism Φ_t of (91). □

The above theorem shows that the Banach $*$-probability spaces $\mathbb{LS}^t$ of (89) are free-homomorphic to the semicircular t-filtrations $\mathbb{LS}_{(t)}$ of (88), for all $t \in \mathbb{R}$. Note that it "seems" they are not free-isomorphic, because:

$$\left(\underset{q\leq t \text{ in } \mathcal{P}}{\star} \mathbb{LS}_q\right) \subsetneq \left(\underset{p\in\mathcal{P}}{\star} \mathbb{LS}_p\right) = \mathbb{LS},$$

set-theoretically, for $t \in \mathbb{R}$. However, we are not sure at this moment that they are free-isomorphic or not, because we have the similar difficulties discussed in [19].

Remark 3. *The famous main result of [19] says that: if $L(F_n)$ are the free group factors (group von Neumann algebras) of the free groups F_n with n-generators, for all:*

$$n \in \mathbb{N}_{>1}^{\infty} = (\mathbb{N} \setminus \{1\}) \cup \{\infty\},$$

then either (I) or (II) holds true, where:

(I) $L(F_n) \overset{*\text{-iso}}{=} L(F_\infty)$, for all $n \in \mathbb{N}_{>1}^{\infty}$,

(II) $L(F_{n_1}) \overset{*\text{-iso}}{\neq} L(F_{n_2})$, if and only if $n_1 \neq n_2 \in \mathbb{N}_{>1}^{\infty}$,

where "$\overset{*\text{-iso}}{=}$" means "being W-isomorphic." Depending on the author's knowledge, he does not know which one is true at this moment.*

We here have similar troubles. Under the similar difficulties, we are not sure at this moment that $\mathbb{LS}^t$ and $\mathbb{LS}_{(t)}$ (or $\mathbb{LS}^t$ and $\mathbb{LS}$) are $*$-isomorphic or not (and hence, free-isomorphic or not).

However, definitely, $\mathbb{LS}^t$ is free-homomorphic "into" $\mathbb{LS}_{(t)}$ in the semicircular filtration $\mathbb{LS}_0$, by the above theorem.

The above free-homomorphic relation (90) lets us understand all
"non-zero" free distributions of free reduced words of $\mathbb{LS}_{(t)}$ as those of $\mathbb{LS}^t$, for all $t \in \mathbb{R}$, by the injectivity of a free-homomorphism Φ_t of (91).

Corollary 2. *All free reduced words T of the semicircular t-filtration $\mathbb{LS}_{(t)}$ in $\mathcal{Q} \cup \Theta$, having non-zero free distributions, are contained in the Banach $*$-probability space $\mathbb{LS}^t$ of (89), whenever t is suitable. The converse holds true, as well.*

Proof. The proof of this characterization is done by (87), (89), and (90). In particular, the injectivity of the free-homomorphism Φ_t of (91) guarantees that this characterization holds. □

Therefore, whenever we consider a non-zero free-distribution having free reduced words T of semicircular t-filtrations $\mathbb{LS}_{(t)}$, they are regarded as free random variables of the Banach $*$-probability spaces $\mathbb{LS}^t$ of (89), for all suitable $t \in \mathbb{R}$.

9.2. Truncated Linear Functionals $\tau_{t_1<t_2}$ on $\mathbb{LS}$

In this section, we generalize the semicircular t-filtrations $\mathbb{LS}_{(t)}$ by defining so-called *truncated linear functionals* on the Banach $*$-algebra $\mathbb{LS}$.

Throughout this section, let $[t_1, t_2]$ be a *closed interval* in $\mathbb{R}$, satisfying:

$$|t_1 - t_2| \neq 0, \text{ for } t_1 < t_2 \in \mathbb{R}.$$

For such a fixed closed interval $[t_1, t_2]$, define the corresponding linear functional $\tau_{t_1<t_2}$ on the semicircular filtration $\mathbb{LS}$ by:

$$\tau_{t_1<t_2} \stackrel{def}{=} \begin{cases} \underset{t_1\leq p\leq t_2 \text{ in } \mathcal{P}}{\star} \tau_p^0 & \text{on } \underset{t_1\leq p\leq t_2 \text{ in } \mathcal{P}}{\star} \mathbb{LS}_p \subset \mathbb{LS} \\ O & \text{on } \mathbb{LS} \setminus \left(\underset{t_1\leq p\leq t_2 \text{ in } \mathcal{P}}{\star} \mathbb{LS} \right), \end{cases} \tag{92}$$

where τ_p^0 are the linear functionals (81) on the Banach $*$-subalgebras $\mathbb{LS}_p$ of (82) in $\mathbb{LS}$, for $p \in \mathcal{P}$. Similar to Section 9.1, if there is no confusion, then we simply write the definition (92) as:

$$\tau_{t_1<t_2} \stackrel{denote}{=} \underset{t_1\leq p\leq t_2}{\star} \tau_p^0 on \mathbb{LS}. \tag{93}$$

To make the linear functionals $\tau_{t_1<t_2}$ of (92) be non-zero-linear functionals on $\mathbb{LS}$, the interval $[t_1, t_2]$ must be taken "suitably." For example,

$$\tau_{t_1<t_2} = O, \text{ whenever } t_2 < 2,$$

and:

$$\tau_{8<10} = O, \tau_{14<16} = O, \text{ and } \tau_{\frac{3}{7}<\frac{3}{2}} = O, \text{ etc.},$$

but:

$$\tau_{\frac{3}{2}<8} = \tau_{(8)} = \tau_2^0 \star \tau_3^0 \star \tau_5^0 \star \tau_7^0$$

and:

$$\tau_{7<14} = \tau_7^0 \star \tau_{11}^0 \star \tau_{13}^0,$$

under (93) on $\mathbb{LS}$.

It is not difficult to check that the definition (92) of truncated linear functionals $\tau_{t_1<t_2}$ covers the definition of linear functionals $\tau_{(t)}$ of (86). In particular, $\tau_{(t)}$ is "suitable" in the sense of **NA 9.1**, then:

$$\tau_{(t)} = \tau_{2<t} = \tau_{s<t}, \text{ for all } 2 \geq s \in \mathbb{R}.$$

For our purposes, we will axiomatize:

$$\tau_{p<p} = \tau_p^0, \text{ for all } p \in \mathcal{P} \subset \mathbb{R},$$

notationally, where τ_p^0 are the linear functionals (81), for all $p \in \mathcal{P}$, under (93). Remark that the very above axiomatized notations $\tau_{p<p}$ will be used only when p are primes.

Definition 17. *Let $[t_1, t_2]$ be a given interval in $\mathbb{R}$ and $\tau_{t_1<t_2}$, the corresponding linear functional (92) on $\mathbb{LS}$. Then, we call it the $[t_1, t_2]$(-truncated)-linear functional on $\mathbb{LS}$. The corresponding Banach $*$-probability space:*

$$\mathbb{LS}_{t_1<t_2} = (\mathbb{LS}, \tau_{t_1<t_2}) \tag{94}$$

is said to be the semicircular a $[t_1, t_2]$(-truncated)-filtration.

As we discussed in the above paragraphs, the semicircular $[t_1, t_2]$-filtration $\mathbb{LS}_{t_1<t_2}$ of (94) will be "meaningful," if $t_1 < t_2$ are suitable in $\mathbb{R}$, as in **NA 9.1**.

Notation and Assumption 9.2 (**NA 9.2**, from below): In the rest of this paper, if we write "$t_1 < t_2$ are suitable," then this means "$\mathbb{LS}_{t_1<t_2}$ is meaningful," in the sense that $\tau_{t_1<t_2} \neq O$ fully on $\mathbb{LS}$, with additional axiomatization:

$$\tau_{p<p} = \tau_p^0, \text{ for } p \in \mathcal{P} \text{ in } \mathbb{R},$$

in the sense of (93). □

Theorem 7. *Let $t_1 \leq 2$ and t_2 be suitable in $\mathbb{R}$ in the sense of* ***NA 9.1****.*

$$\text{The semicircular } [t_1, t_2]\text{-filtration } \mathbb{LS}_{t_1<t_2} \text{ is not only suitable in the sense of } \textbf{NA 9.2}\text{, but also, it is free-isomorphic to the semicircular } t_2\text{-filtration } \mathbb{LS}_{(t_2)} \text{ of (88).} \tag{95}$$

$$\text{The Banach } *-\text{probability space } \mathbb{LS}^{t_2} \text{ of (89) is free-homomorphic to } \mathbb{LS}_{t_1<t_2}. \tag{96}$$

Proof. Suppose $t_1 \leq 2$, and t_2 are suitable in $\mathbb{R}$ in the sense of **NA 9.1**. Then, $t_1 < t_2$ are suitable in $\mathbb{R}$ in the sense of **NA 9.2**. Therefore, both the semicircular t_2-filtration $\mathbb{LS}_{(t_2)}$ and the semicircular $[t_1, t_2]$-filtration $\mathbb{LS}_{t_1<t_2}$ are meaningful.

Since t_1 is assumed to be less than or equal to two, the linear functional $\tau_{t_1<t_2} = \tau_{(t_2)}$, by (86) and (92), including the case where $\tau_{2<2} = \tau_2^0$, in the sense of (93). Therefore,

$$\mathbb{LS}_{t_1<t_2} = (\mathbb{LS},\ \tau_{t_1<t_2}) = \left(\mathbb{LS},\ \tau_{(t_2)}\right) = \mathbb{LS}_{(t_2)}.$$

Therefore, $\mathbb{LS}_{t_1<t_2}$ and $\mathbb{LS}_{(t_2)}$ are free-isomorphic under the identity map on $\mathbb{LS}$, acting as a free-isomorphism. Therefore, the statement (95) holds.

By (90), the Banach $*$-probability space $\mathbb{LS}^{t_2}$ of (89) is free-homomorphic to $\mathbb{LS}_{(t_2)}$. Therefore, under the hypothesis, $\mathbb{LS}^{t_2}$ is free-homomorphic to $\mathbb{LS}_{t_1<t_2}$ by (95). Equivalently, the statement (96) holds. □

The above theorem characterizes the free-probabilistic structures for semicircular $[t_1, t_2]$-filtrations $\mathbb{LS}_{t_1<t_2}$, whenever $t_1 \leq 2$, and t_2 are suitable, by (95) and (96). Therefore, we now restrict our interests to the cases where:

$$t_1 \geq 2 \text{ in } \mathbb{R}.$$

Therefore, we focus on the semicircular $[t_1, t_2]$-filtration $\mathbb{LS}_{t_1<t_2}$, where:

$$2 \leq t_1 < t_2 \text{ are suitable in } \mathbb{R},$$

in the sense of **NA 9.2**.

Theorem 8. *Let $2 \leq t_1 < t_2$ be suitable in $\mathbb{R}$, and let $\mathbb{LS}_{t_1<t_2}$ be the semicircular $[t_1, t_2]$-filtration (94). Then, the Banach $*$-probability space:*

$$\mathbb{LS}^{t_1<t_2} \stackrel{def}{=} \underset{t_1 \leq p \leq t_2 \text{ in } \mathcal{P}}{\star} \left(\mathbb{LS}_p,\ \tau_p^0\right), \tag{97}$$

equipped with its linear functional $\tau^{t_1<t_2} = \underset{t_1 \leq p \leq t_2}{\star} \tau_p^0$, is free-homomorphic to $\mathbb{LS}_{t_1<t_2}$ in $\mathbb{LS}$, i.e., if $2 \leq t_1 < t_2$ are suitable in $\mathbb{R}$,

$$\mathbb{LS}^{t_1<t_2} \text{ is free-homomorphic to } \mathbb{LS}_{t_1<t_2} \text{ in } \mathbb{LS}_0. \tag{98}$$

Proof. Let $\mathbb{LS}^{t_1<t_2}$ be in the sense of (97) in the semicircular filtration $\mathbb{LS}_0$, i.e.,

$$\mathbb{LS}^{t_1<t_2} = \left(\underset{t_1 \leq p \leq t_2}{\star} \mathbb{LS}_p,\ \tau^{t_1<t_2} = \underset{t_1 \leq p \leq t_2}{\star} \tau_p^0\right),$$

as a free-probabilistic sub-structure of the semicircular filtration $\mathbb{LS}_0$.

By (94), one can define the embedding map Φ from $\mathbb{LS}^{t_1<t_2}$ into $\mathbb{LS}$, satisfying:

$$\Phi(T) = T, \text{ for all } T \in \mathbb{LS}^{t_1<t_2}.$$

Then, for any $T \in \mathbb{LS}^{t_1<t_2}$, one can get that:

$$\tau^{t_1<t_2}(T) = \tau_{t_1<t_2}(T) = \tau^0(T).$$

Therefore, the Banach $*$-probability space $\mathbb{LS}^{t_1<t_2}$ is free-homomorphic to $\mathbb{LS}_{t_1<t_2}$ in $\mathbb{LS}$. Therefore, the relation (98) holds. □

Remark again that we are not sure if $\mathbb{LS}^{t_1<t_2}$ and $\mathbb{LS}_{t_1<t_2}$ are free-isomorphic, or not, at this moment (see Remark 9.1 above). However, similar to (90), one can verify that all free reduced words T of $\mathbb{LS}^{t_1<t_2}$ have non-zero free distributions embedded in $\mathbb{LS}_{t_1<t_2}$, and conversely, all free reduced words of $\mathbb{LS}_{t_1<t_2}$ having non-zero free distributions are contained in $\mathbb{LS}^{t_1<t_2}$.

Corollary 3. *Let T be a free reduced word of the semicircular $[t_1, t_2]$-filtration $\mathbb{LS}_{t_1<t_2}$ in $\mathcal{Q} \cup \Theta$, and assume that the free distribution of T is non-zero for $\tau_{t_1<t_2}$. Then, T is an element of the Banach $*$-probability space $\mathbb{LS}^{t_1<t_2}$ of (97). The converse holds true.* □

9.3. More about Free-Probabilistic Information on $\mathbb{LS}_{t_1<t_2}$

In this section, we discuss more about free-probabilistic information in semicircular $[t_1, t_2]$-filtrations $\mathbb{LS}_{t_1<t_2}$, for $t_1 < t_2 \in \mathbb{R}$ (which are not necessarily suitable in the sense of **NA 9.2**).

First, let us mention about the following trivial cases.

Proposition 9. *Let $\mathbb{LS}_{t_1<t_2}$ be the semicircular $[t_1, t_2]$-filtration for $t_1 < t_2$ in $\mathbb{R}$.*

$$\text{If } t_2 < 2 \text{ in } \mathbb{R}, \text{ then all elements of } \mathbb{LS}_{t_1<t_2} \text{ have the zero free distribution.} \tag{99}$$

$$\text{Let } t_1, t_2 \geq 2 \text{ in } \mathbb{R}. \text{ If the closed interval } [t_1, t_2] \text{ does not contain a prime in } \mathbb{R}, \text{ then all elements of } \mathbb{LS}_{t_1<t_2} \text{ have the zero free distribution.} \tag{100}$$

Proof. The proofs of the statements (99) and (100) are done immediately by (90), (95), (96), and (98). □

Even though the above results (99) and (100), themselves, are trivial, they illustrate how our original (non-zero) free-distributional data on the semicircular filtration $\mathbb{LS}_0$ are distorted under our "unsuitable" truncations.

Now, suppose $t_1 < t_2$ are suitable in $\mathbb{R}$, and:

$$t_1 \to \infty \text{ in } \mathbb{R},$$

in the sense that: t_1 is big "enough" in $\mathbb{R}$. The existence of such suitable intervals $[t_1, t_2]$ in $\mathbb{R}$ is guaranteed by the *prime number theorem* (e.g., [5,6]).

More precisely, let us collect all suitable pairs (t_1, t_2) in $\mathbb{R}^2$, i.e.,

$$\{(t_1, t_2) \in \mathbb{R}^2 : t_1 < t_2 \text{ are suitable in } \mathbb{R}\},$$

and consider its boundary.

First, consider that if $p \to \infty$ in $\mathcal{P}$ (under the usual total ordering on $\mathcal{P}$, inherited by that on $\mathbb{R}$), then:

$$\lim_{p \to \infty \text{ in } \mathcal{P}} p^{2(j+1)} = \begin{cases} 0 & \text{if } j < -1 \\ 1 & \text{if } j = -1 \\ \infty, \text{ undefined} & \text{if } j > -1, \end{cases} \tag{101}$$

for an arbitrarily-fixed $j \in \mathbb{Z}$.

Theorem 9. *Let $(t_n)_{n=1}^{\infty}$ and $(s_n)_{n=1}^{\infty}$ be monotonically "strictly"-increasing $\mathbb{R}$-sequences, satisfying:*

$$t_n < s_n \text{ are suitable in } \mathbb{R},$$

for all $n \in \mathbb{N}$. By the suitability, there exists at least one prime $p_n \in \mathcal{P}$, such that:

$$t_n \leq p_n \leq s_n, for all n \in \mathbb{N}, \tag{102}$$

where the corresponding $\mathbb{R}$*-sequence* $(p_n)_{n=1}^{\infty}$ *is monotonically increasing.*

Let $Q_{p_n,j}$ *be the corresponding* $p_n^{2(j+1)}$*-semicircular element in the free weighted-semicircular family* $\mathcal{Q}$*, as a free random variable of the semicircular* $[t_n, s_n]$*-filtration* $\mathbb{LS}_{t_n<s_n}$*, where* p_n *are the primes of* (102)*, for all* $n \in \mathbb{N}$*, for any* $j \in \mathbb{Z}$*. Then:*

$$\lim_{n\to\infty}\left(\tau_{t_n<s_n}\left(Q_{p_n,j}^k\right)\right) = \begin{cases} 0 & \text{if } j<-1 \\ \omega_k c_{\frac{k}{2}} & \text{if } j=-1 \\ \infty & \text{if } j>-1, \end{cases} \tag{103}$$

for all $k \in \mathbb{N}$*.*

Proof. Suppose p_n are the primes satisfying (102) for given suitable:

$$t_n < s_n \text{ in } \mathbb{R},$$

in the sense of **NA 9.2**, for all $n \in \mathbb{N}$. Then, for the $p_n^{2(j+1)}$-semicircular elements $Q_{p_n,j} \in \mathcal{Q}$ (in $\mathbb{LS}_0$), one has that:

$$\tau_{t_n<s_n}\left(Q_{p_n,j}^k\right) = \left(\underset{t_n\le q\le s_n \text{ in } \mathcal{P}}{\star}\tau_q^0\right)\left(Q_{p_n,j}^k\right) = \tau_{p_n}^0\left(Q_{p_n,j}^k\right)$$

by (102)

$$= \tau_{p_n,j}^0\left(Q_{p_n,j}^k\right) = \omega_k p_n^{2(j+1)} c_{\frac{k}{2}}, \tag{104}$$

for all $k \in \mathbb{N}$.

Thus, we have that:

$$\lim_{n\to\infty}\left(\tau_{t_n<s_n}\left(Q_{p_n,j}^k\right)\right) = \lim_{n\to\infty}\left(\omega_k p_n^{2(j+1)} c_{\frac{k}{2}}\right)$$

by (104);

$$= \lim_{p\to\infty}\left(\omega_k p^{2(j+1)} c_{\frac{k}{2}}\right) = \left(\omega_k c_{\frac{k}{2}}\right)\left(\lim_{p\to\infty} p^{2(j+1)}\right)$$

$$= \begin{cases} 0 & \text{if } j<-1 \\ \omega_k c_{\frac{k}{2}} & \text{if } j=-1 \\ \infty & \text{if } j>-1, \end{cases}$$

by (101), for all $k \in \mathbb{N}$. Therefore, the estimation (103) holds. □

The above estimation (103) illustrates the asymptotic free-distributional data of our $p^{2(j+1)}$-semicircular elements $\{Q_{p,j} \in \mathcal{Q}\}_{p\in\mathcal{P}}$ (for a fixed $j \in \mathbb{Z}$), under our suitable truncations, as $p \to \infty$ in $\mathcal{P}$.

Corollary 4. *Let* $t_1 < t_2$ *be suitable in* $\mathbb{R}$ *under* ***NA 9.2****,* t_1 *be suitably big (i.e.,* $t_1 \to \infty$*) in* $\mathbb{R}$*, and* $j \le -1$ *be arbitrarily fixed in* $\mathbb{Z}$*. Then, there exists* $t_0 \in \mathbb{R}$*, such that:*

$$\left|\tau_{t_1<t_2}\left(Q_{p,j}^n\right) - t_0\right| \to 0,$$

where:

$$t_0 = \begin{cases} 0 & \text{if } j<-1 \\ \omega_n c_{\frac{n}{2}} & \text{if } j=-1, \end{cases} \tag{105}$$

for all $n \in \mathbb{N}$*.*

Under the same hypothesis, if $j > -1$ *in* $\mathbb{Z}$*, then:*

$$\left|\tau_{t_1<t_2}\left(Q_{p,j}^n\right)\right| \to \infty, \tag{106}$$

for all $n \in \mathbb{N}$.

Proof. The estimations (105) and (106), for suitably big $t_1 \in \mathbb{R}$, are obtained by (103). □

10. Semicircularity of Certain Free Sums in $\mathbb{LS}_{t_1<t_2}$

As in Section 9, we will let $\mathbb{LS}$ be the Banach $*$-subalgebra (72) of the free Adelic filtration $\mathfrak{LS}$, and let $\mathbb{LS}_0$ be the semicircular filtration $(\mathbb{LS}, \tau^0)$ of (80).

Let (A, φ) be an arbitrary topological $*$-probability space and $a \in (A, \varphi)$. We say a free random variable a is a *free sum* in (A, φ), if:

$$a = \sum_{l=1}^{N} x_l, \text{ with } x_l \in (A, \varphi),$$

and the summands $x_1, ..., x_N$ of a are free from each other in (A, φ), for $N \in \mathbb{N} \setminus \{1\}$.

Let $t_1 < t_2$ be suitable in $\mathbb{R}$ in the sense of **NA 9.2**, and let $\mathbb{LS}_{t_1<t_2}$ be the corresponding semicircular $[t_1, t_2]$-filtration. Now, we define free random variables X and Y of $\mathbb{LS}$,

$$X = \sum_{l=1}^{N} Q_{p_l,j_l}^{n_l} \text{ and } Y = \sum_{l=1}^{N} \Theta_{p_l,j_l}^{n_l}, \tag{107}$$

for $Q_{p_l,j_l} \in \mathcal{Q}$ and $\Theta_{p_l,j_l} \in \Theta$, for all $l = 1, ..., N$, for $N \in \mathbb{N} \setminus \{1\}$.

Remark that, the operator X (or Y) of (107) is a free sum in $\mathbb{LS}$, if and only if the summands $Q_{p_l,j_l}^{n_l}$ (resp., $\Theta_{p_l,j_l}^{n_l}$), which are the free reduced words with their lengths one, are free from each other in $\mathbb{LS}$, if and only if Q_{p_l,j_l} (resp., Θ_{p_l,j_l}) are contained in the mutually-distinct free blocks $\overline{\mathbb{C}[\{Q_{p_l,j_l}\}]}$ of $\mathbb{LS}$ by (74), if and only if the pairs (p_l, j_l) are mutually distinct from each other in the Cartesian product $\mathcal{P} \times \mathbb{Z}$, for all $l = 1, ..., N$. i.e., the given operators X and Y of (107) are free sums in $\mathbb{LS}$, if and only if:

$$(p_{l_1}, j_{l_1}) \neq (p_{l_2}, j_{l_2}) in \mathcal{P} \times \mathbb{Z}, \tag{108}$$

for all $l_1 \neq l_2$ in $\{1, ..., N\}$.

Lemma 4. *Let X and Y be in the sense of (107) in the semicircular filtration $\mathbb{LS}_0$. Assume that the pairs (p_l, j_l) are mutually distinct from each other in $\mathcal{P} \times \mathbb{Z}$, for all $l = 1, ..., N$, for $N \in \mathbb{N} \setminus \{1\}$. Then:*

$$\tau^0(X) = \sum_{l=1}^{N} \left(\omega_{n_l} p_l^{2(j_l+1)} c_{\frac{n_l}{2}} \right),$$

and:

$$\tau^0(Y) = \sum_{l=1}^{N} \left(\omega_{n_l} c_{\frac{n_l}{2}} \right). \tag{109}$$

Proof. Let X and Y be given as above in $\mathbb{LS}_0$. By the assumption that the pairs (p_l, j_l) are mutually distinct from each other in $\mathcal{P} \times \mathbb{Z}$, these operators X and Y satisfy the condition (108); equivalently, they are free sums in $\mathbb{LS}_0$.

Therefore, one has that:

$$\begin{aligned} \tau^0(X) &= \sum_{l=1}^{N} \tau^0 \left(Q_{p_l,j_l}^{n_l} \right) = \sum_{l=1}^{N} \tau_{p_l,j_l}^0 \left(Q_{p_l,j_l}^{n_l} \right) \\ &= \sum_{l=1}^{N} \left(\omega_{n_l} p_l^{2(j_l+1)} c_{\frac{n_l}{2}} \right), \end{aligned}$$

by the $p_l^{2(j_l+1)}$-semicircularity of $Q_{p_l,j_l} \in \mathcal{Q}$, for all $l = 1, ..., N$.

Similarly, one can get that:

$$\tau^0(Y) = \sum_{l=1}^{N} \tau_{p_l,j_l}^0 \left(\Theta_{p_l,j_l}^{n_l} \right) = \sum_{l=1}^{N} \left(\omega_{n_l} c_{\frac{n_l}{2}} \right),$$

by the semicircularity of $\Theta_{p_l,j_l} \in \Theta$, for all $l = 1, ..., N$. □

Now, for the operators X and Y of (107), we consider how our truncation distorts the free-distributional data (109).

For a given closed interval $[t_1, t_2]$ in $\mathbb{R}$, where $t_1 < t_2$ are suitable in $\mathbb{R}$, we define:

$$\mathcal{P}_{[t_1,t_2]} = \{p \in \mathcal{P} : t_1 \leq p \leq t_2\} = \mathcal{P} \cap [t_1, t_2],$$

and:

$$\mathcal{P}^c_{[t_1,t_2]} = \mathcal{P} \setminus \mathcal{P}_{[t_1,t_2]}, \tag{110}$$

in $\mathcal{P}$.

By (110), the family $\{\mathcal{P}_{[t_1,t_2]}, \mathcal{P}^c_{[t_1,t_2]}\}$ forms a partition of the set $\mathcal{P}$ of all primes for the fixed interval $[t_1, t_2]$. Of course, if $t_1 < t_2$ are not suitable, then:

$$\mathcal{P}_{[t_1,t_2]} = \varnothing, \text{ and hence, } \mathcal{P} = \mathcal{P}^c_{[t_1,t_2]}.$$

Theorem 10. *Let X and Y be the operators (107), and assume they are free sums in the semicircular filtration $\mathbb{LS}_0$; and let $\mathbb{LS}_{t_1<t_2}$ be the semicircular $[t_1, t_2]$-filtration for suitable $t_1 < t_2$ in $\mathbb{R}$. Then:*

$$\tau_{t_1<t_2}(X) = \sum_{p_l \in \mathcal{P}_{[t_1,t_2]:(p_1,\ldots,p_N)}} \left(\omega_{n_l} p_l^{2(j_l+1)} c_{\frac{n_l}{2}}\right),$$

and:

$$\tau_{t_1<t_2}(Y) = \sum_{p_l \in \mathcal{P}_{[t_1<t_2]:(p_1,\ldots,p_N)}} \left(\omega_{n_l} c_{\frac{n_l}{2}}\right), \tag{111}$$

where:

$$\mathcal{P}_{[t_1,t_2]:(p_1,\ldots,p_N)} = \mathcal{P}_{[t_1,t_2]} \cap \{p_1, \ldots, p_N\} \text{ in } \mathcal{P},$$

where $\mathcal{P}_{[t_1,t_2]}$ is in the sense of (110) in $\mathcal{P}$. Clearly, if $\mathcal{P}_{[t_1,t_2]:(p_1,\ldots,p_N)}$ is empty in $\mathcal{P}$, then the formulas in (111) vanish.

Proof. The proof of (111) is done by (95), (96), (98), and (109). Indeed, if:

$$\mathcal{P}_{[t_1,t_2]:(p_1,\ldots,p_N)} = \mathcal{P}_{[t_1,t_2]} \cap \{p_1, \ldots, p_N\} \text{ in } \mathcal{P},$$

where $\mathcal{P}_{[t_1,t_2]}$ is in the sense of (110), and if:

$$\mathcal{P}_{[t_1,t_2]:(p_1,\ldots,p_N)} \neq \varnothing,$$

then:

$$\tau_{t_1<t_2}(X) = \sum_{p_l \in \mathcal{P}_{[t_1,t_2]:(p_1,\ldots,p_N)}} \tau^0_{p_l,j_l}\left(Q^{n_l}_{p_l,j_l}\right)$$

by (98)

$$= \sum_{p_l \in \mathcal{P}_{[t_1,t_2]:(p_1,\ldots,p_N)}} \left(\omega_{n_l} p_l^{2(j_l+1)} c_{\frac{n_l}{2}}\right),$$

by the $p^{2(j+1)}$-semicircularity of $Q_{p,j} \in \mathcal{Q}$.

Similarly, one can get that:

$$\tau_{t_1<t_2}(Y) = \sum_{p_l \in \mathcal{P}_{[t_1,t_2]:(p_1,\ldots,p_N)}} \left(\omega_{n_l} c_{\frac{n_l}{2}}\right),$$

by the semicircularity of $\Theta_{p,j} \in \Theta$. Therefore, the free-distributional data (111) holds, whenever:

$$\mathcal{P}_{[t_1,t_2]:(p_1,\ldots,p_N)} \neq \varnothing \text{ in } \mathcal{P}.$$

Definitely, if:

$$\mathcal{P}_{[t_1,t_2]:(p_1,\ldots,p_N)} = \varnothing,$$

then:

$$\tau_{t_1<t_2}(X) = O(X) = 0 = O(Y) = \tau_{t_1<t_2}(Y).$$

Therefore, the truncated free-distributional data (111) hold. □

Remark 4. *Let us compare the free-distributional data* (109) *and* (111)*. One can check the differences between them dictated by the choices of* $[t_1, t_2]$ *in* $\mathbb{R}$*. Thus, the formula* (111) *also illustrates how our truncations on* $\mathcal{P}$ *distort the original free-probabilistic information on the semicircular filtration* $\mathbb{LS}_0$*.*

Let q_0 be a fixed prime in $\mathcal{P}$. Choose $t_0 < s_0 \in \mathbb{R}$ such that: (i) these quantities t_0 and s_0 satisfy:

$$t_0 \leq q_0 \leq s_0 \text{ in } \mathbb{R},$$

and (ii) q_0 is the only prime in the closed interval $[t_0, s_0]$ in $\mathbb{R}$.

By the *Archimedean property* on $\mathbb{R}$ (or *the axiom of choice*), the existence of such interval $[t_0, s_0]$, satisfying (i) and (ii) for the fixed prime q_0, is guaranteed; however, the choices of the quantities $t_0 < s_0$ are of course not unique.

Definition 18. *Let* $q_0 \in \mathcal{P}$*, and let* $t < s \in \mathbb{R}$ *be the real numbers satisfying the conditions (i) and (ii) of the above paragraph. Then, the suitable closed interval* $[t, s]$ *is called a* q_0*-neighborhood.*

Depending on prime-neighborhoods, one can obtain the following semicircularity condition on our semicircular truncated-filtrations.

Corollary 5. *Let* $p \in \mathcal{P}$*,* $[t, s]$ *be a* p*-neighborhood in* $\mathbb{R}$*, and* $\mathbb{LS}_{t<s}$ *be the corresponding semicircular* $[t, s]$*-filtration. If* X *and* Y *are free sums formed by* (107) *in the semicircular filtration* $\mathbb{LS}_0$*, then:*

$$\tau_{t<s}(X) = \sum_{l=1}^{N} \delta_{p,p_l} \left(\omega_{n_l} p_l^{2(j_l+1)} c_{\frac{n_l}{2}} \right),$$

and:

$$\tau_{t<s}(Y) = \sum_{l=1}^{N} \delta_{p,p_l} \left(\omega_{n_l} c_{\frac{n_l}{2}} \right), \tag{112}$$

where δ *is the Kronecker delta.*

Proof. The free-distributional data (112) are a special case of (111), under the prime-neighborhood condition. Indeed, in this case,

$$\mathcal{P}_{[t,s]:(p_1,\ldots,p_N)} = \{p\} \cap \{p_1, \ldots, p_N\} = \begin{cases} \{p\} & \text{or} \\ \varnothing, \end{cases}$$

where $\mathcal{P}_{[t,s]:(p_1,\ldots,p_N)}$ is in the sense of (111). □

More general to (112), we obtain the following result.

Proposition 10. *Let* $p \in \mathcal{P}$ *and* $[t, s]$ *be a* p*-neighborhood in* $\mathbb{R}$*, and let* $\mathbb{LS}_{t<s}$ *be the corresponding semicircular* $[t, s]$*-filtration. Then, a free random variable* $T \in \mathbb{LS}_{t<s}$ *has its non-zero free distribution, if and only if there exists a non-zero summand* T_0 *of* T*, such that:*

$$T_0 \in \mathbb{LS}_p in \mathbb{LS}_{t<s}, \tag{113}$$

where $\mathbb{LS}_p = \underset{j\in\mathbb{Z}}{\star} \overline{\mathbb{C}[\{\Theta_{p,j}\}]}$ *is a Banach* $*$*-subalgebra* (82) *of* $\mathbb{LS}$*.*

Proof. By (98), if $T \in \mathbb{LS}_{t<s}$ has its non-zero free distribution, then there exists a non-zero summand T_0 of T which can be a linear combination of free reduced words contained in $\underset{t\leq q\leq s \text{ in } \mathcal{P}}{\star} \mathbb{LS}_q$, and hence,

$$T_0 \in \underset{t\leq q\leq s \text{ in } \mathcal{P}}{\star} \mathbb{LS}_q, \tag{114}$$

where $\mathbb{LS}_q$ are in the sense of (82), for $q \in \mathcal{P}$.

Since $[t, s]$ is a p-neighborhood, the relation (114) is equivalent to:

$$T_0 \in \mathbb{LS}_p. \tag{115}$$

Clearly, the converse holds true as well, by (98).

Therefore, a free random variable $T \in \mathbb{LS}_{t<s}$ has its non-zero free distribution, if and only if T contains its non-zero summand $T_0 \in \mathbb{LS}_p$, by (115); equivalently, the statement (113) holds true. □

By (112) and (113), we obtain the following interesting result.

Theorem 11. *Let $X_1 = \sum_{l=1}^{N} Q_{p_l,j_l}$ and $Y_1 = \sum_{l=1}^{N} \Theta_{p_l,j_l}$ be in the sense of (107) in the semicircular filtration $\mathbb{LS}_0$, and assume that $(p_l,\ j_l)$ are mutually distinct in $\mathcal{P} \times \mathbb{Z}$, for $l = 1, ..., N$, for $N \in \mathbb{N} \setminus \{1\}$. Suppose we fix:*

$$p_{l_0} \in \{p_1, ..., p_N\},$$

and take a p_{l_0}-neighborhood $[t_0, s_0]$ in $\mathbb{R}$. Then:

$$X_1 is p_{l_0}^{2(j_{l_0}+1)} - \textit{semicircular in } \mathbb{LS}_{t_0<s_0}, \tag{116}$$

$$Y_1 \textit{ is semicircular in } \mathbb{LS}_{t_0<s_0}, \tag{117}$$

where $\mathbb{LS}_{t_0<s_0}$ is the semicircular $[t_0, s_0]$-filtration.

Proof. Let X_1 and Y_1 be given as above in $\mathbb{LS}$, and fix $p_{l_0} \in \{p_1, ..., p_N\}$. Note that, by the assumption, these operators X_1 and Y_1 form free sums in the semicircular filtration $\mathbb{LS}_0$, having N-many summands. Note also that they are self-adjoint in $\mathbb{LS}$ by the self-adjointness of their summands.

By (113), if an operator T has its non-zero free distribution in the semicircular $[t_0, s_0]$-filtration $\mathbb{LS}_{t_0<s_0}$, where $[t_0, s_0]$ is a p_{l_0}-neighborhood in $\mathbb{R}$, then it must have its non-zero summand T_0,

$$T_0 \in \mathbb{LS}_{p_{l_0}} \text{ in } \mathbb{LS}_{t_0<s_0}.$$

By the very construction of X_1 and Y_1, they contain their summands,

$$Q_{p_{l_0},j_{l_0}}, \Theta_{p_{l_0},j_{l_0}} \in \mathbb{LS}_{p_{l_0}} \text{ in } \mathbb{LS}_{t_0<s_0}.$$

Consider now that:

$$\begin{aligned} X_1^n &= \sum_{(i_1,...,i_n)\in\{1,...,N\}^n} \left(\prod_{k=1}^{N} Q_{p_{i_k},j_{i_k}} \right) \\ &= Q_{p_{l_0},j_{l_0}}^n + \sum_{(i_1,...,i_n)\neq(l_0,...,l_0)} \left(\prod_{k=1}^{N} Q_{p_{k_l},j_{k_l}} \right) \\ &= Q_{p_{l_0},j_{l_0}}^n + [\text{Rest Terms}], \end{aligned}$$

and similarly,

$$Y_1^n = \Theta_{p_{l_0},j_{l_0}}^n + [RestTerms]', \tag{118}$$

for all $n \in \mathbb{N}$.

It is not difficult to check that:

$$\tau_{t_0<s_0}\left([\text{Rest Terms}]\right) = 0 = \tau_{t_0<s_0}\left([\text{Rest Terms}]'\right), \tag{119}$$

by (98) and (113), where [Rest Terms], and [Rest Terms]$'$ are from (118).

Therefore, one obtains that:

$$\begin{aligned}\tau_{t_0<s_0}\left(X_1^n\right) &= \tau_{t_0<s_0}\left(Q^n_{p_{l_0},j_{l_0}}\right) = \tau^0_{p_{l_0}}\left(Q^n_{p_{l_0},j_{l_0}}\right)\\ &= \tau^0_{p_{l_0},j_{l_0}}\left(Q^n_{p_{l_0},j_{l_0}}\right) = \omega_n p_{l_0}^{2(j_{l_0}+1)} c_{\frac{n}{2}},\end{aligned}$$

and, similarly,

$$\tau_{t_0<s_0}\left(Y_1^n\right) = \tau^0_{p_{l_0},j_{l_0}}\left(\Theta^n_{p_{l_0},j_{l_0}}\right) = \omega_n c_{\frac{n}{2}}, \tag{120}$$

for all $n \in \mathbb{N}$, by (119).

Therefore, the free sum $X_1 \in \mathbb{LS}$ is $p_{l_0}^{2(j_{l_0}+1)}$-semicircular in $\mathbb{LS}_{t_0<s_0}$; and the free sum $Y_1 \in \mathbb{LS}$ is semicircular in $\mathbb{LS}_{t_0<s_0}$, by (120). Therefore, the statements (116) and (117) hold true. □

The above theorem shows that, if there is a free sum T in the semicircular filtration $\mathbb{LS}_0$ and if we "nicely" truncate the linear functional τ^0 on $\mathbb{LS}$, then one can focus on the non-zero summand T_0 of T, whose the free distribution not only determines the truncated free distribution of T, but also follows the (weighted-)semicircular law.

11. Applications of Prime-Neighborhoods

In Section 9, we considered the semicircular truncated-filtrations $\mathbb{LS}_{t<s}$ for $t < s \in \mathbb{R}$ and studied how $[t, s]$-truncations on $\mathcal{P}$ affect, or distort, the original free-distributional data on the semicircular filtration $\mathbb{LS}_0 = \left(\mathbb{LS},\ \tau^0\right)$. As a special case, in Section 10, we introduced p-neighborhoods for primes p and considered corresponding truncated free distributions on $\mathbb{LS}$.

In this section, by using prime-neighborhoods, we provide a completely "new" model of truncated free probability on $\mathbb{LS}$ and study how the original free-distributional data on $\mathbb{LS}_0$ are distorted under this new truncation model.

Let us now regard the set $\mathcal{P}$ of all primes as a *totally ordered set* (a TOset),

$$\mathcal{P} = \{q_1 < q_2 < q_3 < q_4 < q_5 < ...\} \tag{121}$$

under the usual inequality ($\leq$) on $\mathcal{P}$, i.e.,

$$q_1 = 2, q_2 = 3, q_3 = 5, q_4 = 7, q_5 = 11, \text{etc.}$$

For each $q_k \in \mathcal{P}$ of (121), determine a q_k-neighborhood B_k

$$B_k \overset{denote}{=} [t_k, s_k] in \mathbb{R}, \tag{122}$$

for all $k \in \mathbb{N}$.

Let τ_{B_k} be our truncated linear functionals $\tau_{t_k<s_k}$ of (92) on the Banach $*$-algebra $\mathbb{LS}$, i.e.,

$$\tau_{B_k} = \tau_{t_k<s_k}, for\ all k \in \mathbb{N}. \tag{123}$$

Then, by the truncated linear functionals of (123), one can have the corresponding semicircular B_k-filtrations,

$$\mathbb{LS}_{B_k} = \mathbb{LS}_{t_k<s_k} = \left(\mathbb{LS},\ \tau_{B_k}\right), \tag{124}$$

for all $k \in \mathbb{N}$.

We now focus on the system:

$$\mathbf{T} = \{\tau_{B_k}\}_{k=1}^{\infty} \tag{125}$$

of q_k-neighborhood-truncated linear functionals (123) for all $k \in \mathbb{N}$.

Let F be a "finite" subset of the TOset $\mathcal{P}$ of (121), and for such a set F, define a new linear functional τ_F on $\mathbb{LS}$ induced by the system **T** of (125), by:

$$\tau_F = \sum_{q_k \in F} \tau_{B_k} on \mathbb{LS}. \tag{126}$$

Before proceeding, let us consider the following result obtained from (113).

Lemma 5. *Let $p \in \mathcal{P}$ and $[t, s]$ be a p-neighborhood in $\mathbb{R}$, and let $\mathbb{LS}_{t<s}$ be the semicircular $[t, s]$-filtration. Let $\tau_p^0 = \underset{j \in \mathbb{Z}}{\star} \tau_{p,j}^0$ be the linear functional (81) on the Banach $*$-subalgebra $\mathbb{LS}_p$ of (82) in the semicircular filtration $\mathbb{LS}_0$. Define a linear functional τ^p on the Banach $*$-algebra $\mathbb{LS}$ by:*

$$\tau^p(T) \overset{def}{=} \begin{cases} \tau_p^0(T) & \text{if } T \in \mathbb{LS}_p \text{ in } \mathbb{LS} \\ O(T) = 0 & \text{otherwise,} \end{cases}$$

for all $T \in \mathbb{LS}$. Then, the Banach $*$-probability space $(\mathbb{LS}, \tau^p)$ is free-isomorphic to $\mathbb{LS}_{t<s}$, i.e.,

$$[t, s] \text{ is a } p-\text{neighborhood} \Rightarrow \mathbb{LS}_{t<s} \text{ and } (\mathbb{LS}, \tau^p) \text{ are } free-isomorphic. \tag{127}$$

Proof. Under the hypothesis, it is not hard to check:

$$\tau_{t<s} = \tau^p \text{ on } \mathbb{LS}.$$

Therefore, the identity map on $\mathbb{LS}$ becomes a free-isomorphism from $\mathbb{LS}_{t<s}$ onto $(\mathbb{LS}, \tau^p)$. □

If a finite subset F is a singleton subset of $\mathcal{P}$, then the free probability on $\mathbb{LS}$ determined by the corresponding linear functional τ_F of (126) is already considered in Section 10 and in (127). Therefore, we now restrict our interests to the cases where finite subsets F have more than one element in $\mathcal{P}$.

Lemma 6. *Let F be a finite subset of the TOset $\mathcal{P}$ of (121), and let τ_F be the corresponding linear functional (126) on $\mathbb{LS}$. Then:*

$$\tau_F = \sum_{q_k \in F} \tau^{q_k} on \mathbb{LS}, \tag{128}$$

where τ^{q_k} are in the sense of (127).

Proof. The proof of (128) is done by (126) and (127) because:

$$(\mathbb{LS}, \tau^{q_k}) \text{ and } \mathbb{LS}_{B_k}$$

are free-isomorphic for all $q_k \in F$. Therefore, the linear functional τ_F of (126) satisfies that:

$$\tau_F = \sum_{q_k \in F} \tau_{B_k} = \sum_{q_k \in F} \tau^{q_k} \text{ on } \mathbb{LS}.$$

□

By (113), (116), (117), and (128), one obtains the following result.

Theorem 12. *Let $T = \prod_{l=1}^{N} Q_{p_l,j_l}^{n_l}$ or $S = \prod_{l=1}^{N} \Theta_{p_l,j_l}^{n_l}$ be a free reduced word of $\mathbb{LS}$ with its length-N, for $N \in \mathbb{N}$. If:*

$$F \cap \{p_1, ..., p_N\} = \varnothing \text{ in } \mathcal{P},$$

then:

$$\tau_F(T) = 0 = \tau_F(S). \tag{129}$$

While, if $F \cap \{p_1, ..., p_N\} \neq \varnothing$ in $\mathcal{P}$, then:

$$\tau_F(T) = \sum_{q \in F \cap \{p_1, ..., p_N\}} \left(\omega_n q^{2(j+1)} c_{\frac{n}{2}} \right),$$

respectively,

$$\tau_F(S) = |F \cap \{p_1, ..., p_N\}| \left(\omega_n c_{\frac{n}{2}} \right), \tag{130}$$

where $|X|$ *mean the cardinalities of sets* X.

Proof. Let T and S be given free reduced words with their length-N in $\mathbb{LS}$, for $N \in \mathbb{N}$. If:

$$F \cap \{p_1, ..., p_N\} = \varnothing \text{ in } \mathcal{P},$$

then we obtain the formula (129) by (127) and (128). Indeed,

$$\tau_F(T) = \sum_{q \in F} \tau^q(T) = 0 = \sum_{q \in F} \tau^q(S) = \tau_F(S).$$

Now, assume that:

$$F \cap \{p_1, ..., p_N\} = \{p_{i_1}, ..., p_{i_k}\} \text{ in } \mathcal{P},$$

for some $k \in \mathbb{N}$, such that $1 \leq k \leq N$. Then:

$$\tau_F(T) = \left(\sum_{l=1}^{k} \tau^0_{p_{i_l}} \right)(T) = \sum_{l=1}^{k} \tau^0_{p_{i_l}}(T)$$

by (126) and (128)

$$\begin{array}{l} = \sum_{l=1}^{k} \tau^0_{p_{i_l}} \left(Q^{n_{i_l}}_{p_{i_l}, j_{i_l}} \right) = \sum_{l=1}^{k} \tau^0_{p_{i_l}, j_{i_l}} \left(Q^{n_{i_l}}_{p_{i_l}, j_{i_l}} \right) \\ = \sum_{l=1}^{k} \left(\omega_{n_l} p_{i_l}^{2(j_{i_l}+1)} c_{\frac{n_l}{2}} \right). \end{array} \tag{131}$$

Similarly,

$$\tau_F(S) = \sum_{l=1}^{k} \left(\omega_{n_l} c_{\frac{n_l}{2}} \right) = k \cdot \left(\omega_{n_l} c_{\frac{n_l}{2}} \right).$$

Therefore, the free-distributional data (130) hold. □

The above free-distributional data (129) and (130) characterize the free-probabilistic information on Banach $*$-probability spaces

$$(\mathbb{LS}, \tau_F),$$

for any finite subsets F of $\mathcal{P}$.

Author Contributions: The authors contributted equally in this article.

Funding: This research received no external funding.

Conflicts of Interest: The authors declare no conflict of interest.

References

1. Cho, I. Free Semicircular Families in Free Product Banach *-Algebras Induced by p-Adic Number Fields over Primes p. *Complex Anal. Oper. Theory* **2017**, *11*, 507–565. [CrossRef]
2. Cho, I.; Jorgensen, P.E.T. Semicircular Elements Induced by p-Adic Number Fields. *Opuscula Math.* **2017**, *35*, 665–703. [CrossRef]
3. Deligne, P. *Applications de la Formule des Traces Aux Sommes Trigonometriques, Cohomologies Étale (SGA 4 1/2)*; Lecture Notes in Math; Springer: Berlin, Germany, 1977; Volueme 569.
4. Gillespie, T. Superposition of Zeroes of Automorphic L-Functions and Functoriality. Ph.D. Thesis, University of Iowa, Iowa City, IA, USA, 2010.

5. Gillespie, T. Prime Number Theorems for Rankin-Selberg *L*-Functions over Number Fields. *Sci. China Math.* **2011**, *54*, 35–46. [CrossRef]
6. Iwaniec, H.; Kowalski, E. *Analytic Number Theory*; Colloquium Publications: Providence, RI, USA, 2004; Volume 53.
7. Vladimirov, V.S.; Volovich, I.V.; Zelenov, E.I. *p-Adic Analysis and Mathematical Physics*; World Scientific: Singapore, 1994; Volume 1, ISBN 978-981-02-0880-6.
8. Cho, I. On Dynamical Systems Induced by *p*-Adic Number Fields. *Opuscula Math.* **2015**, *35*, 445–484. [CrossRef]
9. Cho, I. Dynamical Systems on Arithmetic Functions Determined by Prims. *Banach J. Math. Anal.* **2015**, *9*, 173–215. [CrossRef]
10. Cho, I. Free Distributional Data of Arithmetic Functions and Corresponding Generating Functions. *Complex Anal. Oper. Theory* **2014**, *8*, 537–570. [CrossRef]
11. Cho, I.; Jorgensen, P.E.T. Krein-Space Operators Induced by Dirichlet Characters. Available online: https://www.researchgate.net/publication/277682901_Krein-Space_Operators_Induced_by_Dirichlet_Characters (accessed on 9 Feburary 2018).
12. Cho, I. Representations and Corresponding Operators Induced by Hecke Algebras. *Complex Anal. Oper. Theory* **2016**, *10*, 437–477. [CrossRef]
13. Cho, I.; Gillespie, T. Free Probability on the Hecke Algebra. *Complex Anal. Oper. Theory* **2015**, *9*, 1491–1531. [CrossRef]
14. Speicher, R. *Combinatorial Theory of the Free Product with Amalgamation and Operator-Valued Free Probability Theory*; American Mathematical Society: Providence, RI, USA, 1998; p. 132.
15. Voiculescu, D.; Dykema, K.J.; Nica, A. *Free Random Variables*; CRM Monograph Series; American Mathematical Society: Providence, RI, USA, 1992; Volume 1.
16. Kemp, T.; Speicher, R. Strong Haagerup Inequalities for Free R-Diagonal Elements. *J. Funct. Anal.* **2007**, *251*, 141–173. [CrossRef]
17. Larsen, F. Powers of R-Diagonal Elements. *J. Oper. Theory* **2002**, *47*, 197–212.
18. Nica, A.; Shlyakhtenko, D.; Speicher, R. R-Diagonal Elements and Freeness with Amalgamation. *Can. J. Math.* **2001**, *53*, 355–381. [CrossRef]
19. Radulescu, F. Random Matrices, Amalgamated Free Products and Subfactors of the C^*-Algebra of a Free Group of Nonsingular Index. *Invent. Math.* **1994**, *115*, 347–389. [CrossRef]
20. Boedihardjo, M.; Dykema, K.J. On Algebra-Valued R-Diagonal Elements. *arXiv* **2016**, arXiv:1512.06321v2.
21. Cohen, H. *A Course in Computational Algebraic Number Theory*; Graduate Texts in Mathematic; Springer: Berlin, Germany, 1993; Volume 138.
22. Davenport, H. *Multiplicative Number Theory*, 3rd ed.; Springer: Berlin, Germany, 2000; ISBN 978-0-387-95097.

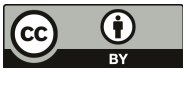

© 2019 by the authors. Licensee MDPI, Basel, Switzerland. This article is an open access article distributed under the terms and conditions of the Creative Commons Attribution (CC BY) license (http://creativecommons.org/licenses/by/4.0/).

mathematics

MDPI

Article

Study on Non-Commutativity Measure of Quantum Discord

Jin Liang * and Chengwei Zhang

School of Mathematical Sciences, Shanghai Jiao Tong University, Shanghai 200240, China; zcw-i0@sjtu.edu.cn
* Correspondence: jinliang@sjtu.edu.cn

Received: 2 May 2019; Accepted: 11 June 2019; Published: 14 June 2019

Abstract: In this paper, we are concerned with the non-commutativity measure of quantum discord. We first present an explicit expression of the non-commutativity measure of quantum discord in the two-qubit case. Then we compare the geometric quantum discords for two dynamic models with their non-commutativity measure of quantum discords. Furthermore, we show that the results conducted by the non-commutativity measure of quantum discord are different from those conducted by both or one of the Hilbert-Schmidt distance discord and trace distance discord. These intrinsic differences indicate that the non-commutativity measure of quantum discord is incompatible with at least one of the well-known geometric quantum discords in the quantitative and qualitative representation of quantum correlations.

Keywords: quantum discord; non-commutativity measure; dynamic models

1. Introduction

In recent years, because quantum information processing is superior to classical information processing, quantum information theory and technology have developed dramatically (cf., e.g., [1–6]). As an important resource in quantum computation, quantum correlations have been investigated extensively in the last decades. So far, many forms of quantum correlations have been proposed; for example, quantum discord [7], quantum deficit [8], quantum correlation derived from the distance between the reduced states [9]. Among various quantum correlations, quantum discord and its derived measures are important (cf., e.g., [3,5–8,10–13]). Most of them are not so hard to calculate and are more robust against the effects of decoherence [10,14]. Quantum discord was initially introduced by Ollivier and Zurek and by Henderson and Vedral [7,8]. In 2010, Dakic, Vedral and Brukner [12] find a "Necessary and Sufficient Condition for Nonzero Quantum Discord" (geometric quantum discord for the Hilbert-Schmidt norm). Since then, several equivalent measures have been introduced. Recently, the non-commutativity measure of quantum discord has been discussed in [13]. In this work, we first study the problem "how to give an explicit expression of the non-commutativity measure of quantum discord in the two-qubit case?" Then we compare the geometric quantum discords (the Hilbert-Schmidt distance discord and trace distance discord) for two dynamic models of open quantum systems with their non-commutativity measure of quantum discords. We select open quantum systems as our resource quantum systems since they are significant quantum systems and they can induce occurrence of decoherence which can cause decreasing of quantum correlations and may induce failure of the algorithms.

2. Non-Commutativity Measure of Quantum Discord and Geometric Quantum Discords

Consider a composite quantum system $\mathcal{H}_{AB}$, which consists of two subsystems A and B. Quantum discord is the difference of two natural quantum extensions of the classical mutual information. In [8], the authors pointed out that the quantum discord reaches zero for and only for the classical-quantum

state. So we can look at the quantum discord as the 'distance' between the state ρ and the set of classical-quantum states. The state $\rho \in \mathcal{H}_{AB}$ is classical-quantum state if and only if ρ can be written the following form (cf. [10]):

$$\rho = \sum_i |i><i|_A \otimes \rho_B^i,$$

where $\{|i>_A\}$ is any orthonormal basis of subsystem A and ρ_B is a quantum state of subsystem B.

It is known that if $\rho \in \mathcal{H}_{AB}$ is a quantum state $\rho \in \mathcal{H}_{AB}$, then (cf. [13])

$$\rho = \sum_{ij} E_{ij} \otimes B_{ij},$$

where $E_{ij} = |i><j|_A$ and $B_{ij} =< i_A|\rho|j_A >$. In [13], two non-commutativity measures are presented by:

$$D'_{N1}(\rho) = \sum_{\Omega} |||[B_{ij}, B_{i'j'}]|||_2, \qquad D_{N1}(\rho) = \sum_{\Omega} |||[B_{ij}, B_{i'j'}]|||_{Tr}, \tag{1}$$

where Ω is the set of all the possible pairs (regardless of the order), $[\cdot,\cdot]$ denotes the commutator, $||\cdot||_2$ is the Hilbert-Schmidt norm (i.e., $\|A\|_2 = \sqrt{Tr(A^\dagger A)}$) and $||\cdot||_{Tr}$ is the trace norm (i.e., $\|A\|_{Tr} = Tr(\sqrt{A^\dagger A})$).

Clearly:

(1) $D_{N1}(\rho) = 0$ and $D'_{N1}(\rho) = 0$ if and only if ρ is a quantum-classical state.
(2) D_{N1} and D'_{N1} are invariant under local unitary operations.

Moreover, we see that if $\rho = \sum_{ij} A_{ij} \otimes E'_{ij}$. According to Equation (1), we have:

$$D'_N(\rho) = \sum_{\Omega'} |||[A_{ij}, A_{i'j'}]|||_2, \qquad D_N(\rho) = \sum_{\Omega'} |||[A_{ij}, A_{i'j'}]|||_{Tr}, \tag{2}$$

where $E'_{ij} = |i><j|_B$, $A_{ij} =< i_B|\rho|j_B >$ and $\{|i>_B\}$ is any orthonormal basis of subsystem B, and $D_N(\rho)$ ($D'_N(\rho)$) equals zero if and only if ρ is a zero-discord state.

The Hilbert-Schmidt distance discord (cf., e.g., [12]) is defined by:

$$D_{Hs}(\rho) = \min_{\chi \in CQ} d_{Hs}(\rho, \chi), \qquad d_{Hs}(\rho, \chi) = \|\rho - \chi\|_2^2,$$

where CQ is the set of classical-quantum states. The trace distance discord (cf., e.g., [15]) is defined by:

$$D_{Tr}(\rho) = \min_{\chi \in CQ} d_{Tr}(\rho, \chi), \qquad d_{Tr}(\rho, \chi) = \|\rho - \chi\|_{Tr},$$

Both the Hilbert-Schmidt distance discord and the trace distance discord are geometric quantum discords.

3. An Explicit Expression of The Non-Commutativity Measure of Quantum Discord in the Two-Qubit Case

Since the non-commutativity measures of quantum discord are invariant under local unitary operations, every state ρ is locally unitary equivalent to:

$$\rho = \frac{1}{4}(I \otimes I + X\sigma \otimes I + I \otimes Y\sigma + \sum_i c_i \sigma_i \otimes \sigma_i), \tag{3}$$

where $X = (x_1, x_2.x_3)$, $Y = (y_1, y_2, y_3)$, $\sigma = \begin{pmatrix} \sigma_1 \\ \sigma_2 \\ \sigma_3 \end{pmatrix}$ in two qubits, and σ_i $(i = 1, 2, 3)$ are the three Pauli matrices (cf. [5]), which is called Bloch's representation. Therefore, if the state ρ satisfies Equation (3), we deduce that:

$$A_{00} = \frac{1}{4}\begin{pmatrix} 1 + x_3 + y_y 3 + c_3 & x_1 - ix_2 \\ x_1 + ix_2 & 1 - x_3 + y_y 3 - c_3 \end{pmatrix}, \quad A_{01} = \frac{1}{4}\begin{pmatrix} y_1 - iy_2 & c_1 - c_2 \\ c_1 + c_2 & y_1 - iy_2 \end{pmatrix},$$
$$A_{10} = \frac{1}{4}\begin{pmatrix} y_1 + iy_2 & c_1 + c_2 \\ c_1 - c_2 & y_1 + iy_2 \end{pmatrix}, \quad A_{11} = \frac{1}{4}\begin{pmatrix} 1 + x_3 - y_y 3 - c_3 & x_1 - ix_2 \\ x_1 + ix_2 & 1 - x_3 - y_y 3 + c_3 \end{pmatrix}.$$

$$[A_{00}, A_{01}]^\dagger [A_{00}, A_{01}] = \frac{1}{64}\begin{pmatrix} u^2 + K_+^2 (c_1 + c_2)^2 & 2c_1 c_2 K_+ (x_1 - ix_2) \\ 2c_1 c_2 K_+ (x_1 + ix_2) & c_1^2 y_2^2 + c_2^2 y_1^2 + K_+^2 (c_1 - c_2)^2 \end{pmatrix},$$
$$[A_{00}, A_{10}]^\dagger [A_{00}, A_{10}] = \frac{1}{64}\begin{pmatrix} u^2 + K_+^2 (c_1 - c_2)^2 & -2c_1 c_2 K_+ (x_1 - ix_2) \\ -2c_1 c_2 K_+ (x_1 + ix_2) & c_1^2 y_2^2 + c_2^2 y_1^2 + K_+^2 (c_1 + c_2)^2 \end{pmatrix},$$
$$[A_{00}, A_{11}]^\dagger [A_{00}, A_{11}] = \frac{1}{16}\begin{pmatrix} (x_1^2 + x_2^2) c_3^2 & 0 \\ 0 & (x_1^2 + x_2^2) c_3^2 \end{pmatrix},$$
$$[A_{01}, A_{10}]^\dagger [A_{01}, A_{10}] = \frac{1}{16}\begin{pmatrix} c_1^2 c_2^2 & 0 \\ 0 & c_1^2 c_2^2 \end{pmatrix},$$
$$[A_{01}, A_{11}]^\dagger [A_{01}, A_{11}] = \frac{1}{64}\begin{pmatrix} u^2 + K_-^2 (c_1 + c_2)^2 & -2c_1 c_2 K_- (x_1 - ix_2) \\ -2c_1 c_2 K_- (x_1 + ix_2) & c_1^2 y_2^2 + c_2^2 y_1^2 + K_-^2 (c_1 - c_2)^2 \end{pmatrix},$$
$$[A_{10}, A_{11}]^\dagger [A_{10}, A_{11}] = \frac{1}{64}\begin{pmatrix} u^2 + K_-^2 (c_1 - c_2)^2 & 2c_1 c_2 K_- (x_1 - ix_2) \\ 2c_1 c_2 K_- (x_1 + ix_2) & c_1^2 y_2^2 + c_2^2 y_1^2 + K_-^2 (c_1 + c_2)^2 \end{pmatrix}.$$

Finally, we obtain:

$$D_N(\rho) = \frac{\sum_{i=1}^4 \mu_i + 4|c_1 c_2| + |c_3|\sqrt{x_1^2 + x_2^2}}{8},$$
$$D_N'(\rho) = \frac{\sqrt{u^2 + K_-^2 (c_1^2 + c_2^2)} + \sqrt{u^2 + K_+^2 (c_1^2 + c_2^2)} + |c_1 c_2| + |c_3|\sqrt{x_1^2 + x_2^2}}{2\sqrt{2}}$$

in Equation (2), where:

$$K_\pm = c3 \pm x3, u = \sqrt{c_1^2 y_2^2 + c_2^2 y_1^2},$$
$$\mu_{1,2} = \sqrt{|u^2 + K_+^2 \pm 2c_1 c_2 K_+ \sqrt{K_+^2 + (x_1^2 + x_2^2)}|},$$
$$\mu_{3,4} = \sqrt{|u^2 + K_-^2 \pm 2c_1 c_2 K_- \sqrt{K_-^2 + (x_1^2 + x_2^2)}|}.$$

4. Comparisons between Two Geometric Quantum Discords for Two Dynamic Models of Open Quantum Systems and Corresponding Non-Commutativity Measure of Quantum Discords

It is known that a real physical system is never perfectly closed. Environment acting on the quantum system are regarded as noise. In mathematics, it means that there exist a series of operators (referred to as $\{ E_u \}$) acting on the density matrix. In this way, quantum operations can be represented in an elegant form known as the operator-sum (Kraus) representation, and by [16] we see that:

$$\sum_{u,v} E_{u,v}^\dagger E_{u,v} = I, \qquad E_{u,v} = E_{u_A} \otimes E_{v_B}.$$

Thus, the related density matrix can be written in the following form:

$$\rho(t) = \sum_{u,v} E_{u,v}\rho(0)E_{u,v}^{\dagger}. \tag{4}$$

Dephasing channel. It is known that the dephasing channel is the only channel that has possibility of having no energy penalty when quantum information loses. If two qubits pass through the dephasing channel respectively, the Hamiltonian ([16]):

$$H = \hbar q a^{\dagger} a(b^{\dagger} + b)$$

where a and $a^{\dagger}$, and b and $b^{\dagger}$ are the annihilation operator and creation operator of A and B respectively, and the Kraus operators are:

$$E_0 = \begin{pmatrix} 1 & 0 \\ 0 & \sqrt{1-\hbar q} \end{pmatrix} \quad E_1 = \begin{pmatrix} 0 & 0 \\ 0 & \sqrt{\hbar q,} \end{pmatrix} \tag{5}$$

$$E_0 = E_{0_A} = E_{0_B}, E_1 = E_{1_A} = E_{1_B}$$

where $q = 1 - e^{-2\gamma t}$ is photon scattering rate for the system, and γ is phase damping dissipation rate. In this paper, we suppose $\hbar = 1$.

For the Hilbert-Schmidt distance discord and trace distance discord, the dephasing channel has an important property: the freezing phenomenon (or the semi-freezing phenomenon). However, the non-commutativity measures of quantum discord is different. Actually, if we consider the initial state:

$$\rho_1(0) = \frac{1}{4}(I \otimes I + \sum_i c_i(0)\sigma_i \otimes \sigma_i)$$

with Equations (4) and (5), we have:

$$\rho_1(t) = \frac{1}{4}(I \otimes I + \sum_i c_i(t)\sigma_i \otimes \sigma_i)$$

where:

$$c_1(t) = c_1(0)e^{-2\gamma t}, \quad c_2(t) = c_2(0)e^{-2\gamma t}, \quad c_3(t) = c_3(0).$$

In Figure 1, we plot the time evolution of four different quantum discords for $c_1(0) = 0.6$, $c_2(0) = 0$, $c_3(0) = 0.2$. The plot clearly shows that the Hilbert-Schmidt distance discord and trace distance discord have the sharp transition when $t^{'} = 0.5493/\gamma$. If $t < t^{'}$, their values keep constant. If we change the initial condition (mainly about c_3), we can increase the time of the values keeping constant. However, the non-commutativity measures of quantum discord do not have this feature. They are strictly monotonous decreasing and strictly convex with time growing. Moreover, no matter what value of c_3 (except zero) could be, they still remain strictly monotonous decreasing.

Multimode vacuum field coupling the qubits. Consider a system consists of two qubits, with ω being the transition frequency and two-level energy separated by the energy gap $\hbar\omega$. The qubits are coupled to a multimode radiation field whose modes are initially in the vacuum state $|0>$. The evolution system in time is governed by the following master equation (cf., e.g., [17–19]):

$$\frac{\partial \rho}{\partial t} = -i\omega \sum_{i=1}^{2}[\sigma_3^i, \rho] - i\sum_{i\neq j}^{2}\xi_{ij}[\sigma_+^i\sigma_-^j, \rho] + \frac{1}{2}\sum_{i,j=1}^{2}\zeta_{ij}(2\sigma_-^j\rho\sigma_+^i - \{\sigma_+^j\sigma_-^i, \rho\}) \tag{6}$$

where $\sigma_{\pm}^i$ are the raising and lowering operators and σ_3^i is the energy operator (Pauli operator) of the ith qubit. The spontaneous decay rates of the qubits caused by the vacuum field $\gamma^{'} = \xi_{ii}$ coupling

with the qubits. If $i \neq j$, ξ_{ij} and ζ_{ij} in Equation (6) are described by the collective damping and the "dipole-dipole" interaction, and take the forms:

$$\xi_{ij} = \frac{3}{2}\gamma'[\frac{sin(kr_{ij})}{kr_{ij}} + \frac{cos(kr_{ij})}{(kr_{ij})^2} - \frac{sin(kr_{ij})}{(kr_{ij})^3}]$$
$$\zeta_{ij} = \frac{3}{4}\gamma'[-\frac{cos(kr_{ij})}{kr_{ij}} + \frac{sin(kr_{ij})}{(kr_{ij})^2} + \frac{cos(kr_{ij})}{(kr_{ij})^3}]$$

where $k = \frac{2\pi}{\lambda}$ is the wave vector with λ being the atomic resonant wavelength and $r_{ij} = |r_i - r_j|$ is the distance between the qubits, we assume that the atomic dipole moments are parallel to each other and are polarized in the direction perpendicular to the interatomic axis.

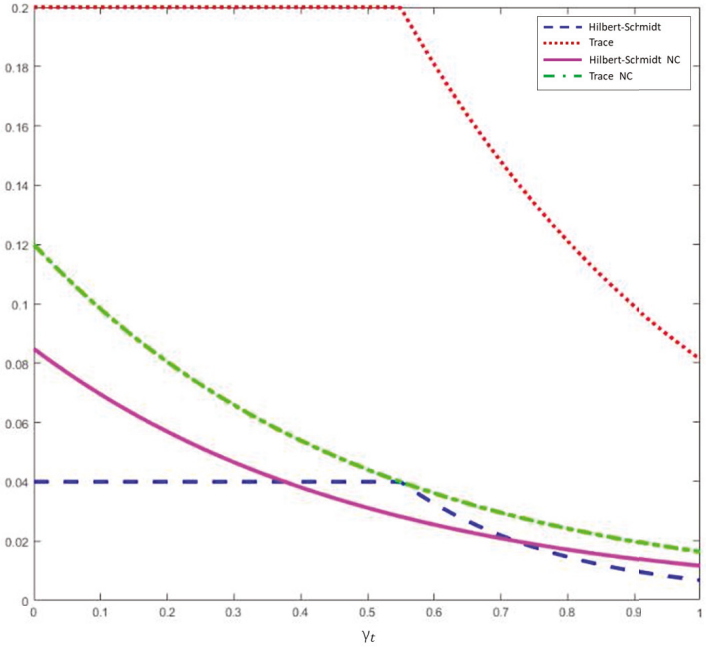

Figure 1. A two-qubit system under the operation of Dephasing channel where $c_1(0) = 0.6$, $c_2(0) = 0$, $c_3(0) = 0.2$, and NC means non-commutativity.

For this model, we consider initial state:

$$\rho_2(0) = |\Psi><\Psi|, |\Psi>= \sqrt{\alpha}|11> + \sqrt{1-\alpha}|00> .$$

Then $\rho_2(t)$ in the standard basis $\{|11>, |10>, |01>, |00>\}$ take the following forms:

$$\begin{aligned}
\rho_{11}^{(2)}(t) &= \alpha e^{-2\gamma' t} \\
\rho_{13,41}^{(2)}(t) &= \sqrt{\alpha(1-\alpha)} e^{-\gamma' t} \\
\rho_{22,33}^{(2)}(t) &= a_1[e^{-\xi_{12}^{+} t} - e^{-2\gamma' t}] + a_2[e^{-\xi_{12}^{-} t} - e^{-2\gamma' t}] \\
\rho_{23,32}^{(2)}(t) &= a_1[e^{-\xi_{12}^{+} t} - e^{-2\gamma' t}] + a_2[e^{-\xi_{12}^{-} t} - e^{-2\gamma' t}] \\
\rho_{44}^{(2)}(t) &= 1 - \rho_{11}^{2}(t) - \rho_{22}^{2}(t) - \rho_{33}^{2}(t)
\end{aligned}$$

where $\xi_{12}^{\pm} = \gamma' \pm \xi_{12}, a_{1,2} = \alpha \xi_{12}^{\pm} / \xi_{12}^{\mp}$. In Figure 2, we show the change of the discord with respect to γt and α as $\xi_{ij} = 0$, where the values are normalized.

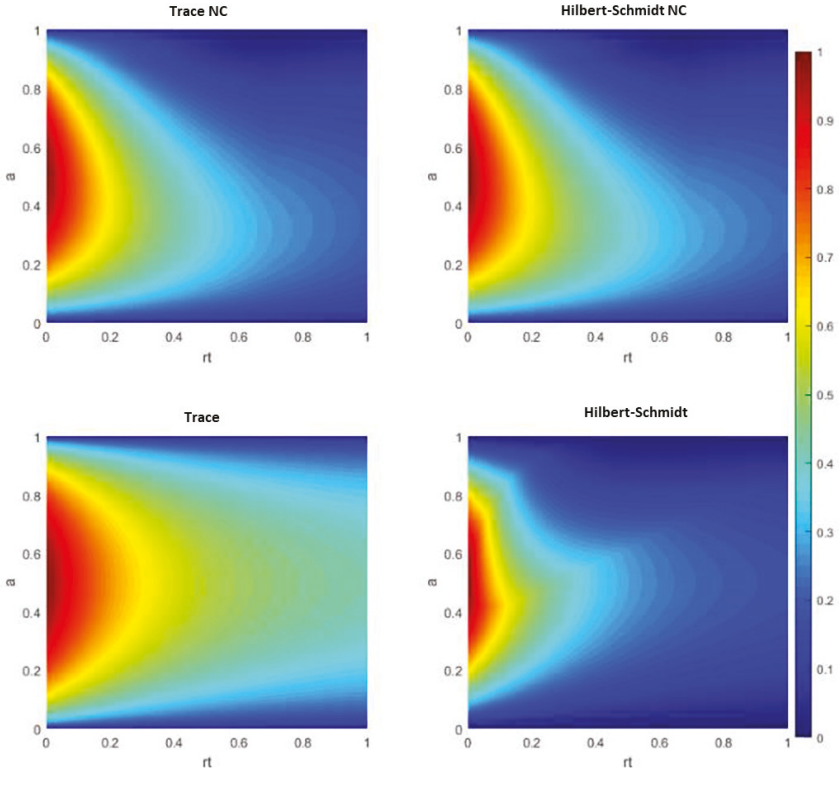

Figure 2. Change of the initial state $|\Psi>$ with respect to γt and α as the interatomic distance is $\xi_{ij} = 0$.

For this model, the trace distance discord is symmetrical about α = 0.5. Moreover, compared to the trace distance discord, we find that the non-commutativity measure of quantum discord and the Hilbert-Schmidt distance discord have more similar properties at different α values. On the other hand, the Hilbert-Schmidt distance discord will revive after α large enough. In this aspect, the non-commutativity measure of quantum discord are closer to the trace distance discord.

5. Conclusions

In conclusion, we present an explicit expression of the non-commutativity measure of quantum discord in the two-qubit case. We also compare the non-commutativity measure of quantum discord with the geometric quantum discord in the models of two qubits passing through the dephasing channel and the multimode vacuum field coupling the qubits, respectively. Our study shows that the non-commutativity measures of quantum discord lose some important features of the geometric quantum discords, such as the freezing phenomenon in the dephasing channel and the revival in the multimode vacuum field coupling the qubits.

Author Contributions: All the authors contributed equally and significantly in writing this paper. All authors read and approved the final manuscript.

Funding: The work was supported partly by the NSF of China (11571229).

Acknowledgments: The authors would like to thank the reviewers very much for valuable comments and suggestions.

Conflicts of Interest: The authors declare that they have no competing interests.

References

1. Das, D.; Bhattacharya, B.; Datta, C.; Roy, A.; Jebaratnam, C.; Majumdar, A.S.; Srikanth, R. Operational characterization of quantumness of unsteerable bipartite states. *Phys. Rev.* **2018**, *97*, 062335. [CrossRef]
2. Gharibian, S. Quantifying nonclassicality with local unitary operations. *Phys. Rev.* **2012**, *86*, 042106. [CrossRef]
3. Hosseini, S.; Rahimi-Keshari, S.; Haw, J.Y.; Assad1, S.M.; Chrzanowski, H.M.; Janousek, J.; Symul, T.; Ralph, T.C.; Lam, P.K.; Gu, M.; et al. Experimental verification of quantum discord in continuousvariable states and operational significance of discord consumption. In Proceedings of the Conference on Lasers and Electro-Optics Europe-Technical Digest 2014, San Jose, CA, USA, 3–4 January 2014.
4. Jebaratnam, C.; Aravinda, S.; Srikanth, R. Nonclassicality of local bipartite correlations. *Phys. Rev.* **2017**, *95*, 032120. [CrossRef]
5. Luo, S.L. Quantum discord for two-qubit systems. *Phys. Rev.* **2008**, *77*, 042303. [CrossRef]
6. Yune, J.; Hong, K.H.; Lim, H.T.; Lee, J.C.; Kwon, O.; Han, S.W.; Moon, S.; Kim, Y.S.; Kim, Y.H. Experimental verification of quantum discord in continuousvariable states and operational significance of discord consumption. In Proceedings of the 2015 11th Conference on Lasers and Electro-Optics Pacific Rim (CLEO-PR), Busan, Korea, 24–28 August 2015.
7. Ollivier, H.; Zurek, W.H. Quantum discord: A measure of the quantumness of correlations. *Phys. Rev. Lett.* **2002**, *88*, 017901. [CrossRef] [PubMed]
8. Henderson, L.; Vedral, V. Classical, quantum and total correlations. *J. Phys. Math. Gen.* **2001**, *34*, 6899–6905. [CrossRef]
9. Guo, Y.; Li, X.L.; Li, B.; Fan, H. Quantum correlation induced by the average distance between the reduced states. *Int. J. Theor. Phys.* **2015**, *54*, 2022–2030. [CrossRef]
10. Adesso, G.; Bromley, T.R.; Cianciaruso, M. Measures and applications of quantum correlations. *J. Phys. Math. Theor.* **2016**, *49*, 473001. [CrossRef]
11. Coecke, B.; Fritz, T.; Spekkens, R.W. A mathematical theory of resources. *Inf. Comput.* **2016**, *250*, 59–86. [CrossRef]
12. Dakic, B.; Vedral, V.; Brukner, C. Necessary and sufficient condition for nonzero quantum discord. *Phys. Rev. Lett.* **2010**, *105*, 190502. [CrossRef] [PubMed]
13. Guo, Y. Non-commutativity measure of quantum discord. *Sci. Rep.* **2016**, *6*, 25241. [CrossRef] [PubMed]
14. Mazzola, L.; Piilo, J.; Maniscalco, S. Sudden transition between classical and quantum decoherence. *Phys. Rev. Lett.* **2010**, *104*, 200401. [CrossRef] [PubMed]
15. Ciccarello, F.; Tufarelli, T.; Giovannetti, V. Toward computability of trace distance discord. *New J. Phys.* **2014**, *16*, 013038. [CrossRef]
16. Nielsen, M.A.; Chuang, I.L. *Quantum Computation and Quantum Information*; Cambridge: Cambridge University Press: London, UK, 2000.

17. Ficek, Z.; Tanas, R. Dark periods and revivals of entanglement in a two-qubit system. *Phys. Rev.* **2006**, *74*, 024304. [CrossRef]
18. Hu, M.L.; Fan, H. Robustness of quantum correlations against decoherence. *Ann. Phys.* **2012**, *327*, 851–860. [CrossRef]
19. Yu, T.; Eberly, J.H. Finite-time disentanglement via spontaneous emission. *Phys. Rev. Lett.* **2004**, *93*, 140404. [CrossRef] [PubMed]

© 2019 by the authors. Licensee MDPI, Basel, Switzerland. This article is an open access article distributed under the terms and conditions of the Creative Commons Attribution (CC BY) license (http://creativecommons.org/licenses/by/4.0/).

mathematics

MDPI

Article

The Prolongation Structure of the Modified Nonlinear Schrödinger Equation and Its Initial-Boundary Value Problem on the Half Line via the Riemann-Hilbert Approach

Tongshuai Liu and Huanhe Dong *

College of Mathematics and Systems Science, Shandong University of Science and Technology, Qingdao 266590, China; Liutongshuaii@163.com
* Correspondence: mathsdong@126.com

Received: 4 January 2019; Accepted: 7 February 2019; Published: 13 February 2019

Abstract: In this paper, the Lax pair of the modified nonlinear Schrödinger equation (mNLS) is derived by means of the prolongation structure theory. Based on the obtained Lax pair, the mNLS equation on the half line is analyzed with the assistance of Fokas method. A Riemann-Hilbert problem is formulated in the complex plane with respect to the spectral parameter. According to the initial-boundary values, the spectral function can be defined. Furthermore, the jump matrices and the global relations can be obtained. Finally, the potential $q(x,t)$ can be represented by the solution of this Riemann-Hilbert problem.

Keywords: prolongation structure; mNLS equation; Riemann-Hilbert problem; initial-boundary value problem

1. Introduction

In mathematics and physics, nonlinear partial differential equations play an important role due to their abundant mathematical structure and properties. Many works on nonlinear evolution equations have been studied, such as the Hamiltonian structure [1,2], the infinite conservation laws [3,4], the Bäcklund transformation [5,6] and so on [7–9]. Besides, the exact solution of these equations, which can be expressed in various forms by different methods, is also a significant subject of soliton research [10–22]. In recent years, with the development of soliton theory, more and more researchers pay attention to the Riemann-Hilbert approach. The Riemann-Hilbert approach was introduced by Fokas to analyze the initial-boundary values problem for linear and nonlinear partial differential equations [23,24]. In the past 20 years, many researchers have discussed a lot of nonlinear integrable equations for the initial-boundary values problem [25–32,32–41]. They have all made a great contribution to the development of this method. The core idea of this method is to construct the associated Riemann-Hilbert problem by the Lax pair of the integrable equation, and then in addition to the initial-boundary values problem, the long-time asymptotic behavior of the solution can be analyzed [42–46]. However, as we all know, it is difficult to determine whether a nonlinear evolution equation possesses a Lax pair or not. As far as we are concerned, the prolongation structure method is an efficient way to obtain the Lax pair, which was firstly proposed in 1975 by Wahlquist and Estabrook [47]. In recent years, a large number of scholars have improved this method, for example, Hermann deduced the prolongation structure method connection in 1976 [48], Deconinck applied the prolongation structure method to semi-discrete systems firstly [49], Wang used this approach to get the integrability of many nonlinear wave equation [50] and so on [51,52]. In this way, we can get the

Lax pair of the nonlinear evolution equation easily as long as it is integrable.

In this paper, we mainly talk about the modified nonlinear Schrödinger(mNLS) equation

$$iq_t + q_{xx} + i(|q|^2 q)_x + 2\rho|q|^2 q = 0, \tag{1}$$

which is very important in plasma physics. Recently, many properties of this equation have been studied, such as the Hamiltonian structure [53], the Darboux transformation [54], the numerical solutions [55,56] and so on [57,58]. Actually, it can become the derivative NLS equation by certain gauge transformation [59]. In this paper, we mainly discuss the mNLS equation on the half line. For simplicity, we let $\rho = 1$. Supposing that the solution $q(x,t)$ of the mNLS equation exists, and the initial-boundary values are defined as follows,
Initial values:

$$q_0(x) = q(x,0), 0 < x < \infty, \tag{2}$$

Boundary values:

$$g_0(t) = q(0,t), g_1(t) = q_x(0,t), 0 < t < T. \tag{3}$$

In order to formulate a Riemann-Hilbert problem, we need to reconstruct the Lax pair of Equation (1). Based on the initial-boundary values, the corresponding spectral functions can be defined. Eventually, the potential function $q(x,t)$ can be expressed in terms of the solution of this Riemann-Hilbert problem.

This paper is divided into four sections. The construction of the prolongation structure for the mNLS equation is in Section 2 and then in Section 3, we reconstruct the Lax pair to formulate the Riemann-Hilbert problem and some conditions and relations are derived. In the last section, we define the spectral functions according to the initial-boundary values and the Riemann-Hilbert problem is investigated.

2. The Prolongation Structures of the mNLS Equation

In order to obtain the Lax pair of the mNLS equation, we analyze the prolongation structure of this equation. This process mainly involves a fundamental theorem in Lie algebra [51].

Theorem 1. *Suppose X and Y are two elements of Lie algebra $g = sl(n+1, C)$ with $[X, Y] = aY$, $(a \neq 0)$ and $X \in$ range ad Y, it means that there exist $Z \in g$ such that $[Y, Z] = X$, so we obtain $Y = e_{\pm}$ and $X = \pm\frac{1}{2}ah$, where $e_{\pm}$ are the nilpotent and h is the neutral elements of g.*

In the beginning, we introduce these variables

$$\bar{u} = p, u_x = v, \bar{u_x} = p_x = q. \tag{4}$$

Then Equation (1) is equivalent to this set of equations as follows

$$\begin{cases} u_x - v = 0, \\ p_x - q = 0, \\ iu_t + v_x + 2iuu_x\bar{u} + iu^2\bar{u}_x + 2u^2\bar{u} = 0, \\ ip_t - q_x + 2i\bar{u}\bar{u}_x u + i\bar{u}^2 u_x - 2\bar{u}^2 u = 0. \end{cases} \tag{5}$$

We define the set of two-forms $I = \{\alpha_1, \alpha_2, \alpha_3, \alpha_4\}$,where

$$\begin{cases} \alpha_1 = du \wedge dt + vdt \wedge dx, \\ \alpha_2 = dp \wedge dt + qdt \wedge dx, \\ \alpha_3 = idu \wedge dx - dv \wedge dt + (2iuvp + iu^2q + 2u^2p)dt \wedge dx, \\ \alpha_4 = idp \wedge dx + dq \wedge dt + (ip^2v + 2ipqu - 2p^2u)dt \wedge dx. \end{cases} \tag{6}$$

It is easy to find that I is a closed ideal, actually, $dI \subset I$. After that, we define the differential one-forms

$$\omega^i = dy^i - F^i(u, v, p, q; y^i)dx - G^i(u, v, p, q; y^i)dt. \tag{7}$$

At the same time, we suppose $F^i = F^i_j y^j, G^i = F^i_j y^j$. According to the general theory of exterior differential systems, if $\tilde{I} = I \bigcup \omega^i$ is a closed ideal, it must satisfy

$$d\omega^i = \sum_{i=1}^{4} (f^i_j \alpha^j) + n^i_j \wedge \omega^j. \tag{8}$$

Combining (5)–(8), we obtain

$$\begin{cases} F_v = F_q = 0, \\ iG_v + F_u = 0, \\ iG_q - F_p = 0, \\ -G_u v - G_p q + (2iuvp + iqu^2 + 2u^2p)G_v \\ -(2ipqu + ip^2v - 2p^2u)G_q + [F, G] = 0. \end{cases} \tag{9}$$

where the bracket $[,]$ denotes the Lie bracket, namely $[F, G] = FG - GF$.

After a lengthy calculation, one solution of this set of equations can be derived

$$\begin{aligned} &F = x_0 + ux_1 + px_2, \\ &G = ix_1v - ix_2q - u^2px_1 - p^2ux_2 + iux_3 - ipx_4 - ipux_5 + x_6. \end{aligned} \tag{10}$$

with the integrability conditions

$$\begin{aligned} &2ix_1 - x_3 - i[x_1, x_5] = 0, 2ix_2 + x_4 + i[x_2, x_5] = 0, \\ &i[x_0, x_3] + [x_1, x_6] = 0, -i[x_0, x_4] + [x_2, x_6] = 0, \\ &[x_0, x_5] + [x_1, x_4] - [x_2, x_3] = 0, [x_1, x_3] = 0, [x_2, x_4] = 0, [x_0, x_6] = 0. \end{aligned} \tag{11}$$

where all $\{x_i\}, i = \{1, 2, ..., 6.\}$ are pending matrices. Here $\{x_1, x_2, ..., x_6\}$ depend on an incomplete Lie algebra, called prolongation algebra.

The next step is to embed the prolongation algebra in $sl(n+1, C)$. According to (11) and Theorem 1, we deduce that x_1 and x_2 is nilpotent and x_5 is neutral element. So we have

$$x_1 = \begin{pmatrix} 0 & \xi \\ 0 & 0 \end{pmatrix}, x_2 = \begin{pmatrix} 0 & 0 \\ -\xi & 0 \end{pmatrix}, x_5 = \begin{pmatrix} -\xi^2 & 0 \\ 0 & \xi^2 \end{pmatrix}. \tag{12}$$

Bringing the above results into (11), we obtain

$$\begin{aligned} x_0 &= \begin{pmatrix} -i\xi^2+i & 0 \\ 0 & i\xi^2-i \end{pmatrix}, x_3 = \begin{pmatrix} 0 & -2i\xi^3+2i\xi \\ 0 & 0 \end{pmatrix}, \\ x_4 &= \begin{pmatrix} 0 & 0 \\ -2i\xi^3+2i\xi & 0 \end{pmatrix}, x_6 = \begin{pmatrix} -2i\xi^4-2i+4i\xi^2 & 0 \\ 0 & 2i\xi^4+2i+4i\xi^2 \end{pmatrix}. \end{aligned} \tag{13}$$

where ξ is spectral parameter. Hence, the expressions of F and G can be presented eventually

$$\begin{aligned} F &= \begin{pmatrix} -i\xi^2+i & \xi q \\ -\xi\bar{q} & i\xi^2-i \end{pmatrix}, \\ G &= \begin{pmatrix} -2i\xi^4-2i+4i\xi^2+i\xi^2|q|^2 & 2\xi^3 q-2\xi q-\xi|q|^2 q+i\xi q_x \\ -2\xi^3\bar{q}+2\xi\bar{q}+\xi|q|^2\bar{q}+i\xi\bar{q}_x & 2i\xi^4+2i-4i\xi^2-i\xi^2|q|^2 \end{pmatrix}. \end{aligned} \tag{14}$$

So, the mNLS equation admits Lax pair

$$\psi_x = F\psi, \psi_t = G\psi, \tag{15}$$

where $\psi = (v_1, v_2)^T$.

3. Spectral Analysis

From the previous paragraph, we know the Lax pair of the mNLS equation. By introducing

$$Q = \begin{pmatrix} 0 & q \\ -\bar{q} & 0 \end{pmatrix}, \sigma_3 \begin{pmatrix} 1 & 0 \\ 0 & -1 \end{pmatrix}. \tag{16}$$

where the $\bar{q}$ denotes the conjugation of q, the Lax pair (15) can be rewritten in this form

$$\begin{cases} \psi_x + i\xi^2\sigma_3\psi - i\sigma_3\psi = \xi Q\psi, \\ \psi_t + 2i\xi^4\sigma_3 + 2i\sigma_3 - 4i\xi^2\sigma_3 = -i\xi^2Q^2 + 2i\xi^3 Q - 2\xi Q + \xi Q^3 + i\xi\sigma_3 Q_x. \end{cases} \tag{17}$$

In our analysis, we assume that q decays to zero sufficiently fast as $x \to \pm\infty$. So, it is correct to extend the column vector ψ to a 2×2 matrix. For simplicity, we substitute λ^2 for $\xi^2 - 1$. Letting $\psi = \Psi e^{-i(\xi^2 x + 2\xi^4 t)\sigma_3}$, then the Lax pair (17) becomes

$$\begin{aligned} &\Psi_x + i\xi^2[\sigma_3, \Psi] = \xi Q\Psi, \\ &\Psi_t + 2i\xi^4[\sigma_3, \Psi] = (-i\xi^2 Q^2\sigma_3 + 2\xi^3 Q - 2\xi Q + \xi Q^3 + i\xi\sigma_3 Q_x)\Psi \end{aligned} \tag{18}$$

We can write (18) in full derivative form

$$d(e^{i(\xi^2 x + 2\xi^4 t)\hat{\sigma}_3}\Psi(x,t;\xi)) = e^{i(\lambda^2 x + 2\lambda^4 t)\hat{\sigma}_3} U(x,t;\xi)\Psi. \tag{19}$$

where

$$\begin{aligned} U &= U_1 dx + U_2 dt \\ &= \xi Q dx + (-i\xi^2 Q^2\sigma_3 + 2\xi^3 Q - 2\xi Q + \xi Q^3 + i\xi\sigma_3 Q_x)dt. \end{aligned} \tag{20}$$

and $\hat{\sigma}_3$ denotes the operator to matrix by $\hat{\sigma}_3 M = [\sigma_3, M]$, hence it is easy to prove $e^{\hat{\sigma}_3} M = e^{\sigma_3} M e^{-\sigma_3}$, where M is a 2×2 matrix.

3.1. The Reconstruction of Lax Pair

Expanding the solution of (19) in this way

$$\Psi = D + \frac{\Psi_1}{\xi} + \frac{\Psi_2}{\xi^2} + \frac{\Psi_3}{\xi^3} + \mathcal{O}(\frac{1}{\xi^4}), \xi \to \infty, \tag{21}$$

where $D, \Psi_1, \Psi_2, \Psi_3$ are independent of ξ. Bringing this equation into the first equation of (18), and comparing the same order of ξ's frequency, we obtain the following equations

$$\begin{aligned} &O(1) : D_x + i[\sigma_3, \Psi_2] - i[\sigma_3, D] = Q\Psi_1; \\ &O(\xi) : i[\sigma_3, \Psi_1] = QD; \\ &O(\xi^2) : i[\sigma_3, D] = 0. \end{aligned} \tag{22}$$

Using the same method, taking (21) into another equation of (18), we have

$$\begin{aligned} &O(1) : D_t - 4i[\sigma_3, \Psi_2] + 2i[\sigma_3, D] = -iQ^2\sigma_3\Psi_2 + 2Q\Psi_3 - 2Q\Psi_1 + Q^3\Psi_1 + i\sigma_3 Q_x\Psi_1; \\ &O(\xi) : 2i[\sigma_3, \Psi_3] - 4i[\sigma_3, \Psi_1] = -iQ^2\sigma_3\Psi_1 + 2Q\Psi_2 - 2QD + Q^3D + i\sigma_3 Q_x D; \\ &O(\xi^2) : 2i[\sigma_3, \Psi_2] - 4i[\sigma_3, D] = -iQ^2\sigma_3 D + 2Q\Psi_1; \\ &O(\xi^3) : 2i[\sigma_3, \Psi_1] = 2QD; \\ &O(\xi^4) : 2i[\sigma_3, D] = 0. \end{aligned} \tag{23}$$

For (22), We find that D is a diagonal matrix from $O(\xi^2)$. Without loss of generality, we suppose

$$D = \begin{pmatrix} D_0^{11} & 0 \\ 0 & D_0^{22} \end{pmatrix}. \tag{24}$$

From $O(\xi)$ we have

$$\Psi_1^o = \frac{i}{2}QD\sigma_3. \tag{25}$$

where Ψ_1^o denotes the off-diagonal part of Ψ_1. So, we can get D_x from $O(1)$ easily

$$D_x = \frac{i}{2}Q^2\sigma_3 D. \tag{26}$$

For (23), after a lengthy calculation, we get

$$\begin{aligned} D_t &= \frac{3i}{4}Q^4\sigma_3 D + \frac{1}{2}QQ_x D - \frac{1}{2}Q_x QD \\ &= (\frac{3i}{4}|q|^4 + \bar{q}q_x - q\bar{q}_x)\sigma_3 D. \end{aligned} \tag{27}$$

The mNLS equation admits the conservation law

$$2(|q|^2)_t = (2iq_x\bar{q} - 3|q|^4 - 2iq\bar{q}_x)_x. \tag{28}$$

From the above results, we find (26) and (27) admit the conservation law. Define

$$D(x,t) = e^{i\int_{(0,0)}^{(x,t)} \Delta(x,t)\sigma_3}. \tag{29}$$

where Δ is the differential one-form, and it is given by

$$\Delta(x,t) = \Delta_1 dx + \Delta_2 dt = -\frac{1}{2}q\bar{q}dx + [\frac{3}{4}q^2\bar{q}^2 + \frac{i}{2}(q\bar{q}_x - q_x\bar{q})]dt. \tag{30}$$

It is not difficult to find that the integral is path independent. So, we introduce

$$\Psi(x,t;\xi) = e^{i\int_{(0,0)}^{(x,t)}\Delta\hat{\sigma}_3}\mu(x,t;\xi)D(x,t), 0<x<\infty, 0<t<T. \tag{31}$$

Then the form of the Lax pair (18) can be replaced with

$$d(e^{i(\lambda^2 x+2\lambda^4 t)\hat{\sigma}_3}\mu(x,t;\xi)) = W(x,t;\xi). \tag{32}$$

where

$$\begin{aligned} W(x,t;\xi) &= e^{i(\lambda^2 x+2\lambda^4 t)\hat{\sigma}_3}V(x,t;\xi)\mu, \\ V = V_1dx + V_2dt &= e^{-i\int_{(0,0)}^{(x,t)}\Delta\hat{\sigma}_3}(U - i\Delta\sigma_3). \end{aligned} \tag{33}$$

Considering the definitions of U and Δ, we have

$$\begin{aligned} V_1(x,t;\xi) &= \begin{pmatrix} \frac{i}{2}q\bar{q} & \xi q e^{-2i\int_{(0,0)}^{(x,t)}\Delta} \\ -\xi\bar{q}e^{2i\int_{(0,0)}^{(x,t)}\Delta} & -\frac{i}{2}q\bar{q} \end{pmatrix}, \\ V_2(x,t;\xi) &= \begin{pmatrix} V_2^{11}(x,t;\xi) & V_2^{12}(x,t;\xi) \\ V_2^{21}(x,t;\xi) & V_2^{22}(x,t;\xi) \end{pmatrix}. \end{aligned} \tag{34}$$

where

$$\begin{aligned} V_2^{11}(x,t;\xi) &= i\xi^2 q\bar{q} - \frac{3i}{4}q^2\bar{q}^2 + \frac{1}{2}(q\bar{q}_x - q_x\bar{q}), \\ V_2^{12}(x,t;\xi) &= (2\xi^3 - 2\xi q - \xi q|q|^2 + i\xi q_x)e^{-2i\int_{(0,0)}^{(x,t)}\Delta}, \\ V_2^{21}(x,t;\xi) &= (-2\xi^3\bar{q} + 2\xi\bar{q} + \xi\bar{q}|q|^2 + i\xi\bar{q}_x)e^{2i\int_{(0,0)}^{(x,t)}\Delta}, \\ V_2^{22}(x,t;\xi) &= -i\xi^2 q\bar{q} + \frac{3i}{4}q^2\bar{q}^2 - \frac{1}{2}(q\bar{q}_x - q_x\bar{q}). \end{aligned}$$

Thus, (32) changes into

$$\begin{cases} \mu_x + i\lambda^2[\sigma_3,\mu] = V_1\mu, \\ \mu_t + 2i\lambda^4[\sigma_3,\mu] = V_2\mu. \end{cases} \tag{35}$$

3.2. The Riemann-Hilbert Problem And Some Relations

Supposing that $q(x,t)$ is smooth function in the domain $D = \{0<x<\infty, 0<t<T\}$. Then we define the eigenfunctions $\mu_j(x,t,;\xi)(j=1,2,3)$ of (34) as follows

$$\mu_j(x,t;\xi) = I + \int_{(x_j,t_j)}^{(x,t)} e^{-i(\lambda x+2\lambda^2 t)\hat{\sigma}_3}W(x',t';\xi), 0<x<\infty, 0<t<T. \tag{36}$$

The integral curve is from (x_j,t_j) to (x,t), where $(x_1,t_1) = (0,T), (x_2.t_2) = (0,0)$ and $(x_3,t_3) = (\infty,t)$. Furthermore, the point (x,t) is an arbitrary point in the domain D. We know that the integral of (36) is independent of the path of integration. Without loss of generality, we will consider the particular integral paths as follows, see Figure 1.

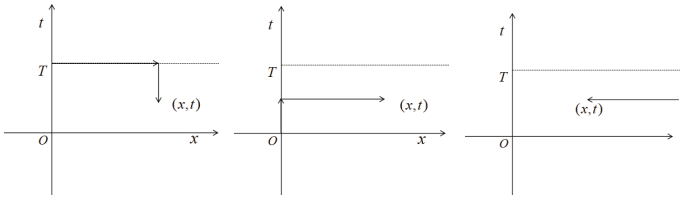

Figure 1. Integral paths.

By this method, we get

$$\begin{cases} \mu_1(x,t;\xi) = I + \int_0^x e^{i\lambda^2(x'-x)\hat{\sigma}_3}(V_1\mu_1)(x',t;\lambda)dx' \\ - e^{-i\lambda^2 x\hat{\sigma}_3}\int_t^T e^{2i\lambda^4(t'-t)\hat{\sigma}_3}(V_2\mu_1)(0,t';\xi)dt', \\ \mu_2(x,t;\xi) = I + \int_0^x e^{i\lambda^2(x'-x)\hat{\sigma}_3}(V_1\mu_2)(x',t;\xi)dx' \\ - e^{-i\lambda^2 x\hat{\sigma}_3}\int_0^t e^{2i\lambda^4(t'-t)\hat{\sigma}_3}(V_2\mu_2)(0,t';\xi)dt', \\ \mu_3(x,t,;\xi) = I - \int_\infty^x e^{i\lambda^2(x'-x)\hat{\sigma}_3}(V_1\mu_3)(x',t;\xi)dx'. \end{cases} \tag{37}$$

Noting that the first column of μ_j includes $e^{-2i[\lambda^2(x'-x)+2\lambda^4(t'-t)]}$. So, in different integral paths, we have the following inequalities

$$\begin{cases} \ell_1 : (x_1,t_1) \to (x,t) : 0 < x' < x, t < t' < T, \\ \ell_2 : (x_2,t_2) \to (x,t) : 0 < x' < x, 0 < t' < t, \\ \ell_3 : (x_3,t_3) \to (x,t) : x < x' < \infty. \end{cases} \tag{38}$$

Due to the exponential function decaying sufficiently, these inequalities imply that the first of the functions $\mu_j(x,t;\xi), (j=1,2,3)$ are analytic if

$$\begin{aligned} &\mu_1^{(1)}(x,t;\xi) : \xi \in \{Im\xi^2 \geq 0\} \cap \{Im\xi^4 \leq 0\}, \\ &\mu_2^{(1)}(x,t;\xi) : \xi \in \{Im\xi^2 \geq 0\} \cap \{Im\xi^4 \geq 0\}, \\ &\mu_3^{(1)}(x,t;\xi) : \xi \in \{Im\xi^2 \leq 0\}. \end{aligned} \tag{39}$$

At the same time, the second column of the functions $\mu_j(x,t;\xi), (j=1,2,3)$ are analytic if

$$\begin{aligned} &\mu_1^{(2)}(x,t;\xi) : \xi \in \{Im\xi^2 \leq 0\} \cap \{Im\xi^4 \geq 0\}, \\ &\mu_2^{(2)}(x,t;\xi) : \xi \in \{Im\xi^2 \leq 0\} \cap \{Im\xi^4 \leq 0\}, \\ &\mu_3^{(2)}(x,t;\xi) : \xi \in \{Im\xi^2 \geq 0\}. \end{aligned} \tag{40}$$

Hence, we get

$$\begin{aligned} \mu_1(x,t;\xi) &= (\mu_1^{D_2}(x,t;\xi), \mu_1^{D_3}(x,t;\xi)), \\ \mu_2(x,t;\xi) &= (\mu_2^{D_1}(x,t;\xi), \mu_2^{D_4}(x,t;\xi)), \\ \mu_3(x,t;\xi) &= (\mu_3^{D_3\cup D_4}(x,t;\xi), \mu_3^{D_1\cup D_2}(x,t;\xi)). \end{aligned} \tag{41}$$

where $\mu_j^{D_i}$ stands for μ_j is analytic if $\xi \in D_i$, where $D_i = \omega_i \cup (-\omega_i), -\omega_i = \{-\xi \in C | \xi \in \omega_i\}, \omega_i = \{\xi \in C | \frac{i-1}{4}\pi < \xi < \frac{i}{4}\pi\}$, see Figure 2.

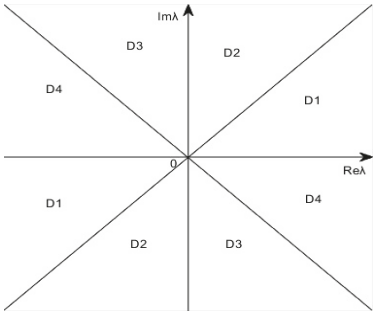

Figure 2. $D_j, j = 1, 2, 3, 4$.

The eigenfunctions $\mu_j (j = 1, 2, 3)$ possess these properties.

- $\det\mu_1(x,t;\xi) = \det\mu_2(x,t;\xi) = \det\mu_3(x,t;\xi) = 1$;
- $\mu_j^{11}(x,t;\xi) = \overline{\mu_j^{22}(x,t;\bar{\xi})}, \mu_j^{12}(x,t;\xi) = \overline{\mu_j^{21}(x,t;\bar{\xi})}$;
- $\mu_j^{11}(x,t;-\xi) = \mu_j^{11}(x,t;\xi), \mu_j^{12}(x,t;-\xi) = -\mu_j^{12}(x,t;\xi)$,
  $\mu_j^{21}(x,t;-\xi) = -\mu_j^{21}(x,t;\xi), \mu_j^{22}(x,t;-\xi) = \mu_j^{22}(x,t;\xi)$.

where the eigenfunctions $\mu_j(x,t;\xi) = \begin{pmatrix} \mu_j^{11}(x,t;\xi) & \mu_j^{12}(x,t;\xi) \\ \mu_j^{21}(x,t;\xi) & \mu_j^{22}(x,t;\xi) \end{pmatrix} (j = 1, 2, 3)$.

For the purpose of formulating a Riemann-Hilbert problem, our main task is to find the jump matrices for every $D_i (i = 1, 2, 3, 4)$ to any other regions. Then we define the spectral functions $s(\xi)$ and $S(\xi)$

$$\begin{cases} \mu_3(x,t;\xi) = \mu_2(x,t;\xi)e^{-i(\lambda^2 x + 2\lambda^4 t)\hat{\sigma}_3}s(\xi), \\ \mu_1(x,t;\xi) = \mu_2(x,t;\xi)e^{-i(\lambda^2 x + 2\lambda^4 t)\hat{\sigma}_3}S(\xi). \end{cases} \tag{42}$$

According to the above definition, we have

$$\mu_1(x,t;\xi) = \mu_3(x,t;\xi)e^{-i(\lambda^2 x + 2\lambda^4 t)\hat{\sigma}_3}(s(\xi))^{-1}S(\xi). \tag{43}$$

Combining (37) with (42), we acquire

$$s(\xi) = \mu_3(0,0;\xi), S(\xi) = (e^{2i\lambda^4 T\hat{\sigma}_3}\mu_2(0,T;\xi))^{-1}. \tag{44}$$

Owing to (37), it is clear to see that

$$\begin{aligned} \mu_1(0,t;\xi) &= I - \int_t^T e^{2i\lambda^4(t'-t)\hat{\sigma}_3}(V_2\mu_1)(0,t';\xi)dt', \\ \mu_2(0,t;\xi) &= I + \int_0^t e^{2i\lambda^4(t'-t)\hat{\sigma}_3}(V_2\mu_2)(0,t';\xi)dt', \\ \mu_3(x,0;\xi) &= I + \int_\infty^x e^{i\lambda^2(x'-x)\hat{\sigma}_3}(V_1\mu_3)(x',0;\xi)dx', \\ \mu_2(x,0;\xi) &= I + \int_0^x e^{i\lambda^2(x'-x)\hat{\sigma}_3}(V_1\mu_2)(x',0;\xi)dx', \end{aligned} \tag{45}$$

Considering the initial values $q(x,0) = u_0(x)$, $q(0,t) = g_0(t)$, boundary values $q(0,t) = g_0(t)$ and $q_x(0,t) = g_1(t)$. For convenience, the initial-boundary values of $\bar{q}(x,t)$ can be written in this form, namely $\bar{q}(x,0) = \bar{u}_0(x), \bar{q}(0,t) = \bar{g}_0(t)$, and $\bar{q}_x(0,t) = \bar{g}_1(t)$. Then $V_2(0,t;\xi)$ and $V_1(x,0;\xi)$ can be expressed with

$$
\begin{aligned}
V_1(x,0;\xi) &= \begin{pmatrix} \frac{i}{2}|u_0|^2 & \xi u_0 e^{i\int_0^x |u_0|^2 dx'} \\ -\xi \bar{u}_0 e^{-i\int_0^x |u_0|^2 dx'} & -\frac{i}{2}|u_0|^2 \end{pmatrix}, \\
V_2(0,t;\xi) &= \begin{pmatrix} V_2^{11}(0,t;\xi) & V_2^{12}(0,t;\xi) \\ V_2^{21}(0,t;\xi) & V_2^{22}(0,t;\xi) \end{pmatrix}.
\end{aligned} \tag{46}
$$

where

$$
\begin{aligned}
V_2^{11}(0,t;\xi) &= i\xi^2|g_0|^2 - \frac{3i}{4}|g_0|^4 - \frac{1}{2}(g_0\bar{g}_1 - g_1\bar{g}_0) = -V_2^{22}(x,t;\xi), \\
V_2^{12}(0,t;\xi) &= (2\xi^3 g_0 - 2\xi g_0 - \xi g_0|g_0|^2 + i\xi g_1)e^{-2i\int_0^t \Delta_2(0,t')dt'}, \\
V_2^{21}(0,t;\xi) &= (-2\xi^3 \bar{g}_0 + 2\xi\bar{g}_0 + \xi\bar{g}_0|g_0|^2 + i\xi\bar{g}_1)e^{2i\int_0^t \Delta_2(0,t')dt'}.
\end{aligned}
$$

with

$$
\Delta_2(0,t') = \tfrac{3}{4}|g_0|^4 + \tfrac{i}{2}(g_0\bar{g}_1 - g_1\bar{g}_0).
$$

Due to μ_j have symmetry, the $s(\xi)$ and $S(\xi)$ also have symmetry

$$
\begin{aligned}
s_{11}(\xi) &= \overline{s_{22}(\bar{\xi})}, s_{21}(\xi) = \overline{s_{12}(\bar{\xi})}, \\
S_{11}(\xi) &= \overline{S_{22}(\bar{\xi})}, S_{21}(\xi) = \overline{S_{12}(\bar{\xi})}.
\end{aligned}
$$

Without loss of generality, we assume

$$
s(\xi) = \begin{pmatrix} \overline{a(\bar{\xi})} & b(\xi) \\ \overline{b(\bar{\xi})} & a(\xi) \end{pmatrix}, S(\xi) = \begin{pmatrix} \overline{A(\bar{\xi})} & B(\xi) \\ \overline{B(\bar{\xi})} & A(\xi) \end{pmatrix}. \tag{47}
$$

According to (42) and (44), we have

$$
\begin{aligned}
s(\xi) &= I - \int_{\infty}^{0} e^{i\lambda^2(x'-x)\hat{\sigma}_3}(V_1\mu_3)(x',0;\xi)dx', \\
S(\xi) &= (I + \int_0^T e^{2i\lambda^4 t'\hat{\sigma}_3}(V_2\mu_2)(0,t';\xi)dt')^{-1}.
\end{aligned} \tag{48}
$$

The spectral functions $s(\xi), S(\xi)$ have the following properties

- $\begin{pmatrix} b(\xi) \\ a(\xi) \end{pmatrix} = \begin{pmatrix} \mu_3^{12}(0,0;\xi) \\ \mu_3^{22}(0,0;\xi) \end{pmatrix} = \mu_3^{(2)}(0,0;\xi)$,
  $\begin{pmatrix} e^{-4i\lambda^4 T}B(\xi) \\ \overline{A(\bar{\xi})} \end{pmatrix} = \begin{pmatrix} \mu_2^{12}(0,T;\xi) \\ \mu_2^{22}(0,T;\xi) \end{pmatrix} = \mu_2^{(2)}(0,T;\xi)$.
- $a(-\xi) = a(\xi), b(-\xi) = -b(\xi)$,
  $A(-\xi) = A(\xi), B(-\xi) = -B(\xi)$.
- $\det s(\xi) = \det S(\xi) = 1$.
- $a(\xi) = 1 + O(\frac{1}{\xi}), b(\xi) = O(\frac{1}{\xi}), \xi \to \infty, Im\xi^2 \geq 0$,
  $A(\xi) = 1 + O(\frac{1}{\xi}), B(\xi) = O(\frac{1}{\xi}), \xi \to \infty, Im\xi^4 \geq 0$.

These spectral functions do not exist independently, but depend on each other and satisfy certain relationships, we call it global relation

$$
B(\xi)a(\xi) - A(\xi)b(\xi) = e^{4i\lambda^4 T}c^+(\xi), Im\xi^2 \geq 0. \tag{49}
$$

where

$$
c^+(\xi) = \int_0^{\infty} e^{2i\lambda^2 x'}(V_1\mu_3)(x',T;\xi)dx'.
$$

For simplicity, we define $M(x,t;\xi)$

$$\begin{aligned} M_+ &= (\frac{\mu_2^{D_1}}{a(\xi)}, \mu_3^{D_1\cup D_2}), \xi \in D_1, \\ M_- &= (\frac{\mu_1^{D_2}}{d(\xi)}, \mu_3^{D_1\cup D_2}), \xi \in D_2, \\ M_+ &= (\mu_3^{D_3\cup D_4}, \frac{\mu_1^{D_3}}{\overline{d(\bar{\xi})}}), \xi \in D_3, \\ M_- &= (\mu_3^{D_3\cup D_4}, \frac{\mu_2^{D_4}}{\overline{a(\bar{\xi})}}), \xi \in D_4. \end{aligned} \tag{50}$$

where

$$d(\xi) = a((\xi)\overline{A(\bar{\xi})} - b(\xi)\overline{B(\bar{\xi})}, \xi \in \bar{D}_2. \tag{51}$$

Synthesizing the above definitions, we can get

$$detM(x,t;\xi) = 1, \tag{52}$$

and

$$M(x,t;\xi) = I + O(\frac{1}{\xi}), \xi \to \infty. \tag{53}$$

Theorem 2. *Given a smooth function $q(x,t)$. Define $M(x,t;\xi)$ as (50), and define $\mu_j(x,t;\xi)(j=1,2,3)$ like (37). Then the jump matrices can be derived through*

$$M_+(x,t;\xi) = M_-(x,t;\xi)J(x,t;\xi), \xi^4 \in R, \tag{54}$$

where

$$J = \begin{cases} J_1(x,t;\xi), & arg\xi^2 = 0, \\ J_2(x,t;\xi), & arg\xi^2 = \frac{\pi}{2}, \\ J_3(x,t;\xi) = J_2J_1^{-1}J_4, & arg\xi^2 = \pi, \\ J_4(x,t;\xi), & arg\xi^2 = \frac{3}{2}\pi. \end{cases} \tag{55}$$

and

$$\begin{aligned} J_1 &= \begin{pmatrix} \frac{1}{a\bar{a}} & \frac{b}{\bar{a}}e^{-2i\theta(\xi)} \\ \frac{\bar{b}}{a}e^{2i\theta(\xi)} & 1 \end{pmatrix}, \\ J_2 &= \begin{pmatrix} 1 & 0 \\ -\Gamma(\xi)e^{2i\theta(\xi)} & 1 \end{pmatrix}, \\ J_4 &= \begin{pmatrix} 1 & \overline{\Gamma(\bar{\xi})}e^{2i\theta(\xi)} \\ 0 & 1 \end{pmatrix}. \end{aligned} \tag{56}$$

with

$$\begin{aligned} \theta(\xi) &= \lambda^2 x + 2\lambda^4 t = (\xi^2-1)x + 2(\xi^2-1)^2 t, \\ \Gamma(\xi) &= \frac{\overline{B(\bar{\xi})}}{a(\xi)d(\xi)}. \end{aligned} \tag{57}$$

According to definition, we have to consider the residue conditions of $M(x,t;\xi)$. By analyzing, we can know that both $a(\xi)$ and $d(\xi)$ have an even zero. Hence, we suppose that

1. $a(\xi)$ has $2n$ simple zeros $\{\varepsilon_j\}_{j=1}^{2n}$, $2n = 2n_1 + 2n_2$. Furthermore, $\varepsilon_j(j=1,2,...,2n_1)$ lie in D_1, $\bar{\varepsilon}_j(j=1,2,...,2n_2)$ lie in D_2.

2. $d(\xi)$ has $2N$ simple zeros $\{\gamma_j\}_{j=1}^{2N}$, $2N = 2N_1 + 2N_2$. In addition, $\gamma_j (j = 1, 2, ..., 2N_1)$ lie in D_3, $\bar{\gamma}_j (j = 1, 2, ..., 2N_2)$ lie in D_4.
3. $a(\xi)$ and $d(\xi)$ do not have any of the same zeros.

Theorem 3. *For convenience, the mark $[M(x,t;\xi)]_1$ denotes the first column of $M(x,t;\xi)$. Similarly, $[M(x,t;\xi)]_2$ denotes the second column. At the same time, we let $\dot{a}(\xi) = \frac{da}{d\xi}$. Then, we get the residue condition as follows:*

$$\begin{aligned}
&(i) \quad Res\{[M(x,t;\xi)]_1, \varepsilon_j\} = \frac{1}{\dot{a}(\varepsilon_j) b(\varepsilon_j)} e^{2i\theta(\varepsilon_j)} [M(x,t;\varepsilon_j)]_2, j = 1, 2, ..., 2n_1,\\
&(ii) \quad Res\{[M(x,t;\xi)]_2, \bar{\varepsilon}_j\} = \frac{1}{\overline{\dot{a}(\bar{\varepsilon}_j) b(\bar{\varepsilon}_j)}} e^{-2i\theta(\bar{\varepsilon}_j)} [M(x,t;\bar{\varepsilon}_j)]_1, j = 1, 2, ..., 2n_2,\\
&(iii) \quad Res\{[M(x,t;\xi)]_1, \gamma_j\} = \frac{\overline{B(\bar{\gamma}_j)}}{a(\gamma_j)\dot{d}(\gamma_j)} e^{2i\theta(\gamma_j)} [M(x,t;\gamma_j)]_2, j = 1, 2, ..., 2N_1,\\
&(iv) \quad Res\{[M(x,t;\xi)]_2, \bar{\gamma}_j\} = \frac{B(\bar{\gamma}_j)}{\overline{a(\bar{\gamma}_j)\dot{d}(\bar{\gamma}_j)}} e^{2i\theta(\bar{\gamma}_j)} [M(x,t;\bar{\gamma}_j)]_1, j = 1, 2, ..., 2N_2.
\end{aligned} \tag{58}$$

Proof. Just prove (i), and the other proof can be proved in the same way. Firstly, we take account of $M(x,t;\xi) = (\frac{\mu_2^{D_1} a(\xi)}{,} \mu_3^{D_1 \cup D_2})$, the simple zeros $\varepsilon_j (j = 1, 2, ..., 2n_1)$ of $a(\xi)$ are the simple poles of $\frac{\mu_2^{D_1}}{a(\xi)}$. Then we get

$$Res\{\frac{\mu_2^{D_1}(x,t;\xi)}{a(\xi)}, \varepsilon_j\} = \lim_{\xi \to \varepsilon_j} (\xi - \varepsilon_j) \frac{\mu_2^{D_1}(x,t;\xi)}{a(\xi)} = \lim_{\xi \to \varepsilon_j} \frac{\mu_2^{D_1}(x,t;\varepsilon_j)}{\frac{a(\xi) - a(\varepsilon_j)}{\xi - \varepsilon_j}} = \frac{\mu_2^{D_1}(x,t;\varepsilon_j)}{\dot{a}(\varepsilon_j)},$$

Then taking $\xi = \varepsilon_j$ into the equation

$$\mu_3^{D_1 \cup D_2} = e^{-2i\theta(\xi)} b(\xi) \mu_2^{D_1} + a(\xi) \mu_2^{D_4},$$

we obtain

$$\mu_3^{D_1 \cup D_2}(x,t;\varepsilon_j) = e^{-2i\theta(\varepsilon_j)} b(\varepsilon_j) \mu_2^{D_1}(x,t;\varepsilon_j) + a(\varepsilon_j) \mu_2^{D_4}(x,t;\varepsilon_j),$$

Finally,

$$Res\{\frac{\mu_2^{D_1}}{a(\xi)}, \varepsilon_j\} = \frac{e^{2i\theta(\varepsilon_j)}}{\dot{a}(\varepsilon_j) b(\varepsilon_j)} \mu_3^{D_1 \cup D_2}(x,t;\varepsilon_j).$$

□

Now, we discuss how to derive the potential $q(x,t)$ from the spectral functions $\mu_j(x,t;\xi)$ $(j = 1, 2, 3)$. Reviewing what we did before, when (21) is a solution of (19), we have $\Psi_1^o = \frac{i}{2} Q D \sigma_3$. Suppose

$$\mu = I + \frac{m^{(1)}}{\xi} + \frac{m^{(2)}}{\xi^2} + \frac{m^{(3)}}{\xi^3} + O(\xi^4), \xi \to \infty,$$

is a solution of (32).

As $\xi \to \infty$, letting $m(x,t) = m_{12}^{(1)}(x,t)$, namely

$$m(x,t) = \lim_{\xi \to \infty} (\xi \mu_j(x,t;\xi))_{12}.$$

By direct calculation, we have

$$q(x,t) = 2im(x,t) e^{2i \int_{(0,0)}^{(x,t)} \Delta} m(x,t), \tag{59}$$

After that, it is clear to find that

$$q\bar{q} = 4|m|^2, q\bar{q}_x - q_x\bar{q} = 4(m\bar{m}_x - m_x\bar{m}) - 32i|m|^4. \tag{60}$$

and

$$\Delta = -2|m|^2 dx + [2i(m\bar{m}_x - m_x\bar{m}) + 28|m|^4]dt. \tag{61}$$

Eventually, we can get the final form of the potential $q(x,t)$.

4. The Spectral Map and the Regular Riemann-Hilbert Problem

4.1. The Spectral Map

Definition 1. *For initial values $q_0(x) = q(x,0)$, the map $\mathbb{S}$ can be defined by*

$$\mathbb{S} : \{q_0(x)\} \to \{a(\xi), b(\xi)\}$$

with

$$\begin{pmatrix} b(\xi) \\ a(\xi) \end{pmatrix} = \mu_3^{(2)}(x,0;\xi), Im\xi^2 \geq 0,$$

where $\mu_3(x,0;\xi)$ is the unique solution of the Volterra linear integral equation

$$\mu_3(x,0;\xi) = I + \int_\infty^x e^{i\lambda^2(x'-x)\hat{\sigma}_3} V_1(x',0;\xi)\mu_3(x',0;\xi)dx'$$

and $V_1(x,0;\xi)$ is given by Equation (46).

Proposition 1. *$a(\xi)$ and $b(\xi)$ possess these properties.*

(i) *$a(\xi)$ and $b(\xi)$ are analytic for $\{\xi \in C | Im\xi^2 > 0\}$ and continuous for $\{\xi \in C | Im\xi^2 \geq 0\}$,*

(ii) *$a(\xi)\overline{a(\bar{\xi})} - b(\xi)\overline{b(\bar{\xi})} = 1, \xi^2 \in R$,*

(iii) *$a(\xi) = 1 + O(\frac{1}{\xi}), b(\xi) = O(\frac{1}{\xi}), \xi \to \infty, Im\xi^2 \geq 0$,*

(iv) *$a(-\xi) = a(\xi), b(-\xi) = -b(\xi), Im\xi^2 \geq 0$,*

(v) *We define $\mathbb{Q} : \{a(\xi), b(\xi)\} \to \{q_0(x)\}$, as the inverse of map $\mathbb{S}$, with*

$$q_0(x) = 2im(x)e^{4i\int_0^x |m(x')|^2 dx'}, m(x) = \lim_{\xi\to\infty}(\xi M^{(x)}(x,\xi))_{12}. \tag{62}$$

where $M^{(x)}(x,\xi)$ is the unique solution of the following Riemann-Hilbert problem.

- $M^{(x)}(x,\xi) = \begin{cases} M_-^{(x)}(x,\xi), & Im\xi^2 \leq 0 \\ M_+^{(x)}(x,\xi), & Im\xi^2 \geq 0 \end{cases}$ *is a meromorphic function.*
- $M_+^{(x)}(x,\xi) = M_-^{(x)}(x,\xi)J^{(x)}(x,\xi), \xi^2 \in R$,
  where

$$J^{(x)}(x,\xi) = \begin{pmatrix} \frac{1}{a(\xi)\overline{a(\bar{\xi})}} & \frac{b(\xi)}{a(\xi)}e^{-2i\lambda^2 x} \\ -\frac{\overline{b(\bar{\xi})}}{a(\xi)}e^{2i\lambda^2 x} & 1 \end{pmatrix}, \xi^2 \in R. \tag{63}$$

- $M^{(x)}(x,\xi) = I + O(\frac{1}{\xi}), \xi \to \infty$.
- *$a(\xi)$ has $2n$ simple zeros $\{\varepsilon_j\}_{j=1}^{2n}$, $2n = 2n_1 + 2n_2$, such that $\varepsilon_j, (j = 1,2,...,2n_1)$ lie in D_1, and $\bar{\varepsilon}_j$, $(j = 1,2,...,2n_2)$ lie in D_2.*
- *The first column of $M_+^{(x)}$ has simple poles at $\xi = \varepsilon_j, j = 1,2,...,2n_1$. Furthermore, the second column of $M_-^{(x)}$ has simple poles at $\xi = \bar{\varepsilon}_j, j = 1,2,...,2n_2$. The relevant residues are given by*

$$Res\{[M^{(x)}(x,\xi)]_1, \varepsilon_j\} = \frac{e^{2i(\varepsilon_j^2 - 1)x}}{\dot{a}(\varepsilon_j)b(\varepsilon_j)}[M^{(x)}(x,\varepsilon_j)]_2, j = 1,2,...,2n_1, \tag{64}$$

$$Res\{[M^{(x)}(x,\xi)]_2, \bar{\varepsilon}_j\} = \frac{e^{-2i(\bar{\varepsilon}_j^2 - 1)x}}{\overline{\dot{a}(\bar{\varepsilon}_j)b(\bar{\varepsilon}_j)}}[M^{(x)}(x,\bar{\varepsilon}_j)]_1, j = 1,2,...,2n_2. \tag{65}$$

Definition 2. *For boundary values $g_0(t) = q(0,t), g_1(t) = q_x(0,t)$, the map $\tilde{\mathbb{S}}$ can be defined by*

$$\tilde{\mathbb{S}} : \{g_0(t), g_1(t)\} \to \{A(\xi), B(\xi)\}$$

with

$$\begin{pmatrix} B(\xi) \\ A(\xi) \end{pmatrix} = \mu_1^{(2)}(0,t;\xi), Im\xi^2 \geq 0,$$

where $\mu_1(0,t;\xi)$ is the unique solution of the Volterra linear integral equation

$$\mu_1(0,t;\xi) = I - \int_t^T e^{2i\lambda^4(t'-t)\hat{\sigma}_3} V_2(0,t';\xi)\mu_1(0,t',\xi)dt'$$

and $V_2(0,t;\xi)$ is given by (46).

Proposition 2. *$A(\xi)$ and $B(\xi)$ possess these properties.*

(i) *$A(\xi)$ and $B(\xi)$ are analytic for $\{\xi \in C | Im\xi^4 > 0\}$ and continuous $\{\xi \in C | Im\xi^4 \geq 0\}$,*

(ii) *$A(\xi)\overline{A(\bar{\xi})} - B(\xi)\overline{B(\bar{\xi})} = 1, \xi^4 \in R,$*

(iii) *$A(\xi) = 1 + O(\frac{1}{\xi}), B(\xi) = O(\frac{1}{\xi}), \xi \to \infty, Im\xi^4 \geq 0,$*

(iv) *$A(-\xi) = A(\xi), B(-\xi) = -B(\xi), Im\xi^4 \geq 0,$*

(v) *We define $\tilde{\mathbb{Q}} : \{A(\xi), B(\xi)\} \to \{g_0(t), g_1(t)\}$, as the inverse of map $\tilde{\mathbb{S}}$, with*

$$\begin{aligned} g_0(t) &= 2im_{12}^{(1)}(t)e^{2i\int_0^t \Delta_2(t')dt'}, \\ g_1(t) &= (4m_{12}^{(2)} + |g_0(t)|^2 m_{12}^{(1)}(t))e^{2i\int_0^t \Delta_2(t')dt'} + ig_0(t)(2m_{22}^{(2)}(t) + |g_0(t)|^2), \end{aligned} \tag{66}$$

where

$$\Delta_2(t) = 4|m_{12}^{(1)}|^4 + 8(Re[m_{12}^{(1)}\bar{m}_{12}^{(3)}] - |m_{12}^{(1)}|^2 Re[m_{22}^{(2)}]),$$

with the functions $m^{(i)}(t)(i = 1,2,3.)$ are depend on

$$M^{(t)}(t,\xi) = I + \frac{m^{(1)}(t)}{\xi} + \frac{m^{(2)}(t)}{\xi^2} + \frac{m^{(3)}(t)}{\xi^3} + O(\frac{1}{\xi^4}), \xi \to \infty,$$

where $M^t(t,\xi)$ is the unique solution of the following Riemann-Hilbert problem

- $M^{(t)}(t,\xi) = \begin{cases} M_-^{(t)}(t,\xi), & Im\xi^4 \leq 0 \\ M_+^{(t)}(t,\xi), & Im\xi^4 \geq 0 \end{cases}$ *is a meromorphic function.*
- $M_+^{(t)}(t,\xi) = M_-^{(t)}(t,\xi)J^{(t)}(t,\xi), \xi^4 \in R,$
  where

$$J^{(t)}(t,\xi) = \begin{pmatrix} \frac{1}{A(\xi)\overline{A(\bar{\xi})}} & \frac{B(\xi)}{\overline{A(\bar{\xi})}}e^{-4i\lambda^4 t} \\ -\frac{\overline{B(\bar{\xi})}}{A(\xi)}e^{4i\lambda^4 t} & 1 \end{pmatrix}, \xi^4 \in R. \tag{67}$$

- $M^{(t)}(t,\xi) = I + O(\frac{1}{\xi}), \xi \to \infty.$
- *$A(\xi)$ has $2N$ simple zeros $\{\gamma_j\}_{j=1}^{2N}$, $2N = 2N_1 + 2N_2$, such that $\gamma_j (j = 1,2,...,2N_1)$ lie in D_3, and $\bar{\gamma}_j (j = 1,2,...,2N_2)$ lie in D_4.*
- *The first column of $M_+^{(t)}$ has simple poles at $\xi = \gamma_j, j = 1,2,...,2N_1$. And the second column of $M_-^{(t)}$ has simple poles at $\xi = \bar{\gamma}_j, j = 1,2,...,2N_2$. The relevant residues are given by*

$$Res\{[M^{(t)}(t,\xi)]_1, \gamma_j\} = \frac{e^{4i(\gamma_j^2-1)^2 t}}{\dot{A}(\gamma_j)B(\gamma_j)}[M^{(t)}(t,\gamma_j)]_2, j = 1,2,...,2N_1, \tag{68}$$

$$Res\{[M^{(t)}(t,\xi)]_2, \bar{\gamma}_j\} = \frac{e^{-4i(\bar{\gamma}_j^2-1)^2 t}}{\dot{A}(\bar{\gamma}_j)b(\bar{\gamma}_j)}[M^{(t)}(t,\bar{\gamma}_j)]_1, j = 1,2,...,2N_2. \tag{69}$$

4.2. The Regular Riemann-Hilbert Problem

Theorem 4. *Given the smooth function $q_0(x)$, which is compatible with $g_0(t)$ and $g_1(t)$. The spectral functions $a(\xi)$,$b(\xi)$,$A(\xi)$, and $B(\xi)$ are defined according to the previous definitions. Furthermore, they satisfy the global relation (49). Clearly, it becomes $B(\xi)a(\xi) - A(\xi)b(\xi) = 0$ when $\xi \to \infty$. Define the $M(x,t;\xi)$ as the solution of this following Riemann-Hilbert problem.*

- *$M(x,t;\xi)$ is a sectionally meromorphic function in $\{\xi \in C | \xi^4 \in R\}$.*
- *The residue condition of $M(x,t;\xi)$ satisfies Theorem 3*
- *$M(x,t;\xi)$ satisfies the jump condition*

$$M_+(x,t;\xi) = M_-(x,t;\xi)J(x,t;\xi), \xi^4 \in R,$$

where the jump matrices are defined by (55)–(57).

- *$M(x,t;\xi) = I + O(\frac{1}{\xi}), \xi \to \infty$.*

Then, $M(x,t;\xi)$ not only exists but is unique. In this way, the solution of the mNLS equation can be derived, which can be defined by

$$\begin{aligned} &q(x,t) = 2im(x,t)e^{2i\int_{(0,0)}^{(x,t)}\Delta}, \\ &m(x,t) = \lim_{\xi\to\infty}(\xi\mu_j(x,t;\xi))_{12}, \\ &\Delta = -2|m|^2dx + [2i(m\bar{m}_x - m_x m) + 28|m|^4]dt. \end{aligned} \tag{70}$$

Besides, $q(x,t)$ also satisfies the initial-boundary values condition

$$q(x,0) = q_0(x), q(0,t) = g_0(t), \text{ and } q_x(0,t) = g_1(t).$$

Proof. Actually, if there are no zeros of $a(\xi)$ and $d(\xi)$, then the 2×2 function $M(x,t;\xi)$ satisfies a non-singular Riemann-Hilbert problem. Due to the jump matrices $J(x,t;\xi)$ possessing symmetry, we can find that this problem has a unique solution. On the other hand, when $a(\xi)$ and $d(\xi)$ have a certain number of zeros, by specific mapping, the singular Riemann-Hilbert problem can become no zeros with a system of algebraic equations; the unique solvability can be proved by the following theorem. □

Theorem 5. *The Riemann-Hilbert problem in Theorem 4 with the vanishing boundary condition*

$$M(x,t;\xi) \to 0, \xi \to \infty,$$

has only the zero solution.

Proof. Firstly, we suppose that the matrix function $M(x,t;\xi)$ is a solution of the Riemann-Hilbert problem in Theorem 4. At the same time, $A^\dagger$ means the complex conjugate transpose of A, where A is a 2×2 matrix. We define

$$\begin{aligned} &H_+(\xi) = M_+(\xi)M_-^\dagger(-\bar{\xi}), Im\xi^4 \geq 0, \\ &H_-(\xi) = M_-(\xi)M_+^\dagger(-\bar{\xi}), Im\xi^4 \leq 0, \end{aligned} \tag{71}$$

where the x and t are dependent with each other. $H_+(\xi)$ and $H_-(\xi)$ are analytic in $\{\xi \in C | Im\xi^4 > 0\}$ and $\{\xi \in C | Im\xi^4 < 0\}$, respectively. Due to the symmetry, we can obtain from (54) and (55)

$$J_1^\dagger(-\bar{\xi}) = J_1(\xi), J_3^\dagger(-\bar{\xi}) = J_3(\xi), J_2^\dagger(-\bar{\xi}) = J_4(\xi). \tag{72}$$

Then

$$\begin{aligned} &H_+(\xi) = M_-(\xi)J(\xi)M_-^\dagger(-\bar{\xi}), Im\xi^4 \in R, \\ &H_-(\xi) = M_-(\xi)J^\dagger(-\bar{\xi})M_-^\dagger(-\bar{\xi}), Im\xi^4 \in R. \end{aligned} \tag{73}$$

From the above two equations, it is easy to find that $H_+(\xi) = H_-(\xi)$. This means that $H_+(\xi)$ and $H_-(\xi)$ define an entire function decaying at infinity, hence the $H_+(\xi) \equiv 0$ and $H_-(\xi) \equiv 0$. Finding $J_3(i\hbar)(\hbar \in R)$ is a 2×2 unit Hermitian matrix for any $\hbar \in R$. It is not difficult to see that $J_3(i\hbar)(\hbar \in R)$ is a positive definite matrix. Now that $H_-(\hbar) = 0$ for $\hbar \in iR$, we have

$$M_+(i\hbar)J_3(i\hbar)M_+^\dagger(i\hbar) = 0. \tag{74}$$

After simple calculation, we have $M_+(i\hbar) = 0$ for $\hbar \in R$. Therefore, $M_+(\xi) = 0$, $M_-(\xi) = 0$. □

Remark 1. *$q(x,t)$ satisfies the mNLS equation.*

In fact, if $M(x,t;\xi)$ is the solution of the Riemann-Hilbert problem defined by Theorem 4 and $q(x,t)$ is defined as the previous definition, with the help of the dressing method [45], we can find that $q(x,t)$ satisfies the Lax pair (18). Hence, $q(x,t)$ satisfies the mNLS equation.

Remark 2. *Using the same proof method in Reference [32] can we prove that $q(x,t)$ satisfies the initial values $q(x,0) = q_0(x)$ and boundary values $q(0,t) = g_0(t), q_x(0,t) = g_1(t)$, so in this paper, we leave this proof out.*

5. Conclusions

In this paper, we mainly studied the initial-boundary values problem for the mNLS equation on the half line. Before we did this, with the help of prolongation structure theory, the Lax pair of this equation was derived. Then we reconstructed the Lax pair to obtain a Riemann-Hilbert problem, and therefore, the potential function has been represented by its solution. In future work, the long time asymptotic behavior for the solutions will be analyzed.

Author Contributions: All authors contributed equally to the writing of this paper. All authors read and approved the final manuscript.

Funding: This work was supported by Nature Science Foundation of Shandong Province of China (No.ZR2018MA017), China Postdoctoral Science Foundation funded project (No.2017M610436), Open Fund of the Key Laboratory of Meteorological Disaster of Ministry of Education (Nanjing University of Information Science and Technology) (No.KLME201801).

Conflicts of Interest: The authors declare no conflict of interest.

References

1. Xu, X.X.; Sun, Y.P. Two symmetry constraints for a generalized Dirac integrable hierarchy. *J. Math. Anal. Appl.* **2018**, *458*, 1073–1090. [CrossRef]
2. Mcanally, M.; Ma, W.X. An integrable generalization of the D-Kaup-Newell soliton hierarchy and its bi-Hamiltonian reduced hierarchy. *Appl. Math. Comput.* **2018**, *323*, 220–227. [CrossRef]
3. Ma, W.X. Conservation laws by symmetries and adjoint symmetries. *Discret. Contin. Dynam. Syst. Ser. S* **2017**, *11*, 707–721. [CrossRef]
4. Xu, X.X. A deformed reduced semi-discrete Kaup-Newell equation, the related integrable family and Darboux transformation. *Appl. Math. Comput.* **2015**, *251*, 275–283. [CrossRef]
5. Hirota, R. A new form of Bäcklund transformations and its relation to the inverse scattering problem. *Progr. Theor. Phys.* **1974**, *52*, 1498–1512. [CrossRef]
6. Xu, X.X.; Sun, Y.P. An integrable coupling hierarchy of Dirac integrable hierarchy, its Liouville integrability and Darboux transformation. *J. Nonlinear Sci. Appl.* **2017**, *10*, 3328–3343. [CrossRef]
7. Zhang, L.J.; Khalique, M. Classification and bifurcation of a class of second-order ODEs and its application to nonlinear PDEs. *Discret. Contin. Dynam. Syst. Ser. S* **2017**, *11*, 777–790. [CrossRef]
8. Lou, S.Y.; Ruan, H.Y.; Chen, D.F.; Chen, W.Z. Similarity reductions of the KP equation by a direct method. *J. Phys. A Gen. Phys.* **1999**, *24*, 1455. [CrossRef]
9. Ablowitz, M.J.; Segur, H. *Solitons and the Inverse Scattering Transform*; Siam: Philadelphia, PA, USA, 1981.
10. Gu, J.Y.; Zhang, Y.; Dong, H.H. Dynamic behaviors of interaction solutions of (3+1)-dimensional Shallow Water wave equation. *Comput. Math. Appl.* **2018**, *76*, 1408–1419. [CrossRef]

11. Liu, Y.; Dong, H.H.; Zhang, Y. Solutions of a discrete integrable hierarchy by straightening out of its continuous and discrete constrained flows. *Anal. Math. Phys.* **2018**. [CrossRef]
12. Ma, W.X.; Zhou, Y. Lump solutions to nonlinear partial differential equations via Hirota bilinear forms. *J. Differ. Eq.* **2018**, *264*, 2633–2659. [CrossRef]
13. Zhang, Y.; Dong, H.H.; Zhang, X.E.; Yang, H.W. Rational solutions and lump solutions to the generalized (3+1)-dimensional Shallow Water-like equation. *Comput. Math. Appl.* **2016**, *73*, 246–252. [CrossRef]
14. Wang, H.; Wang, Y.H.; Dong, H.H. Interaction solutions of a (2+1)-dimensional dispersive long wave system. *Comput. Math. Appl.* **2018**, *75*, 2625–2628. [CrossRef]
15. Dong, H.Y.; Lu, C.N.; Yang, H.W. The finite volume WENO with Lax-Wendroff scheme for nonlinear system of Euler equations. *Mathematics* **2018**, *6*, 211. [CrossRef]
16. Lu, C.N.; Gao, Q.Q.; Fu, C.; Yang, H.W. Finite element method of BBM-Burgers equation with dissipative term based on Adaptive Moving Mesh. *Discret. Dynam. Nat. Soc.* **2017**, *2017*, 3427376. [CrossRef]
17. Tao, M.S.; Dong, H.H. Algebro-Geometric solutions for a discrete integrable equation. *Discret. Dynam. Nat. Soc.* **2017**, *2017*, 5258375. [CrossRef]
18. Hirota, R. Exact N-soliton solutions of the wave equation of long waves in Shallow-Water and in nonlinear lattices. *J. Math. Phys.* **1973**, *14*, 180–184. [CrossRef]
19. Feng, B.F.; Maruno, K.; Ohta, Y. A two-component generalization of the reduced Ostrovsky equation and its integrable semi-discrete analogue. *J. Phys. A Math. Theor.* **2016**, *50*, 055201. [CrossRef]
20. Feng, B.F.; Kawahara, T. Stationary travelling-wave solutions of an unstable KdV-Burgers equation. *Phys. D Nonlinear Phenom.* **2000**, *137*, 228–236. [CrossRef]
21. Tao, M.S.; Zhang, N.; Gao, D.Z.; Yang, H.W. Symmetry analysis for three-dimensional dissipation Rossby waves. *Adv. Differ. Eq.* **2018**, *2018*, 300. [CrossRef]
22. Ma, W.X.; Li, J.; Khalique, C.M. A Study on Lump Solutions to a Generalized Hirota-Satsuma-Ito Equation in (2+1)-Dimensions. *Complexity* **2018**, *2018*, 9059858. [CrossRef]
23. Fokas, A.S. A unified transform method for solving linear and certain nonlinear PDEs. *Proc. R. Soc. Math. Phys. Eng. Sci.* **1997**, *453*, 1411–1443. [CrossRef]
24. Fokas, A.S. On a class of physically important integrable equations. *Phys. D Nonlinear Phenom.* **1995**, *87*, 145–150. [CrossRef]
25. Fokas, A.S. *A Unified Approach to Boundary Value Problems*; Society for Industrial and Applied Mathematics: Philadelphia, PA, USA, 2008.
26. Fokas, A.S. Integrable nonlinear evolution equations on the half-Line. *Commun. Math. Phys.* **2002**, *230*, 1–39. [CrossRef]
27. Lenells, J. The derivative nonlinear Schrödinger equation on the half-line. *Phys. D Nonlinear Phenom.* **2009**, *237*, 3008–3019. [CrossRef]
28. Lenells, J. Initial-boundary value problems for integrable evolution equations with 3×3 Lax pairs. *Phys. D Nonlinear Phenom.* **2012**, *241*, 857–875. [CrossRef]
29. Lenells, J. The Degasperis-Procesi equation on the half-line. *Nonlinear Anal. Theory Methods Appl.* **2013**, *76*, 122–139. [CrossRef]
30. Lenells, J.; Fokas, A. Boundary-value problems for the stationary axisymmetric Einstein equations: A rotating disc. *Nonlinearity* **2009**, *24*, 177–206. [CrossRef]
31. Lenells, J. An integrable generalization of the sine-Gordon equation on the half-line. *Ima J. Appl. Math.* **2012**, *76*, 554–572. [CrossRef]
32. Xu, J.; Fan, E.G. A Riemann-Hilbert approach to the initial-boundary problem for derivative nonlinear Schröingder equation. *Acta Math. Sci.* **2014**, *34*, 973–994. [CrossRef]
33. Xu, J.; Fan, E.G. The initial-boundary value problem for the Ostrovsky-Vakhnenko equation on the half-line. *Math. Phys. Anal. Geom.* **2016**, *19*, 20. [CrossRef]
34. Xu, J.; Fan, E.G. Initial-boundary value problem for integrable nonlinear evolution equation with 3×3 Lax pairs on the interval. *Stud. Appl. Math.* **2016**, *136*, 321–354. [CrossRef]
35. Xu, J.; Fan, E.G. The three-wave equation on the half-line. *Phys. Lett. A* **2014**, *378*, 26–33. [CrossRef]
36. Geng, X.G.; Liu, H.; Zhu, J.Y. Initial-boundary value problems for the coupled nonlinear Schrödinger equation on the half-Line. *Stud. Appl. Math.* **2015**, *135*, 310–346. [CrossRef]
37. Tian, S.F. Initial-boundary value problems for the general coupled nonlinear Schrödinger equation on the interval via the Fokas method. *J. Differ. Eq.* **2017**, *262*, 506–558. [CrossRef]

38. Xu, J.; Fan, E.G. The unified transform method for the Sasa-Satsuma equation on the half-line. *Physics* **2013**, *17*, 445–452. [CrossRef] [PubMed]
39. Zhang, N.; Xia, T.C.; Fan, E.G. A Riemann-Hilbert approach to the Chen-Lee-Liu equation on the half line. *Acta Math. Appl. Sin. Engl. Ser.* **2018**, *34*, 493–515. [CrossRef]
40. Ma, W.X. Application of the Riemann-Hilbert approach to the multicomponent AKNS integrable hierarchies. *Nonlinear Anal. Real World Appl.* **2019**, *47*, 1–17. [CrossRef]
41. Hu, B.B.; Xia, T.C.; Ma, W.X. Riemann-Hilbert approach for an initial-boundary value problem of the two-component modified Korteweg-de Vries equation on the half-line. *Appl. Math. Comput.* **2018**, *332*, 148–159. [CrossRef]
42. Deift, P.; Zhou, X. A steepest descent method for oscillatory Riemann-Hilbert problems. Asymptotics for the mKdV equation. *Ann. Math.* **1993**, *137*, 295–368. [CrossRef]
43. Lenells, J. The nonlinear steepest descent method: Asymptotics for initial-boundary value problems. *SIAM J. Math. Anal.* **2015**, *48*, 273–311. [CrossRef]
44. Xu, J.; Fan, E.G. Long-time asymptotic for the derivative nonlinear Schrödinger equation with step-like initial value. *Math. Phys. Anal. Geom.* **2013**, *16*, 253–288. [CrossRef]
45. Lenells, J. Dressing for a novel integrable generalization of the nonlinear Schrödinger equation. *J. Nonlinear Sci.* **2009**, *20*, 709–722. [CrossRef]
46. Deift, P.; Zhou, X. Long-time asymptotics for solutions of the NLS equation with initial data in a weighted Sobolev space. *Commun. Pure Appl. Math.* **2010**, *56*, 1029–1077. [CrossRef]
47. Wahlquist, H.D.; Estabrook, F.B. Prolongation structures of nonlinear evolution equations. *J. Math. Phys.* **2008**, *16*, 1293–1297. [CrossRef]
48. Hermann, R. Pseudopotentials of Estabrook and Wahlquist, the Geometry of Solitons, and the Theory of Connections. *Phys. Rev. Lett.* **1976**, *36*, 791–795. [CrossRef]
49. Deconinck, B. A Constructive Test for Integrability of Semi-Discrete Systems. *Phys. Lett. A* **1996**, *223*, 45–54. [CrossRef]
50. Wang, D.S. Integrability of the coupled KdV equations derived from two-layer fluids: Prolongation structures and Miura transformations. *Nonlinear Anal.* **2010**, *73*, 270–281. [CrossRef]
51. Humphreys, J.E. *Introduction to Lie Algebras and Representation Theory*; Springer: New York, NY, USA, 1972.
52. Morris, H.C. Prolongation structures and nonlinear evolution equations in two spatial dimensions. II. A generalized nonlinear Schrödinger equation. *J. Math. Phys.* **1977**, *18*, 285–288. [CrossRef]
53. Karsten, T. Hamiltonian form of the modified nonlinear Schrödinger equation for gravity waves on arbitrary depth. *J. Fluid Mech.* **2011**, *670*, 404–426.
54. Wen, X.Y.; Yang, Y.Q.; Yan, Z.Y. Generalized perturbation (n, M)-fold Darboux transformations and multi-rogue-wave structures for the modified self-steepening nonlinear Schrödinger equation. *Phys. Rev. E Stat. Nonlinear Soft Matter Phys.* **2015**, *92*, 012917. [CrossRef] [PubMed]
55. Brizhik, L.; Eremko, A.; Piette, B.; Zakrzewski, W. Static solutions of a D-dimensional modified nonlinear Schrödinger equation. *Nonlinearity* **2003**, *16*, 1481–1497. [CrossRef]
56. Liu, J.Q.; Wang, Z.Q. Symmetric solutions to a modified nonlinear Schrödinger equation. *Nonlinearity* **2007**, *21*, 121. [CrossRef]
57. Strampp, W. Lax-pairs, spectral problems, and recursion operators. *J. Math. Phys.* **1984**, *25*, 2905–2909. [CrossRef]
58. Maimistov, A.I. Evolution of solitary waves which are approximately solitons of a nonlinear Schrödinger equation. *Soviet J. Exp. Theor. Phys.* **1993**, *77*, 727–731.
59. Mihalache, D.; Truta, N.; Panoiu, N.; Baboiu, D. Analytic method for solving the modified nonlinear Schrödinger equation describing soliton propagation along optical fibers. *Phys. Rev. A* **1993**, *47*, 3190–3194. [CrossRef] [PubMed]

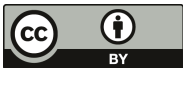

© 2019 by the authors. Licensee MDPI, Basel, Switzerland. This article is an open access article distributed under the terms and conditions of the Creative Commons Attribution (CC BY) license (http://creativecommons.org/licenses/by/4.0/).

mathematics

MDPI

Article

On the Connection between Spherical Laplace Transform and Non-Euclidean Fourier Analysis

Enrico De Micheli †

IBF –Consiglio Nazionale delle Ricerche, Via De Marini, 6-16149 Genova, Italy; enrico.demicheli@cnr.it
† Dedicated to the memory of Professor Giovanni Alberto Viano.

Received: 17 January 2020; Accepted: 17 February 2020; Published: 20 February 2020

Abstract: We prove that, if the coefficients of a Fourier–Legendre expansion satisfy a suitable Hausdorff-type condition, then the series converges to a function which admits a holomorphic extension to a cut-plane. Next, we introduce a Laplace-type transform (the so-called *Spherical Laplace Transform*) of the jump function across the cut. The main result of this paper is to establish the connection between the *Spherical Laplace Transform* and the *Non-Euclidean Fourier Transform* in the sense of Helgason. In this way, we find a connection between the unitary representation of $\mathrm{SO}(3)$ and the principal series of the unitary representation of $\mathrm{SU}(1,1)$.

Keywords: holomorphic extension; spherical Laplace transform; non-Euclidean Fourier transform; Fourier–Legendre expansion

MSC: 42A38; 44A10; 44A12; 42C10

1. Introduction

It is well known that the classical Fourier transform refers to the decomposition of a function belonging to an appropriate space into exponentials, which can be viewed as the irreducible unitary representations of the additive group of the real numbers. However, in the current most popular interpretation, particularly in connection with non-commutative groups, the phrase *harmonic analysis* has lost its original function-theoretic meaning and now it generally refers not to functions but to representations. It thus becomes natural to regard irreducible representations as the basic building blocks of the theory in place of exponential functions [1]. There are however examples in the theory of the semi-simple non-compact Lie groups where the classical setup prevails, in the sense that one can find a class of functions which play a role similar to that played by the exponentials on the real line. A typical example thereof is the group $\mathrm{SU}(1,1)$: hereafter, we shall work at the level of homogeneous spaces associated with this group and, accordingly, we shall study the spherical functions that can be constructed in these spaces.

Within this framework, a fundamental role is played by the Helgason construction of the so-called *non-Euclidean Fourier analysis* [2]. The working ambient is the symmetric space $\mathrm{SU}(1,1)/\mathrm{SO}(2)$, i.e., the non-Euclidean disk. By the use of the Poisson kernel, the analog of the plane waves are constructed in the case of the hyperbolic disk and, successively, an integral representation of the conical functions $P_{-\frac{1}{2}+\mathrm{i}\mu}(\cosh r)$ (i.e., the Legendre functions of the first kind with index $(-\frac{1}{2}+\mathrm{i}\mu)$, $\mu \in \mathbb{R}$) is derived in terms of these *hyperbolic waves*. It can thus be proved for these functions a product formula, which corresponds to the classical product formula of the exponentials. Finally, a Fourier transform on the non-Euclidean disk can be set up, which is exactly the tool analogous to the classical Fourier transform. In this connection, it is worth recalling that the conical functions can be associated with the

principal series of the irreducible unitary representation of the group $\mathrm{SU}(1,1)$, which acts transitively on the hyperbolic disk.

Consider now an isotropic cone in $\mathbb{R}^3$. We focus on the two-sheeted hyperboloid interior to the cone. By stereographic projection, the upper sheet of the two-sheeted hyperboloid can be mapped into the interior of the unit disk. Since the connected component of the two-sheeted hyperboloid is the homogeneous space $\mathrm{SO}_0(1,2)/\mathrm{SO}(2)$, the non-Euclidean Fourier analysis coincides with the harmonic analysis on $\mathrm{SO}_0(1,2)/\mathrm{SO}(2)$. We can thus define and study the Fourier transform on the two-sheeted hyperboloid.

Harmonic analysis can be studied also on the one-sheeted hyperboloid, which is a pseudo-Riemannian symmetric space $\mathrm{SO}_0(1,2)/\mathrm{SO}_0(1,1)$. It is then possible to construct on this symmetric space spherical functions, which turn out to be the Legendre functions of the second kind. A peculiar feature of this space is that it can be equipped with the partial ordering associated with the light cone in $\mathbb{R}^3$: namely, $x \geqslant y \Leftrightarrow (x-y)$ belongs to the closed future cone of $\mathbb{R}^3$. The one-sheeted hyperboloid equipped with this ordering relation is a *causal symmetric space* [3]. Accordingly, we can introduce a *Volterra algebra* of kernels, i.e., kernels $K(x,y)$ whose support is contained in the set $\Gamma \doteq \{(x,y) \in X_2 \times X_2 : x \geqslant y\}$, where X_2 is the one-sheteed hyperboloid. A kernel K is said to be invariant under $G \equiv \mathrm{SO}_0(1,2)$ if for any $g \in G$: $K(gx,gy) = K(x,y)$, $(x,y) \in \Gamma$. An invariant Volterra kernel K can be identified with a function f on G through the equality: $K(ge_2,e_2) = f(g)$, where $g \in G$ and $e_2 = (0,0,1)$ (see next Figure 1) is the point which features $he_2 = e_2$, with $h \in \mathrm{SO}_0(1,1)$ [4–7]. Successively, the *spherical Laplace transform* for this class of functions can be defined. This transform, as the ordinary Laplace transform, is holomorphic in a half-plane and, in the specific case of the spherical Laplace transform, this analyticity property follows from the analyticity property of the Legendre functions of the second kind $Q_\lambda(\cdot)$, which are holomorphic in the half-plane $\mathbb{C}^{(+)}_{(-1)} \doteq \{\lambda \in \mathbb{C} : \mathrm{Re}\,\lambda > -1\}$. These latter functions are indeed the spherical functions on ordered symmetric spaces in the sense of Faraut et al. [7].

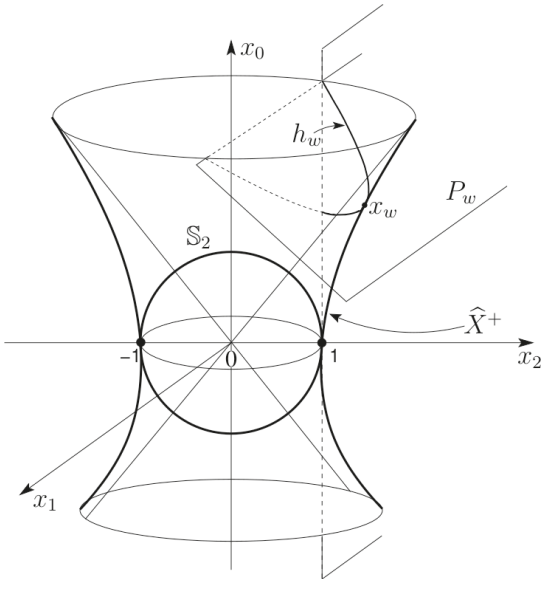

Figure 1. Horocyclic fibration of the one-sheteed hyperboloid X_2^+.

Another question closely related to this type of problems is the holomorphic extension associated with Fourier–Legendre expansions of the type: $\frac{1}{4\pi}\sum_{n=0}^{\infty}(2n+1)a_nP_n(\cos\theta)$, where $P_n(\cdot)$ denotes the Legendre polynomials. In this paper, we prove that, if the sequence $\{(n+1)^2a_n\}_{n=0}^{\infty}$ satisfies a suitable Hausdorff-type condition [8], then the function $f(\cos\theta)$, to which the Fourier–Legendre series converges in the interval $(-1,1)$, admits a holomorphic extension to the complex $\cos\theta$-plane cut along the semi-axis $[1,+\infty)$. The first result we prove is a basic feature of the holomorphic extension associated with Fourier–Legendre series: the *dual analyticity property*. To classes of functions which are holomorphic in the $\cos\theta$-plane cut along $[1,+\infty)$, there correspond classes of functions, denoted $\tilde{a}(\lambda)$ ($\lambda\in\mathbb{C}$), which are expressed as a spherical Laplace transform, holomorphic in the half-plane $\operatorname{Re}\lambda>-\frac{1}{2}$, of Carlsonian-type (i.e., of suitable exponential growth; see next Theorem 1) and, therefore, unique interpolants of the coefficients a_n of the Fourier-Legendre series, i.e., $\tilde{a}(\lambda)|_{\lambda=n}=a_n$ ($n=0,1,2,\ldots$).

At this point, two strictly related problems emerge. On the one hand, the possibility of connecting, via analytic continuation, the completeness of the spherical functions for $\mathrm{SO}(3)$ to the completeness of the corresponding expansion of $\mathrm{SL}(2,\mathbb{R})$, which is the group acting transitively on the upper half-plane, where the model of the non-Euclidean geometry can be realized, while, on the other hand, continuing the unitary representations of $\mathrm{SO}(3)$ to give the unitary representations of $\mathrm{SL}(2,\mathbb{R})$. The first problem has been initially tackled by Stein and Wainger [9], while, for what concerns the second one, the reader is referred to the work of R. Hermann [10]. However, both of these problems require linking the spherical Laplace transform to the non-Euclidean Fourier analysis. When we consider the ordinary Laplace transform of a function $f\in L^1(0,+\infty)\cap L^2(0,+\infty)$,

$$\widetilde{f}(\lambda)=\int_0^{+\infty}e^{-\lambda v}f(v)\,\mathrm{d}v\qquad(\lambda\in\mathbb{C},\operatorname{Re}\lambda>0),$$

we obtain for $\lambda=\mathrm{i}\mu$ ($\mu\in\mathbb{R}$):

$$\widetilde{f}(\mathrm{i}\mu)=\int_{-\infty}^{+\infty}e^{-\mathrm{i}\mu v}f(v)\,\mathrm{d}v\qquad(\mu\in\mathbb{R}),$$

which is precisely the Fourier transform of $f(v)$, it being well-defined in view of the assumption $f\in L^1(0,+\infty)$. Since $f\in L^1(0,+\infty)\cap L^2(0,+\infty)$, the Fourier transform can be inverted to recover $f(v)$ in terms of $\widetilde{f}(\mathrm{i}\mu)$ through the *inverse Fourier transform*, which converges to $f(v)$ as a limit in the mean order two. Correspondingly, we pass from the non-unitary representation $e^{-\lambda v}$ ($\lambda\in\mathbb{C},\operatorname{Re}\lambda>0,\mu\equiv\operatorname{Im}\lambda\in\mathbb{R}$) to the unitary irreducible representation $e^{-\mathrm{i}\mu v}$ ($\mu,v\in\mathbb{R}$) that we mentioned at the beginning of the Introduction. This connection can be extended. One of our results consists indeed of proving that the spherical Laplace transform reduces to the non-Euclidean Fourier transform at $\operatorname{Re}\lambda=-\frac{1}{2}$, which is precisely the value corresponding to the principal series of the unitary representations of the group $\mathrm{SU}(1,1)$, which acts transitively on the hyperbolic disk. This result has been obtained by establishing a bridge between the harmonic analysis on the one-sheeted hyperboloid and the harmonic analysis on the two-sheeted hyperboloid.

The harmonic analysis in causal symmetric spaces has been a subject of growing interest in the last three decades, and the research on these topics has flowed in various directions. Some papers have been devoted to the proof of the Paley–Wiener theorem for spherical Laplace transform [11,12] and others have treated the inversion problem extended up to the so-called Θ-transform [13]. In [14], Bertram has studied the compact symmetric space and its non-compact dual, both realized as real forms of their common complexification; this analysis has been performed by exploring the Ramanujan garden and by the use of the so-called *Master Theorem*. Working in a different direction, Gindinkin and Krötz [15] have studied the complex crown of Riemannian symmetric spaces and non-compactly causal symmetric spaces.

This allowed them to prove the conjecture that every non-compactly causal symmetric space occurs as a component of a distinguished boundary of some complex crown [15]. Finally, it is worth recalling that the question of relating the harmonic analysis of different real forms of a complex symmetric space has been studied also in the context of scattering theory and resonances [16–20].

The paper is organized as follows. In Section 2, we study the holomorphic extension associated with the Fourier–Legendre expansion by means of the spherical Laplace transform. We are thus led to develop the harmonic analysis on the complex one-sheeted hyperboloid $X_2^{(c)}$, which contains as submanifolds either the Euclidean sphere $(\mathrm{i}\mathbb{R} \times \mathbb{R}^2) \cap X_2^{(c)}$ on which the Fourier–Legendre expansion can be developed, and the real one-sheeted hyperboloid, which contains the support of the cut. In Section 3, we analyze the relationship between the spherical Laplace transform and the *non-Euclidean Fourier transform*. For this purpose, we consider a real two-sheeted hyperboloid, and, in this geometrical setting, we can recover the non-Euclidean Fourier transform in the sense of Helgason. Finally, in Section 4, some conclusions will be drawn.

2. Holomorphic Extension Associated with the Fourier–Legendre Expansion and the Spherical Laplace Transform

2.1. The Complex One-Sheeted Hyperboloid

In the space $\mathbb{C}^3$ of the variable $z = (z_0, z_1, z_2)$, we consider the complex quadric $X_2^{(c)}$ with equation

$$-z_0^2 + z_1^2 + z_2^2 = 1,$$

which is a one-sheeted complex hyperboloid. Next, we introduce two systems of coordinates: polar and horocyclic coordinates.

Polar Coordinates:

$$z_0 = -\mathrm{i} \sin\theta \cosh\varphi, \tag{1a}$$
$$z_1 = -\mathrm{i} \sin\theta \sinh\varphi, \qquad (\theta, \varphi \in \mathbb{C}), \tag{1b}$$
$$z_2 = \cos\theta. \tag{1c}$$

If $\theta = u$ $(u \in \mathbb{R})$ and $\varphi = \mathrm{i}\psi$ $(\psi \in \mathbb{R})$, (1) reads

$$x_0 = -\mathrm{i} \sin u \cos\psi, \tag{2a}$$
$$x_1 = \sin u \sin\psi, \qquad (u, \psi \in \mathbb{R}), \tag{2b}$$
$$x_2 = \cos u. \tag{2c}$$

It can be easily verified that: $-x_0^2 + x_1^2 + x_2^2 = \sin^2 u + \cos^2 u = 1$ that is, one obtains as a real submanifold of the complex one-sheeted hyperboloid $X_2^{(c)}$ the *Euclidean sphere* $\mathbb{S}_2 = (\mathrm{i}\mathbb{R} \times \mathbb{R}^2) \cap X_2^{(c)}$ ($\mathrm{i}\mathbb{R}$ referring to the coordinate z_0 of z).

Similarly, if $\theta = \mathrm{i}v$ $(v \in \mathbb{R})$ and $\varphi = \psi$ $(\psi \in \mathbb{R})$, (1) becomes

$$x_0 = \sinh v \cosh\psi, \tag{3a}$$
$$x_1 = \sinh v \sinh\psi, \qquad (v, \psi \in \mathbb{R}), \tag{3b}$$
$$x_2 = \cosh v. \tag{3c}$$

In this case, it is easily verified that: $-x_0^2 + x_1^2 + x_2^2 = \cosh^2 v - \sinh^2 v = 1$. Equation (3) describes only the subset $X_2^+ \doteq \{x \in X_2 : x_2 \geqslant 1\}$ of the real one-sheeted hyperboloid X_2, which is precisely what we need for the current analysis. Finally, let $\widehat{X}^+$ denote the (real) meridian lying in the plane $x_1 = 0$ with equation: $x_0^2 - x_2^2 = -1$.

Horocyclic Coordinates:

We now introduce another system of coordinates (τ, ζ) as follows:

$$z_0 = -\mathrm{i}\sin\tau + \frac{1}{2}\zeta^2 e^{-\mathrm{i}\tau}, \tag{4a}$$

$$z_1 = \zeta e^{-\mathrm{i}u}, \qquad (\tau, \zeta \in \mathbb{C}), \tag{4b}$$

$$z_2 = \cos\tau - \frac{1}{2}\zeta^2 e^{-\mathrm{i}\tau}. \tag{4c}$$

For $\tau = \mathrm{i}w$ ($w \in \mathbb{R}$) and $\zeta \in \mathbb{R}$, Equation (4) reads

$$x_0 = \sinh w + \frac{1}{2}\zeta^2 e^{w}, \tag{5a}$$

$$x_1 = \zeta e^{w}, \qquad (w, \zeta \in \mathbb{R}), \tag{5b}$$

$$x_2 = \cosh w - \frac{1}{2}\zeta^2 e^{w}. \tag{5c}$$

Then, we consider the intersection points x_w of $\widehat{X}^+$ with the family of planes $P_w : x_0 + x_2 = e^w$ ($w \in \mathbb{R}$) (see Equation (5)), i.e., the points $x_w = (\sinh w, 0, \cosh w)$. The sections of X_2 by these planes are the (real) parabolae Π_w^+ (except in the case $x_0 + x_2 = 0$). When $\zeta = 0$ in (5), we obtain the point x_w, which is the apex of the corresponding parabola Π_w^+ (see Figure 1).

This geometrical construction can now be extended to the complex one-sheeted hyperboloid $X_2^{(c)}$. We consider the (complex) hyperbola $\widehat{X}^{(c)}$ lying in the plane $z_1 = 0$, whose equation is: $z_0^2 - z_2^2 = -1$ (see Equation (4)), and its intersections with the family of planes P_τ with equation $z_0 + z_2 = e^{-\mathrm{i}\tau}$ ($\tau \in \dot{\mathbb{C}} \doteq \mathbb{C}/2\pi\mathbb{Z}$). Each plane P_τ intersects the hyperbola $\widehat{X}^{(c)}$ at the (unique) point $z_\tau = (z_0 = -\mathrm{i}\sin\tau, z_1 = 0, z_2 = \cos\tau)$, thus defining a bijection from the set of planes $\mathcal{P} \doteq \{P_\tau : \tau \in \dot{\mathbb{C}}\}$ onto $\widehat{X}^{(c)} = \{z_\tau : \tau \in \dot{\mathbb{C}}\}$. For each $\tau \in \dot{\mathbb{C}}$, the manifold $P_\tau \cap X_2^{(c)}$ is a complex parabola Π_τ, which we call a *complex horocycle*. The set of horocycles $\{\Pi_\tau : \tau \in \dot{\mathbb{C}}\}$ defines a fibration with basis $\widehat{X}^{(c)}$ on the dense domain $X_2'^{(c)} \doteq \{z \in X_2^{(c)} : z_0 + z_2 \neq 0\}$ of $X_2^{(c)}$. We can therefore associate with this fibration the parametric representation of $X_2'^{(c)}$ given by Equation (4), (τ, ζ) being the horocyclic coordinates of the point $z \in X_2'^{(c)}$.

2.2. The Radon Transform

We now define a Radon-type transformation in X_2, where the horocycles defined above play the same role as the planes do in the ordinary Radon transformation. We introduce the following integral:

$$\int_{h_w} \underline{F}\left(\cosh w - \frac{1}{2}\zeta^2 e^{w}\right) \mathrm{d}\zeta = \widehat{F}(w), \tag{6}$$

where h_w is the oriented segment of horocycle, which is represented by the arc of parabola whose apex is obtained by setting $\zeta = 0$ in (5) (i.e., its coordinates are: $x_0 = \sinh w$, $x_1 = 0$, $x_2 = \cosh w$; $w \in \mathbb{R}$), and whose endpoints lie on the plane $x_2 = 1$. The function $\underline{F}$ is assumed to satisfy the regularity conditions that make integral (6) convergent.

Remark 1. *Legendre expansions, which will be our concern later, involve functions depending only on* $\cos u = x_2$ *(see (2c)). This is why, in the integral (6), we limit ourselves to consider functions only of the form* $\underline{F} = \underline{F}(\cosh w - \frac{1}{2}\zeta^2 e^w)$ *(see (5c)).*

Since the integrand in (6) is an even function of ζ, the integration domain can be restricted to the part h_w^+ of h_w with $x_1 \geqslant 0$, which can be parametrized as follows (see (5)):

$$h_w^+ = \{x \in \Pi_w^+; x = x(\zeta, w);\ \zeta(\delta) = \left[2e^{-w}(1-\delta)(\cosh w - 1)\right]^{\frac{1}{2}};\ 0 \leqslant \delta \leqslant 1\} \qquad (w \in \mathbb{R}), \tag{7}$$

positively oriented from the apex to the endpoint lying on $x_2 = 1$. For $\delta = 1$, we have $\zeta = 0$, which yields the apex of the parabola representing the horocycle; for $\delta = 0$, we have $\zeta = [2e^{-w}(\cosh w - 1)]^{1/2}$, which gives the intersection of the horocycle with the plane $x_2 = 1$.

We may now introduce another parametrization of the segment of horocycle h_w^+, which is obtained by setting $x_2 = \cosh v$ (see (3c)):

$$h_w^+ = \{x \in \Pi_w^+; x = x(\zeta, w);\ \zeta(v) = \left[2e^{-w}(\cosh w - \cosh v)\right]^{\frac{1}{2}};\ 0 \leqslant v \leqslant w\} \qquad (w \in \mathbb{R}). \tag{8}$$

Indeed, we have $\zeta = 0$ for $v = w$ (the apex of the parabola) and $\zeta = [2e^{-w}(\cosh w - 1)]^{1/2}$ for $v = 0$ (endpoint of the parabola: $x_2 = \cosh v = 1$). Since $\mathrm{d}\zeta/\mathrm{d}v = -e^{-w/2}\sinh v[2(\cosh w - \cosh v)]^{-1/2}$, integral (6) takes the form:

$$\widehat{F}(w) = 2e^{-w/2}\int_0^w \underline{F}(\cosh v)\,\frac{\sinh v}{[2(\cosh w - \cosh v)]^{\frac{1}{2}}}\,\mathrm{d}v \doteq e^{-w/2}\,(\mathcal{A}F)\,(w) \qquad (w \in \mathbb{R}), \tag{9}$$

where $(\mathcal{A}F)\,(w)$ is an Abel-type integral.

The fibration realized by the horocycles Π_w^+ can now be extended to the complex domain by using the complex horocycles Π_τ ($\tau = t + \mathrm{i}w; t, w \in \mathbb{R}$), whose intersection with the (complex) meridian hyperbola $\widehat{X}^{(c)}$ is the point $z_\tau = (-\mathrm{i}\sin\tau, 0, \cos\tau)$. Accordingly, we introduce the following integral:

$$2\int_{h_\tau^+} \underline{f}\left(\cos\tau - \frac{1}{2}\zeta^2\, e^{-\mathrm{i}\tau}\right)\,\mathrm{d}\zeta = \widehat{f}(\tau), \tag{10}$$

h_τ^+ being the (oriented) arc of the complex horocycle defined by (see (4) and (7)):

$$h_\tau^+ = \{z \in \Pi_\tau; z = z(\zeta, \tau);\ \zeta(\delta) = [2e^{\mathrm{i}\tau}(1-\delta)(\cos\tau - 1)]^{\frac{1}{2}};\ 0 \leqslant \delta \leqslant 1\} \qquad (\tau \in \mathbb{C}).$$

For $\delta = 1$, we have $\zeta = 0$, i.e., the point z_τ belonging to $\widehat{X}^{(c)}$, while for $\delta = 0$ we have $\zeta = [2e^{\mathrm{i}\tau}(\cos\tau - 1)]^{1/2}$, which is the intersection of h_τ^+ with the plane $z_2 = 1$. Similarly to what done before, we may now introduce the following parametrization of h_τ^+, obtained by setting $z_2 = \cos\theta$ ($\theta \in \mathbb{C}, \theta = u + \mathrm{i}v$; see (1) and (8)):

$$h_\tau^+ = \{z \in \Pi_\tau; z = z(\zeta, \tau);\ \zeta(\theta) = [2e^{\mathrm{i}\tau}(\cos\tau - \cos\theta)]^{\frac{1}{2}};\ \theta \in \gamma_\tau\} \qquad (\tau \in \mathbb{C}),$$

where γ_τ denotes the ray in the θ-plane oriented from 0 to τ:

$$\gamma_\tau = \{\theta = \theta(\delta);\ \cos\theta(\delta) - 1 = \delta(\cos\tau - 1);\ 0 \leqslant \delta \leqslant 1\} \qquad (\tau \in \mathbb{C}).$$

Now, since $\mathrm{d}\zeta/\mathrm{d}\theta = e^{\mathrm{i}\tau/2}[2(\cos\tau - \cos\theta)]^{-1/2}\sin\theta$, integral (10) can be rewritten in the form:

$$\widehat{f}(\tau) = -2e^{\mathrm{i}\tau/2}\int_{\gamma_\tau} f(\theta)\,\frac{\sin\theta}{[2(\cos\tau-\cos\theta)]^{\frac{1}{2}}}\,\mathrm{d}\theta, \tag{11}$$

where $f(\theta) \equiv \underline{f}(\cos\theta)$. The relevant branch of the function $[2(\cos\tau - \cos\theta)]^{-1/2}$ is specified by the condition that, for $\tau = \mathrm{i}w$ and $\theta = \mathrm{i}v$ (with $w > v$), it takes the value $[2(\cosh w - \cosh v)]^{-1/2} \geqslant 0$. Putting in (11) $\tau = \mathrm{i}w$, $\theta = \mathrm{i}v$, we re-obtain precisely the r.h.s. of formula (9), once $\underline{f}$ is identified with $\underline{F}$.

Restricting formula (11) to the set of real values for the variables τ and θ, namely, $\tau = t$ and $\theta = u$ ($t, u \in \mathbb{R}$), from (11), we obtain

$$\widehat{f}(t) = -2e^{\mathrm{i}t/2}\int_0^t f(u)\,\frac{\sin u}{[2(\cos t-\cos u)]^{\frac{1}{2}}}\,\mathrm{d}u. \tag{12}$$

Accounting for the relevant branch of the factor $[2(\cos\tau - \cos\theta)]^{-1/2}$ in (11), formula (12) can be written in the following more precise form (involving a positive bracket):

$$\widehat{f}(t) = -2\mathrm{i}\,\varepsilon(t)\,e^{\mathrm{i}t/2}\int_0^t f(u)\,\frac{\sin u}{[2(\cos u-\cos t)]^{\frac{1}{2}}}\,\mathrm{d}u, \tag{13}$$

where $\varepsilon(t)$ denotes the sign function.

2.3. Holomorphic Extension Associated with Trigonometric Series

2.3.1. Fourier–Legendre Expansions as Trigonometric Series

Consider the following Legendre series

$$\frac{1}{4\pi}\sum_{n=0}^{\infty}(2n+1)\,a_n\,P_n(\cos u), \tag{14}$$

where $P_n(\cdot)$ denotes the Legendre polynomials, which satisfy the following integral representation:

$$P_n(\cos u) = \frac{1}{\pi}\int_0^\pi (\cos u + \mathrm{i}\sin u\cos\eta)^n\,\mathrm{d}\eta.$$

Suppose that expansion (14) converges to a function $\underline{f}(\cos u)$ absolutely integrable in the interval $u \in [0,\pi]$. Then, the Legendre coefficients a_n can be written as

$$a_n = 2\pi\int_0^\pi \underline{f}(\cos u)\,P_n(\cos u)\,\sin u\,\mathrm{d}u.$$

In Ref. [21], we proved the following proposition.

Proposition 1. *The Legendre coefficients $\{a_n\}_{n=0}^{\infty}$ coincide with the Fourier coefficients of the following form:*

$$a_n = \int_{-\pi}^{\pi}\widehat{f}(t)\,e^{\mathrm{i}nt}\,\mathrm{d}t \qquad (n = 0,1,2,\ldots), \tag{15}$$

where

$$\widehat{f}(t) = -2\mathrm{i}\,\varepsilon(t)\,e^{\mathrm{i}t/2}\int_0^t f(u)\,\frac{\sin u}{[2(\cos u-\cos t)]^{\frac{1}{2}}}\,\mathrm{d}u, \tag{16}$$

with $f(u) \equiv \underline{f}(\cos u)$, *and* $\varepsilon(t)$ *being the sign function.*

Proof. See Proposition 3.1 of Ref. [21]. □

Note that (16) coincides with (13). From (16), it is easy to verify that

$$\widehat{f}(t) = -e^{\mathrm{i}t}\widehat{f}(-t), \tag{17}$$

which, through (15), yields the following symmetry relation for the Legendre coefficients:

$$a_n = -a_{-n-1} \qquad (n \in \mathbb{Z}). \tag{18}$$

Now, we can introduce the following trigonometric series, assuming (18) to hold:

$$\begin{aligned} \frac{1}{2\pi}\sum_{n=-\infty}^{+\infty} a_n e^{-\mathrm{i}nt} &= \frac{1}{2\pi}\left[\sum_{n=0}^{+\infty} a_n e^{-\mathrm{i}nt} - e^{\mathrm{i}t}\sum_{n=0}^{+\infty} a_n e^{\mathrm{i}nt}\right] \\ &= \frac{1}{2\pi}e^{\mathrm{i}(t-\pi)/2}\sum_{n=-\infty}^{+\infty}(-1)^n a_n \cos\left[\left(n+\tfrac{1}{2}\right)(t-\pi)\right] = \frac{1}{2\pi}e^{\mathrm{i}(t-\pi)/2}\sum_{n=-\infty}^{+\infty} a_n \sin\left[\left(n+\tfrac{1}{2}\right)t\right], \end{aligned} \tag{19}$$

and study the associated holomorphic extension.

2.3.2. Holomorphic Extension Associated with Trigonometric Series

Consider a sequence $\{f_n\}_{n=0}^{\infty}$ of (real) numbers, and denote by Δ the difference operator:

$$\Delta f_n = f_{n+1} - f_n.$$

We have:

$$\Delta^k f_n = \underbrace{\Delta \times \Delta \times \cdots \Delta}_{k-\text{times}} f_n = \sum_{m=0}^{k}(-1)^m \binom{k}{m} f_{n+k-m}$$

(for any integer $k \geqslant 0$); Δ^0 is the identity operator, by definition. Suppose that there exists a positive constant M such that

$$(n+1)^{(1+\varepsilon)}\sum_{i=0}^{n}\binom{n}{i}^{(2+\varepsilon)}\left|\Delta^i f_{(n-i)}\right|^{(2+\varepsilon)} < M \qquad (n = 0, 1, 2, \ldots; \varepsilon > 0). \tag{20}$$

We shall refer to (20) as the *Hausdorff condition* for its relevance in the solution of the Hausdorff moment problem [8]. The tool we use to guarantee uniqueness of the interpolation of a sequence of numbers $\{f_n\}_{n=0}^{\infty}$ is Carlson's theorem [22]. Essentially, it gives growth conditions under which a function is uniquely determined by its values on non-negative integers. Let us recall that an entire function $f(z)$ is of exponential type $\tau < \infty$ if

$$\limsup_{r\to\infty}\frac{M_f(r))}{r} = \tau, \tag{21}$$

where $M_f(r)$ denotes the maximum modulus of $f(z)$ for $|z| = r$. The rate of growth of entire functions can be specified along different directions by the Phragmén-Lindelöf indicator function,

$$h_f(\theta) = \limsup_{r\to\infty}\frac{\log\left|f(re^{\mathrm{i}\theta})\right|}{r}. \tag{22}$$

Note that the preceding definitions can be extended to functions which are not entire, but regular (that is, analytic and single-valued) in a sector with vertex at the origin [22].

Theorem 1 (Carlson's theorem (Section 9.2, p. 153, [22])). *Let $f(z)$ be regular in the half-plane $\operatorname{Re} z \geqslant 0$ and*

(i) $f(z)$ *is of exponential type* $\tau < \infty$,
(ii) $h_f(\pi/2) + h_f(-\pi/2) < 2\pi$,
(iii) $f(n) = 0$ *for* $n = 0, 1, 2, \ldots$,

then $f(z)$ vanishes identically.

Among the functions of exponential type, condition (ii) requires $f(z)$ to be of exponential type less than π on the imaginary axis that is: $f(\mathrm{i}y) = O(1)\,\exp(c|y|)$ for some $c < \pi$. We shall refer to conditions (i) and (ii) as *Carlson's bound*. Moreover, an analytic function which interpolates a sequence of numbers $\{f_n\}_{n=0}^{\infty}$ and satisfy conditions (i) and (ii) above will be called a *Carlsonian interpolant*, in view of the fact that the uniqueness of the interpolation is guaranteed by Carlson's theorem.

Proposition 2. *Suppose that the set of numbers $\{f_n\}_{n=0}^{\infty}$, with $f_n \doteq (n+1)^2 a_n$ (a_n being the Fourier–Legendre coefficients of the series (14)), satisfies condition (20). Then:*

(i) There exists a unique Carlsonian interpolant $\widetilde{a}(\lambda)$ ($\lambda \in \mathbb{C}, \operatorname{Re}\lambda \geqslant -\frac{1}{2}$) of the coefficients $\{a_n\}_{n=0}^{\infty}$, which is holomorphic in the half-plane $\operatorname{Re}\lambda > -\frac{1}{2}$. Moreover, $\widetilde{a}(\lambda)$ belongs to the Hardy space $H^2(\mathbb{C}_{-1/2}^{(+)})$.
(ii) $\lambda^2\widetilde{a}(\lambda) \in L^2(-\infty, +\infty)$ for any fixed value of $\operatorname{Re}\lambda \geqslant -\frac{1}{2}$.
(iii) $\lambda^2\widetilde{a}(\lambda)$ tends uniformly to zero as $\lambda \to \infty$ inside any fixed half-plane $\operatorname{Re}\lambda \geqslant \delta > -\frac{1}{2}$.
(iv) $\lambda\widetilde{a}(\lambda) \in L^1(-\infty, +\infty)$ for any fixed value of $\operatorname{Re}\lambda \geqslant -\frac{1}{2}$.
(v) $\widetilde{a}(-\frac{1}{2} + \mathrm{i}\mu)$ ($\mu \in \mathbb{R}$) is a continuous function which tends to zero as $\mu \to \pm\infty$.
(vi) $\sup_{\substack{\sigma > -1/2 \\ \mu \in \mathbb{R}}} |\widetilde{a}(\sigma + \mathrm{i}\mu)| = \left|\widetilde{a}\left(-\frac{1}{2} + \mathrm{i}\mu\right)\right|$;

Proof. (i) Since the sequence $\{f_n\}_{n=0}^{\infty}$ satisfies condition (20), the numbers f_n are moments of a suitable function, that is, the following representation holds [8]:

$$f_n = \int_0^1 x^n\, \varphi(x)\, \mathrm{d}x \qquad (n = 0, 1, 2, \ldots), \tag{23}$$

where $\varphi \in L^{(2+\varepsilon)}(0,1)$. Let $x = e^{-s}$ in formula (23):

$$f_n = \int_0^{+\infty} e^{-(n+\frac{1}{2})s}\, e^{-s/2}\, \varphi(e^{-s})\, \mathrm{d}s \qquad (n = 0, 1, 2, \ldots).$$

Then, the numbers $\{f_n\}_{n=0}^{\infty}$ can be formally regarded as the restriction to the (non-negative) integers of the following Laplace transform:

$$\widetilde{f}(\lambda) = \int_0^{+\infty} e^{-(\lambda+\frac{1}{2})s}\, e^{-s/2}\, \varphi(e^{-s})\, \mathrm{d}s \qquad \left(\operatorname{Re}\lambda > -\tfrac{1}{2}\right), \tag{24}$$

being $\widetilde{f}(\lambda)|_{\lambda=n} = f_n$. We see that $e^{-s/2}\varphi(e^{-s}) \in L^2(0, +\infty)$: in fact, $\int_0^{+\infty} |e^{-s/2}\varphi(e^{-s})|^2\, \mathrm{d}s = \int_0^1 |\varphi(x)|^2\, \mathrm{d}x < \infty$, since $\varphi \in L^{(2+\varepsilon)}(0,1)$ and, a fortiori, $\varphi(x) \in L^2(0,1)$. Then, by the Paley–Wiener theorem [23], we have $\widetilde{f}(\lambda) \in H^2(\mathbb{C}_{-1/2}^{(+)})$, which is the Hardy space whose norm is: $\|\widetilde{f}\|_2 \doteq \sup_{\sigma > -1/2}(\int_{-\infty}^{+\infty} |\widetilde{f}(\sigma + \mathrm{i}\mu)|^2\, \mathrm{d}\mu)^{1/2}$, and $\mathbb{C}_{-1/2}^{(+)} \doteq \{\lambda \in \mathbb{C}, \lambda = \sigma + \mathrm{i}\mu; \sigma > -\frac{1}{2}, \mu \in \mathbb{R}\}$. Hence, use can

be made of Carlson's theorem, which guarantees that $\widetilde{f}(\lambda)$ is the unique Carlsonian interpolant of the sequence $\{f_n\}_{n=0}^{\infty}$. Let $\widetilde{a}(\lambda) \doteq \widetilde{f}(\lambda)/(\lambda+1)^2$. $\widetilde{a}(\lambda)$ is a function holomorphic for $\mathrm{Re}\,\lambda > -\frac{1}{2}$, which satisfies Carlson's bound since $\widetilde{f}(\lambda)$ does. Then, $\widetilde{a}(\lambda)$ is the unique Carlsonian interpolant of the set of Fourier–Legendre coefficients $\{a_n\}_{n=0}^{\infty}$ since $\widetilde{a}(\lambda)|_{\lambda=n} = \frac{\widetilde{f}(\lambda)}{(\lambda+1)^2}\Big|_{\lambda=n} = \frac{f_n}{(n+1)^2} = a_n$. Finally, it is readily shown that $\widetilde{a}(\lambda) \in H^2(\mathbb{C}^{(+)}_{-1/2})$:

$$\|\widetilde{a}\|_2^2 = \sup_{\sigma>-\frac{1}{2}} \int_{-\infty}^{+\infty} \left| \frac{\widetilde{f}(\sigma+\mathrm{i}\mu)}{(\sigma+1+\mathrm{i}\mu)^2} \right|^2 \mathrm{d}\mu \leqslant 16 \sup_{\sigma>-\frac{1}{2}} \int_{-\infty}^{+\infty} \left|\widetilde{f}(\sigma+\mathrm{i}\mu)\right|^2 \mathrm{d}\mu < \infty, \tag{25}$$

and statement (i) is then proved. Regarding point (ii), since $\widetilde{f}(\lambda) \in H^2(\mathbb{C}^{(+)}_{-1/2})$, then $\widetilde{f}(\sigma+\mathrm{i}\mu) \in L^2(-\infty,+\infty)$ for any fixed value of $\sigma \geqslant -\frac{1}{2}$. Regarding point (iii), since $\widetilde{f}(\lambda) \in H^2(\mathbb{C}^{(+)}_{-1/2})$, then $\widetilde{f}(\lambda)$ tends to zero as $\lambda \to \infty$ inside any fixed half-plane $\mathrm{Re}\,\lambda \geqslant \delta > -\frac{1}{2}$ [23]. By Schwarz's inequality, we have for $\sigma \geqslant -\frac{1}{2}$,

$$\int_{-\infty}^{+\infty} |(\sigma+\mathrm{i}\mu)\,\widetilde{a}(\sigma+\mathrm{i}\mu)|\,\mathrm{d}\mu \leqslant \left(\int_{-\infty}^{+\infty} \left| \frac{\sigma+\mathrm{i}\mu}{(\sigma+1+\mathrm{i}\mu)^2} \right|^2 \mathrm{d}\mu \right)^{\frac{1}{2}} \left(\int_{-\infty}^{+\infty} \left|\widetilde{f}(\sigma+\mathrm{i}\mu)\right|^2 \mathrm{d}\mu \right)^{\frac{1}{2}} < \infty,$$

which proves statement (iv). Concerning point (v), return to the Laplace integral representation of $\widetilde{f}(\lambda)$ in (24). First, we want to prove that $e^{-s/2}\varphi(e^{-s}) \in L^1(0,+\infty)$, which amounts to showing that $\int_0^1 \left|\frac{\varphi(x)}{\sqrt{x}}\right| \mathrm{d}x < \infty$. By Hölder's inequality,

$$\int_0^1 \frac{|\varphi(x)|}{\sqrt{x}}\,\mathrm{d}x \leqslant \left(\int_0^1 |\varphi(x)|^{(2+\varepsilon)}\,\mathrm{d}x \right)^{\frac{1}{2+\varepsilon}} \cdot \left(\int_0^1 x^{-\frac{2+\varepsilon}{2+2\varepsilon}}\,\mathrm{d}x \right)^{\frac{1+\varepsilon}{2+\varepsilon}} < \infty,$$

where the rightmost integral converges since $\frac{2+\varepsilon}{2+2\varepsilon} < 1$ for $\varepsilon > 0$, and $\varphi \in L^{(2+\varepsilon)}(0,1)$. Then, from representation (24):

$$\left(\tfrac{1}{2}+\mathrm{i}\mu\right)^2 \widetilde{a}\left(-\tfrac{1}{2}+\mathrm{i}\mu\right) = \widetilde{f}\left(-\tfrac{1}{2}+\mathrm{i}\mu\right) = \int_0^{+\infty} e^{-\mathrm{i}\mu s} e^{-s/2}\varphi(e^{-s})\,\mathrm{d}s = \mathcal{F}\left\{h(s)e^{-s/2}\varphi(e^{-s})\right\},$$

where $\mathcal{F}$ denotes the Fourier integral operator, and $h(s)$ is the Heaviside step function. The Riemann–Lebesgue theorem guarantees that $\widetilde{a}(-\frac{1}{2}+\mathrm{i}\mu)$ is a continuous function tending to zero as $\mu \to \pm\infty$, and statement (v) is proved. Finally, in order to prove statement (vi), we note that the Laplace transform (24) holds also for $\mathrm{Re}\,\lambda = -\frac{1}{2}$ since $e^{-s/2}\varphi(e^{-s}) \in L^1(0,+\infty) \cap L^2(0,+\infty)$. It follows that $\sup_{\substack{\sigma>-1/2 \\ \mu\in\mathbb{R}}} |\widetilde{f}(\sigma+\mathrm{i}\mu)| = |\widetilde{f}\left(-\frac{1}{2}+\mathrm{i}\mu\right)|$. Therefore, recalling that $\widetilde{a}(\lambda) = \widetilde{f}(\lambda)/(\lambda+1)^2$:

$$\sup_{\substack{\sigma>-1/2 \\ \mu\in\mathbb{R}}} |\widetilde{a}(\sigma+\mathrm{i}\mu)| = \sup_{\substack{\sigma>-1/2 \\ \mu\in\mathbb{R}}} \frac{|\widetilde{f}(\sigma+\mathrm{i}\mu)|}{|\sigma+1+\mathrm{i}\mu|^2} = \frac{|\widetilde{f}(-\frac{1}{2}+\mathrm{i}\mu)|}{\mu^2+1/4} = \left|\widetilde{a}\left(-\tfrac{1}{2}+\mathrm{i}\mu\right)\right|,$$

where $\widetilde{a}(-\frac{1}{2}+\mathrm{i}\mu) \in L^1(-\infty,+\infty)$ (see statements (iv) and (v)). □

Let $\xi_0 \geqslant 0$. We introduce in the complex plane $\mathbb{C}$ of the variable $\tau = t + \mathrm{i}w$ $(t, w \in \mathbb{R})$ the following domains: ${}^{\tau}\mathcal{I}_{+}^{(\pm\xi_0)} \doteq \{\tau \in \mathbb{C} : \mathrm{Im}\,\tau > \pm\xi_0\}$ and ${}^{\tau}\mathcal{I}_{-}^{(\pm\xi_0)} \doteq \{\tau \in \mathbb{C} : \mathrm{Im}\,\tau < \pm\xi_0\}$. Correspondingly, we introduce the following cut-domains: ${}^{\tau}\mathcal{I}_{+}^{(\xi_0)} \setminus {}^{\tau}\Xi_{+}^{(\xi_0)}$, where ${}^{\tau}\Xi_{+}^{(\xi_0)} \doteq \{\tau \in \mathbb{C} : \tau = 2k\pi + \mathrm{i}w,\ w > \xi_0,\ k \in$

$\mathbb{Z}\}$ (see Figure 2a) and ${}^{\tau}\mathcal{I}_{-}^{(-\xi_0)} \setminus {}^{\tau}\Xi_{-}^{(-\xi_0)}$, where ${}^{\tau}\Xi_{-}^{(-\xi_0)} \doteq \{\tau \in \mathbb{C} : \tau = 2k\pi + \mathrm{i}w,\ w < -\xi_0,\ k \in \mathbb{Z}\}$ (see Figure 2b). Finally, we denote by $\dot{A} \doteq A/2\pi\mathbb{Z}$ any subset A of $\mathbb{C}$, which is invariant under the translation group $2\pi\mathbb{Z}$. We are now ready to state the following proposition.

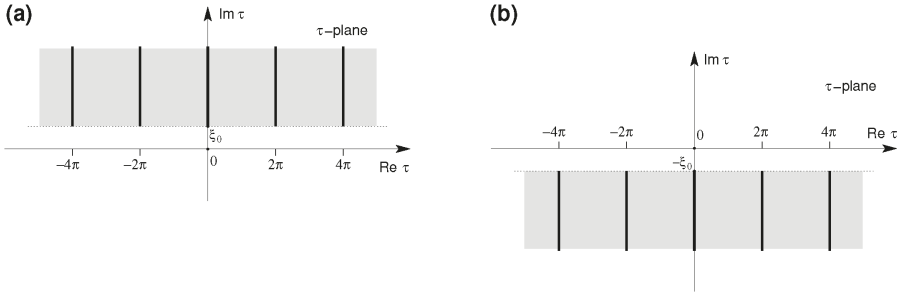

Figure 2. In the complex τ-plane, the grey regions represent: (**a**) the cut-domain ${}^{\tau}\mathcal{I}_{+}^{(\xi_0)} \setminus {}^{\tau}\Xi_{+}^{(\xi_0)}$, (**b**) the cut-domain ${}^{\tau}\mathcal{I}_{-}^{(-\xi_0)} \setminus {}^{\tau}\Xi_{-}^{(-\xi_0)}$. The cuts (thick lines) are located at $\operatorname{Re}\tau = 2k\pi$, $k \in \mathbb{Z}$.

Proposition 3. *Consider the trigonometric series*

$$\frac{1}{2\pi}\sum_{n=0}^{+\infty} a_n\, e^{-\mathrm{i}n\tau} \qquad (\tau = t + \mathrm{i}w; t, w \in \mathbb{R}), \tag{26}$$

and suppose that the set of numbers $\{f_n\}_{n=0}^{\infty}$, *with* $f_n \doteq (n+1)^2\, a_n$, *satisfies condition* (20). *Then:*

(i) The series (26) *converges uniformly on any compact subdomain of* ${}^{\tau}\mathcal{I}_{-}^{(0)}$ *to a function* $\widehat{f}^{(+)}(\tau)$ *holomorphic in* ${}^{\tau}\mathcal{I}_{-}^{(0)}$, *continuous on the axis* $\operatorname{Im}\tau = 0$.

(ii) The function $\widehat{f}^{(+)}(\tau)$ *admits a holomorphic extension to the cut-domain* ${}^{\tau}\mathcal{I}_{+}^{(0)} \setminus {}^{\tau}\dot{\Xi}_{+}^{(0)}$: *i.e., it is analytic in* $\mathbb{C} \setminus \{\tau \in \mathbb{C} : \tau = 2k\pi + \mathrm{i}w; k \in \mathbb{Z}, w > 0\}$.

(iii) The jump function $\widehat{F}^{(+)}(w)$, *which is the discontinuity of* $(\mathrm{i}\widehat{f}^{(+)}(\tau))$ *across the cut* ${}^{\tau}\dot{\Xi}_{+}^{(0)}$, *is a function of class* C^1 *that satisfies the bound*

$$\left|\widehat{F}^{(+)}(w)\right| \leqslant \|\widetilde{a}_\sigma\|_1\, e^{\sigma w} \qquad \left(\sigma \geqslant -\tfrac{1}{2},\ w \in \mathbb{R}^+\right),$$

where $\widetilde{a}(\sigma + \mathrm{i}\mu)$ $(\mu \in \mathbb{R})$ *is the unique Carlsonian interpolant of the coefficients* a_n, *and*

$$\|\widetilde{a}_\sigma\|_1 \doteq \frac{1}{2\pi}\int_{-\infty}^{+\infty} |\widetilde{a}(\sigma + \mathrm{i}\mu)|\, \mathrm{d}\mu < \infty \qquad \left(\sigma \geqslant -\tfrac{1}{2}\right). \tag{27}$$

(iv) $\widehat{F}^{(+)}(w) = o\left(e^{-w/2}\right)$ *for* $w \to +\infty$ *and* $\widehat{F}^{(+)}(0) = 0$.

(v) $\widetilde{a}(\sigma + \mathrm{i}\mu)$ *is the Laplace transform of the jump function* $\widehat{F}^{(+)}(w)$:

$$\widetilde{a}(\sigma + \mathrm{i}\mu) = \int_0^{+\infty} \widehat{F}^{(+)}(w)\, e^{-(\sigma+\mathrm{i}\mu)w}\, \mathrm{d}w \qquad \left(\sigma > -\tfrac{1}{2}\right), \tag{28}$$

holomorphic in the half-plane $\sigma > -\frac{1}{2}$.

(vi) The following Plancherel equality holds:

$$\int_{-\infty}^{+\infty} |\widetilde{a}(\sigma + \mathrm{i}\mu)|^2\, \mathrm{d}\mu = 2\pi \int_{-\infty}^{+\infty} \left|\widehat{F}^{(+)}(w) e^{-\sigma w}\right|^2 \mathrm{d}w \qquad \left(\sigma \geqslant -\tfrac{1}{2}\right).$$

Proof. Since the sequence $\{f_n\}_{n=0}^{\infty}$ satisfies condition (20), then, given an arbitrary constant C, there exists an integer n_0 such that $|a_n| \leqslant C$ for $n > n_0$ and, accordingly,

$$\left| \frac{1}{2\pi} \sum_{n=0}^{\infty} a_n \, e^{-in\tau} \right| \leqslant \frac{C}{2\pi} \sum_{n=n_0+1}^{\infty} e^{nw} \qquad (w \doteq \operatorname{Im} \tau, \; C = \text{constant}). \tag{29}$$

The series on the r.h.s. of (29) converges uniformly on any compact subdomain contained in the half-plane $w < 0$. Since

$$\frac{1}{2\pi} \sum_{n=0}^{\infty} a_n \, e^{-in\tau} = \frac{1}{2\pi} \sum_{n=n_0+1}^{\infty} a_n \, e^{-in\tau} + T_{n_0}(\tau),$$

where $T_{n_0}(\tau)$ is a trigonometric polynomial, by the Weierstrass theorem on the uniformly convergent series of analytic functions, series (26) converges uniformly on any compact subdomain of ${}^{\tau}\mathcal{I}_{-}^{(0)}$ to a function $\widehat{f}^{(+)}(\tau)$ holomorphic in ${}^{\tau}\mathcal{I}_{-}^{(0)}$. Furthermore, since $(n+1)^2 \, a_n \xrightarrow[n\to\infty]{} 0$, given an arbitrary constant C', there exists an integer n_1 such that for $w = 0$:

$$\left| \frac{1}{2\pi} \sum_{n=n_1}^{\infty} a_n \, e^{-int} \right| \leqslant \frac{1}{2\pi} \sum_{n=n_1}^{\infty} |a_n| \leqslant \frac{C'}{2\pi} \sum_{n=n_1}^{\infty} \frac{1}{n^2} \leqslant C' \frac{\pi}{12}.$$

Then, applying once again the Weierstrass theorem on the uniformly convergent series of continuous functions, the series $\frac{1}{2\pi} \sum_{n=0}^{\infty} a_n \, e^{-int}$ converges to a continuous function $\widehat{f}^{(+)}(t)$, and statement (i) is proved. Regarding statement (ii), we write the following integral:

$$\widehat{f}_{\eta}^{(+)}(t) = \frac{\mathrm{i}}{4\pi} \int_{\mathcal{C}} \widetilde{a}(\lambda) \frac{e^{-\mathrm{i}\lambda(t-\eta\pi)}}{\sin \pi\lambda} \, \mathrm{d}\lambda \qquad (\eta = \pm), \tag{30}$$

where $\widetilde{a}(\lambda)$ ($\operatorname{Re}\lambda \geqslant -\frac{1}{2}$) is the unique Carlsonian interpolant of the coefficients $\{a_n\}_{n=0}^{\infty}$, which is holomorphic in the half-plane $\operatorname{Re}\lambda > -\frac{1}{2}$ (see statement (i) of Proposition 2). The contour $\mathcal{C}$ is contained in the half-plane $\mathbb{C}_{-1/2}^{(+)}$, which encircles the semi-axis $\operatorname{Re}\lambda > -\frac{1}{2}$, and is chosen to cross the latter at a point $\sigma > -\frac{1}{2}$, $\sigma \notin \mathbb{N}$ (see Figure 3). Consider now the term $\frac{\exp[-\mathrm{i}\lambda(t-\eta\pi)]}{\sin \pi\lambda}$; the following inequalities hold ($\lambda = \sigma + \mathrm{i}\mu$):

$$\left| e^{-\mathrm{i}(\sigma+\mathrm{i}\mu)(t-\eta\pi)} \right| \leqslant 2\cosh \pi\mu \quad \text{for} \quad \begin{cases} 0 \leqslant t \leqslant 2\pi & \text{if} \quad \eta = +, \\ -2\pi \leqslant t \leqslant 0 & \text{if} \quad \eta = -, \end{cases} \tag{31}$$

$$|\sin \pi(\sigma + \mathrm{i}\mu)| \geqslant \sinh \pi\mu, \tag{32}$$

$$|\sin \pi(\sigma + \mathrm{i}\mu)| \geqslant |\sin \pi\sigma| \, \cosh \pi\mu. \tag{33}$$

From (31) and (32):

$$\left| \frac{e^{-\mathrm{i}(\sigma+\mathrm{i}\mu)(t-\eta\pi)}}{\sin \pi(\sigma + \mathrm{i}\mu)} \right| \leqslant 2 \left| \frac{\cosh \pi\mu}{\sinh \pi\mu} \right| \quad \text{for} \quad \begin{cases} 0 \leqslant t \leqslant 2\pi & \text{if} \quad \eta = +, \\ -2\pi \leqslant t \leqslant 0 & \text{if} \quad \eta = -, \end{cases} \tag{34}$$

while, combining (31) and (33):

$$\left| \frac{e^{-\mathrm{i}(\sigma+\mathrm{i}\mu)(t-\eta\pi)}}{\sin \pi(\sigma + \mathrm{i}\mu)} \right| \leqslant \frac{2}{|\sin \pi\sigma|} < \infty \quad \text{for} \quad \begin{cases} 0 \leqslant t \leqslant 2\pi & \text{if} \quad \eta = +, \\ -2\pi \leqslant t \leqslant 0 & \text{if} \quad \eta = -, \end{cases} \quad \text{and } \sigma \notin \mathbb{N}. \tag{35}$$

Integral (30) converges since $\lambda^2\widetilde{a}(\lambda)$ tends uniformly to zero as $\lambda \to \infty$ in any fixed half-plane $\mathrm{Re}\,\lambda \geqslant \delta > -\frac{1}{2}$ (statement (iii) of Proposition 2); the term $\left|\frac{\exp[-\mathrm{i}(\sigma+\mathrm{i}\mu)(t-\eta\pi)]}{\sin\pi(\sigma+\mathrm{i}\mu)}\right|$ is bounded by a constant for $\sigma \notin \mathbb{N}$ (see (35)), and is bounded by 2 as $\mu \to \pm\infty$ in view of inequality (34). The contour $\mathcal{C}$ can be distorted and replaced by a line L_σ parallel to the imaginary axis and crossing the real axis at $\mathrm{Re}\,\lambda = \sigma$ with $\sigma \geqslant -\frac{1}{2}$ ($\sigma \notin \mathbb{N}$) (see Figure 3) provided the real variable t is kept in $[0, 2\pi]$ for $\widehat{f}_+^{(+)}(t)$, and in $[-2\pi, 0]$ for $\widehat{f}_-^{(+)}(t)$, respectively. Note that the integral along L_σ converges since $\lambda\widetilde{a}(\lambda) \in L^1(-\infty, +\infty)$ for any fixed value of $\mathrm{Re}\,\lambda \geqslant -\frac{1}{2}$ (statement (iv) of Proposition 2) and by inequality (35). We may now apply the Watson resummation to integral (30). For $t \in [0, 2\pi]$, we obtain:

$$\frac{\mathrm{i}}{4\pi}\int_{\mathcal{C}} \widetilde{a}(\lambda)\,\frac{e^{-\mathrm{i}\lambda(t-\pi)}}{\sin\pi\lambda}\,\mathrm{d}\lambda = \frac{1}{2\pi}\sum_{n=0}^{\infty} a_n\, e^{-\mathrm{i}nt} \qquad (0 \leqslant t \leqslant 2\pi)\,,$$

where the contour $\mathcal{C}$ encircles the semi-axis $\mathrm{Re}\,\lambda > -\frac{1}{2}$ and crosses it at a point $-\frac{1}{2} \leqslant \sigma < 0$. Then, distorting the contour $\mathcal{C}$ into the line L_σ ($-\frac{1}{2} \leqslant \sigma < 0$), which is admissible as explained above, we obtain for $-\frac{1}{2} \leqslant \sigma < 0$:

$$\widehat{f}_+^{(+)}(t) = -\frac{1}{4\pi}\int_{-\infty}^{+\infty} \widetilde{a}(\sigma+\mathrm{i}\mu)\,\frac{e^{-\mathrm{i}(\sigma+\mathrm{i}\mu)(t-\pi)}}{\sin\pi(\sigma+\mathrm{i}\mu)}\,\mathrm{d}\mu = \frac{1}{2\pi}\sum_{n=0}^{\infty} a_n\, e^{-\mathrm{i}nt} \quad (0 \leqslant t \leqslant 2\pi)\,, \tag{36}$$

and, analogously, for $t \in [-2\pi, 0]$:

$$\widehat{f}_-^{(+)}(t) = -\frac{1}{4\pi}\int_{-\infty}^{+\infty} \widetilde{a}(\sigma+\mathrm{i}\mu)\,\frac{e^{-\mathrm{i}(\sigma+\mathrm{i}\mu)(t+\pi)}}{\sin\pi(\sigma+\mathrm{i}\mu)}\,\mathrm{d}\mu = \frac{1}{2\pi}\sum_{n=0}^{\infty} a_n\, e^{-\mathrm{i}nt} \quad (-2\pi \leqslant t \leqslant 0)\,. \tag{37}$$

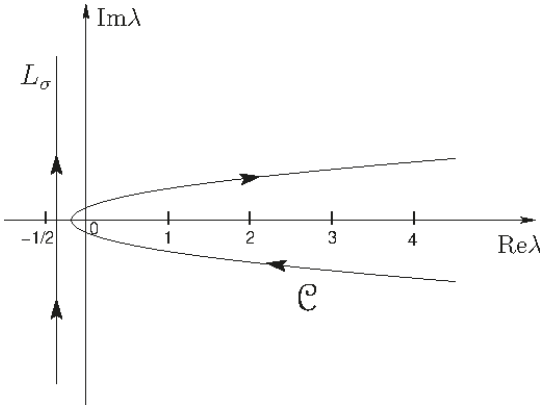

Figure 3. Integration path of integral (30).

Now, substitute into integral (36) the real variable t with the complex variable $\tau = t + \mathrm{i}w$. The resulting integral can be proved to provide an analytic continuation of $\widehat{f}_+^{(+)}(t)$ in the strip $0 < t < 2\pi$, $w \in \mathbb{R}^+$, continuous in the closure of the latter. In fact, from the first equality in (36), we formally obtain:

$$\widehat{f}_+^{(+)}(t+\mathrm{i}w) = \frac{1}{2\pi}\,e^{\sigma w}\int_{-\infty}^{+\infty} H_\sigma^t(\mu)\,e^{\mathrm{i}\mu w}\,\mathrm{d}\mu \qquad \left(0 \leqslant t \leqslant 2\pi;\, w \in \mathbb{R}^+,\, -\tfrac{1}{2} \leqslant \sigma < 0\right), \tag{38}$$

where

$$H_\sigma^t(\mu) \doteq -\frac{\widetilde{a}(\sigma+\mathrm{i}\mu)e^{-\mathrm{i}(\sigma+\mathrm{i}\mu)(t-\pi)}}{2\sin\pi(\sigma+\mathrm{i}\mu)}. \tag{39}$$

By inequality (35) and statement (vi) of Proposition 2:

$$\left|H_\sigma^t(\mu)\right| \leqslant \frac{\left|\widetilde{a}(-\frac{1}{2}+\mathrm{i}\mu)\right|}{\left|\sin\pi\sigma\right|} \qquad \left(0 \leqslant t \leqslant 2\pi; \sigma \geqslant -\tfrac{1}{2}, \sigma \notin \mathbb{N}\right), \tag{40}$$

which, along with statements (iv) and (v) of Proposition 2, guarantees that $H_\sigma^t(\mu) \in L^1(-\infty,+\infty)$ for $0 \leqslant t \leqslant 2\pi, \sigma > -\frac{1}{2}, \sigma \notin \mathbb{N}$. Therefore, formulas (38), (39), and (40) define $\widehat{f}_+^{(+)}(\tau)$ ($\tau = t+\mathrm{i}w$) as an analytic continuation of $\widehat{f}_+^{(+)}(t)$ in the strip $\{\tau = t+\mathrm{i}w,\ 0 < t < 2\pi, w \in \mathbb{R}^+\}$, continuous in the closure of the latter in view of the Riemann–Lebesgue theorem. Proceeding analogously, we can obtain an analytic continuation of $\widehat{f}_-^{(+)}(t)$ in the strip $\{\tau = t+\mathrm{i}w,\ -2\pi < t < 0, w \in \mathbb{R}^+\}$, continuous on the closure of the latter. It then follows that the function $\widehat{f}^{(+)}(\tau)$ admits a holomorphic extension to the cut-domain ${}^\tau\mathcal{I}_+^{(0)} \setminus {}^\tau\Xi_+^{(0)}$, and statement (ii) is proved.

The discontinuity $\widehat{F}^{(+)}(w)$ of $(\mathrm{i}\widehat{f}^{(+)}(\tau))$ across the cut at $t = 0$ equals $\mathrm{i}[\widehat{f}_+^{(+)}(\mathrm{i}w) - \widehat{f}_-^{(+)}(\mathrm{i}w)]$ ($w \in \mathbb{R}^+$) (for the 2π-periodicity of $\widehat{f}^{(+)}(\tau)$, we may consider only the cut at $t = 0$). It can be computed by replacing t by $\mathrm{i}w$ into integrals (36) and (37) and then subtracting Equation (37) from Equation (36):

$$\widehat{F}^{(+)}(w) \doteq \mathrm{i}\left[\widehat{f}_+^{(+)}(\mathrm{i}w) - \widehat{f}_-^{(+)}(\mathrm{i}w)\right] = \frac{1}{2\pi}\int_{-\infty}^{+\infty}\widetilde{a}(\sigma+\mathrm{i}\mu)e^{(\sigma+\mathrm{i}\mu)w}\,\mathrm{d}\mu \qquad \left(w \in \mathbb{R}^+, \sigma \geqslant -\tfrac{1}{2}\right), \tag{41}$$

which yields:

$$\left|\widehat{F}^{(+)}(w)\right| \leqslant \|\widetilde{a}_\sigma\|_1\, e^{\sigma w} \qquad \left(w \in \mathbb{R}^+, \sigma \geqslant -\tfrac{1}{2}\right),$$

where $\|\widetilde{a}_\sigma\|_1$, defined in (27), is guaranteed to be finite by statement (iv) of Proposition 2. Rewrite (41) as follows:

$$\widehat{F}^{(+)}(w)e^{-\sigma w} = \frac{1}{2\pi}\int_{-\infty}^{+\infty}\widetilde{a}(\sigma+\mathrm{i}\mu)\,e^{\mathrm{i}\mu w}\,\mathrm{d}\mu \qquad \left(w \in \mathbb{R}^+, \sigma \geqslant -\tfrac{1}{2}\right). \tag{42}$$

Since for any fixed $\mathrm{Re}\,\lambda \geqslant -\frac{1}{2}$, $\lambda\widetilde{a}(\lambda)$ and $\widetilde{a}(\lambda)$ belong to $L^1(-\infty,+\infty)$, the Riemann–Lebesgue theorem guarantees that $\widehat{F}^{(+)}(w)e^{-\sigma w}$ is a function of class C^1 tending to zero as $w \to +\infty$, and statement (iii) is proved. Hence, $\widehat{F}^{(+)}(w)$ is a continuous function of w ($w \in \mathbb{R}^+$) and $\widehat{F}^{(+)}(w) = o(e^{-w/2})$ as $w \to +\infty$. Moreover, $\widehat{F}^{(+)}(0) = 0$ for the continuity of $\widehat{f}^{(+)}(\tau)$ on the real axis, and statement (iv) is proved. Inverting (42), we have:

$$\widetilde{a}(\sigma+\mathrm{i}\mu) = \int_0^{+\infty}\widehat{F}^{(+)}(w)\,e^{-(\sigma+\mathrm{i}\mu)w}\,\mathrm{d}w \qquad \left(\sigma > -\tfrac{1}{2}\right),$$

where the integral on the r.h.s. converges for $\sigma > -\frac{1}{2}$. It defines the Laplace transform of $\widehat{F}^{(+)}(w)$, holomorphic in the half-plane $\mathrm{Re}\,\lambda > -\frac{1}{2}$, and statement (v) follows. Finally, recalling that $\widetilde{a}(\sigma+\mathrm{i}\mu)$ ($\mu \in \mathbb{R}$) belongs to $L^2(-\infty,+\infty)$ for any fixed value $\sigma \geqslant -\frac{1}{2}$ (statement (ii) of Proposition 2 and inequality (25)), we obtain the Plancherel equality:

$$\int_{-\infty}^{+\infty}\left|\widetilde{a}\,(\sigma+\mathrm{i}\mu)\right|^2\,\mathrm{d}\mu = 2\pi\int_0^{+\infty}\left|\widehat{F}^{(+)}(w)\,e^{-\sigma w}\right|^2\,\mathrm{d}w \qquad \left(\sigma \geqslant -\tfrac{1}{2}\right),$$

proving statement (vi). □

Proposition 4. *If in the trigonometric series (see (19))*

$$\frac{1}{2\pi}\left[\sum_{n=0}^{\infty} a_n e^{-\mathrm{i}nt} - e^{\mathrm{i}t}\sum_{n=0}^{\infty} a_n e^{\mathrm{i}nt}\right] \qquad (t \in \mathbb{R}), \tag{43}$$

the coefficients a_n satisfy the assumptions required by Propositions 2 and 3, i.e., the set of numbers $f_n = (n+1)^2 a_n$ satisfies condition (20), then:

(i) The series (43) converges to a continuous function $\widehat{f}(t)$ ($t \in \mathbb{R}$).
(ii) The function $\widehat{f}(t)$ admits a holomorphic extension to the cut-domain $({}^{\tau}\mathcal{I}_{+}^{(0)} \setminus {}^{\tau}\dot{\Xi}_{+}^{(0)}) \cup ({}^{\tau}\mathcal{I}_{-}^{(0)} \setminus {}^{\tau}\dot{\Xi}_{-}^{(0)})$, i.e., it is analytic in $\mathbb{C} \setminus \{\tau = 2k\pi + \mathrm{i}w; k \in \mathbb{Z}, w \in \mathbb{R}, w \neq 0\}$.
(iii) The jump function across the cuts ${}^{\tau}\dot{\Xi}_{\pm}^{(0)}$ enjoys properties, mutatis mutandis, *analogous to conditions (iii)–(vi) of Proposition 3.*

Proof. These statements can be proved by using obvious extensions of the arguments used in the proof of Proposition 3. □

Through the holomorphic extension associated with the trigonometric series (43), we obtain a function, denoted by $\widehat{f}(\tau)$ ($\tau = t + \mathrm{i}w; t, w \in \mathbb{R}$), which is the analytic continuation of $\widehat{f}(t)$ ($t \in \mathbb{R}$) from the real axis to the domain ${}^{\tau}\dot{\mathcal{I}} \doteq ({}^{\tau}\mathcal{I}_{+}^{(0)} \setminus {}^{\tau}\dot{\Xi}_{+}^{(0)}) \cup ({}^{\tau}\mathcal{I}_{-}^{(0)} \setminus {}^{\tau}\dot{\Xi}_{-}^{(0)})$. We can then prove the following corollary to Proposition 4.

Corollary 1. *The function $\widehat{f}(\tau)$ is holomorphic in the 2π-periodic strips $\Sigma_\tau \doteq \{\tau \in \mathbb{C} : \tau = t + \mathrm{i}w, 2\pi k < t < 2\pi(k+1), k \in \mathbb{Z}, w \in \mathbb{R}\}$.*

Proof. We start from statement (ii) of Proposition 4. Next, by applying the Schwarz reflection principle and taking into account that the function $\widehat{f}(t)$ (i.e., the restriction of $\widehat{f}(\tau)$ to the real axis) is continuous (statement (i) of Proposition 4), the statement of the corollary follows. □

Remark 2. *In Ref. [21], the Hausdorff condition (20) was assumed to hold for the set of numbers $f_n = n^p a_n$ ($p \geqslant 2$). However, this condition does not guarantee obtaining a unique Carlsonian interpolation of the whole sequence a_n, including the first coefficient a_0. Therefore, it must be replaced by the same condition on the numbers $f_n = (n+1)^p a_n$ ($p \geqslant 2$). However, for the purpose of the current analysis, it is sufficient to take $p = 2$. Let us note that the results of Ref. [21] hold true and, in particular, the proofs of Propositions 5.1 and 6.1 of that paper, which will be used below, are correct modulo the following change: $f_n = n^p a_n \to f_n = (n+1)^p a_n$.*

2.4. Inversion of the Radon–Abel Transformation and Holomorphic Extension Associated with the Legendre Series

The first step consists of determining the inversion of the Radon–Abel transformation (12). We can prove the following proposition.

Proposition 5. *Suppose that the sequence $f_n = (n+1)^2 a_n$ (a_n being the coefficients of the Legendre expansion (14)) satisfies the Hausdorff condition (20). Then, the Radon–Abel transformation (see (12))*

$$\widehat{f}(t) = -2\, e^{\mathrm{i}t/2} \int_0^t f(u)\, \frac{\sin u}{[2(\cos t - \cos u)]^{\frac{1}{2}}}\, \mathrm{d}u \tag{44}$$

admits the following inversion:

$$f(u) = \frac{1}{\pi \sin u} \frac{\mathrm{d}}{\mathrm{d}u} \int_0^u e^{-\mathrm{i}t/2} \widehat{f}(t) \frac{\sin t}{[2(\cos u - \cos t)]^{\frac{1}{2}}} \, \mathrm{d}t.$$

Proof. See Proposition 5.1 of Ref. [21]. □

By following the same procedure used in the proof of Proposition 5 (i.e., introducing Riemann–Liouville integrals and related properties), Proposition 5 can be extended to give the inversion of the Radon–Abel transformation (11). We can state, without proof, the following proposition.

Proposition 6. *Assume that the coefficients a_n (see (14)) satisfy the conditions of Proposition 5; then, the function $\widehat{f}(\tau)$, i.e., the analytic continuation of the function $\widehat{f}(t)$ given in (44), is holomorphic in the strips Σ_τ and can be represented by the following Radon–Abel transformation (see (11)):*

$$\widehat{f}(\tau) = -2\, e^{\mathrm{i}\tau/2} \int_{\gamma_\tau} f(\theta) \frac{\sin \theta}{[2(\cos \tau - \cos \theta)]^{\frac{1}{2}}} \, \mathrm{d}\theta,$$

which admits the following inversion:

$$f(\theta) = \frac{1}{\pi \sin \theta} \frac{\mathrm{d}}{\mathrm{d}\theta} \int_{\gamma_\theta} e^{-\mathrm{i}\tau/2} \widehat{f}(\tau) \frac{\sin \tau}{[2(\cos \theta - \cos \tau)]^{\frac{1}{2}}} \, \mathrm{d}\tau, \tag{45}$$

γ_τ and γ_θ denoting the rays from zero to τ and from zero to θ, respectively.

We can now prove the following proposition.

Proposition 7. *Suppose that the sequence $f_n = (n+1)^2 a_n$ ($n = 0, 1, 2, \ldots$) satisfies the Hausdorff condition (20), then the function $f(\theta)$ ($\theta \in \mathbb{C}$), represented by formula (45), is even, 2π-periodic, and holomorphic in ${}^{\theta}\dot{\mathcal{I}} = ({}^{\theta}\mathcal{I}_+^{(0)} \setminus {}^{\theta}\ddot{\Xi}_+^{(0)}) \cup ({}^{\theta}\mathcal{I}_-^{(0)} \setminus {}^{\theta}\ddot{\Xi}_-^{(0)})$.*

Proof. The assumptions on the Legendre coefficients a_n allow us to state that $\widehat{f}(\tau)$ is a 2π-periodic function, holomorphic in the domain ${}^{\tau}\dot{\mathcal{I}}$ (see Corollary 1). Moreover, it enjoys the symmetry property:

$$\widehat{f}(\tau) = -e^{\mathrm{i}\tau} \widehat{f}(-\tau),$$

which follows from (17) and from the uniqueness of the analytic continuation. The properties mentioned above imply that $\widehat{f}(\tau)$ is of the form: $\widehat{f}(\tau) = e^{\mathrm{i}\tau/2}(1 - \cos \tau)^{\frac{1}{2}}\, b(\cos \tau)$, with $b(\cos \tau)$ analytic in ${}^{\tau}\underline{D} = \{\cos \tau \in \mathbb{C},\, \tau \in {}^{\tau}\dot{\mathcal{I}}\}$. Through the following parametrization of γ_θ: $\cos \tau = 1 + \delta(\cos \theta - 1)$, $(0 \leqslant \delta \leqslant 1)$, formula (45) can be rewritten as:

$$f(\theta) = \frac{\mathrm{i}}{\sqrt{2}\pi} \frac{\mathrm{d}}{\mathrm{d}(\cos \theta)} \left[(\cos \theta - 1) \int_0^1 b(1 + \delta(\cos \theta - 1)) \delta^{\frac{1}{2}} (1 - \delta)^{-\frac{1}{2}} \, \mathrm{d}\delta \right],$$

which represents a function holomorphic in ${}^{\theta}\underline{D} = \{\cos \theta \in \mathbb{C},\, \theta \in {}^{\theta}\dot{\mathcal{I}}\}$. Accordingly, regarded as a function of θ, it represents an even function, 2π-periodic, and holomorphic in ${}^{\theta}\dot{\mathcal{I}}$. □

From the previous proposition and Corollary 1, it derives the following corollary.

Corollary 2. *If the sequence* $\{a_n\}_{n=0}^{\infty}$ *of the Legendre coefficients satisfies the conditions of Proposition 7, then* $f(\theta)$ *is a function analytic in the* 2π*-periodic strips* $\Sigma_\theta \doteq \{\theta \in \mathbb{C} : \theta = u + \mathrm{i}v, 2\pi k < u < 2\pi(k+1), k \in \mathbb{Z}, v \in \mathbb{R}\}$.

Formula (45) allows us to compute the boundary values $f_{\pm}^{(+)}(\mathrm{i}v)$, which are defined by $f_{\eta}^{(+)}(v) \doteq \lim_{u\to 0^+} f^{(+)}(\eta\, u + \mathrm{i}v), \eta = \pm, v \geqslant 0$, on the semi-axis $\theta = \mathrm{i}v$, $v \geqslant 0$, with $\gamma_{\mathrm{i}v} = \{\tau = \mathrm{i}w, 0 \leqslant w \leqslant v\}$, in terms of the corresponding boundary values $\widehat{f}_{\pm}^{(+)}(\mathrm{i}w)$, provided $\widehat{f}_{\pm}^{(+)}(\mathrm{i}w)$ satisfies a C^1-type regularity condition; the latter condition is necessary in order to perform the inversion of the Radon–Abel transform at the boundary. The C^1-continuity of the boundary values follows from the fact that the sequence $f_n = (n+1)^2 a_n$ is required to satisfy the Hausdorff condition (20) (see Propositions 2 and 3). We thus obtain:

$$F^{(+)}(v) \doteq \mathrm{i}[f_{+}^{(+)}(\mathrm{i}v) - f_{-}^{(+)}(\mathrm{i}v)] = \frac{1}{\pi \sinh v} \frac{\mathrm{d}}{\mathrm{d}v} \int_0^v e^{w/2} \widehat{F}^{(+)}(w) \frac{\sinh w}{[2(\cosh v - \cosh w)]^{\frac{1}{2}}}\, \mathrm{d}w, \qquad (46)$$

where $\widehat{F}^{(+)}(w) \doteq \mathrm{i}[\widehat{f}_{+}^{(+)}(\mathrm{i}w) - \widehat{f}_{-}^{(+)}(\mathrm{i}w)]$, $\widehat{f}_{\eta}^{(+)}(\mathrm{i}w) = \lim_{t\to 0^+} \widehat{f}^{(+)}(\eta\, t + \mathrm{i}w), \eta = \pm$. At this point, let us note that, for the current analysis, it is sufficient to consider the cuts in the τ- and θ-planes at $\tau = 2k\pi + \mathrm{i}w$ ($k \in \mathbb{Z}, w > 0$) and $\theta = 2k\pi + \mathrm{i}v$ ($k \in \mathbb{Z}, v > 0$), respectively. Therefore, we can limit ourselves to consider the functions: $\widehat{F}^{(+)}(w) = e^{-v/2}(\mathcal{A}F)(w)$ ($w \geqslant 0$) and, correspondingly, $F^{(+)}(v) \equiv \underline{F}^{(+)}(\cosh v)$ ($v \geqslant 0$). For simplicity, hereafter we shall omit the superscript $(+)$ in these notations.

Next, we can apply the inverse Radon–Abel operator (defined by (45)) to the series on the r.h.s. of formula (19), i.e.,

$$\widehat{f}(t) = \frac{1}{2\pi} e^{\mathrm{i}(t-\pi)/2} \sum_{n=-\infty}^{+\infty} (-1)^n a_n \cos\left[\left(n + \tfrac{1}{2}\right)(t - \pi)\right],$$

whose term by term integration is legitimate for the uniform convergence of the series, which follows from the Hausdorff conditions satisfied by the coefficients $\{a_n\}$. We now introduce the functions

$$\psi_n(\cos u) \doteq -\frac{\mathrm{i}}{\pi \sin u} \frac{\mathrm{d}}{\mathrm{d}u} \int_0^u \cos\left[\left(n + \tfrac{1}{2}\right)(t - \pi)\right] \frac{\sin t}{[2(\cos u - \cos t)]^{\frac{1}{2}}}\, \mathrm{d}t \qquad (0 < u < 2\pi),$$

which are related to the Legendre polynomials $P_n(\cos u)$ by [21]:

$$\psi_n(\cos u) = \frac{(-1)^n}{4}(2n+1)\, P_n(\cos u).$$

Recalling that $a_n = -a_{-n-1}$ ($n \in \mathbb{Z}$) (formula (18)), we finally obtain the original Legendre expansion

$$f(u) = \underline{f}(\cos u) = \frac{1}{\pi} \sum_{n=0}^{\infty} (-1)^n a_n \psi_n(\cos u) = \frac{1}{4\pi} \sum_{n=0}^{\infty} (2n+1)\, a_n\, P_n(\cos u).$$

All the results obtained for the function $\underline{f}(\cos\theta)$ in the $\cos\theta$-plane can be summarized in the following theorem.

Theorem 2. *If the sequence* $f_n = (n+1)^2 a_n$ $(n = 0, 1, 2, \ldots)$ *satisfies the Hausdorff condition* (20)*, then:*

(i) Series (14) *converges to a function* $\underline{f}(\cos u)$ $(u \equiv \mathrm{Re}\,\theta)$*, analytic in the interval* $-1 < \cos u < 1$.
(ii) The function $\underline{f}(\cos u)$ *admits a holomorphic extension to the complex* $\cos\theta$*-plane* ($\theta = u + \mathrm{i}v$) *cut along the semi-axis* $[1, +\infty)$.

2.5. Spherical Laplace Transform and Analyticity Properties in the Complex λ-Plane

A basic feature of the holomorphic extensions associated with the series expansions is the *dual analyticity* that we shall illustrate in the specific case that we have considered here, of the Legendre series (14). To classes of functions $\underline{f}(\cos\theta)$ holomorphic in the $\cos\theta$-plane cut along the semi-axis $[1,+\infty)$ (see Theorem 2), there correspond classes of analytic functions $\widetilde{a}(\lambda)$ ($\lambda \in \mathbb{C}$), which enjoy the following properties:

(a) $\widetilde{a}(\lambda)$ is the composition of the standard Laplace transform with the Abel transform (multiplied by the factor $e^{-w/2}$) of the jump function of $[\mathrm{i}\widehat{f}(\theta)]$ across the cut ${}^{\theta}\ddot{\Xi}_{+}^{(0)}$, that is, the spherical Laplace transform.
(b) $\widetilde{a}(\lambda)$ is holomorphic in the half-plane $\operatorname{Re}\lambda > -\frac{1}{2}$.
(c) $\widetilde{a}(\lambda)$ is the (unique) Carlsonian interpolant of the Fourier–Legendre coefficients: $\widetilde{a}(\lambda)|_{\lambda=n} = a_n$.

Formulas (9) and (28) give

$$\widetilde{a}(\lambda) = \int_0^{+\infty} e^{-(\lambda+\frac{1}{2})w}\,(\mathcal{A}F)(w)\,\mathrm{d}w \qquad \left(\operatorname{Re}\lambda > -\tfrac{1}{2}\right),$$

which is precisely the spherical Laplace transform, holomorphic in the half-plane $\operatorname{Re}\lambda > -\frac{1}{2}$ (statement (v) of Proposition 3). Moreover, $\widetilde{a}(\lambda)|_{\lambda=n} = a_n$ (statement (i) of Proposition 2). Writing explicitly the Abel transform $(\mathcal{A}F)(w)$ (see (9)), we obtain

$$\widetilde{a}(\lambda) = 2\int_0^{+\infty} e^{-(\lambda+\frac{1}{2})w}\left\{\int_0^{w} \underline{F}(\cosh v)\,\frac{\sinh v}{[2(\cosh w-\cosh v)]^{\frac{1}{2}}}\,\mathrm{d}v\right\}\mathrm{d}w \quad \left(\operatorname{Re}\lambda > -\tfrac{1}{2}\right),$$

which, interchanging the order of integration, becomes

$$\widetilde{a}(\lambda) = 2\int_0^{+\infty} \underline{F}(\cosh v)\sinh v\left\{\int_v^{+\infty} \frac{e^{-(\lambda+\frac{1}{2})w}}{[2(\cosh w-\cosh v)]^{\frac{1}{2}}}\,\mathrm{d}w\right\}\mathrm{d}v \quad \left(\operatorname{Re}\lambda > -\tfrac{1}{2}\right). \tag{47}$$

Using the integral representation of the Legendre functions of the second kind [24]

$$Q_\lambda(\cosh v) = \int_v^{+\infty} \frac{e^{-(\lambda+\frac{1}{2})w}}{[2(\cosh w-\cosh v)]^{\frac{1}{2}}}\,\mathrm{d}w \qquad (\operatorname{Re}\lambda > -1, v > 0), \tag{48}$$

formula (47) can be written as follows:

$$\widetilde{a}(\lambda) = 2\int_0^{+\infty} \underline{F}(\cosh v)\,Q_\lambda(\cosh v)\,\sinh v\,\mathrm{d}v \qquad \left(\operatorname{Re}\lambda > -\tfrac{1}{2}\right). \tag{49}$$

Remark 3. *The Legendre function of the second kind has a logarithmic singularity at $v = 0$, then the integral representation (48) holds if $v > 0$; nevertheless, the integral in (49) converges if $\underline{F}(\cosh v)$ is regular at $v = 0$.*

We can now state the following theorem.

Theorem 3. *If the sequence $f_n = (n+1)^2 a_n$ $(n = 0, 1, 2, \ldots)$, a_n being the Legendre coefficients of expansion (14), satisfies the Hausdorff condition (20), then the jump function $F(v) = \underline{F}(\cosh v)$ (defined in (46)) admits the following integral representation:*

$$\begin{aligned} F(v) = \underline{F}(\cosh v) &= \frac{1}{2\pi} \int_{-\infty}^{+\infty} \widetilde{a}(\sigma + \mathrm{i}\mu) \left(\sigma + \tfrac{1}{2} + \mathrm{i}\mu\right) P_{\sigma+\mathrm{i}\mu}(\cosh v)\, \mathrm{d}\mu \\ &= \frac{1}{2\pi \mathrm{i}} \int_{\sigma-\mathrm{i}\infty}^{\sigma+\mathrm{i}\infty} \widetilde{a}(\lambda) \left(\lambda + \tfrac{1}{2}\right) P_{\lambda}(\cosh v)\, \mathrm{d}\lambda \qquad \left(\lambda = \sigma + \mathrm{i}\mu; \sigma \geqslant -\tfrac{1}{2}\right), \end{aligned} \tag{50}$$

where $P_\lambda(\cdot)$ denotes the Legendre function of the first kind.

Proof. See Proposition 6.1 of Ref. [21]. □

3. From Spherical Laplace Transform to Non-Euclidean Fourier Transform

3.1. Formal Derivation of Mehler's Transform from the Spherical Laplace Transform

Let us begin by considering the integral representation (48) of the Legendre function of the second kind $Q_\lambda(\cosh v)$. If $\operatorname{Re}\lambda = -\frac{1}{2}$, the function $Q_{-\frac{1}{2}+\mathrm{i}\mu}(\cosh v)$ can be written as the sum of its even (in μ) and odd parts, which are defined as follows:

$$\begin{aligned} Q^{(\mathrm{E})}_{-\frac{1}{2}+\mathrm{i}\mu}(\cosh v) &= \int_v^{+\infty} \frac{\cos \mu w}{[2(\cosh w - \cosh v)]^{\frac{1}{2}}}\, \mathrm{d}w, \\ Q^{(\mathrm{O})}_{-\frac{1}{2}+\mathrm{i}\mu}(\cosh v) &= -\,\mathrm{i} \int_v^{+\infty} \frac{\sin \mu w}{[2(\cosh w - \cosh v)]^{\frac{1}{2}}}\, \mathrm{d}w. \end{aligned}$$

Recalling the relation between the Legendre functions of first and second kind (p. 140, [24])

$$P_\lambda(z) = \frac{\tan \pi\lambda}{\pi} \left[Q_\lambda(z) - Q_{-\lambda-1}(z)\right],$$

and exploiting the evenness (in μ) of the conical Legendre functions, i.e., $P_{-\frac{1}{2}+\mathrm{i}\mu}(\cosh v) = P_{-\frac{1}{2}-\mathrm{i}\mu}(\cosh v)$ $(\mu \in \mathbb{R})$, we obtain:

$$P_{-\frac{1}{2}+\mathrm{i}\mu}(\cosh v) = P_{-\frac{1}{2}-\mathrm{i}\mu}(\cosh v) = \frac{2}{\pi} \tan\left[\pi\left(-\tfrac{1}{2} + \mathrm{i}\mu\right)\right] Q^{(\mathrm{O})}_{-\frac{1}{2}+\mathrm{i}\mu}(\cosh v). \tag{51}$$

Let us now return to Theorem 3 and to formula (50) in the specific case $\sigma = -\frac{1}{2}$. By the μ-evenness of $P_{-\frac{1}{2}+\mathrm{i}\mu}(\cosh v)$, it follows that only the odd component $\widetilde{a}^{(\mathrm{O})}(-\frac{1}{2} + \mathrm{i}\mu)$ of $\widetilde{a}(-\frac{1}{2} + \mathrm{i}\mu)$ $(\mu \in \mathbb{R})$ contributes to the integral in formula (50):

$$F(v) = \underline{F}(\cosh v) = \frac{\mathrm{i}}{\pi} \int_0^{+\infty} \widetilde{a}^{(\mathrm{O})}\left(-\tfrac{1}{2} + \mathrm{i}\mu\right) P_{-\frac{1}{2}+\mathrm{i}\mu}(\cosh v)\, \mu\, \mathrm{d}\mu. \tag{52}$$

Moving back to formula (49), which for the moment we assume to hold also for $\operatorname{Re}\lambda = -\frac{1}{2}$ (this statement will be proved later in Section 3.4.3), and accounting for relationship (51), we can *formally* rewrite the odd component of $\widetilde{a}(-\frac{1}{2} + \mathrm{i}\mu)$ $(\mu \in \mathbb{R})$ as follows:

$$\widetilde{a}^{(\mathrm{O})}\left(-\tfrac{1}{2} + \mathrm{i}\mu\right) = \frac{\pi}{\tan\left[\pi\left(-\frac{1}{2} + \mathrm{i}\mu\right)\right]} \int_0^{+\infty} \underline{F}(\cosh v)\, P_{-\frac{1}{2}+\mathrm{i}\mu}(\cosh v) \sinh v\, \mathrm{d}v \qquad (\mu \in \mathbb{R}). \tag{53}$$

Noting that $(\tan[\pi(-\frac{1}{2}+\mathrm{i}\mu)])^{-1} = -\mathrm{i}\tanh\pi\mu$, we may introduce the following function: $\widetilde{F}(\mu) \doteq \widetilde{a}(-\frac{1}{2}+\mathrm{i}\mu)/(-\mathrm{i}\pi\tanh\pi\mu)$ (we omit here the superscript "(O)" in $\widetilde{a}^{(\mathrm{O})}\left(-\frac{1}{2}+\mathrm{i}\mu\right)$ since only the odd part of $\widetilde{a}(-\frac{1}{2}+\mathrm{i}\mu)$ plays a role in these transformations). Then, formulas (52) and (53) can be rewritten as

$$F(v) = \underline{F}(\cosh v) = \int_0^{+\infty} \widetilde{F}(\mu)\, P_{-\frac{1}{2}+\mathrm{i}\mu}(\cosh v)\, \tanh(\pi\mu)\, \mu\, \mathrm{d}\mu, \tag{54a}$$

$$\widetilde{F}(\mu) = \int_0^{+\infty} \underline{F}(\cosh v)\, P_{-\frac{1}{2}+\mathrm{i}\mu}(\cosh v) \sinh v\, \mathrm{d}v, \tag{54b}$$

which coincide with the Mehler transform pair, indeed (see (p. 175, [24])).

Remark 4. *(i) As we have already remarked above, we do not consider the whole spherical Laplace transform but only its odd (with respect to μ) component since only this component plays a role in the transformations being treated here.*

(ii) The class of functions $F(v)$ which we are led to consider here are of the form $\underline{F} = \underline{F}(\cosh v)$. Accordingly, the connection between spherical Laplace transform and non-Euclidean Fourier transform can be limited to this class of functions. In the non-Euclidean geometry, these functions belong to the class of radial functions *in a sense that will be clarified in what follows (see Remarks 5 and 6).*

3.2. Geometry of the Two-Sheeted Hyperboloid: Polar and Horocyclic Coordinates

Let us now return to the geometrical representation of the real one-sheeted hyperboloid X_2. It can be easily noted that, by simply swapping two coordinate axes (see Figures 1 and 4), the real meridian $\widehat{X}^+$ can be regarded as the real meridian of one of the sheets of a suitable real two-sheeted hyperboloid. It is therefore reasonable to expect that an integral representation of $\underline{F}(\cosh v)$ can be obtained also from the geometry of the two-sheeted hyperboloid.

In the space $\mathbb{R}^3$ of variables $x = (x_0, x_1, x_2)$, we consider the two-sheeted hyperboloid with equation:

$$x_0^2 - x_1^2 - x_2^2 = 1. \tag{55}$$

In the present analysis, we can limit ourselves to consider the upper sheet of this two-sheeted hyperboloid, the one with $x_0 \geqslant 1$ that will be denoted by ${}^2\mathrm{X}_2^+$. By analogy with what we have done is Section 2, we consider two systems of coordinates: polar and horocyclic coordinates.

Polar Coordinates:

$$x_0 = \cosh v, \tag{56a}$$

$$x_1 = \sinh v \sin\psi, \qquad (v \geqslant 0, \psi \in [0, 2\pi)), \tag{56b}$$

$$x_2 = \sinh v \cos\psi. \tag{56c}$$

It is easy to verify that $x_0^2 - x_1^2 - x_2^2 = \cosh^2 v - \sinh^2 v = 1$, and $x_0 \geqslant 1$.

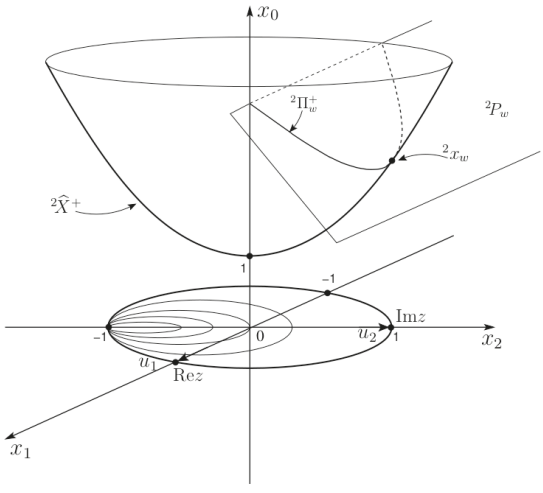

Figure 4. Upper sheet ${}^2X_2^+$ of the real two-sheeted hyperboloid. Re z is directed along u_1 and Im z along u_2.

Horocyclic Coordinates:

$$x_0 = \cosh w + \frac{1}{2}\zeta^2 e^w, \tag{57a}$$

$$x_1 = \zeta e^w, \qquad (w, \zeta \in \mathbb{R}), \tag{57b}$$

$$x_2 = \sinh w - \frac{1}{2}\zeta^2 e^w. \tag{57c}$$

Even in this case, it is straightforward to verify that $x_0^2 - x_1^2 - x_2^2 = 1$, and $x_0 \geqslant 1$; accordingly, the horocyclic coordinates (57) are appropriate for describing the upper sheet ${}^2X_2^+$ of the real two-sheeted hyperboloid. In particular, we focus our attention on the meridian section ${}^2\widehat{X}^+$ of the upper sheet ${}^2X_2^+$, which lies in the plane $x_1 = 0$ and whose equation is $x_0^2 - x_2^2 = 1$. We consider the intersections of ${}^2\widehat{X}^+$ with the family of planes ${}^2P_w$ with equation $x_0 + x_2 = e^w$ ($w \in \mathbb{R}$), i.e., the points ${}^2x_w$, whose coordinates are $x_0 = \cosh w$, $x_1 = 0$, $x_2 = \sinh w$. The sections of ${}^2X_2^+$ by these planes are the (real) parabolae ${}^2\Pi_w^+$. Setting $\zeta = 0$ in (57), we obtain the point ${}^2x_w$ ($w \in \mathbb{R}$), which is the apex of the corresponding parabola ${}^2\Pi_w^+$ (see Figure 4).

Remark 5. *As we shall see in the next section, the parabolae ${}^2\Pi_w^+$ generate (through a stereographic projection on the non-Euclidean disk) a family of horocycles, represented by the Euclidean circles (illustrated in Figure 4) which are tangent to the boundary of the unit disk at the point $x_1 = 0, x_2 = -1$. It is worth emphasizing that this is the sole family of horocycles which is generated by the fibration illustrated above. On the other hand, the non-Euclidean Fourier transform, which will be studied in the next section, demands considering in the non-Euclidean disk all the families of horocycles which are obtained by moving the point of tangency along the entire horizon from 0 to 2π. We shall see in Lemma 2 of Section 3.4.1 how this difficulty will be overcome (see also Remark 6).*

3.3. Stereographic Projection from the Upper Sheet of the Two-Sheeted Hyperboloid to the Non-Euclidean Unit Disk

Let $u = (u_1, u_2)$ denote the Cartesian coordinate system in the open unit disk $D \doteq \{u : u_1^1 + u_2^2 < 1\}$, which lies in the plane $x_0 = 0$:

$$u_1 = \tanh\left(\frac{v}{2}\right)\sin\psi \qquad (v \geqslant 0, \psi \in [0, 2\pi)), \tag{58a}$$

$$u_2 = \tanh\left(\frac{v}{2}\right)\cos\psi. \tag{58b}$$

Then: $|u|^2 = u_1^2 + u_2^2 = \tanh^2(v/2)$. Let $B \doteq \{u : u_1^1 + u_2^2 = 1\}$ denote the boundary of D, i.e., the horizon. Consider the Riemannian structure

$$\mathrm{d}s^2 = \frac{4(\mathrm{d}u_1^2 + \mathrm{d}u_2^2)}{[1 - (u_1^2 + u_2^2)]^2} = \mathrm{d}v^2 + \sinh^2 v\,\mathrm{d}\psi^2, \tag{59}$$

where $\mathrm{d}v^2 + \sinh^2 v\,\mathrm{d}\psi^2$ can also be obtained from (56) through the equality: $\mathrm{d}s^2 = -\mathrm{d}x_0^2 + \mathrm{d}x_1^2 + \mathrm{d}x_2^2$. Let us embed the non-Euclidean disk in the complex z-plane so that each point of the unit disk can be represented either by the coordinates (u_1, u_2) in (58) or through the polar representation of z, which in the present case reads: $z = |z|\exp[\mathrm{i}(\frac{\pi}{2} - \psi)]$, $|z| = \tanh(\frac{v}{2})$. Note that in this latter representation we are forced to write $\exp[\mathrm{i}(\frac{\pi}{2} - \psi)]$ with ψ induced by (56) (instead of the standard expression $\exp(\mathrm{i}\psi)$) in order to have the correct correspondence between Cartesian and polar representations. Accordingly, the points b of the boundary B of the non-Euclidean disk will be described by $b = \exp[\mathrm{i}(\frac{\pi}{2} - \phi)]$, ϕ being defined analogously to ψ that is, measured from the positive u_2-axis and increasing toward the positive u_1-axis. The Riemannian structure (59) induces the usual non-Euclidean distance on D:

$$d(0, z) = \ln\frac{1 + |z|}{1 - |z|} \qquad z = |z|\,e^{\mathrm{i}(\frac{\pi}{2} - \psi)},$$

where $|z| = \tanh(v/2)$ and 0 is the center of the unit disk. In D, the geodesics are circular arcs intersecting the unit circle at right angles. In particular, all diameters of the unit circle are straight lines since these diameters can be considered as arcs of infinite large radius. A pencil of parallel straight lines is given by arcs of Euclidean circles orthogonal to the unit circle, lying in its interior and intersecting the boundary B at a common point b. The lines orthogonal to this pencil of parallel geodesics are the circles tangent from within to the horizon at the point b. Since these circles are the Euclidean images of the horocycles, we shall refer to the point of contact b as the normal to the horocycle.

The coordinates (x_0, x_1, x_2) that describe the point P varying on the upper sheet ${}^2\mathrm{X}_2^+$ of the two-sheeted hyperboloid are related to the coordinates (u_1, u_2) in the open non-Euclidean unit disk D through the following formulas (Lemma 1, p. 49, [25]):

$$x_0 = \frac{1 + |u|^2}{1 - |u|^2}, \qquad x_1 = \frac{2u_1}{1 - |u|^2}, \qquad x_2 = \frac{2u_2}{1 - |u|^2}. \tag{60}$$

Each line of intersection of ${}^2\mathrm{X}_2^+$ with the plane $ax_0 + bx_1 + cx_2 = 0$ $(a, b, c \in \mathbb{R})$ is mapped by the transformation (60) into a circular arc intersecting the horizon at right angles (Lemma 3, p. 51, [25]). In order to find the curve into which a straight line on ${}^2\mathrm{X}_2^+$ is mapped, it is sufficient to substitute into

the equation of the plane $ax_0 + bx_1 + cx_2 = 0$ the explicit expression (60) of the variables x_i $(i = 0, 1, 2)$ in terms of u_1, u_2. Then, the equation

$$a\,\frac{1+|u|^2}{1-|u|^2} + \frac{2bu_1}{1-|u|^2} + \frac{2cu_2}{1-|u|^2} = 0 \tag{61}$$

is reduced after simple algebra to the equation of the circle

$$\left(u_1 + \frac{b}{a}\right)^2 + \left(u_2 + \frac{c}{a}\right)^2 = \frac{b^2+c^2-a^2}{a^2} \qquad (a \neq 0), \tag{62}$$

with radius $r = \sqrt{b^2+c^2-a^2}/|a|$ and center at the point $(-b/a, -c/a)$ if $a \neq 0$, and to the line $bu_1 + cu_2 = 0$ if $a = 0$. Note that the image into D of a straight line on ${}^2\mathrm{X}_2^+$ is not the entire circle (62) but only its part contained in the unit disk.

Let us now map the hyperbola ${}^2\widehat{\mathrm{X}}^+ = {}^2\mathrm{X}_2^+ \cap \{x_1 = 0\}$, namely, the meridian of the upper sheet of the two-sheeted hyperboloid, into the non-Euclidean unit disk. By setting $a = c = 0$ and $b = 1$ in the equation of the planes given above, from (61), we see that ${}^2\widehat{\mathrm{X}}^+$ is mapped into the diameter $u_1 = 0$ of the non-Euclidean disk: precisely (see (58)), we have the diameter $u_1 = 0$, $u_2 = \tanh(v/2)$, which tends to $u_2 = +1$ (i.e., $z = +\mathrm{i}$) for $v \to +\infty$ and $\psi = 0$, and to $u_2 = -1$ (i.e., $z = -\mathrm{i}$) for $v \to +\infty$ and $\psi = \pi$ (see Figure 4).

Next, we map the parabola ${}^2\Pi_w^+$, with apex ${}^2x_w = (\cosh w, 0, \sinh w)$ lying on the meridian ${}^2\widehat{\mathrm{X}}^+$, which is represented in horocyclic coordinates by Equation (57). The apex ${}^2x_w$ of the parabola lies on the right branch $x_2 > 0$ of the meridian ${}^2\widehat{\mathrm{X}}^+$ for $w > 0$, and on the left branch $x_2 < 0$ for $w < 0$; for $w = 0$, the apex of the parabola has coordinates $(1, 0, 0)$. These parabolae are generated by the intersection of ${}^2\mathrm{X}_2^+$ with the plane ${}^2P_w$ whose equation is: $x_0 + x_2 = e^w$. By substituting in this latter equation the expressions of x_0 and x_2 given in (60), we obtain:

$$u_1^2 + \left(u_2 + \frac{1}{1+e^w}\right)^2 = \frac{e^{2w}}{(1+e^w)^2}, \tag{63}$$

which represents a circle. In view of (63), we can thus say that the mapping of the parabolae ${}^2\Pi_w^+$ into the unit non-Euclidean disk are the Euclidean circles (images of horocycles) with center in $(u_1 = 0,\ u_2 = -(1+e^w)^{-1})$, radius $r_w = (1+e^{-w})^{-1}$, and tangent from within to the horizon at the point $(u_1 = 0, u_2 = -1)$ (i.e., $z = -\mathrm{i}$; see Figure 4). Moreover, these circles cut orthogonally the diameter $u_1 = 0$ of D in the point $(u_1 = 0, u_2 = \tanh(w/2))$, which lies above the center of D when $w > 0$ and below the center of D when $w < 0$.

3.4. Connection between Spherical Laplace Transform and Non-Euclidean Fourier Transform

3.4.1. Preparatory Lemmas

Lemma 1. *(i) The Poisson kernel*

$$\mathrm{P}(z, b) = \frac{1-|z|^2}{1+|z|^2-2|z|\cos(\psi-\phi)} \qquad \left(z = |z|e^{\mathrm{i}\psi'}, \psi' = \frac{\pi}{2} - \psi;\ b = e^{\mathrm{i}\phi'}, \phi' = \frac{\pi}{2} - \phi\right),$$

is constant on each horocycle $H_b(z)$ with normal b and passing through $z \in D$.

(ii) The function

$$[\mathrm{P}(z, b)]^\lambda = \left[\frac{1-|z|^2}{1+|z|^2-2|z|\cos(\psi-\phi)}\right]^\lambda \qquad (\lambda \in \mathbb{C}), \tag{64}$$

is an eigenfunction of the Laplace–Beltrami operator on the hyperbolic disk D, corresponding to the eigenvalue $\lambda(\lambda-1)$.

(iii) The hyperbolic waves (horocyclic waves) are represented by the following expression:

$$e^{\lambda\langle z,b\rangle}=\left[\frac{1-|z|^2}{1+|z|^2-2|z|\cos(\psi-\phi)}\right]^{\lambda}\qquad(\lambda\in\mathbb{C}),\tag{65}$$

where $\langle z,b\rangle$ *is the signed non-Euclidean distance between the center of the unit disk D and the horocycle* $H_b(z)$ *with normal b that passes through* $z\in D$.

(iv) The following equality holds:

$$\left[\frac{1-|z|^2}{1+|z|^2-2|z|\cos(\psi-\phi)}\right]^{\lambda}=\frac{1}{[\cosh v-\sinh v\cos(\psi-\phi)]^{\lambda}}\qquad(\lambda\in\mathbb{C}).\tag{66}$$

Proof. (i) The level lines of the Poisson kernel $\mathsf{P}(z,b)$ are the circles tangent from within to the unit circle at the point $b=e^{i\phi'}$; when interpreted in a non-Euclidean fashion, they represent horocycles $H_b(z)$ with normal b (p. 7, [26]).

(ii) The Laplace–Beltrami operator Δ_D on the non-Euclidean unit disk D is given by [2,27]

$$\Delta_D=\frac{1}{4}\left[1-(u_1^2+u_2^2)\right]^2\left(\frac{\partial^2}{\partial u_1^2}+\frac{\partial^2}{\partial u_2^2}\right).$$

For $\lambda\in\mathbb{C}$, a direct computation gives [2,27]

$$\Delta_D\,[\mathsf{P}(z,b)]^{\lambda}=\lambda(\lambda-1)\,[\mathsf{P}(z,b)]^{\lambda}\qquad(\lambda\in\mathbb{C}).\tag{67}$$

(iii) In the Euclidean case, the function $\boldsymbol{x}\mapsto e^{\mathrm{i}k(\boldsymbol{x},\boldsymbol{\omega})}$, $k\in\mathbb{R}$, $\boldsymbol{\omega}\in\mathbb{S}^{(n-1)}$, $\boldsymbol{x}\in\mathbb{R}^n$, represents a plane wave with normal $\boldsymbol{\omega}$: it is an eigenfunction of the Laplacian in $\mathbb{R}^n$ and is constant on every hyperplane perpendicular to $\boldsymbol{\omega}$. In the case of the non-Euclidean disk D, the geometric analog of the plane wave is the function represented by Equation (65) [2,27]. In fact, it is an eigenfunction of the Laplace–Beltrami operator on D, as proved by statement (ii) (see (67)). Let $z_{\min}=|z_{\min}|e^{i\chi}$ denote the point on the horocycle $H_b(z)$ (i.e., the one with normal $b=e^{\mathrm{i}\phi'}$ and passing through z) that is closest to the center of D. Then, $\chi=\phi'$ or $\chi=\phi'+\pi$ depending on whether the origin of D lies, respectively, outside or inside the horocycle $H_b(z)$. Therefore, from the definition of $\langle z,b\rangle$, we have:

$$|\langle z,b\rangle|\doteq\ln\frac{1+|z_{\min}|}{1-|z_{\min}|}=|\ln\,\mathsf{P}(z_{\min},b)|=|\ln\,\mathsf{P}(z,b)|\,,$$

the last equality following from statement (i). If we define $\langle z,b\rangle\doteq\ln\,\mathsf{P}(z,b)$, then $\langle z,b\rangle$ is indeed constant on each horocycle $H_b(z)$ and represents the hyperbolic analog of $(\boldsymbol{x},\boldsymbol{\omega})$. Moreover, $\langle z,b\rangle$ is positive if z is such that the origin of D lies outside the horocycle $H_b(z)$, whereas it is negative if the origin falls inside.

(iv) Equality (66) follows by plugging $|z|=\tanh(v/2)$ in formula (64). □

We now introduce the Spherical Functions $\Phi_\lambda(g)$ on G/K ($g\in G=\mathrm{SU}(1,1)$, $K=\mathrm{SO}(2)$).

Definition 1. *The* Spherical Functions *on* G/K *are defined by [28]*

$$\Phi_\lambda(g)\doteq\int_B\left|\frac{\mathrm{d}(g^{-1}\cdot b)}{\mathrm{d}b}\right|^{\lambda}\mathrm{d}b\qquad(g\in G,\lambda\in\mathbb{C}),$$

where $B = \{z : |z| = 1\}$ *is the boundary of the non-Euclidean disk* D.

Lemma 2 (Eymard [28]). *The functions* $\Phi_\lambda(g)$ *satisfy the following properties:*

(i) $\Phi_\lambda(g) = P_{-\lambda}(\cosh v)$, $(g \in G, \lambda \in \mathbb{C}, v \in \mathbb{R})$, *where* $P_{-\lambda}(\cdot)$ *are the Legendre functions of the first kind.*
(ii) $\Delta_D \Phi_\lambda(g) = \lambda(\lambda - 1)\Phi_\lambda(g)$, $(g \in G, \lambda \in \mathbb{C})$, *where* Δ_D *is the non-Euclidean Laplace–Beltrami operator.*
(iii) For $\lambda = -\frac{1}{2} + \mathrm{i}\mu$ $(\mu \in \mathbb{R})$*:*

$$
\begin{aligned}
&(iii.a) \quad P_{-\frac{1}{2}+\mathrm{i}\mu}(\cosh v) = P_{-\frac{1}{2}-\mathrm{i}\mu}(\cosh v),\\
&(iii.b) \quad P_{-\frac{1}{2}+\mathrm{i}\mu}(\cosh v) = \frac{1}{2\pi}\int_0^{2\pi}\left(\frac{1}{\cosh v - \sinh v\cos(\psi-\phi)}\right)^{\frac{1}{2}-\mathrm{i}\mu}\mathrm{d}\phi\\
&\qquad\qquad = \frac{1}{2\pi}\int_0^{2\pi}\left(\frac{1-|z|^2}{1+|z|^2-2|z|\cos(\psi-\phi)}\right)^{\frac{1}{2}-\mathrm{i}\mu}\mathrm{d}\phi \qquad (68)\\
&\qquad\qquad = \frac{1}{2\pi}\int_B e^{(\frac{1}{2}-\mathrm{i}\mu)\langle z,b\rangle}\,\mathrm{d}b \qquad (z \in D).
\end{aligned}
$$

Proof. See Ref. [28]. □

Remark 6. *Representation* (68) *of the conical function is attained by varying within the integral the angle* ϕ *(or, equivalently, the normal* b*) in such a way as to span the entire horizon* ($\phi \in [0, 2\pi]$*). This amounts to considering in the non-Euclidean disk all the families of horocycles which are obtained by varying the normal* b *on the horizon. On the other hand, we have seen in Section 3.2 that only one family of horocycles (the one with tangency point at* $z = -\mathrm{i}$*) results from the fibration of the upper sheet* ${}^2X_2^+$ *of the real two-sheeted hyperboloid. However, from formula* (68)*, we see that the same representation of the conical function can be obtained by keeping* ϕ *fixed and varying* ψ *in the range* $[0, 2\pi]$*. Let us recall once again that here we consider only functions of the form* $\underline{F} = \underline{F}(\cosh v)$ *and therefore not depending on* b *(see Remark 4(ii)). Consequently, in the non-Euclidean transform (that will be analyzed in the next subsection), the* b*-dependence of the integrand derives solely from the integral representation* (68) *of the conical function.*

3.4.2. Non-Euclidean Fourier Transform

It is well known that the classical Fourier transform refers to the decomposition of a function, belonging to an appropriate space, into exponentials of the form $e^{\mathrm{i}kx}$ (k real), which can also be viewed as the irreducible unitary representations of the additive group of the real numbers. However, the non-Euclidean disk is not a group. Therefore, a straightforward generalization of this viewpoint is not applicable here. Nevertheless, in view of the fact that the functions $P_{-\lambda}(\cosh v)$ correspond for $\lambda = \frac{1}{2} - \mathrm{i}\mu$ to the principal series of the irreducible unitary representations of the group $\mathrm{SU}(1,1)$, the exponentials $e^{(\frac{1}{2}-\mathrm{i}\mu)\langle z,b\rangle}$ ($\mu \in \mathbb{R}$) (see statement (iii.b) of Lemma 2) represent the analog of the Euclidean exponentials and play the same role in the non-Euclidean Fourier analysis. We can now state the following classical theorem due to Helgason.

Theorem 4 (Helgason [2,27]). *For* $f \in C_c^\infty(D)$*, let* $\widetilde{f}$ *denote the Fourier transform*

$$\widetilde{f}(\mu, b) = \int_D e^{(\frac{1}{2}-\mathrm{i}\mu)\langle z,b\rangle} f(z)\,\mathrm{d}z \qquad (\mu \in \mathbb{R}, b \in B), \tag{69}$$

where $\mathrm{d}z$ *is the invariant surface element on* D*. Then:*

(i) The inverse Fourier transform is given by

$$f(z) = \frac{1}{(2\pi)^2} \int_{\mathbb{R}^+} \int_B e^{(\frac{1}{2}+\mathrm{i}\mu)\langle z,b\rangle} \widetilde{f}(\mu, b)\ \mu \tanh \pi\mu \,\mathrm{d}\mu \,\mathrm{d}b, \tag{70}$$

where $\mathrm{d}b$ *is the angular measure on* B.

(ii) The mapping $f \to \widetilde{f}$ *extends to an isometry of the space* $L^2(D, \mathrm{d}z)$ *onto the space* $L^2(\mathbb{R}^+ \times B, \frac{1}{2\pi}\mu \tanh \pi\mu \,\mathrm{d}\mu \,\mathrm{d}b)$.

Proof. See Refs. [2,27]. □

Remark 7. *(i) Since we are considering functions of the form* $\underline{F} = \underline{F}(\cosh v)$, *we can restrict the integrals* (69) *and* (70) *to the case of radial functions [27] that is, to functions* $f(z) = F(d(0,z))$, F *even. In fact, since* $d(0,z) = \ln \frac{1+|z|}{1-|z|}$ *and* $|z| = \tanh(v/2)$, *then* $d(0,z) = v$ *and* $f(z) = F(v) = \underline{F}(\cosh v)$. *Hence,* $\widetilde{f}(\mu, b)$ *is an even function of* μ *alone. In view of statements (iii.a) and (iii.b) of Lemma 2 (see also Remark 6), noting that the expression of the invariant surface element* $\mathrm{d}z$ *in the coordinates* (v, ψ) *is* $\mathrm{d}z = \sinh v \,\mathrm{d}v \,\mathrm{d}\psi$, *and writing* $\widetilde{f}(\mu, b) = 2\pi\widetilde{F}(\mu)$, *then formulas* (69) *and* (70) *read*

$$\widetilde{F}(\mu) = \int_0^{+\infty} \underline{F}(\cosh v)\, P_{-\frac{1}{2}+\mathrm{i}\mu}(\cosh v) \sinh v \,\mathrm{d}v, \tag{71a}$$

$$F(v) = \underline{F}(\cosh v) = \int_0^{+\infty} \widetilde{F}(\mu)\ P_{-\frac{1}{2}+\mathrm{i}\mu}(\cosh v)\ \mu \tanh \pi\mu \,\mathrm{d}\mu, \tag{71b}$$

which coincide with formulas (54), *i.e., the Mehler transform pair.*

(ii) It is worth noting the close analogy between the non-Euclidean Fourier transform pair (69) *and* (70) *and the Euclidean Fourier transform in the plane* $\mathbb{R}^2$. *The Fourier transform* $\widetilde{f}$ *of a function* f *on* $\mathbb{R}^2$ *is given by*

$$\widetilde{f}(\mu\boldsymbol{\omega}) = \int_{\mathbb{R}^2} f(\boldsymbol{x}) e^{-\mathrm{i}\mu\,(\boldsymbol{x},\boldsymbol{\omega})}\,\mathrm{d}\boldsymbol{x}.$$

Then, the Fourier inversion formula, valid, for example, if $f \in C_c^\infty(\mathbb{R}^2)$, *reads*

$$f(\boldsymbol{x}) = \frac{1}{(2\pi)^2} \int_{\mathbb{R}^+} \int_{\mathbb{S}^1} \widetilde{f}(\mu\boldsymbol{\omega})\, e^{\mathrm{i}\mu\,(\boldsymbol{x},\boldsymbol{\omega})}\ \mu \,\mathrm{d}\boldsymbol{\omega} \,\mathrm{d}\mu,$$

$\mathrm{d}\boldsymbol{\omega}$ *denoting the circular measure on* $\mathbb{S}^1$ *(p. 4, [2]).*

3.4.3. Connection between the Spherical Laplace Transform at $\mathrm{Re}\,\lambda = -\frac{1}{2}$ and the Non-Euclidean Fourier Transform

We can now prove the following theorem.

Theorem 5. *Suppose that the sequence* $\{f_n\}_{n=0}^\infty$, *where* $f_n = (n+1)^2 a_n$ (a_n *being the Legendre coefficients of expansion* (14)) *satisfies the Hausdorff condition* (20). *Then:*

(i) The spherical Laplace transform at $\mathrm{Re}\,\lambda = -\frac{1}{2}$, *restricted to the odd component (in* μ*) of* $\widetilde{a}(\sigma + \mathrm{i}\mu)$ *(see Section 3.1) reads*

$$\widetilde{F}(\mu) = \int_0^{+\infty} \underline{F}(\cosh v) P_{-\frac{1}{2}+\mathrm{i}\mu}(\cosh v) \sinh v \,\mathrm{d}v, \tag{72}$$

where the equality holds in the sense of the L^2*-norm. Precisely,* $\underline{F}(\cosh v) \in L^2(1, +\infty)$ *and* $\widetilde{F}(\mu)$ *is an even function of* μ *which belongs to* $L^2(\mathbb{R}^+, \mu \tanh \pi\mu \,\mathrm{d}\mu)$.

(ii) The inverse of formula (72) reads

$$F(v) = \underline{F}(\cosh v) = \int_0^{+\infty} \widetilde{F}(\mu) P_{-\frac{1}{2}+\mathrm{i}\mu}(\cosh v)\ \mu \tanh \pi\mu \,\mathrm{d}\mu. \tag{73}$$

(iii) The following equality holds:

$$\int_0^{+\infty} \left|\widetilde{F}(\mu)\right|^2 \mu \tanh \pi\mu \,\mathrm{d}\mu = \int_1^{+\infty} |\underline{F}(\cosh v)|^2 \,\mathrm{d}(\cosh v). \tag{74}$$

(iv) The spherical Laplace transform coincides at $\mathrm{Re}\,\lambda = -\frac{1}{2}$ *with the non-Euclidean Fourier transform.*

Proof. We start by proving statements (ii) and (iii) and, successively, we shall prove (i) and (iv).

(ii) In view of the assumptions on $\{f_n\}_{n=0}^{\infty}$, we may use the results of Theorem 3 and from formula (50) with $\sigma \equiv \mathrm{Re}\,\lambda = -\frac{1}{2}$:

$$F(v) = \underline{F}(\cosh v) = \frac{1}{4\pi} \int_{-\infty}^{+\infty} \widetilde{a}\left(-\tfrac{1}{2} + \mathrm{i}\mu\right) (2\mathrm{i}\mu) P_{-\frac{1}{2}+\mathrm{i}\mu}(\cosh v)\,\mathrm{d}\mu. \tag{75}$$

Let $\widetilde{F}(\mu) \doteq \frac{\widetilde{a}(-1/2+\mathrm{i}\mu)}{-\mathrm{i}\pi \tanh \pi\mu}$, as we already did when passing from (53) to (54b). Formula (75) can be rewritten as

$$F(v) = \underline{F}(\cosh v) = \int_0^{+\infty} \widetilde{F}(\mu)\ P_{-\frac{1}{2}+\mathrm{i}\mu}(\cosh v)\ \mu\ \tanh \pi\mu \,\mathrm{d}\mu, \tag{76}$$

which coincides with the inverse spherical Laplace transform (73). Note that formula (76) coincides with the inversion of the non-Euclidean Fourier transform (70) in the specific case of radial functions.

(iii) First, we prove that the l.h.s. of (74) is convergent. The integral $\int_0^{+\infty} |\widetilde{F}(\mu)|^2 \mu \tanh \pi\mu \,\mathrm{d}\mu$ is split into the integral over $[0,1]$ plus the integral over $[1,+\infty)$. We have $\int_0^1 |\widetilde{F}(\mu)|^2 \mu \tanh \pi\mu \,\mathrm{d}\mu = \frac{1}{\pi^2} \int_0^1 |\widetilde{a}(-\frac{1}{2} + \mathrm{i}\mu)|^2 \frac{\mu}{\tanh \pi\mu} \,\mathrm{d}\mu$, which is convergent since $\lim_{\mu\to 0}(\mu/\tanh \pi\mu) = 1/\pi$, and $\widetilde{a}(-\frac{1}{2} + \mathrm{i}\mu)$ belongs to $L^2(0,1)$ for inequality (25). The integral $\int_1^{+\infty} |\widetilde{F}(\mu)|^2 \mu \tanh \pi\mu \,\mathrm{d}\mu$ is convergent since $|\tanh \pi\mu|^{-1} \leqslant M$ (M constant) for $\mu \in [1,+\infty)$ and $\int_1^{+\infty} |\sqrt{\mu}\ \widetilde{a}(-\frac{1}{2} + \mathrm{i}\mu)|^2 \,\mathrm{d}\mu < \int_1^{+\infty} |\mu^2\, \widetilde{a}(-\frac{1}{2} + \mathrm{i}\mu)|^2 \,\mathrm{d}\mu < \infty$ in view of statement (ii) of Proposition 2. We have proved above that (76) coincides with the inverse non-Euclidean Fourier transform (70). From statement (ii) of Theorem 4, we know that the mapping $f \to \widetilde{f}$ (which, in our case, corresponds to the mapping $F(v) = \underline{F}(\cosh v) \to \widetilde{F}(\mu)$) is an isometry of $L^2(D, \mathrm{d}z)$ onto $L^2(\mathbb{R}^+ \times B, \frac{1}{2\pi}\mu \tanh \pi\mu \,\mathrm{d}\mu\mathrm{d}b)$. Therefore, the convergence of integral $\int_0^{+\infty} |\widetilde{F}(\mu)|^2 \mu \tanh \pi\mu \,\mathrm{d}\mu$ along with the above mentioned isometry allows us to state equality (74) and that $\underline{F}(\cosh v) \in L^2(1,+\infty)$.

(i) Consider formula (54b), which is the formal expression of the spherical Laplace transform at $\mathrm{Re}\,\lambda = -\frac{1}{2}$ (restricted to its odd component with respect to the variable $\mu \in \mathbb{R}$). We note that it coincides with formula (72) which, by formula (74) proved above, holds as an equality in the sense of the L^2-norm, as specified by statement (i).

(iv) We have indeed proved that formulas (72) and (73) coincide, respectively, with formulas (71a) and (71b), which are the Mehler reduction of the non-Euclidean Fourier transform pair (69) and (70). □

4. Conclusions

In summary, we have proved the following results. Let the Fourier–Legendre expansion $\frac{1}{4\pi}\sum_{n=0}^{\infty}(2n+1)a_n P_n(\cos\theta)$, and assume the numbers $\{f_n\}_{n=0}^{\infty}$ ($f_n = (n+1)^2 a_n$) to satisfy the Hausdorff-type condition (20). Then:

1. (a) The Fourier–Legendre expansion converges to a function $\underline{f}(\cos u)$ analytic in the interval $-1 < \cos u < 1$.
   (b) The function $\underline{f}(\cos u)$ admits a holomorphic extension to the complex $(\cos\theta)$-plane ($\theta = u + \mathrm{i}v$) cut along the semi-axis $[1, +\infty)$.
2. (a) The Fourier–Legendre coefficients $\{a_n\}_{n=0}^{\infty}$ are the restrictions to non-negative integers of a transform, called spherical Laplace transform, which is the composition of the ordinary Laplace transform with the Abel transform of $F(v) \equiv \underline{F}(\cosh v)$, which is the jump function across the cut $[1, +\infty)$. Namely, for $\operatorname{Re}\lambda > -\frac{1}{2}$,

$$\widetilde{a}(\lambda) = \int_0^{+\infty} e^{-(\lambda+\frac{1}{2})w}\,(\mathcal{A}F)(w)\,\mathrm{d}w = 2\int_0^{+\infty} \underline{F}(\cosh v)\,Q_\lambda(\cosh v)\sinh v\,\mathrm{d}v, \tag{77}$$

   $Q_\lambda(\cdot)$ being the Legendre function of the second kind.
   (b) The function $\widetilde{a}(\lambda)$, holomorphic in the half-plane $\operatorname{Re}\lambda > -\frac{1}{2}$, satisfies Carlson's bound and interpolates uniquely the coefficients $\{a_n\}_{n=0}^{\infty}$, that is, $a_n = \widetilde{a}(\lambda)|_{\lambda=n}$.
3. The jump function across the cut admits the following integral representation:

$$\begin{aligned} F(v) = \underline{F}(\cosh v) &= \frac{1}{2\pi}\int_{-\infty}^{+\infty} \widetilde{a}(\sigma+\mathrm{i}\mu)\left(\sigma+\tfrac{1}{2}+\mathrm{i}\mu\right) P_{\sigma+\mathrm{i}\mu}(\cosh v)\,\mathrm{d}\mu \\ &= \frac{1}{2\pi\mathrm{i}}\int_{\sigma-\mathrm{i}\infty}^{\sigma+\mathrm{i}\infty} \widetilde{a}(\lambda)\left(\lambda+\tfrac{1}{2}\right) P_\lambda(\cosh v)\,\mathrm{d}\lambda \qquad \left(\sigma \geqslant -\tfrac{1}{2}\right), \end{aligned} \tag{78}$$

   where $P_\lambda(\cdot)$ denotes the Legendre function of the first kind. Representation (78) is the inverse of the spherical Laplace transform (77).
4. (a) For $\operatorname{Re}\lambda = -\frac{1}{2}$ the spherical Laplace transform, restricted to the odd component in μ of $\widetilde{a}(\sigma+\mathrm{i}\mu)$, reads

$$\widetilde{F}(\mu) = \int_0^{+\infty} \underline{F}(\cosh v) P_{-\frac{1}{2}+\mathrm{i}\mu}(\cosh v)\sinh v\,\mathrm{d}v, \tag{79}$$

   where $\widetilde{F}(\mu) = \frac{\widetilde{a}^{(\mathrm{O})}(-\frac{1}{2}+\mathrm{i}\mu)}{-\mathrm{i}\pi\tanh\pi\mu}$ ($\widetilde{a}^{(\mathrm{O})}(-\frac{1}{2}+\mathrm{i}\mu)$ denoting the odd component of $\widetilde{a}(-\frac{1}{2}+\mathrm{i}\mu)$). Equality (79) holds in the sense of L^2-norm: $\underline{F}(\cosh v) \in L^2(1,+\infty)$, $\widetilde{F}(\mu) \in L^2(\mathbb{R}^+, \mu\tanh\pi\mu\,\mathrm{d}\mu)$. The inverse of formula (79) reads

$$F(v) = \underline{F}(\cosh v) = \int_0^{+\infty} \widetilde{F}(\mu) P_{-\frac{1}{2}+\mathrm{i}\mu}(\cosh v)\;\mu\tanh\pi\mu\,\mathrm{d}\mu. \tag{80}$$

   (b) Formulas (79) and (80) can be written explicitly, passing through Mehler transform, in terms of non-Euclidean Fourier transform as follows:

$$\widetilde{f}(\mu, b) = \int_D e^{(\frac{1}{2}-\mathrm{i}\mu)\langle z,b\rangle}\,f(z)\,\mathrm{d}z \qquad (\mu\in\mathbb{R}, b\in B), \tag{81}$$

   where $\widetilde{f}(\mu,b) = 2\pi\widetilde{F}(\mu)$ and $\mathrm{d}z$ is the invariant surface element on the non-Euclidean disk D. The inverse of (81) is

$$f(z) = \frac{1}{(2\pi)^2}\int_{\mathbb{R}^+}\int_B e^{(\mathrm{i}\mu+\frac{1}{2})\langle z,b\rangle}\,\widetilde{f}(\mu,b)\;\mu\tanh\pi\mu\,\mathrm{d}\mu\,\mathrm{d}b,$$

   where $\mathrm{d}b$ is the angular measure on the boundary B of the unit disk D.
   (c) The functions $P_{-\frac{1}{2}+\mathrm{i}\mu}(\cosh v)$ can be represented as follows:

$$P_{-\frac{1}{2}+\mathrm{i}\mu}(\cosh v) = \frac{1}{2\pi}\int_B e^{(\frac{1}{2}-\mathrm{i}\mu)\langle z,b\rangle}\,\mathrm{d}b \qquad (\mu\in\mathbb{R}, z\in D, |z| = \tanh(v/2)),$$

where: $\langle z, b\rangle = \ln \mathsf{P}(z, b)$ is the *signed* non-Euclidean distance from the center of D to the horocycle with normal b passing through $z \in D$, and P denotes the Poisson kernel.
(d) The conical functions $P_{-\frac{1}{2}+\mathrm{i}\mu}(\cosh v) = P_{-\frac{1}{2}-\mathrm{i}\mu}(\cosh v)$ correspond to the fundamental series of the unitary irreducible representation of the group $\mathrm{SU}(1,1)$, which acts transitively on the non-Euclidean disk D.

5. Last but not least, we wish to spend a few words to emphasize the differences between the classical Stein and Wainger approach and ours. First of all, we want to stress the great relevance of the pioneering work of Stein and Wainger; nevertheless, we believe that some remarks are in order.
(a) Stein and Wainger [9] assume that the Legendre coefficients are the restriction to the integers of a function (denoted by $a(s)$ in their notation), which belongs to a space $H^2_*(\mathrm{Re}\, s > -\frac{1}{2})$. This latter is the space of functions $a(s)$ which belong to $H^2(\mathrm{Re}\, s > -\frac{1}{2})$ and, for which, in addition, the squared norm $\|a\|^2_* = \int_{-\infty}^{+\infty} |a(-\frac{1}{2} + \mathrm{i}t) - a(-\frac{1}{2} - it)|^2 \frac{t\,\mathrm{d}t}{\tanh \pi t}$ is finite. In their approach, it remained open and rather obscure the following question: How can it be established if the coefficients $\{a_n\}$ are the restriction of a function belonging to $H^2_*(\mathrm{Re}\, s > -\frac{1}{2})$? Conversely, in our approach, we start directly from the Legendre coefficients, which are required to satisfy a suitable Hausdorff-type condition strictly connected with the moment theory. This second approach seems more direct, especially in the applications (e.g., scattering theory), where only the coefficients of the expansion are known.
(b) A geometrical analysis of the problem (see Section 3 of this paper) is missing in Stein and Wainger's work. Correspondingly, the remarkable results of Helgason on the non-Euclidean Fourier analysis are not mentioned.
(c) In Stein and Wainger's paper, the analytical properties of the Spherical Laplace Transform, as well as its character of being the composition of a Laplace and an Abel-type transform, do not emerge. This also makes the connection between the Mehler transform and the spherical Laplace transform not transparent.

Funding: This research received no external funding.

Conflicts of Interest: The author declares no conflict of interest.

References

1. Furstenberg, H. Translation-invariant cones of functions on semi-simple Lie groups. *Bull. Am. Math. Soc.* **1965**, *71*, 271–326. [CrossRef]
2. Helgason, S. *Groups and Geometric Analysis: Integral Geometry, Invariant Differential Operators, and Spherical Functions*; Academic Press: Orlando, FL, USA, 1984.
3. Hilgert, J.; Ólafsson, G. *Causal Symmetric Spaces: Geometry and Harmonic Analysis*; Academic Press: San Diego, CA, USA, 1997.
4. Faraut, J.; Viano, G.A. Volterra algebra and the Bethe–Salpeter equation. *J. Math. Phys.* **1986**, *27*, 840–848. [CrossRef]
5. Faraut, J. Algèbres de Volterra et Transformation de Laplace Sphérique sur Certains Espaces Symétriques Ordonnés. In *Symposia Mathematica*; Istituto Nazionale di Alta Matematica: Roma, Italy, 1987; Volume 29, pp. 183–196.
6. Faraut, J. Espaces symétriques ordonnés et algèbres de Volterra. *J. Math. Soc. Jpn.* **1991**, *43*, 133–147. [CrossRef]
7. Faraut, J.; Hilgert, J.; Ólafsson, G. Spherical functions and ordered symmetric spaces. *Ann. Inst. Fourier* **1994**, *44*, 927–966. [CrossRef]
8. Widder, D.V. *The Laplace Transform*; Princeton University Press: Princeton, NJ, USA, 1966.
9. Stein, E.M.; Wainger, S. Analytic properties of expansions, and some variants of Parseval–Plancherel formulas. *Ark. Mat.* **1965**, *5*, 553–567. [CrossRef]
10. Hermann, R. *Lie Groups for Physicists*; W.A. Benjamin: New York, NY, USA, 1966.

11. Andersen, N.B.; Ólafsson, G. A Paley-Wiener theorem for the spherical Laplace transform on causal symmetric space of rank 1. *Proc. Am. Math. Soc.* **2001**, *129*, 173–179. [CrossRef]
12. Ólafsson, G.; Schlichtkrull, H. A local Paley–Wiener theorem for compact symmetric spaces. *Adv. Math.* **2008**, *129*, 202–215. [CrossRef]
13. Pasquale, A. The Θ-spherical transform and its inversion. *Math. Scand.* **2004**, *95*, 265–284. [CrossRef]
14. Bertram, W. Ramanujan's Master Theorem and duality of symmetric spaces. *J. Funct. Anal.* **1997**, *148*, 117–151. [CrossRef]
15. Gindinkin, S.; Krötz, B. Complex crowns of Riemannian symmetric spaces and non-compactly causal symmetric spaces. *Trans. Am. Math. Soc.* **2002**, *354*, 3299–3327. [CrossRef]
16. Guillopè, L.; Zworski, M. The wave trace for Riemann surfaces. *Geom. Funct. Anal.* **1999**, *9*, 1156–1168. [CrossRef]
17. Hilgert, J.; Pasquale, A.; Przebinda, T. Resonances for the Laplacian on products of two rank one Riemannian symmetric spaces. *J. Funct. Anal.* **2017**, *272*, 1477–1523. [CrossRef]
18. Mazzeo, R.; Vasy, A. Analytic continuation of the resolvent of the Laplacian on $\mathrm{SL}(3) \setminus \mathrm{SO}(3)$. *Am. J. Math* **2004**, *126*, 821–844. [CrossRef]
19. Miatello, R.; Wallach, N.R. The resolvent of the Laplacian on locally symmetric spaces. *J. Differ. Geom.* **1992**, *36*, 663–698. [CrossRef]
20. Strohmaier, A. Analytic continuation of resolvent kernels on noncompact symmetric spaces. *Math. Z.* **2005**, *250*, 411–425. [CrossRef]
21. De Micheli, E.; Viano, G.A. Holomorphic extension associated with Fourier–Legendre expansions. *J. Geom. Anal.* **2002**, *12*, 355–374. [CrossRef]
22. Boas, R.P. *Entire Functions*; Academic Press: New York, NY, USA, 1954.
23. Hoffman, K. *Banach Spaces of Analytic Functions*; Prentice–Hall Inc.: Englewood Cliffs, NJ, USA, 1962.
24. Erdélyi, A. (Ed.) Higher Transcendental Functions. In *Bateman Manuscript Project*; McGraw–Hill: New York, NY, USA, 1953; Volume 1.
25. Mishchenko, A.; Fomenko, A. *A Course of Differential Geometry and Topology*; Mir: Moscow, Russia, 1980.
26. Nevanlinna, R. *Analytic Functions*; Springer: Berlin, Germany, 1970.
27. Helgason, S. Lie Groups and Symmetric Spaces. In *Battelle Rencontres – 1967 Lectures in Mathematics and Physics*; De Witt-Morette, C., Wheeler, J.A., Eds.; Benjamin: New York, NY, USA, 1968; pp. 1–71.
28. Eymard, P. Le noyau de Poisson et la theorie des groupes. In *Symposia Mathematica*; Istituto Nazionale di Alta Matematica: Roma, Italy, 1977; Volume 22, pp. 107–132.

© 2020 by the author. Licensee MDPI, Basel, Switzerland. This article is an open access article distributed under the terms and conditions of the Creative Commons Attribution (CC BY) license (http://creativecommons.org/licenses/by/4.0/).

mathematics

MDPI

Article

A Deformed Wave Equation and Huygens' Principle

Salem Ben Saïd *, Sara al-Blooshi, Maryam al-Kaabi, Aisha al-Mehrzi and Fatima al-Saeedi

Department of Mathematical Sciences, College of Science, United Arab Emirates University, P. O. Box No. 15551, Al Ain, Abu Dhabi, UAE; 201502530@uaeu.ac.ae (S.a.-B.); 201506313@uaeu.ac.ae (M.a.-K.); 201601854@uaeu.ac.ae (A.a.-M.); 201735617@uaeu.ac.ae (F.a.-S.)

* Correspondence: salem.bensaid@uaeu.ac.ae

Received: 1 October 2019; Accepted: 4 November 2019; Published: 19 December 2019

Abstract: We consider a deformed wave equation where the Laplacian operator has been replaced by a differential-difference operator. We prove that this equation does not satisfy Huygens' principle. Our approach is based on the representation theory of the Lie algebra $\mathfrak{sl}(2,\mathbb{R})$.

Keywords: generalized Fourier transform; deformed wave equation; Huygens' principle; representation of $\mathfrak{sl}(2,\mathbb{R})$

MSC: 43A30; 22E70

1. Introduction

The wave problem consists of the wave equation and some initial data,

$$\Delta u(x,t) = \partial_{tt} u(x,t), \quad u(x,0) = f(x),\ \partial_t u(x,0) = g(x), \qquad \text{for } x \in \mathbb{R}^n \text{ and } t \in \mathbb{R}.$$

This problem is certainly one of the most interesting problems of mathematical physics. Standard techniques involving the Fourier transform show that there are two distributions P_1 and P_2 on $\mathbb{R}^n \times \mathbb{R}$ such that $u = P_1 * f + P_2 * g$. Here $*$ represents the Euclidean convolution product. The distributions P_1 and P_2 are called propagators.

One of the most celebrated features of the wave equation is Huygens' principle: When the dimension n is odd and starting from 3, the propagators are supported entirely on spherical shells. This is the reason why in our three-dimensional word, transmission of signals is possible and we can hear each other. A two-dimensional world would be drastically different from this point of view.

The problem of classifying all second order differential operators which obey Huygens' principle is known as the Hadamard problem [1]. This problem has received a good deal of attention and the literature is extensive (see, for instance, [2–13]). Nevertheless, this problem is still far from being fully solved.

In this paper we will consider a deformed wave equation where the Laplacian Δ is replaced by a certain differential-difference operator. We will prove the non-existence of Huygens' principle for the deformed wave equation for all $n \geqslant 1$. The main tool is the representation theory of the Lie algebra $\mathfrak{sl}(2,\mathbb{R})$.

More precisely, we will consider the deformed wave equation $2\|x\|\Delta_k u(x,t) = \partial_{tt} u(x,t)$ with compactly supported initial data (f,g). Here Δ_k is the differential-difference Dunkl Laplacian (see (2)), where k is a multiplicity function for the Dunkl operators. The operator $\|x\|\Delta_k$ appeared in [14] and played a crucial rule in the study of the so-called $(k,1)$-generalized Fourier transform. When $k \equiv 0$, the deformed wave equation becomes $2\|x\|\Delta u(x,t) = \partial_{tt} u(x,t)$ and the $(0,1)$-generalized Fourier transform reduces to a Hankel type transform on $\mathbb{R}^n$. We refer the reader to [14] for a detailed study on the generalized Fourier transform.

We begin with a straightforward treatment of the Cauchy problem for the deformed wave equation by means of the $(k,1)$-generalized Fourier transform, and derive the existence of propagators $P_{k,1}$ and $P_{k,2}$, in terms of which, the Cauchy problem is solved. Huygens' principle for the deformed wave equation is that $P_{k,1}$ and $P_{k,2}$ are supported entirely on the set $\{(x,t) \in \mathbb{R}^n \times \mathbb{R} : \|x\| - \frac{1}{2}t^2 = 0\}$. It is not a simple task to study the support property from the precise form of the propagators. However, subtler dilatation properties of the propagators allow us to show that Huygens' principle holds true if, and only if, $P_{k,1}$ and $P_{k,2}$ generate a finite dimensional representation of the Lie algebra $\mathfrak{sl}(2,\mathbb{R})$. It is here that the construction of a representation of $\mathfrak{sl}(2,\mathbb{R})$ plays a crucial role. This construction was inspired by [14]. A closer investigation shows that $P_{k,1}$ and $P_{k,2}$ cannot generate finite dimensional representations of $\mathfrak{sl}(2,\mathbb{R})$, and therefore, Huygens' principle does not hold for the deformed wave equation for any $n \geqslant 1$ and any multiplicity function k. The strategy uses proof by contradiction. It is noteworthy mentioning that the case $k \equiv 0$ is already new.

It would be interesting to understand the interpretation(s) of the non-existence of Huygens' principle for the deformed wave equation from the physics point of view. It would also be fascinating to ask whether Huygens's principle holds for other seminal Dunkl-type equations such as the Dunkl–Dirac equation (see [15] for more details about the Dunkl–Dirac operator). For the Euclidean Dirac equation, this problem has been investigated in [16].

2. Background

Let $\langle \cdot, \cdot \rangle$ be the standard Euclidean scalar product in $\mathbb{R}^n$. For $x \in \mathbb{R}^n$, denote $\|x\| = \langle x, x \rangle^{1/2}$.

For α in $\mathbb{R}^n \backslash \{0\}$, we write r_α for the reflection with respect to the hyperplane $\alpha^\perp$ orthogonal to α defined by

$$r_\alpha(x) := x - 2\frac{\langle \alpha, x \rangle}{\langle \alpha, \alpha \rangle}\alpha, \quad x \in \mathbb{R}^n.$$

A finite set $\mathcal{R} \subset \mathbb{R}^n \backslash \{0\}$ is called a root system if $r_\alpha(\mathcal{R}) \subset \mathcal{R}$ for every $\alpha \in \mathcal{R}$. The finite group $G \subset O(n)$ generated by the reflections $\{r_\alpha : \alpha \in \mathcal{R}\}$ is called the finite Coxeter group associated with $\mathcal{R}$. A multiplicity function for G is a function $k : \mathcal{R} \to \mathbb{R}_{\geqslant 0}$ which is constant on G-orbits.

For $1 \leqslant j \leqslant n$, the Dunkl operator is defined in [17] by

$$T_j f(x) = \partial_j f(x) + \frac{1}{2}\sum_{\alpha \in \mathcal{R}} k(\alpha)\frac{f(x) - f\big(r_\alpha(x)\big)}{\langle \alpha, x \rangle}\langle \alpha, e_j \rangle, \quad x \in \mathbb{R}^n,$$

where ∂_j is the standard directional derivative and $\{e_1, \ldots, e_n\}$ is the canonical orthonormal basis in $\mathbb{R}^n$. The most important property of these operators is that they commute. The operators T_j and ∂_j are intertwined by the following Laplace type operator

$$V_k f(x) = \int_{\mathbb{R}^n} f(y) d\mu_x^k(y), \tag{1}$$

where μ_x^k is a unique compactly supported probability measure with $\operatorname{supp}(\mu_x^k) \subset \{y \in \mathbb{R}^n : \|y\| \leqslant \|x\|\}$ (see [17,18]).

The Dunkl Laplacian, which is akin to the Euclidean Laplace operator Δ, is defined by $\Delta_k := T_1^2 + \cdots + T_n^2$ and is given explicitly, for suitable function f, by

$$\Delta_k f(x) = \Delta f(x) + \sum_{\alpha \in \mathcal{R}} k(\alpha)\left(\frac{\langle \nabla f(x), \alpha \rangle}{\langle \alpha, x \rangle} - \frac{\|\alpha\|^2}{2}\frac{f(x) - f\big(r_\alpha(x)\big)}{\langle \alpha, x \rangle^2}\right), \quad x \in \mathbb{R}^n, \tag{2}$$

where ∇ is the gradient. It is worth mentioning that if $k(\alpha) = 0$ for all $\alpha \in \mathcal{R}$, then Δ_k reduces to the Euclidean Laplacian Δ. We refer the reader to [19] for the theory of Dunkl's operators. This theory,

which started with the seminal paper [17], was developed extensively afterwards and continues to receive considerable attention (see, e.g., [20–32]).

Next we will introduce some definitions and results for the generalized Fourier transform; for details we refer to [14]. For $a > 0$, let

$$\Delta_{k,a} := \|x\|^{2-a}\Delta_k - \|x\|^a,$$

where $\|x\|^a$ on the right-hand side of the formula stands for the multiplication operator by $\|x\|^a$. The operator $\Delta_{k,a}$ is symmetric on the Hilbert space $L^2(\mathbb{R}^n, \vartheta_{k,a})$ consisting of square integrable functions against the measure $\vartheta_{k,a}(x)dx := \|x\|^{a-2}\prod_{\alpha\in\mathcal{R}}|\langle\alpha, x\rangle|^{k(\alpha)}dx$.

The (k, a)-generalized Fourier transform $\mathcal{F}_{k,a}$ was defined in [14] to be

$$\mathcal{F}_{k,a} := \mathrm{e}^{i\frac{\pi}{2}\left(\frac{n+2\langle k\rangle+a-2}{a}\right)}\ \exp\Big(i\frac{\pi}{2a}\Delta_{k,a}\Big),$$

where $\langle k\rangle := \frac{1}{2}\sum_{\alpha\in\mathcal{R}}k(\alpha)$. We pin down that $\mathcal{F}_{k,a}$ is a unitary operator from $L^2(\mathbb{R}^n, \vartheta_{k,a})$ onto itself and the inversion formula is given as

$$\mathcal{F}^{-1}_{k,\frac{1}{r}} = \mathcal{F}_{k,\frac{1}{r}}, \qquad \big(\mathcal{F}^{-1}_{k,\frac{2}{2r+1}}f\big)(x) = \big(\mathcal{F}_{k,\frac{2}{2r+1}}f\big)(-x), \tag{3}$$

where r is any nonnegative integer. The transform $\mathcal{F}_{k,a}$ reduces to the Euclidean Fourier transform if $k \equiv 0$ and $a = 2$; to the Kobayashi–Mano Hankel transform [33] if $k \equiv 0$ and $a = 1$; to the Dunkl transform [34] if $k > 0$ and $a = 2$. In this paper we consider the case $k > 0$ and $a = 1$. For more details, we refer the reader to ([14] Sections 4 and 5) (see also [35–41]).

Let us collect the main properties of the $(k, 1)$-transform $\mathcal{F}_{k,1} := \mathcal{F}_k$. In ([14] Theorem 4.23), the authors proved that for $n + 2\langle k\rangle > 1$, there exists a kernel $B_k(x, y)$ such that for every $f \in L^2(\mathbb{R}^n, \vartheta_{k,1})$,

$$\mathcal{F}_k f(x) = c_k^{-1}\int_{\mathbb{R}^n} f(y)B_k(x, y)\vartheta_{k,1}(y)dy, \quad x \in \mathbb{R}^n,$$

where, for $x = r\theta'$ and $y = t\theta''$, the kernel B_k is given by

$$B_k(x, y) = V_k\Big(\widetilde{J}_{\frac{n-3}{2}+\langle k\rangle}\big(\sqrt{2rt(1 + \langle\theta', \cdot\rangle)}\big)\Big)(\theta'').$$

Here V_k is the Dunkl intertwining operator (1) and $\widetilde{J}_\nu(z)$ is the normalized Bessel function. Above,

$$c_k := \Gamma(n + 2\langle k\rangle - 1)\int_{S^{n-1}}\prod_{\alpha\in\mathcal{R}}|\langle\alpha, \eta\rangle|^{k(\alpha)}d\sigma(\eta).$$

It is noteworthy mentioning that

$$\mathcal{F}_k \circ \|x\| = -\|x\|\Delta_k\mathcal{F}_k, \qquad \mathcal{F}_k \circ (-\|x\|\Delta_k) = -\|x\| \circ \mathcal{F}_k. \tag{4}$$

Recently, in [42] the authors defined a translation operator τ_x, for $x \in \mathbb{R}^n$, on the space $L^1 \cap L^\infty(\mathbb{R}^n, \vartheta_{k,1})$ by

$$\mathcal{F}_k(\tau_x f)(\xi) = B(x, \xi)\mathcal{F}_k(f)(\xi), \qquad \xi \in \mathbb{R}^n.$$

Here are some basic properties of the translation operator:

(i) $\tau_0 = \mathrm{Id}$;
(ii) $\tau_x f(y) = \tau_y f(x)$;
(iii) $\tau_x f_\lambda = (\tau_{\lambda x}f)_\lambda$, where $f_\lambda(x) = f(\lambda x)$ for $\lambda > 0$.

By means of the translation operator, a convolution $\circledast$ on the Schwartz space $\mathcal{S}(\mathbb{R}^n)$ was defined by

$$f \circledast g(x) = c_k^{-1} \int_{\mathbb{R}^n} f(y)\tau_x g(y)\vartheta_{k,1}(y)dy, \quad x \in \mathbb{R}^n.$$

In particular, $f \circledast g = g \circledast f$ and $\mathcal{F}_k(f \circledast g) = \mathcal{F}_k f \cdot \mathcal{F}_k g$ (see [42] for more details).

Next we turn our attention to the convolution of distributions (see [42,43]). Denote by $\mathcal{S}'(\mathbb{R}^n)$ the dual of the Schwartz space $\mathcal{S}(\mathbb{R}^n)$. If $T \in \mathcal{S}'(\mathbb{R}^n)$, then $\mathcal{F}_k(T)$ is defined by

$$\langle \mathcal{F}_k(T), \varphi \rangle := \langle T, \mathcal{F}_k(\varphi) \rangle, \qquad \forall \varphi \in \mathcal{S}(\mathbb{R}^n).$$

It is worth mentioning that $\mathcal{S}(\mathbb{R}^n)$ is stable by $\mathcal{F}_k$ (see [36]). The convolution $T \circledast f$ of $T \in \mathcal{S}'(\mathbb{R}^n)$ and $f \in \mathcal{S}(\mathbb{R}^n)$ is defined in [42] by

$$T \circledast f(x) = \langle T, \tau_x f \rangle.$$

In particular, a result analogous to the Euclidean convolution shows that $T \circledast f \in \mathcal{S}'(\mathbb{R}^n) \cap C^\infty(\mathbb{R}^n)$ and $\mathcal{F}_k(T \circledast f) = \mathcal{F}_k T \cdot \mathcal{F}_k f$.

3. The Deformed Wave Equation and Huygens' Principle

For $n + 2\langle k \rangle - 1 > 0$, where $\langle k \rangle = \frac{1}{2}\sum_{\alpha \in \mathcal{R}} k(\alpha)$, we consider the following Cauchy problem for the wave equation

$$\begin{gathered} 2\|x\|\Delta_k^x u_k(x,t) = \partial_{tt} u_k(x,t), \quad (x,t) \in \mathbb{R}^n \times \mathbb{R}, \\ u_k(x,0) = f(x), \;\; \partial_t u_k(x,0) = g(x), \end{gathered} \tag{5}$$

where the functions f and g belong to the space $\mathcal{D}(\mathbb{R}^n)$ of smooth functions with compact support. Here the superscript in Δ_k^x indicates the relevant variable, while the subscript t indicates differentiation in the t-variable. Next, we will prove the following statements:

($\mathcal{S}$) Let $u_k(x,t)$, $x \in \mathbb{R}^n$ and $t \in \mathbb{R}$, satisfy $2\|x\|\Delta_k^x u_k(x,t) - \partial_{tt} u_k(x,t) = 0$, then u_k does not satisfy Huygen's principle. In other words, the solution u_k is expressed as a sum of $\circledast$-convolution of f and g with distributions that are not supported entirely on the set $\{(x,t) \in \mathbb{R}^n \times \mathbb{R} : \|x\| = \frac{1}{2}t^2\}$.

For $t \in \mathbb{R}$, denote by $P_{k,t}$ the 2×2 matrix of tempered distributions on $\mathbb{R}^n$

$$P_{k,t} = \begin{pmatrix} P_{k,t}^{11} & P_{k,t}^{12} \\ P_{k,t}^{21} & P_{k,t}^{22} \end{pmatrix} := \begin{pmatrix} \mathcal{F}_k\big(\cos(t\sqrt{2\|\cdot\|})\big) & \mathcal{F}_k\big(\sin(t\sqrt{2\|\cdot\|})/\sqrt{2\|\cdot\|}\big) \\ \mathcal{F}_k\big(-\sqrt{2\|\cdot\|}\sin(t\sqrt{2\|\cdot\|})\big) & \mathcal{F}_k\big(\cos(t\sqrt{2\|\cdot\|})\big) \end{pmatrix}. \tag{6}$$

Set $U_k(x,0) := \begin{pmatrix} f(x) \\ g(x) \end{pmatrix}$, where the initial data $(f,g) \in \mathcal{D}(\mathbb{R}^n) \times \mathcal{D}(\mathbb{R}^n)$. Thus, we may define the vector column $U_k(x,t)$ by

$$\begin{aligned} U_k(x,t) &:= \big\{P_{k,t} \circledast U_k(\cdot,0)\big\}(x) \\ &= \left\{ \begin{pmatrix} P_{k,t}^{11} & P_{k,t}^{12} \\ P_{k,t}^{21} & P_{k,t}^{22} \end{pmatrix} \circledast \begin{pmatrix} f \\ g \end{pmatrix} \right\}(x). \end{aligned} \tag{7}$$

By applying the Fourier transform $\mathcal{F}_k$ to (7), in the x-variable, we get

$$\mathcal{F}_k(U_k(\cdot,t))(\xi) = e^{t\mathbb{A}}\mathcal{F}_k(U_k(\cdot,0))(\xi), \tag{8}$$

where

$$\mathbb{A} := \begin{pmatrix} 0 & 1 \\ -2\|\xi\| & 0 \end{pmatrix}. \tag{9}$$

Above we have used the fact that $\mathcal{F}_k^{-1} = \mathcal{F}_k$ (see (3)). That is $\mathcal{F}_k(U_k(\cdot,t))(\xi)$ is a solution to the following ordinary differential equation

$$\partial_t \mathcal{F}_k(U_k(\cdot,t))(\xi) = \mathbb{A}\mathcal{F}_k(U_k(\cdot,t))(\xi) = \begin{pmatrix} 0 & 1 \\ -2\|\xi\| & 0 \end{pmatrix} \mathcal{F}_k(U_k(\cdot,t))(\xi). \tag{10}$$

Now, recall from (4) that $-\|\xi\|\mathcal{F}_k(f)(\xi) = \mathcal{F}_k(\|x\|\Delta_k f)(\xi)$, and using the injectivity of the Fourier transform $\mathcal{F}_k$, we deduce that

$$\partial_t U_k(x,t) = \begin{pmatrix} 0 & 1 \\ 2\|x\|\Delta_k & 0 \end{pmatrix} U_k(x,t). \tag{11}$$

Hence, if we write $U_k(x,t) = \begin{pmatrix} u_k(x,t) \\ v_k(x,t) \end{pmatrix}$, then $u_k(x,t)$ satisfies the following equation

$$\partial_{tt} u_k(x,t) = 2\|x\|\Delta_k u_k(x,t).$$

Moreover, since $f, g \in \mathcal{D}(\mathbb{R}^n)$, it follows from (7) and the properties of the $\circledast$-convolution that $u_k(\cdot,t) \in C^\infty(\mathbb{R}^n)$ for all $t \in \mathbb{R}$.

Furthermore, $u_k(x,t) \to f(x)$ as $t \to 0$. Indeed, if δ denotes the Dirac functional, then, as $t \to 0$, $\mathcal{F}_k(\cos(t\sqrt{2\|\cdot\|})) \to \delta$ in $\mathcal{S}'(\mathbb{R}^n)$ and thus in $\mathcal{D}'(\mathbb{R}^n)$. On the other hand $\mathcal{F}_k(\sin(t\sqrt{2\|\cdot\|})/\sqrt{2\|\cdot\|}) \to 0$ as $t \to 0$. Using the continuity of the convolution $\circledast$, we deduce that

$$u_k(x,t) \to (\delta \circledast f)(x) = f(x) \qquad \text{as} \quad t \to 0.$$

Similarly, one can prove that $(\partial_t u_k)(x,t) \to g(x)$ as $t \to 0$.

We mention that the solution u_k constructed above is unique. To prove this claim, we need the lemma below. Let

$$\mathcal{E}_k[u_k](t) = \int_{\mathbb{R}^n} \left\{ |\partial_t \mathcal{F}_k(u_k(\cdot,t))(\xi)|^2 + 2\|\xi\||\mathcal{F}_k(u_k(\cdot,t))(\xi)|^2 \right\} \vartheta_{k,1}(\xi) d\xi. \tag{12}$$

Lemma 1. *Assume that $n + 2\langle k \rangle - 1 > 0$ and that the initial data $f, g \in \mathcal{D}(\mathbb{R}^N)$. Then the total energy $\mathcal{E}_k[u_k]$ is independent of t.*

Proof. Since

$$\mathcal{F}_k(u_k(\cdot,t))(\xi) = \cos(t\sqrt{2\|\xi\|})\mathcal{F}_k f(\xi) + \frac{\sin(t\sqrt{2\|\xi\|})}{\sqrt{2\|\xi\|}} \mathcal{F}_k g(\xi), \qquad \text{for all } \ t \in \mathbb{R},$$

we deduce that

$$\begin{aligned} |\mathcal{F}_k(u_k(\cdot,t))(\xi)|^2 &= \cos^2(t\sqrt{2\|\xi\|})|\mathcal{F}_k f(\xi)|^2 + \frac{\sin^2(t\sqrt{2\|\xi\|})}{2\|\xi\|}|\mathcal{F}_k g(\xi)|^2 \\ &\quad + \sqrt{2}\frac{\cos(t\sqrt{\|\xi\|})\sin(t\sqrt{\|\xi\|})}{\sqrt{\|\xi\|}} \mathrm{Re}\left(\mathcal{F}_k f(\xi)\overline{\mathcal{F}_k g(\xi)}\right), \end{aligned}$$

and

$$\begin{aligned} |\partial_t \mathcal{F}_k(u_k(\cdot,t))(\xi)|^2 &= \cos^2(t\sqrt{2\|\xi\|})|\mathcal{F}_k g(\xi)|^2 + 2\|\xi\|\sin^2(t\sqrt{2\|\xi\|})|\mathcal{F}_k f(\xi)|^2 \\ &\quad - 2\sqrt{2\|\xi\|}\cos(t\sqrt{2\|\xi\|})\sin(t\sqrt{2\|\xi\|})\mathrm{Re}\left(\mathcal{F}_k f(\xi)\overline{\mathcal{F}_k g(\xi)}\right). \end{aligned}$$

Thus we have

$$\mathcal{E}_k[u_k](t) = \int_{\mathbb{R}^n} \left\{ 2\|\xi\| |\mathcal{F}_k f(\xi)|^2 + |\mathcal{F}_k g(\xi)|^2 \right\} \vartheta_{k,1}(\xi) d\xi. \tag{13}$$

Hence, we established the lemma. □

Now let us go back to the uniqueness of the solution u_k. Assume that $u_k^{(1)}$ and $u_k^{(2)}$ are two solutions of the wave equation with the same initial data, then $u_k^{(1)} - u_k^{(2)}$ is a solution of the wave equation with zero initial data. Therefore, by (13), we have $\mathcal{E}_k[u_k^{(1)} - u_k^{(2)}](t) = 0$. Hence, (12) implies $\partial_t \mathcal{F}_k((u_k^{(1)} - u_k^{(2)})(\cdot, t))(\xi) = 0$ for every $t \in \mathbb{R}$. That is, the function $t \mapsto \mathcal{F}_k((u_k^{(1)} - u_k^{(2)})(\cdot, t))(\xi)$ is a constant, which implies $\mathcal{F}_k((u_k^{(1)} - u_k^{(2)})(\cdot, t))(\xi) = \mathcal{F}_k((u_k^{(1)} - u_k^{(2)})(\cdot, 0))(\xi) = 0$. Using the injectivity of the Fourier transform $\mathcal{F}_k$, we deduce that $(u_k^{(1)} - u_k^{(2)})(x, t) = 0$ for all $x \in \mathbb{R}^n$ and $t > 0$. This proves that the solutions of the wave equation are uniquely determined by the initial Cauchy data.

The following theorem collects all the above facts and discussions.

Theorem 1. *The solution to the Cauchy problem* (5) *is given uniquely by*

$$u_k(x, t) = (P_{k,t}^{11} \circledast f)(x) + (P_{k,t}^{12} \circledast g)(x),$$

where, for a fixed t, $P_{k,t}^{11}$ *and* $P_{k,t}^{12}$ *are the tempered distributions on* $\mathbb{R}^n$ *given by*

$$P_{k,t}^{11} = \mathcal{F}_k\big(\cos(t\sqrt{2\|\cdot\|})\big), \qquad P_{k,t}^{12} = \mathcal{F}_k\big(\sin(t\sqrt{2\|\cdot\|})/\sqrt{2\|\cdot\|}\big).$$

The distributions $P_{k,t}^{ij}$ *will be called the propagators.*

We shall now prove the statement ($\mathcal{S}$). To do so, we will assume that the propagators $P_{k,t}^{11}$ and $P_{k,t}^{12}$ are supported entirely on the set $\mathcal{C} = \{(x, t) \in \mathbb{R}^n \times \mathbb{R} : \|x\| = \frac{1}{2}t^2\}$ and we will show that this assumption cannot hold. Our approach uses the representation theory of the Lie algebra $\mathfrak{sl}(2, \mathbb{R})$, following [43,44].

Assume that the propagators $P_{k,t}^{11}$ and $P_{k,t}^{12}$ are supported entirely on the set $\mathcal{C} = \{(x, t) \in \mathbb{R}^n \times \mathbb{R} : \|x\| = \frac{1}{2}t^2\}$.

We start by investigating certain properties of the wave equation, which are reflected in properties of the propagators. To see this, we define the 2×2 matrix $P_k = \begin{pmatrix} P_k^{11} & P_k^{12} \\ P_k^{21} & P_k^{22} \end{pmatrix}$ of entrywise distributions on $\mathbb{R}^{n+1}$, where

$$P_k^{ij}(\psi_1 \otimes \psi_2) := \int_{\mathbb{R}} P_{k,t}^{ij}(\psi_1)\psi_2(t) dt, \qquad i, j = 1, 2,$$

for $\psi_1 \in \mathcal{S}(\mathbb{R}^n)$ and $\psi_2 \in \mathcal{S}(\mathbb{R})$. Here we used the fact that $\mathcal{S}(\mathbb{R}^{n+1}) \simeq \mathcal{S}(\mathbb{R}^n)\hat{\otimes}\mathcal{S}(\mathbb{R})$ is the unique topological tensor product of $\mathcal{S}(\mathbb{R}^n)$ and $\mathcal{S}(\mathbb{R})$ as nuclear spaces. From the constructive proof of Theorem 1, it follows that

$$2\|x\| \Delta_k P_k^{ij} = \partial_{tt} P_k^{ij}, \qquad i, j = 1, 2.$$

Next, we will investigate the dilations of the propagators under a dilation operator. This will inform us on the degree of the "homogeneity" of the distributions P_k^{ij}, with $i, j = 1, 2$. For $\lambda > 0$ and a function ψ on $\mathbb{R}^{n+1}$, let

$$S_\lambda^x \psi(x, t) := \psi(\lambda^2 x, t), \qquad S_\lambda^t \psi(x, t) := \psi(x, \lambda t),$$

where the superscript denotes the relevant variable. Set $S_\lambda := S_\lambda^x \circ S_\lambda^t$. By duality, the operators S_λ^x, S_λ^t, and S_λ act on distributions in the standard way.

We begin by looking to the properties of $P_{k,t}^{ij}$ under the dilation S_λ. Observe that if $u_k(x,t)$ is a solution to (5) with initial data $(f(x), g(x))$, then $S_\lambda u_k(x,t)$ solves the wave equation with initial data $(S_\lambda^x f(x), \lambda S_\lambda^x g(x))$. Thus

$$S_\lambda U_k(x,t) = P_{k,t} \circledast \begin{bmatrix} S_\lambda^x f \\ \lambda S_\lambda^x g \end{bmatrix}. \tag{14}$$

On the other hand

$$\begin{aligned} S_\lambda U_k(x,t) = \begin{bmatrix} S_\lambda u_k(x,t) \\ \partial_t\{S_\lambda u_k(x,t)\} \end{bmatrix} &= \begin{bmatrix} u_k(\lambda^2 x, \lambda t) \\ \lambda\{\partial_t u_k\}(\lambda^2 x, \lambda t) \end{bmatrix} \\ &= \begin{bmatrix} u_k \\ \lambda \partial_t u_k \end{bmatrix}(\lambda^2 x, \lambda t) \\ &= \begin{bmatrix} 1 & 0 \\ 0 & \lambda \end{bmatrix} \begin{bmatrix} u_k \\ \partial_t u_k \end{bmatrix}(\lambda^2 x, \lambda t) \\ &= \begin{bmatrix} 1 & 0 \\ 0 & \lambda \end{bmatrix} \Big\{ P_{k,\lambda t} \circledast \begin{bmatrix} f \\ g \end{bmatrix} \Big\}(\lambda^2 x) \\ &= \begin{bmatrix} 1 & 0 \\ 0 & \lambda \end{bmatrix} S_\lambda^x \Big\{ P_{k,\lambda t} \circledast \begin{bmatrix} f \\ g \end{bmatrix} \Big\}(x). \end{aligned}$$

Using the fact that S_λ^x preserves the convolution of a distribution with a function, a fact that can be easily checked using the properties of the translation operator, we get

$$\begin{aligned} S_\lambda U_k(x,t) &= \begin{bmatrix} 1 & 0 \\ 0 & \lambda \end{bmatrix} \Big\{ S_\lambda^x P_{k,\lambda t} \circledast \begin{bmatrix} S_\lambda^x f \\ S_\lambda^x g \end{bmatrix} \Big\}(x) \\ &= \begin{bmatrix} 1 & 0 \\ 0 & \lambda \end{bmatrix} \Big\{ S_\lambda^x P_{k,\lambda t} \circledast \begin{bmatrix} 1 & 0 \\ 0 & \lambda^{-1} \end{bmatrix} \begin{bmatrix} S_\lambda^x f \\ \lambda S_\lambda^x g \end{bmatrix} \Big\}(x). \end{aligned} \tag{15}$$

Comparing (14) with (15) gives $S_\lambda^x P_{k,\lambda t}^{ij} = \lambda^{j-i} P_{k,t}^{ij}$, for $i, j = 1, 2$. Now we can obtain the dilation properties of P_k^{ij} as follows: For $\psi_1 \in \mathcal{S}(\mathbb{R}^n)$ and $\psi_2 \in \mathcal{S}(\mathbb{R})$, we have

$$\begin{aligned} S_\lambda(P_k^{ij})(\psi_1 \otimes \psi_2) &= P_k^{ij}(S_{\lambda^{-1}}^x(\psi_1) \otimes S_{\lambda^{-1}}^t(\psi_2)) \\ &= \int_{\mathbb{R}} P_{k,t}^{ij}(S_{\lambda^{-1}}^x(\psi_1)) S_{\lambda^{-1}}^t(\psi_2)(t)dt \\ &= \lambda \int_{\mathbb{R}} P_{k,\lambda t}^{ij}(S_{\lambda^{-1}}^x(\psi_1))\psi_2(t)dt \\ &= \lambda \int_{\mathbb{R}} S_\lambda^x(P_{k,\lambda t}^{ij}(\psi_1))\psi_2(t)dt \\ &= \lambda^{1+j-i} \int_{\mathbb{R}} P_{k,t}^{ij}(\psi_1)\psi_2(t)dt \\ &= \lambda^{1+j-i} P_k^{ij}(\psi_1 \otimes \psi_2). \end{aligned}$$

We summarize the above computations.

Proposition 1. *For $n + 2\langle k \rangle - 1 > 0$, we have*

(1) *The distribution P_k^{ij} satisfies the deformed wave equation, i.e.,*

$$(\|x\|\Delta_k - \frac{1}{2}\partial_{tt})P_k^{ij} = 0, \qquad i, j = 1, 2. \tag{16}$$

(2) *For* $\lambda > 0$,

$$S_\lambda P_k^{ij} = \lambda^{1+j-i} P_k^{ij}, \qquad i,j = 1,2.$$

Next we shall describe the structure of a representation of the Lie algebra $\mathfrak{sl}(2,\mathbb{R})$ on $\mathcal{S}(\mathbb{R}^{n+1})$. This structure, together with Proposition 1, will allow us to prove that the Assumption 3 does not hold true.

We take a basis for the Lie algebra $\mathfrak{sl}(2,\mathbb{R})$ as

$$\mathbf{e} := \begin{pmatrix} 0 & 1 \\ 0 & 0 \end{pmatrix}, \qquad \mathbf{f} := \begin{pmatrix} 0 & 0 \\ 1 & 0 \end{pmatrix}, \qquad \mathbf{h} := \begin{pmatrix} 1 & 0 \\ 0 & -1 \end{pmatrix}.$$

The triple $\{\mathbf{e}, \mathbf{f}, \mathbf{h}\}$ satisfies the commutation relations

$$[\mathbf{e}, \mathbf{f}] = \mathbf{h}, \qquad [\mathbf{h}, \mathbf{e}] = 2\mathbf{e}, \qquad [\mathbf{h}, \mathbf{f}] = -2\mathbf{f},$$

where $[A, B] := AB - BA$.

Choose $x_1, x_2, \ldots, x_n$ as the usual system of coordinates on $\mathbb{R}^n$. Let

$$\mathbb{E}_{n,1} := i(\|x\| - \frac{1}{2}t^2), \quad \mathbb{F}_{n,1} := i(\|x\|\Delta_k - \frac{1}{2}\partial_{tt}), \quad \mathbb{H}_{n,1} := n + 2\langle k\rangle - \frac{1}{2} + 2\sum_{\ell=1}^{n} x_\ell \partial_\ell + t\partial_t.$$

Using ([14] Theorem 3.2), the following commutation relations hold

$$[\mathbb{E}_{n,1}, \mathbb{F}_{n,1}] = \mathbb{H}_{n,1}, \quad [\mathbb{H}_{N,1}, \mathbb{E}_{N,1}] = 2\mathbb{E}_{N,1}, \quad [\mathbb{H}_{n,1}, \mathbb{F}_{n,1}] = -2\mathbb{F}_{n,1}. \tag{17}$$

These are the commutation relations of a standard basis of the Lie algebra $\mathfrak{sl}(2,\mathbb{R})$. Equation (17) gives rise to a representation ω_k of the Lie algebra $\mathfrak{sl}(2,\mathbb{R})$ on the Schwartz space $\mathcal{S}(\mathbb{R}^{n+1})$ by setting

$$\omega_k(\mathbf{h}) = \mathbb{H}_{n,1}, \qquad \omega_k(\mathbf{e}) = \mathbb{E}_{n,1}, \qquad \omega_{k,a}(\mathbf{f}) = \mathbb{F}_{n,1}. \tag{18}$$

An analogue of the representation ω_k has been intensively studied in [14].

Recall that the Huygens' principle is equivalent to the fact that the propagators P_k^{11} and P_k^{12} are supported on the set $\mathcal{C} = \{(x,t) \in \mathbb{R}^n \times \mathbb{R} \mid \|x\| - \frac{1}{2}t^2 = 0\}$. Since $\mathcal{C}$ is the locus of zeros of $\|x\| - \frac{1}{2}t^2$, then, P_k^{ij} is supported on $\mathcal{C}$ if and only if

$$\mathbb{E}_{n,1}^m \cdot P_k^{ij} = 0 \tag{19}$$

for some positive integer m (see, for instance, ([44] p. 173)). In the light of Proposition 1(1) together with the dilatation property of P_k^{ij}, which implies that P_k^{ij} is an eigen-distribution for $\mathbb{H}_{n,1}$, Equation (19) amounts to saying the distribution P_k^{ij} generates a finite-dimensional representation ω_k^* for $\mathfrak{sl}(2,\mathbb{R})$ on $\mathcal{S}'(\mathbb{R}^{n+1})$. Thus, the qualitative part of Huygens' principle holds.

Theorem 2. *Huygens' principle holds if and only if* P_k^{ij} *is supported on the set* $\mathcal{C}$*, if and only if* P_k^{ij} *generates a finite-dimensional representation* ω_k^* *for* $\mathfrak{sl}(2,\mathbb{R})$ *on* $\mathcal{S}'(\mathbb{R}^{n+1})$.

Theorem 3. *Huygens' principle cannot hold when*

$$n - 1 + 2\langle k\rangle \notin \mathbb{Z}.$$

Proof. In ([14] Theorem 3.21) the authors proved that the spectrum of the element $\mathbf{k} := i(\mathbf{f} - \mathbf{e})$ acting on $\mathcal{S}'(\mathbb{R}^{n+1})$ via the dual representation ω_k^* is $n - 1 + 2\langle k\rangle + 2\mathbb{Z}$, whereas, it is well known, the spectrum of $\mathbf{k}$ in finite-dimensional representations of $\mathfrak{sl}(2,\mathbb{R})$ is contained in $\mathbb{Z}$. □

The above theorem leaves the possibility that the wave equation may satisfy Huygens' principle when $n-1+2\langle k\rangle \in \mathbb{Z}$.

Now, using Proposition 1(2), we get

$$\Big\{2\sum_{\ell=1}^{n} x_\ell\partial_\ell + t\partial_t\Big\}P_k^{ij} = (1+j-i)P_k^{ij}.$$

Therefore

$$\mathbb{H}_{n,1}P_k^{ij} = -\left(n+2\langle k\rangle - \frac{1}{2} + i - j - 1\right)P_k^{ij}, \qquad i,j = 1,2.$$

That is P_k^{ij} is an eigendistributation for $\mathbb{H}_{n,1}$ with eigenvalue $-(n+2\langle k\rangle - \frac{1}{2} + i - j - 1)$. Keeping in mind the fact that $\mathbb{F}_{n,1}\cdot P_k^{ij} = 0$, and in the light of Theorem 3, clearly each distribution P_k^{ij} cannot generate a finite-dimensional ω_k^* for $\mathfrak{sl}(2,\mathbb{R})$ on $\mathcal{S}'(\mathbb{R}^{n+1})$; otherwise $n+2\langle k\rangle - \frac{1}{2} + i - j - 1 \in \mathbb{Z}$ which is impossible in view of Theorem 3. That is our Assumption 3 does not hold true.

Theorem 4. *The solution $u_k(x,t)$ to the Cauchy problem (5) does not satisfy the Huygens' principle.*

Author Contributions: Investigation, S.a.-B., M.a.-K., A.a.-M., F.a.-S.; methodology, S.B.S.; supervision, S.B.S.; writing–original draft preparation, S.B.S.; writing–review and editing, S.B.S. All authors have read and agreed to the published version of the manuscript.

Funding: This research was funded by United Arab Emirates University (UAEU), SURE Plus 2019 grant # G00003109.

Acknowledgments: The authors would like to thankfully acknowledge the financial support awarded by UAEU through the SURE Plus 2019 grant # G00003109. We thank the referees for their valuable comments.

Conflicts of Interest: The authors declare no conflict of interest.

References

1. Hadamard, J. *Lectures on Cauchy's Problem in Linear Partial Differential Equations*; Dover Publications: New York, NY, USA, 1923.
2. Ben Saïd, S. Huygens' principle for the wave equation associated with the trigonometric Dunkl-Cherednik operators. *Math. Res. Lett.* **2006**, *13*, 43–58. [CrossRef]
3. Berest, Y.; Veselov, A.P. Huygens' principle and integrability. *Russ. Math. Surv.* **1994**, *49*, 5–77. [CrossRef]
4. Branson, T.; Ólafsson, G.; Schlichtkrull, H. Huygens' Principle in Riemannian Symmetric Spaces. *Math. Ann.* **1995**, *301*, 445-462. [CrossRef]
5. Courant, R.; Hilbert, D. *Methods of Mathematical Physics*; Interscience Publ.: New York, NY, USA, 1962; Volume II.
6. Chalykh, O.A.; Feigin, M.V.; Veselov, A.P. New integrable generalizations Calogero-Moser Quantumproblem. *J. Math. Phys.* **1998**, *39*, 695–703. [CrossRef]
7. Günther, P. *Huygens' Principle and Hyperbolic equations*; Academic Press: Boston, MA, USA, 1988.
8. Lagnese, J.E.; Stellmacher, K.L. A method of generating classes of Huygens's operators. *J. Math. Mech.* **1967**, *17*, 461–472.
9. Lax, P.D.; Phillips, R.S. *Scattering Theory;* Academic Press: New York, NY, USA; London, UK, 1967.
10. McLenaghan, R.G. Huygens' principle. *Ann. Inst. Henri Poincaré* **1982**, *37*, 211–236.
11. Ørsted, B. The conformal invariance of Huygens' principle. *J. Diff. Geom.* **1981**, *16*, 1–9. [CrossRef]
12. Stellmacher, K. Ein Beispiel einer Huygensschen Differentialgleichung. *Nachr. Akad. Wiss. Göttingen Math.* **1953**, *10*, 133–138.
13. Schimming, R. A review on Huygens' principle for linear hyperbolic differential operators. In Proceedings of the International Symposium Group-Theoretical Methods in Mechanics, Novosibirsk, Russia, 25–29 August 1978;
14. Ben Saïd, S.; Kobayashi, T.; Ørsted, B. Laguerre semigroup and Dunkl operators. *Compos. Math.* **2012**, *148*, 1265–1336. [CrossRef]

15. de Bie, H.; Genest, V.; Vinet, L. Dirac-Dunkl equation on S2 and the Bannai-Ito algebra. *Comm. Math. Phys.* **2016**, *344*, 447–464. [CrossRef]
16. Pascazio, S.; Pepe, F.V.; Pérez-Pardo, J.M. Huygens' principle and Dirac-Weyl equation. *Eur. Phys. J. Plus* **2017**, *132*, 287. [CrossRef]
17. Dunkl, C.F. Differential-difference operators associated to reflection groups. *Trans. Am. Math. Soc.* **1989**, *311*, 167–183. [CrossRef]
18. Rösler, M. Positivity of Dunkl's intertwining operator. *Duke Math. J.* **1999**, *98*, 445–463. [CrossRef]
19. Dunkl, C.F.; Xu, Y. *Orthogonal Polynomials of Several Variables*; Cambridge Univ. Press: Cambridge, UK, 2001.
20. Amri, B.; Gaidi, M. $L^p - L^q$ estimates for the solution of the Dunkl wave equation. *Manuscripta Math.* **2019**, *159*, 379–396. [CrossRef]
21. Dai, F.; Ye, W. Almost everywhere convergence of Bochner-Riesz means with critical index for Dunkl transforms. *J. Approx. Theory* **2016**, *205*, 43–59. [CrossRef]
22. Deleaval, L. On the boundedness of the Dunkl spherical maximal operator. *J. Topol. Anal.* **2016**, *8*, 475–495. [CrossRef]
23. Gorbachev, D.V.; Ivanov, V.I.; Tikhonov, S.Y. Positive L^p-bounded Dunkl-type generalized translation operator and its applications. *Constr. Approx.* **2019**, *49*, 555–605. [CrossRef]
24. De Jeu, M. The Dunkl transform. *Invent. Math.* **1993**, *113*, 147–162. [CrossRef]
25. Mejjaoli, H. Dunkl-Schrödinger semigroups and applications. *Appl. Anal.* **2013**, *92*, 1597–1626. [CrossRef]
26. Mejjaoli, H.; Trimèche, K. On a mean value property associated with the Dunkl Laplacian operator and applications. *Integral Transform. Spec. Funct.* **2001**, *12*, 279–302. [CrossRef]
27. Mejjaoli, H. Nonlinear generalized Dunkl-wave equations and applications. *J. Math. Anal. Appl.* **2011**, *375*, 118–138. [CrossRef]
28. Mejjaoli, H. Strichartz estimates for the Dunkl wave equation and application. *J. Math. Anal. Appl.* **2008**, *346*, 41–54. [CrossRef]
29. Thangavelu, S.; Xu, Y. Convolution operator and maximal function for the Dunkl transform. *J. Anal. Math.* **2005**, *97*, 25–55. [CrossRef]
30. Trimèche, K. Paley-Wiener theorems for the Dunkl transform and Dunkl translation operators. *Integral Transform. Spec. Funct.* **2002**, *13*, 17–38. [CrossRef]
31. Trimèche, K. Harmonic analysis on measures spaces attached to some Dunkl operators on $\mathbb{R}^d$ and applications. *J. Inequal. Spec. Funct.* **2017**, *8*, 104–117.
32. Gallardo, L.; Rejeb, C. A new mean value property for harmonic functions relative to the Dunkl Laplacian operator and applications. *Trans. Am. Math. Soc.* **2015**, *368*, 3727–3753. [CrossRef]
33. Kobayashi, T.; Mano, G. The inversion formula and holomorphic extension of the minimal representation of the conformal group. In *Harmonic Analysis, Group Representations, Automorphic Forms and Invariant Theory: In Honor of Roger Howe*; Li, J.S., Tan, E.C., Wallach, N., Zhu, C.B., Eds.; World Scientific: Singapore, 2007; pp. 159–223.
34. Dunkl, C.F. Hankel transforms associated to finite reflection groups. *Contemp. Math.* **1992**, *138*, 123–138.
35. Mejjaoli, H. Wavelet-multipliers analysis in the framework of the k-Laguerre theory. *Linear Multilinear Algebra* **2019**, *67*, 70–93. [CrossRef]
36. Johansen, T.R. Weighted inequalities and uncertainty principles for the (k,a)-generalized Fourier transform. *Internat. J. Math.* **2016**, *27*, 44. [CrossRef]
37. Ben Saïd, S. Strichartz estimates for Schrödinger-Laguerre operators. *Semigroup Forum* **2015**, *90*, 251–269. [CrossRef]
38. Ben Saïd, S.; Kobayashi, T.; Ørsted, B. Generalized Fourier transforms $\mathcal{F}_{k,a}$. *C. R. Math. Acad. Sci. Paris* **2009**, *347*, 1119–1124. [CrossRef]
39. de Bie, H.; Oste, R.; van der Jeugt, J. Generalized Fourier transforms arising from the enveloping algebras of (2) and $\mathfrak{osp}(1|2)$. *Int. Math. Res. Not. IMRN* **2016**, *15*, 4649–4705. [CrossRef]
40. de Bie, H.; Ørsted, B.; Somberg, P.; Soucek, V. Dunkl operators and a family of realizations of $\mathfrak{osp}(1|2)$. *Trans. Am. Math. Soc.* **2012**, *364*, 3875–3902. [CrossRef]
41. de Bie, H.; Pan, L.; Constales, D. Explicit formulas for the Dunkl dihedral kernel and the (k,a)-generalized Fourier kernel. *J. Math. Anal. Appl.* **2018**, *460*, 900–926.
42. Ben Saïd, S.; Deleaval, L. Translation operator and maximal operator for the $(k,1)$-generalized Fourier transform. *J. Geom. Anal.* **2019**, in press. [CrossRef]

43. Ben Saïd, S.; Ørsted, B. The wave equation for Dunkl operators. *Indag. Math. (N.S.)* **2005**, *16*, 351–391. [CrossRef]
44. Howe, R.; Tan, E.C. *Nonabelian Harmonic Analysis. Applications of* SL(2, $\mathbb{R}$); Universitext; Springer: New York, NY, USA, 1992.

© 2019 by the authors. Licensee MDPI, Basel, Switzerland. This article is an open access article distributed under the terms and conditions of the Creative Commons Attribution (CC BY) license (http://creativecommons.org/licenses/by/4.0/).

mathematics

MDPI

Article

On the Gibbs Effect Based on the Quasi-Affine Dual Tight Framelets System Generated Using the Mixed Oblique Extension Principle

Mutaz Mohammad

Department of Mathematics and Statistics, College of Natural and Health Sciences, Zayed University, 144543 Abu Dhabi, UAE; Mutaz.Mohammad@zu.ac.ae; Tel.: +971-2-599-3496

Received: 14 September 2019; Accepted: 2 October 2019; Published: 12 October 2019

Abstract: Gibbs effect represents the non-uniform convergence of the nth Fourier partial sums in approximating functions in the neighborhood of their non-removable discontinuities (jump discontinuities). The overshoots and undershoots cannot be removed by adding more terms in the series. This effect has been studied in the literature for wavelet and framelet expansions. Dual tight framelets have been proven useful in signal processing and many other applications where translation invariance, or the resulting redundancy, is very important. In this paper, we will study this effect using the dual tight framelets system. This system is generated by the mixed oblique extension principle. We investigate the existence of the Gibbs effect in the truncated expansion of a given function by using some dual tight framelets representation. We also give some examples to illustrate the results.

Keywords: Gibbs phenomenon; quasi-affine; shift-invariant system; dual tight framelets; oblique extension principle; B-splines

1. Introduction

The Gibbs effect was first recognized over a century ago by Henry Wilbraham in 1848 (see Ref. [1]). However, in 1898 Albert Michelson and Samuel Stratton (see Ref. [2]) observed it via a mechanical machine that they used to calculate the Fourier partial sums of a square wave function. Soon after, Gibbs explained this effect in two publications [3,4]. In his first short paper, Gibbs failed to notice the phenomenon and the limits of the graphs of the Fourier partial sums was inaccurate. In the second paper, he published a correction and gave the description of overshoot at the point of jump discontinuity. In fact, Gibbs did not provide a proof for his argument but only in 1906 a detailed mathematical description of the effect was introduced and named after Gibbs phenomenon by Maxime (see Ref. [5]) as he believed Gibbs to be the first person noticing it. This phenomenon has been studied extensively in Fourier series and many other situations such as the classical orthogonal expansions (see Refs. [6–8]), spline expansion (see Refs. [9,10]), wavelets and framelets series (see Refs. [11–17]), sampling approximations (see Ref. [18]), and many other theoretical investigations (see Refs. [19–23]). By considering Fourier series, it is impossible to recover accurate point values of a periodic function with many finitely jump discontinuities from its Fourier coefficients. Wavelets and their generalizations (framelets) have great success in coefficients recovering and have many applications in signal processing and numerical approximations (see Refs. [24–27]). However, many of these applications are represented by smooth functions that have jump discontinuities. However, expanding these functions will create (most often) unpleasant ringing effect near the gaps. It is the aim of this article to analyze the Gibbs effect of dual tight framelets using a different/higher order of vanishing moments.

Let us recall the preliminary background by introducing some notations (e.g., see Refs. [28–30]). Let $L_2(\mathbb{R})$ denote the space of all square integrable functions over the space $\mathbb{R}$, where

$$L_2(\mathbb{R}) = \left\{ f : \mathbb{R} \to \mathbb{R}; \int_{\mathbb{R}} |f|^2 < \infty \right\}.$$

Definition 1 ([31]). *Let $\psi \in L_2(\mathbb{R})$. For $j, k \in \mathbb{Z}$, define the function $\psi_{j,k}$ by*

$$\psi_{j,k} = 2^{j/2}\psi(2^j \cdot -k).$$

Then, we say the function ψ is a wavelet if the set $\left\{\psi_{j,k}\right\}_{j,k\in\mathbb{Z}}$ forms an orthonormal basis for $L_2(\mathbb{R})$.

Every square integrable function $f \in L_2(\mathbb{R})$ has a wavelet representation and this requires an orthonormal basis. However, the existence of such complete orthonormal basis is in general hard to construct and their representation is too restrictive and rigid. Therefore, frames were defined by the idea of an additional lower bound of the Bessel sequence which does not constitute an orthonormal set and are not linearly independent. In this paper, we will use dual tight framelets constructed by the mixed oblique extension principle (MOEP) (see Ref. [32]) which enables us to construct dual tight framelets for $L_2(\mathbb{R})$ of the form $\{\psi^\ell_{j,k}, \tilde{\psi}^\ell_{j,k}, \ell = 1, \cdots, r\}_{j,k}$. The MOEP provides an important method to construct dual framelets from refinable functions and gives us a better number of vanishing moments for ψ_ℓ and therefore a better imation orders. In fact, using the unitary extension principle UEP (see Ref. [32]), it is known that the approximation order of the system will not exceed 2, whereas the MOEP will give us a better approximation (see Ref. [33]). Please note that the MOEP is a generalization of the UEP and the oblique extension principle OEP. extension principle OEP (see Ref. [34]), which is again given to ensure that the system

$$\{\psi^\ell_{j,k}, \tilde{\psi}^\ell_{j,k}, \ell = 1, \cdots, r\}_{j,k\in\mathbb{Z}},$$

forms a dual tight framelets for $L_2(\mathbb{R})$. We refer the reader to Ref. [34] for the general setup of the MOEP.

Definition 2 ([31]). *A sequence $\Psi = \{\psi^\ell_{j,k}, \ell = 1, \cdots, r\}_{j,k}$ of elements in $L_2(\mathbb{R})$ is a framelet for $L_2(\mathbb{R})$ if there exists constants $A, B > 0$ such that*

$$A\|f\|^2 \leq \sum_{\ell=1}^{r}\sum_{j,k}^{\infty} |\langle f, \psi^\ell_{j,k}\rangle|^2 \leq B\|f\|^2, \forall f \in L_2(\mathbb{R}). \tag{1}$$

The numbers A, B are called frame bounds. If we can choose $A = B = 1$, then Ψ is called a tight framelet for $L_2(\mathbb{R})$.

Please note that we obtain a family of functions $\tilde{\Psi} = \{\tilde{\psi}^\ell_{j,k}, \ell = 1, \cdots, r\}_{j,k}$ such that

$$B^{-1}\|f\|^2 \leq \sum_{\ell=1}^{r}\sum_{j,k} |\langle f, \tilde{\psi}^\ell_{j,k}\rangle|^2 \leq A^{-1}\|f\|^2, \forall f \in L_2(\mathbb{R}). \tag{2}$$

The family $\tilde{\Psi}$ is called dual (reciprocal) framelet of the framelet Ψ. Equations (1) and (2) implies, respectively, the following equation

$$\langle f, g\rangle = \sum_{\ell=1}^{r}\sum_{j,k} \langle f, \tilde{\psi}^\ell_{j,k}\rangle\langle \psi^\ell_{j,k}, g\rangle \tag{3}$$

It follows directly from Equation (3) that any function $f \in L_2(\mathbb{R})$ has the following framelet representation

$$f = \sum_{\ell=1}^{r} \sum_{j\in\mathbb{Z}} \sum_{k\in\mathbb{Z}} \langle f, \tilde{\psi}_{j,k}^{\ell} \rangle \psi_{j,k}^{\ell} = \sum_{\ell=1}^{r} \sum_{j\in\mathbb{Z}} \sum_{k\in\mathbb{Z}} \langle f, \psi_{j,k}^{\ell} \rangle \tilde{\psi}_{j,k}^{\ell}. \tag{4}$$

The framelet constructions of Ψ and $\tilde{\Psi}$ require mother wavelets, called refinable functions ϕ and $\tilde{\phi}$, where a compactly supported function $\phi \in L_2(\mathbb{R})$ is said to be refinable if

$$\phi(x) = 2 \sum_{k\in\mathbb{Z}} h_0[k]\, \phi(2x-k), \tag{5}$$

for some finite supported sequence $h_0[k] \in \ell_2(\mathbb{Z})$. The sequence h_0 is called the *low pass filter* of ϕ. For convenience, we define $\psi_{0,k}^{\ell}(\cdot) = \phi_{0,k}(\cdot)$ and $\tilde{\psi}_{0,k}^{\ell}(\cdot) = \tilde{\phi}_{0,k}(\cdot)$. Therefore, Equation (4) can be rewritten as

$$f = \sum_{k} \langle f, \tilde{\phi}(\cdot - k) \rangle \phi(\cdot - k) + \sum_{\ell=1}^{r} \sum_{j=1}^{\infty} \sum_{k\in\mathbb{Z}} \langle f, \tilde{\psi}_{j,k}^{\ell} \rangle \psi_{j,k}^{\ell} \tag{6}$$

The above series expansion (6) can be truncated as

$$\mathcal{Q}_n f = \sum_{\ell=1}^{r} \sum_{j<n} \sum_{k\in\mathbb{Z}} \langle f, \tilde{\psi}_{j,k}^{\ell} \rangle \psi_{j,k}^{\ell}. \tag{7}$$

which is typical in kernel-based system identification approaches (see Ref. [35])

Please note that $\mathcal{Q}_n f$ can be described by a reproducing kernel Hilbert space which is given by a linear combination of its frame and dual frame product.

$$\mathcal{Q}_n f(x) = \int_{\mathbf{R}} f(y)\, \mathcal{D}_n(x,y)\, dy, \tag{8}$$

where

$$\mathcal{D}_n(x,y) = \sum_{\ell=1}^{r} \sum_{j<n} \sum_{k\in\mathbb{Z}} \tilde{\psi}_{j,k}^{\ell}(y)\, \psi_{j,k}^{\ell}(x),$$

is called the kernel of $\mathcal{Q}_n f$. Figure 1 shows the graphs of the kernel $\mathcal{D}_2(x,y)$ for different framelets.

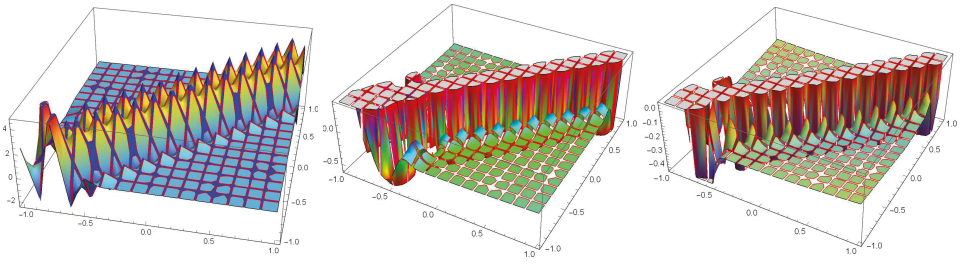

Figure 1. The graphs of the kernel, $\mathcal{D}_2(x,y)$, using the framelets of Example 2, 3 and 4, respectively.

It is known from the approximation theory, see e.g., Refs. ([28,35]), that the truncated expansion (7) is equivalent to

$$\mathcal{Q}_n f = \sum_{k\in\mathbb{Z}} \langle f, \tilde{\phi}_{n,k} \rangle \phi_{n,k}, \quad n \in \mathbb{Z}^+, \ f \in L_2(\mathbb{R}). \tag{9}$$

The general setup is to construct a set of functions as the form of Ψ, which can be summarized as follows: Let V_0 be the closed space generated by $\{\phi(\cdot - k)\}_{k\in\mathbb{Z}}$, i.e., $V_0 = \overline{span}\,\{\phi(\cdot - k)\}_{k\in\mathbb{Z}}$, and

$V_j = \left\{ f(2^j x) : f(x) \in V_0, x \in \mathbb{R} \right\}$. Let $\left\{ V_j, \phi \right\}_{j \in \mathbb{Z}}$ be the multiresolution analysis (MRA) generated by the function ϕ and $\Psi \subset V_1$ such that

$$\psi^\ell = 2 \sum_{k \in \mathbb{Z}} h_\ell[k] \, \phi(2 \cdot - k), \tag{10}$$

where $\{h_\ell[k], k \in \mathbb{Z}\}_{\ell=1}^r$ is a finitely supported sequence called *high pass filters* of the system. Please note that from Equation (7), the functions ϕ, ψ^ℓ and $\tilde{\phi}, \tilde{\psi}^\ell$ are playing a great role. They are used for computing the coefficients of the expansion of the function f in terms of ϕ and ψ, and recovering the projection of f onto V_j from the coefficients $\langle f, \tilde{\psi}_{j,k}^\ell \rangle$. The Fourier transform of a function $f \in L_2(\mathbb{R})$ is defined to be

$$\mathcal{F}(f)(\omega) = \hat{f}(\omega) = \int_{\mathbb{R}} f(x) \, e^{-i\omega x} dx, \quad \omega \in \mathbb{R},$$

and the Fourier series of a sequence $h \in \ell_2(\mathbb{Z})$ is defined by

$$\mathcal{F}(h)(\omega) = \hat{h}(\omega) = \sum_{k \in \mathbb{Z}} h[k] e^{-i\omega k}, \ \omega \in \mathbb{R}.$$

2. Gibbs Effect in Quasi-Affine Dual Tight Framelet Expansions

In this section, we study the Gibbs effect by using dual tight framelet in the quasi-affine tight framelet expansions generated via the MOEP. In general, and by using the expansion in Equation (7), we have $\lim_{n \to \infty} \mathcal{Q}_n f(x) = f(x)$ around x, where f is continuous except at many finite points. Hence, it is sufficient to study this effect by considering the following function

$$f(x) = \begin{cases} 1 - x, & 0 < x \leq 1 \\ -1 - x, & -1 \leq x < 0 \\ 0, & \text{else} \end{cases}.$$

In fact, this function is useful in the sense that other functions that have the same type of gaps, can be represented as expansions in terms of f plus a continuous function at $x = 0$. Please note that if we define $\mathcal{S}$ as

$$\mathcal{S}(x) = \begin{cases} \xi + 1 - x, & \xi < x \leq \xi + 1 \\ \xi - 1 - x, & \xi - 1 \leq x < \xi \\ 0, & \text{else} \end{cases},$$

then, $\mathcal{S}$ has a jump discontinuity at the point ξ and $\mathcal{S}(x) = f(x - \xi)$. Thus, we have the following result.

Theorem 1. *Any function with finitely many jump discontinuities can be written in terms of $\mathcal{S}$ plus a continuous function at the origin.*

Proof. Let g be a discontinuous function with a jump discontinuity, say at $x = \xi$, of magnitude D. We could put several of these together for g but we would likely only be looking at one such function at a time. Suppose that $\mathcal{S}$ and g are in the same direction of the needed jump (i.e., if $g(\xi^+) > g(\xi^-)$, then $J(\xi^+) > J(\xi^-)$, and similarly for $g(\xi^+) < g(\xi^-)$) or multiply $\mathcal{S}$ by (- or +)D to create the needed jump in the same direction. Define

$$F(x) = (+ \, or \, -) D \mathcal{S}(x) + d,$$

so that d is a constant that makes the jump endpoints of F and g matched at $x = \xi$. Our continuous function in the neighborhood of the point ξ will then be $g(x) - F(x)$. □

The definition of the Gibbs effect under the quasi-projection approximation $\mathcal{Q}_n$ is defined as follows.

Definition 3. *Suppose a function f is smooth and continuous everywhere except at $x_\circ$, i.e., limits $\lim_{x\to x_\circ^+} f(x)$ and $\lim_{x\to x_\circ^-} f(x)$ exist, and that $f(x_\circ^+)$ & $\neq$ & $f(x_\circ^-)$. Define $\mathcal{Q}_n f$ to be the truncated partial sum of Equation (7). We say that the framelet expansion of f exhibits the Gibbs effect at the right-hand side of $x_\circ$ if there is a sequence $d_s > 0$ converging to $x_\circ$, and*

$$\lim_{n,s\to\infty} \mathcal{Q}_n f(d_s) \begin{cases} > f(x_\circ^+), & if \quad f(x_\circ^+) > f(x_\circ^-) \\ < f(x_\circ^+), & if \quad f(x_\circ^+) < f(x_\circ^-) \end{cases}.$$

Similarly, we can define the Gibbs effect on the left-hand side of $x_\circ$.

Let Ψ to be the system defined by Definition 2. Thus, the corresponding quasi-affine system $X^J(\Psi)$ generated by Ψ is defined by a collection of translations and dilation of the elements in Ψ such that

$$X^J(\Psi) = \left\{ \psi_{j,k}^\ell : 1 \le \ell \le r, j, k \in \mathbb{Z}, \right\}$$

where

$$\psi_{j,k}^\ell = \begin{cases} 2^{j/2}\psi^\ell(2^j \cdot -k), & j \ge J \\ 2^j \psi^\ell(2^j \cdot -2^j k)), & j < J \end{cases}.$$

In the study of our expansion, we consider $J = 0$. Many applications in framelet and approximation theory are modeled by non-negative functions. One family of such important functions are the B-splines, where the B-spline B_m of order m is defined by

$$B_m = B_{m-1} * B_1 = \int_{(0,1]} B_{m-1}(\cdot - x)dx$$

where

$$B_1 = \chi_{(0,1]}.$$

Figure 2 shows the graphs of the B-splines B_m for different order.

It is known that sparsity of the framelets representations is due to the vanishing moments of the underling refinable wavelet (see Ref. [29]). We say ψ has N vanishing moments if

$$\int x^r \psi_{j,k}^\ell(x)dx = 0, \ for \ \ r = 0, 1, \cdots, N-1, \tag{11}$$

which is equivalent to that $\hat{\psi}_{j,k}^{(r)}(0) = 0$, for all $r = 0, 1, \cdots, N-1$. This implies that the framelet $\psi_{j,k}^\ell(x)$ is orthogonal to the polynomials $1, x, \cdots, x^{N-1}$. The following statement is well known in the literature [13] for wavelets, but we present the proof for the reader's convenience by considering the general quasi-affine dual framelet system.

Proposition 1. *Assume that $\tilde{\Psi}, \Psi$ is a quasi-affine dual framelet system for $L_2(\mathbb{R})$ and that ψ, where $\psi \in \Psi$ has a vanishing moment of order N. Then for any polynomial $d(x)$ of degree at most $N-1$, we have*

$$\mathcal{Q}d = d,$$

where $\mathcal{Q} = \mathcal{Q}_0$ is defined by Equation (9) for $n = 0$.

Proof. From the definition of $\tilde{\Psi}, \Psi$, we know that all the generators must have a compact support. Therefore, we can find a positive integer A such that the support of all these generators lie in the interval $[-A, A]$. Define

$$C_B = \chi_{[-B,B]}, \ \ where \ \ B \geq A. \tag{12}$$

Let $d(\cdot)$ be a polynomial of degree at most $N-1$. Then, by the vanishing moment property of $\psi_{j,k}^{\ell}$ we have

$$\int_{\mathbb{R}} C_B d(x) \psi_{j,k}^{\ell} dx = \int_{-B}^{B} d(x) \psi_{j,k}^{\ell} dx = 0, \ \ where \ \ x < |B - A|. \tag{13}$$

Now, the proof is completed by taking $B \to \infty$ and using Equations (6) and (13). Thus, we have

$$d(\cdot) = C_B d(\cdot) = \sum_k \langle d, \tilde{\phi}_{0,k} \rangle \phi_{0,k}(\cdot) = \mathcal{Q} d(\cdot).$$

□

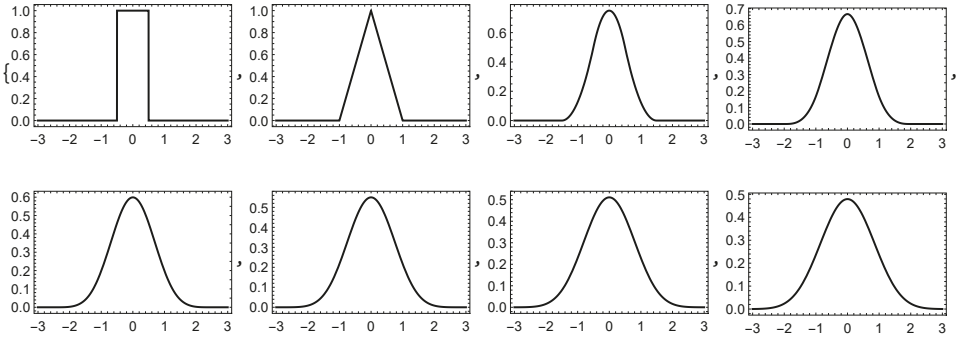

Figure 2. *B*-splines of order 1 through 8, respectively.

Now, we present some examples of dual tight framelets constructed by the MOEP in Ref. [34].

Example 1. *Let* $B_1 = \phi = \chi_{[0,1)}$. *Define,*

$$\begin{aligned} \psi_1(x) &= \frac{529}{1497}\chi_{[0,1)}(2x) + \frac{-173}{489}\chi_{[0,1)}(2x-1), \\ \tilde{\psi}_1(x) &= \frac{-1208}{3415}\chi_{[0,1)}(2x) + \frac{489}{1384}\chi_{[0,1)}(2x-1). \end{aligned}$$

Then, the resulting system generates a dual tight framelet for $L_2(\mathbf{R})$. *We illustrate the framelet and its dual framelet generators in Figure 3.*

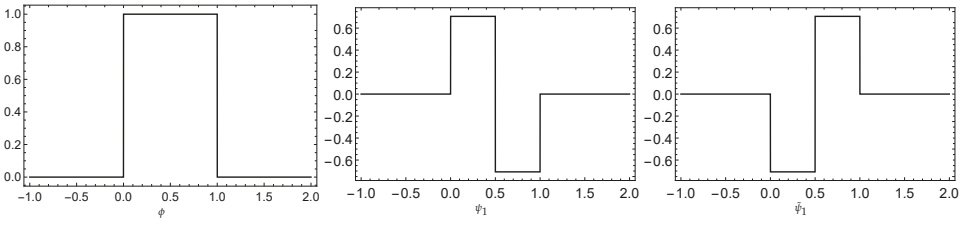

Figure 3. The graph of the Haar dual tight framelet of Example 1.

Example 2. *Let $B_2 = \phi = \tilde{\phi}$. Then,*

$$\mathcal{F}(h_0)(\xi) = \hat{h_0}(\xi) = \hat{\tilde{h}_0}(\xi) = 0.25(1 + \cos(\xi) - i\sin(\xi))^2.$$

Thus, by using the MOEP, one can find the following high pass filters,

$$\begin{aligned}
\hat{h}_1(\xi) &= -(1 - \cos(\xi) + i\sin(\xi))^2,\\
\hat{h}_2(\xi) &= -16\sin^4(\xi/2)(\cos(\xi) - i\sin(\xi)),\\
\hat{\tilde{h}}_1(\xi) &= \frac{1}{480}e^{-i\xi}\sin^4(\xi/2)(32{,}668 + 57{,}569\cos(\xi) + 39{,}422\cos(2\xi) + 21{,}191\cos(3\xi) +\\
&\quad 8428\cos(4\xi) + 2233\cos(5\xi) + 426\cos(6\xi) + 71\cos(7\xi)),\\
\hat{\tilde{h}}_2(\xi) &= -\frac{1}{480}e^{-i\xi}\sin^2(\xi/2)(-614 - 726\cos(\xi) + 85\cos(2\xi) + 412\cos(3\xi) + 458\cos(4\xi)\\
&\quad +284\cos(5\xi) + 71\cos(6\xi)).
\end{aligned}$$

Then, $\psi^\ell, \tilde{\psi}^\ell, \ell = 1, 2$ forms a dual tight framelets for $L_2(\mathbb{R})$. These functions have vanishing moments (vm) as follows, $vm(\psi_1) = vm(\tilde{\psi}_2) = 2$ while $vm(\psi_2) = vm(\tilde{\psi}_1) = 4$. See Figure 4 for their graphs.

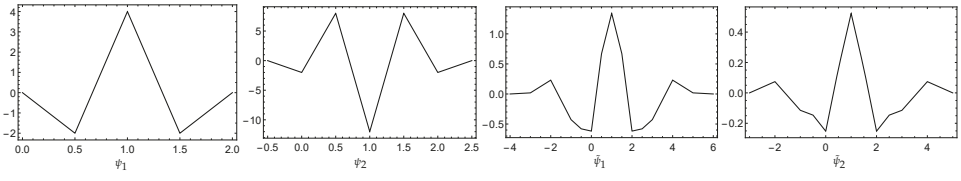

Figure 4. The graphs of the framelets and its dual framelets of Example 2.

Example 3. *Let $B_4 = \phi = \tilde{\phi}$. Then,*

$$\hat{h}_0(\xi) = \hat{\tilde{h}}_0(\xi) = 0.0625(1 + \cos(\xi) - i\sin(\xi))^4.$$

We have the following high pass filters,

$$\begin{aligned}
\hat{h}_1(\xi) &= (1 - \cos(\xi) + i\sin(\xi))^4,\\
\hat{h}_2(\xi) &= 16\sin^4(\xi/2)(\cos(3\xi) - i\sin(3\xi)).
\end{aligned}$$

The high pass filters for the dual framelets in $\ell_2(\mathbb{Z})$, where $k \in \mathbb{Z}$, is given by

$$\begin{cases}
\tilde{h}_1[k] = [\frac{311}{3{,}870{,}720}, \frac{311}{967{,}680}, \frac{865}{387{,}072}, \frac{473}{64{,}512}, \frac{1783}{4{,}83{,}840}, \frac{-19{,}967}{967{,}680}, \frac{-67{,}453}{1{,}935{,}360}, \frac{-17{,}887}{967{,}680}, \frac{233{,}473}{1{,}935{,}360}, \frac{17{,}887}{967{,}680},\\
\frac{67{,}453}{1{,}935{,}360}, \frac{19{,}967}{967{,}680}, \frac{1783}{483{,}840}, \frac{473}{64{,}512}, \frac{865}{387{,}072}, \frac{311}{967{,}680}, \frac{311}{3{,}870{,}720}],\\
\tilde{h}_2[k] = [\frac{311}{483{,}840}, \frac{311}{120{,}960}, \frac{2119}{483{,}840}, \frac{47}{10{,}080}, \frac{-4111}{483{,}840}, \frac{-5687}{120{,}960}, \frac{-21{,}103}{483{,}840}, \frac{2627}{15{,}120}, \frac{-21{,}103}{483{,}840}, \frac{-5687}{120{,}960},\\
\frac{-4111}{483{,}840}, \frac{47}{10{,}080}, \frac{2119}{483{,}840}, \frac{311}{120{,}960}, \frac{311}{483{,}840}].
\end{cases}$$

Then, $\psi^\ell, \tilde{\psi}^\ell, \ell = 1, 2$ forms a dual tight framelets for $L_2(\mathbb{R})$. Here we have $vm(\psi_1) = vm(\psi_2) = vm(\tilde{\psi}_1) = vm(\tilde{\psi}_2) = 4$. Their graphs are depicted in Figure 5.

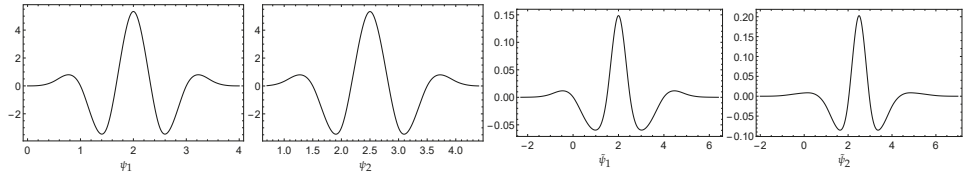

Figure 5. The graphs of the framelets and its dual framelets of Example 3.

Example 4. *Let* $B_4 = \phi$, *and* $B_2 = \tilde{\phi}$. *Thus,*

$$\hat{h}_0(\xi) = 0.0625(1 + \cos(\xi) - i\sin(\xi))^4, \text{ and } \hat{\tilde{h}}_0(\xi) = 0.25(1 + \cos(\xi) - i\sin(\xi))^2.$$

Then, we have the following tight framelets,

$$\psi_1(x) = \begin{cases} -8x^3/3 & \text{if } 0 \le x \le 1/2 \\ -2 + 12x - 24x^2 + 40x^3/3 & \text{if } 1/2 < x \le 1 \\ 38 - 108x + 96x^2 - 80x^3/3 & \text{if } 1 < x < 3/2 \\ -142 + 252x - 144x^2 + 80x^3/3 & \text{if } 3/2 \le x < 2 \\ 178 - 228x + 96x^2 - 40x^3/3 & \text{if } 2 \le x < 5/2 \\ (8/3)(-3 + x)^3 & \text{if } 5/2 \le x \le 3 \\ 0 & \text{if otherwise,} \end{cases}$$

$$\psi_2(x) = \begin{cases} -(1/3)(-1 + 2x)^3 & \text{if } 1/2 \le x \le 1 \\ -47/3 + 46x - 44x^2 + 40x^3/3 & \text{if } 1 < x < 3/2 \\ 358/3 - 224x + 136x^2 - 80x^3/3 & \text{if } 3/2 \le x < 2 \\ (2/3)(-461 + 624x - 276x^2 + 40x^3) & \text{if } 2 \le x < 5/2 \\ 953/3 - 334x + 116x^2 - 40x^3/3 & \text{if } 5/2 \le x \le 3 \\ (1/3)(-7 + 2x)^3 & \text{if } 3 < x \le 7/2 \\ 0 & \text{if otherwise} \end{cases}$$

and the high pass filters for its dual tight framelets in $\ell_2(\mathbb{Z})$, *where* $k \in \mathbb{Z}$, *are given by:*

$$\begin{cases} \tilde{h}_1[k] = [\frac{13}{15{,}360}, \frac{13}{7680}, \frac{61}{7680}, \frac{109}{7680}, \frac{-733}{15{,}360}, \frac{-35}{256}, \frac{409}{1280}, \frac{-35}{256}, \frac{-733}{15{,}360}, \frac{109}{7680}, \frac{61}{7680}, \frac{13}{7680}, \frac{13}{15{,}360},], \\ \tilde{h}_2[k] = [\frac{13}{2560}, \frac{13}{1280}, \frac{-89}{7680}, \frac{-1}{30}, \frac{-199}{3840}, \frac{313}{1920}, \frac{-199}{3840}, \frac{-1}{30}, \frac{-89}{7680}, \frac{13}{1280}, \frac{13}{2560}]. \end{cases}$$

Then, again $\psi^\ell, \tilde{\psi}^\ell, \ell = 1, 2$ *forms a dual tight framelets for* $L_2(\mathbb{R})$. *Here we have* $vm(\psi_1) = vm(\psi_2) = 2, vm(\tilde{\psi}_1) = vm(\tilde{\psi}_2) = 4$. *Their graphs are depicted in Figure 6.*

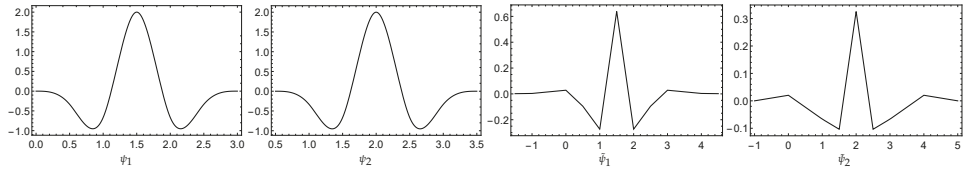

Figure 6. The graphs of the framelets and its dual framelets of Example 4.

We will use the framelet expansion defined by Equation (7) to present the numerical evidence of the Gibbs effect by determining the maximal overshoot and undershoot of the truncated expansion

$\mathcal{Q}_n f$ near the origin. The behavior of the truncated functions $\mathcal{Q}_n$ of a function with jump discontinuities is related to the existence of the Gibbs phenomenon, which is unpleasant in application, and not so easy to avoid. Therefore, examining a series of representations to avoid it or at least reduce it, is very important.

Proposition 2. *For any two refinable compactly supported functions ϕ and $\tilde{\phi}$ in $L_2(\mathbb{R})$. If*

$$\mathcal{Q}\,\mathrm{sgn} \leq 1 \text{ on } (x_\circ, \infty) \text{ and } \mathcal{Q}\,\mathrm{sgn} \geq -1 \text{ on } (-\infty, x_\circ),$$

then $\mathcal{Q}_n f$ exhibits no Gibbs effect.

Proof. Please note that $(\mathcal{Q}_n f)(2^{-n}x) = \mathcal{Q}(f(2^{-n}x))$ for all $n \in \mathbb{N}$. In particular, $(\mathcal{Q}_n\,\mathrm{sgn})(2^{-n}x) = \mathcal{Q}(\mathrm{sgn}(2^{-n}x))$. Suppose that the truncated function $\mathcal{Q}_n f$ do exhibit the Gibbs effect near $x_\circ^+$. Thus, there exists an open interval $\mathcal{U} \subseteq (x_\circ, \infty)$ such that $\mathcal{Q}f(x) > 1$, $\forall x \in \mathcal{U}$. Therefore, $\exists u > x_\circ$ such that $\max_{x\in(x_\circ,u)} \mathcal{Q}f(x) = U > 1$. Define a sequence $u_n > x_\circ$, $\forall n$ such that $u_n \to x_\circ$ as $n \to \infty$ (one can take $u_n = \epsilon_n + x_\circ$ such that $\epsilon_n \to 0$ as $n \to \infty$). Hence, $\max_{x\in(x_\circ,u_n)} \mathcal{Q}_n f(x) = \max_{x\in(x_\circ,u)} \mathcal{Q}f(x) = U > 1$, a contradiction. Similarly, we can prove the case when $x < x_\circ^-$ in the same fashion. □

Please note that it is important to use non-negative functions in framelet analysis due to its use in a variety of applications. One of those functions is the *B*-splines. The following statement will require such non-negativity to avoid the Gibbs effect.

Theorem 2. *Let ϕ and $\tilde{\phi}$ be any two non-negative refinable real valued compactly supported functions in $L_2(\mathbb{R})$ such that*

$$\int \mathrm{sgn}(x)\phi(x-k) > 0 \text{ and } \int \mathrm{sgn}(x)\tilde{\phi}(x-k) > 0 \text{ on } \mathbb{R}.$$

Assume further $\sum_k \phi(x-k) = 1$. If the vanishing moment of ϕ and $\tilde{\phi}$ is one, then $\tilde{\mathcal{Q}}f$ exhibit no Gibbs effect.

Proof. It suffices to show this for $\mathrm{sgn}(x)$ as $f(x) = \mathrm{sgn}(x) - x$ on $[-1, 1]$. Please note that Proposition 1 is held for $d = 1$, i.e.,

$$\tilde{Q}1 = 1.$$

Now, for $x \in \mathbb{R}$, and since

$$\langle \mathrm{sgn}(x), \phi(x-k)\rangle = \hat{\phi}(0),$$

by assumption, we have

$$\begin{aligned} \tilde{\mathcal{Q}}\,\mathrm{sgn}(x) - 1 &= \sum_k \langle \mathrm{sgn}(x), \phi(x-k)\rangle \tilde{\phi}(x-k) \\ &= -\sum_k \left(\int_{-\infty}^{-k} \phi(x)dx \right) \tilde{\phi}(x-k) < 0. \end{aligned}$$

The other side is analogue. Thus, $-1 \leq \tilde{\mathcal{Q}}\,\mathrm{sgn} \leq 1$ for all $x \in \mathbb{R}$. □

3. Results and Discussion

We present some numerical illustration by using the dual tight framelets which will generalize the result in Ref. [14]. The results show that if the dual framelet has vanishing moments of order of at least two, then $\mathcal{Q}_n f$ must exhibit the Gibbs effect. However, $\mathcal{Q}_n f$ has no Gibbs effect by using dual tight framelets of vanishing moments of order one.

Now we present an illustration for the Gibbs effect using the above dual tight framelets by showing the maximum overshoots, undershoots of $f(x)$, and some related graphs. This is to showcase the absence of the effect in Table 1 and Figures 7 and 8.

Table 1. Approximate maximum overshoot and undershoot in neighborhoods of $x = 0$ using $\mathcal{Q}_n f$ of Example 1.

Level	Maximum	Minimum
$n = 2$	0.907276	−0.907276
$n = 3$	0.964562	−0.964562
$n = 5$	0.994801	−0.994802
$n = 10$	0.999968	−0.999972

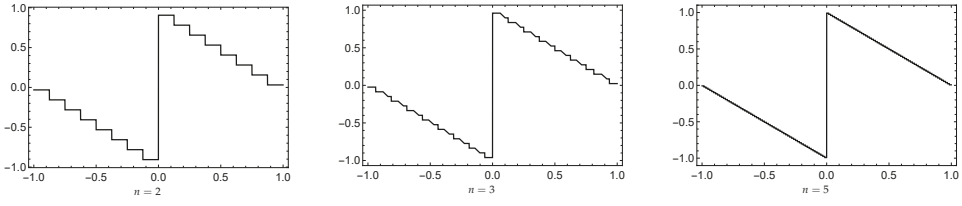

Figure 7. Illustration for the absence of the Gibbs effect using the quasi-operator $\mathcal{Q}_n f$ of Example 1.

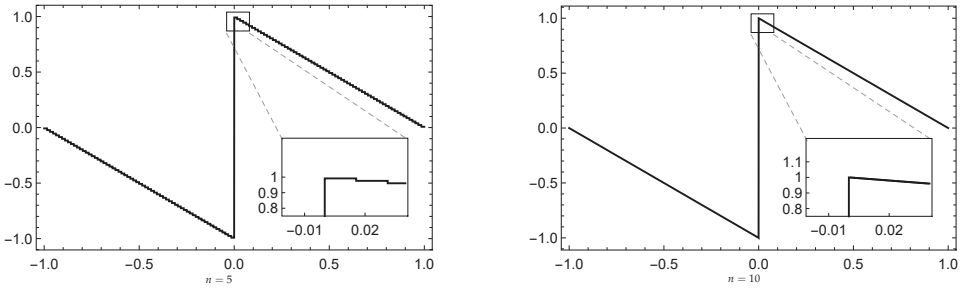

Figure 8. Illustration for the absence of the Gibbs effect using the quasi-operator $\mathcal{Q}_n f$ of Example 1 for $n = 5, 10$, respectively.

In Figures 9 and 10 we illustrate the graphs of the function $\mathcal{Q}f$ and $\mathcal{Q}\,\mathrm{sgn}$, receptively, generated using the B-splines dual tight framelets. In Tables 2–4 we show the approximated values for the overshoots and undershoots of $\mathcal{Q}_n f$. Figures 11–14 illustrate the graphs of the Gibbs effect.

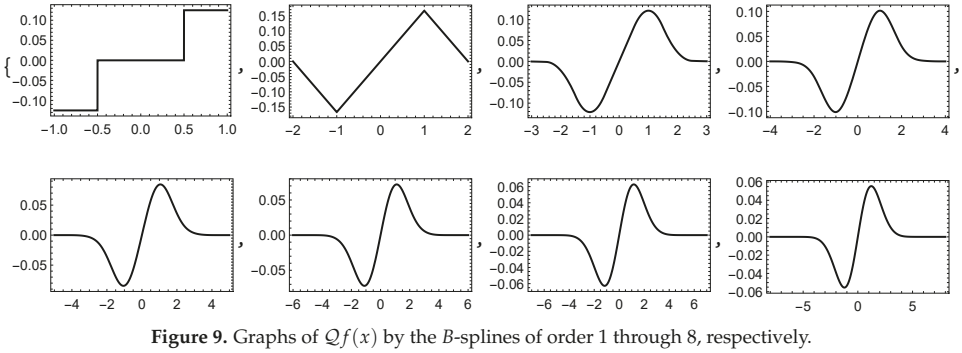

Figure 9. Graphs of $\mathcal{Q}f(x)$ by the B-splines of order 1 through 8, respectively.

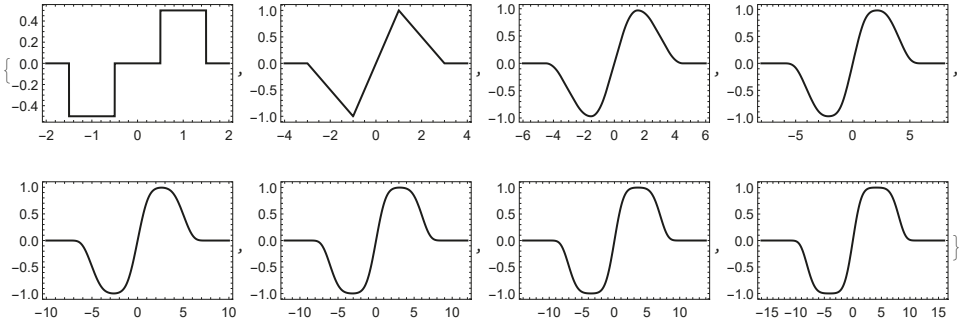

Figure 10. Graphs of $\mathcal{Q}\,\mathrm{sgn}(x)$ by the B-splines of order 1 through 8, respectively.

Table 2. Approximate maximum overshoot and undershoot in neighborhoods of $x = 0$ using $\mathcal{Q}_n f$ of Example 2 for $n = 2, 3, 5, 10$.

Level	Maximum	Minimum
$n = 2$	1.0021	−1.01204
$n = 3$	1.12708	−1.12708
$n = 5$	1.22083	−1.18958
$n = 10$	1.25111	−1.25111

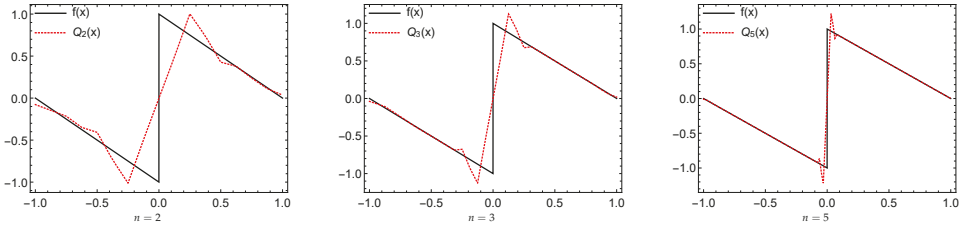

Figure 11. Illustration of the Gibbs effect using the quasi-operator $\mathcal{Q}_n f$ of Example 2.

Table 3. Approximate maximum overshoot and undershoot in neighborhoods of $x = 0$ using $\mathcal{Q}_n f$ of Example 3 for $n = 2, 3, 5, 10$.

Level	Maximum	Minimum
$n = 2$	0.997622	−0.996194
$n = 3$	1.07451	−1.07451
$n = 5$	1.13384	−1.13384
$n = 10$	1.15337	−1.15337

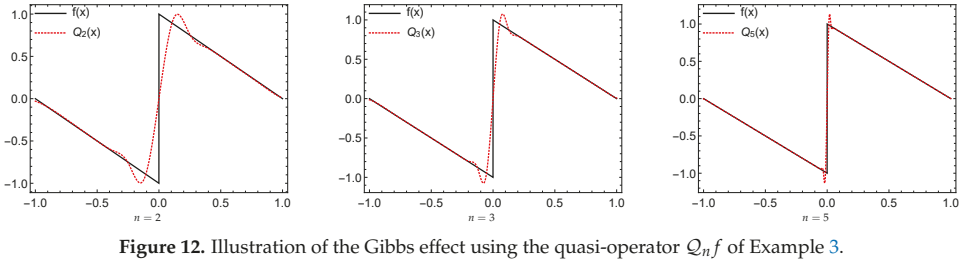

Figure 12. Illustration of the Gibbs effect using the quasi-operator $\mathcal{Q}_n f$ of Example 3.

Table 4. Approximate maximum overshoot and undershoot in neighborhoods of $x = 0$ using $\mathcal{Q}_n f$ of Example 4 for $n = 2, 3, 5, 10$.

Level	Maximum	Minimum
$n = 2$	1.08519	−1.08526
$n = 3$	1.14823	−1.14823
$n = 5$	1.19514	−1.19514
$n = 10$	1.21028	−1.21028

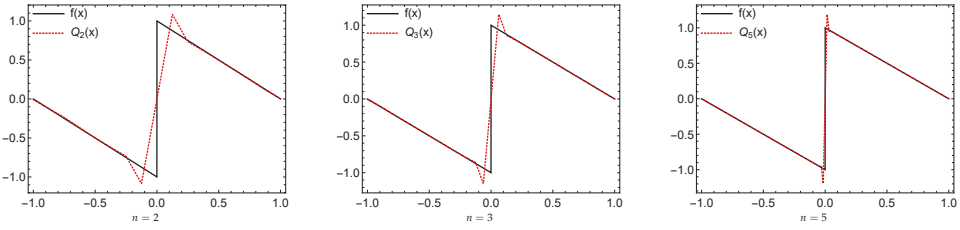

Figure 13. Illustration of the Gibbs effect using the quasi-operator $\mathcal{Q}_n f$ of Example 4.

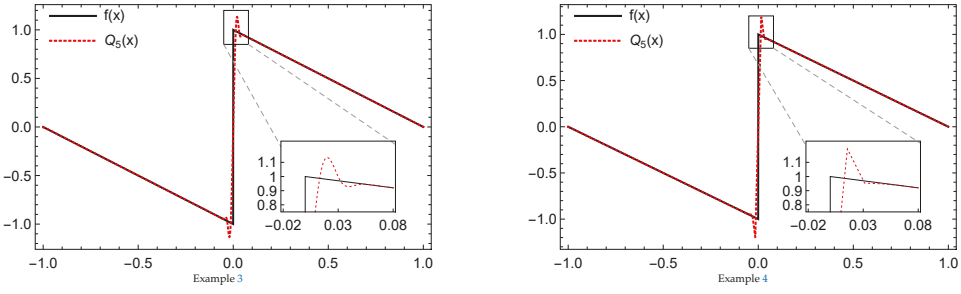

Figure 14. Gibbs effect illustrations by $\mathcal{Q}_5 f(x)$ of Example 3 and 4, respectively.

4. Conclusions

According to the above results, we show that the Gibbs effect is absent when the dual tight framelets of vanishing moments of order one are used to represent a function with jump discontinuities at the origin. Please note that increasing the vanishing moments, e.g., using the MOEP, will increase the approximation order of the framelet representation $\mathcal{Q}_n f$ that used to expand the function f; however, the Gibbs effects cannot be avoided for any level of n. Quite a few examples of dual tight framelets, numerical results, and graphical illustrations have been presented for the absence and presence of Gibbs effect.

Funding: This research was funded by Zayed University Research Fund.

Acknowledgments: I would like to thank the anonymous reviewers for their valuable comments to improve the quality of the paper.

Conflicts of Interest: The author declares no conflict of interest.

Abbreviations

The following abbreviations are used in this manuscript:

$L_2(\mathbb{R})$	The space of all square integrable functions over $\mathbb{R}$
$\psi, \tilde{\psi}$	The wavelet and its dual function
$\Psi, \tilde{\Psi}$	The framelets and its dual framelets system
UEP	The unitary extension principle
OEP	The oblique extension principle
MOEP	The mixed oblique extension principle
$\langle f, g \rangle$	The inner product of f and g
ϕ	The refinable function
$\mathcal{D}_n f$	The reproducing kernel Hilbert space of the function f
$\mathcal{Q}_n f$	The truncated partial sum of the framelet system
$h_0[k]$	Low pass filter of the framelet system
$h_\ell[k]$	High pass filters of the framelet system
V_j	The multiresolution analysis generated by the function ϕ
$\mathcal{F}(f)$	The Fourier transform of a function f
B_m	The B-spline of order m
$vm(f)$	The vanishing moments of the function f

References and Note

1. Wilbraham, H. On a certain periodic function. *Camb. Dublin Math. J.* **1848**, *3*, 198–201.
2. Michelson, A.; Stratton, S. A new harmonic analyser. *Philos. Mag.* **1898**, *45*, 85–91. [CrossRef]
3. Gibbs, J.W. Fourier's Series. *Nature* **1898**, *59*, 200. [CrossRef]
4. Gibbs, J.W. Fourier's Series. *Nature* **1899**, *59*, 606. [CrossRef]
5. Maxime, B. Introduction to the theory of Fourier's series. *Ann. Math.* **1906**, *7*, 81–152.
6. Shim, H.T. A summability for Meyer wavelets. *J. Appl. Math. Comput.* **2002**, *9*, 657–666. [CrossRef]
7. Shen, X. On Gibbs phenomenon in wavelet expansions. *J. Math. Study* **2002**, *35*, 343–357.
8. Shen, X. Gibbs Phenomenon for Orthogonal Wavelets with Compact Support. In *Advances in the Gibbs Phenomenon*; Jerri, J., Ed.; Sampling Publishing: Potsdam, Germany, 2011; pp. 337–369,
9. Foster, J.; Richards, F. The Gibbs phenomenon for piecewise-linear approximation. *Am. Math. Mon.* **1991**, *98*, 47–49. [CrossRef]
10. Richards, F.B. A Gibbs phenomenon for spline functions. *J. Approx. Theory* **1991**, *66*, 334–351. [CrossRef]
11. Han, B. Gibbs Phenomenon of Framelet Expansions and Quasi-projection Approximation. *J. Fourier Anal. Appl.* **2018**. [CrossRef]
12. Gribonval, R.; Nielsen, M. On approximation with spline generated framelets. *Constr. Approx.* **2004**, *20*, 207–232.
13. Kelly, S. Gibbs phenomenon for wavelets. *Appl. Comp. Harmon. Anal.* **1996**, *3*, 72–81. [CrossRef]
14. Mohammad, M.; Lin, E.B. Gibbs phenomenon in tight framelet expansions. *Commun. Nonlinear Sci. Numer. Simul.* **2018**, *55*, 84–92. [CrossRef]
15. Mohammad, M.; Lin, E.B. Gibbs Effects Using Daubechies and Coiflet Tight Framelet Systems. *Contemp. Math. AMS* **2018**, *706*, 271–282.
16. Mohammad, M. Special B-spline Tight Framelet and It's Applications. *J. Adv. Math. Comput. Sci.* **2018**, *29*, 1–18. [CrossRef]
17. Shim, H.T.; Volkmer, H. On the Gibbs Phenomenon for Wavelet Expansions. *J. Approx. Theory* **1996**, *84*, 74–95. [CrossRef]
18. Zygmund, A. *Trigonometric Series*, 2nd ed.; Cambridge Univ. Press: Cambridge, UK, 1959.
19. Adcock, B.; Hansen, A. Stable reconstructions in Hilbert spaces and the resolution of the Gibbs phenomenon. *Appl. Comput. Harmon. Anal.* **2012**, *32*, 357–388. [CrossRef]
20. Conditions on shape preserving of stationary polynomial reproducing subdivision schemes.
21. Aldwairi, M.; Flaifel, Y. Baeza-Yates and Navarro Approximate String Matching for Spam Filtering. In Proceedings of the Second International Conference on Innovative Computing Technology (INTECH 2012), Casablanca, Morocco, 18–20 September 2012; pp. 16–20.

22. Gottlib, D.; Shu, C. On the Gibbs phenomenon and its resolution. *SIAM Rev.* **1997**, *39*, 644–668. [CrossRef]
23. Jerri, A. *The Gibbs Phenomenon in Fourier Analysis, Splines and Wavelet Approximations*; Kluwer Academic Publishers: Dordrecht, The Netherlands, 1998.
24. Li, B.; Chen, X. Wavelet-based numerical analysis: A review and classification. *Finite Elem. Anal. Des.* **2014**, *81*, 14–31. [CrossRef]
25. Barg, A.; Glazyrin, A.; Okoudjou, K.A.; Yu, W. Finite two-distance tight frames. *Linear Algebra Appl.* **2015**, *475*, 163–175. [CrossRef]
26. Ganiou, A.; Atindehou, D.; Kouagou, Y.B.; Okoudjou, K.A. On the frame set for the 2-spline. *arXiv* **2018**, arXiv:1806.05614.
27. Hussein, R.; Shaban, K.; El-Hag, H. Energy conservation-based thresholding for effective wavelet denoising of partial discharge signals. *Sci. Meas. Technol. IET* **2016**, *10*, 813–822. [CrossRef]
28. Han, B. Framelets and wavelets: Algorithms, analysis, and applications. In *Applied and Numerical Harmonic Analysis*; Birkhauser/Springer: Cham, Switzerland, 2017; p. 724.
29. Daubechies, I. *Ten Lectures on Wavelets*; SIAM: Philadelphia, PA, USA, 1992.
30. Daubechies, I.; Grossmann, A.; Meyer, Y. Painless nonorthogonal expansions. *J. Math. Phys.* **1986**, *27*, 1271–1283. [CrossRef]
31. Christensen, O. *An Introduction to Frames and Riesz Bases*; Birkhauser: Boston, MA, USA, 2003.
32. Ron, A.; Shen, Z. Affine systems in $L^2(\mathbf{R}^d)$: the analysis of the analysis operators. *J. Funct. Anal.* **1997**, *148*, 408–447. [CrossRef]
33. Ron, A.; Shen, Z. Affine systems in $L^2(\mathbb{R}^d)$ II: dual systems. *J. Fourier Anal. Appl.* **1997**, *3*, 617–637. [CrossRef]
34. Daubechies, I.; Han, B.; Ron, A.; Shen, Z. Framelets: MRA-based constructions of wavelet frames. *Appl. Comput. Harmon.* **2003**, *14*, 1–46. [CrossRef]
35. Zorzi, M.; Chiuso, A. The harmonic analysis of kernel functions. *Automatica* **2018**, *94*, 125–137. [CrossRef]

© 2019 by the authors. Licensee MDPI, Basel, Switzerland. This article is an open access article distributed under the terms and conditions of the Creative Commons Attribution (CC BY) license (http://creativecommons.org/licenses/by/4.0/).

mathematics

MDPI

Article

Preliminary Analysis of a Fully Ceramic Microencapsulated Fuel Thermal–Mechanical Performance

Ping Chen [1,2,*], Suizheng Qiu [1,*], Shichao Liu [2], Yi Zhou [2], Yong Xin [2], Shixin Gao [2], Xi Qiu [2] and Huaiyu Lu [2]

1 Shanxi Key Lab. of Advanced Nuclear Energy and Technology, School of Nuclear Science and Technology, Xi'an Jiaotong University, Xi'an 710049, China

2 Science and Technology on Reactor System Design Technology Laboratory, Nuclear Power Institute of China, Chengdu 610200, China; hit_lsc@163.com (S.L.); hit_yf@163.com (Y.Z.); hit_yf306@163.com (Y.X.); liushichao19861010@163.com (S.G.); qiuxi_drsi@163.com (X.Q.); luhuaiyu0424@163.com (H.L.)

* Correspondence:chenping_npic@163.com (P.C.); szqiu@mail.xjtu.edu.cn (S.Q.); Tel./Fax: +86-028-8590-8295 (P.C.)

Received: 20 March 2019; Accepted: 30 April 2019; Published: 20 May 2019

Abstract: In this paper, a two-dimensional characteristic unit was used to simulate the thermal–mechanical performance of a fully ceramic microencapsulated (FCM) fuel pellet, and the criterion of FCM structure integrity was discussed. FCM structure integrity can be reflected though the integrity of the silicon carbide (SiC) matrix or SiC layers because of the excellent fission retention capability of SiC ceramics. The maximum temperature of the SiC matrix under normal conditions of the pressure water reactor (PWR) environment was about 1390 K, which was lower than the decomposition point of SiC. The maximum hoop stress of the SiC matrix, especially the inner part, was up to about 1200 MPa, and the hoop stress of the non-fuel region part was lower than the inner part, which can be attributed to the deformation of tristructural-isotopic (TRISO) particles. The hoop stress of the SiC layers at the end of life was only about 180 MPa, which is much lower than the strength of the chemical vapor deposition (CVD)-SiC. The failure probability of the SiC layer was lower than 9×10^{-5}; thus, the integrity of SiC layers and the fission retention capability were maintained. The structure integrity of FCM fuel was broken because the SiC matrix cracked.

Keywords: FCM fuel; thermal–mechanical performance; failure probability; silicon carbide

1. Introduction

Fully ceramic microencapsulated (FCM) fuel, which can improve the accident tolerance of light water reactors (LWRs), receives much attention because of its excellent oxidation resistance, fission retention capability, high thermal conductivity, and irradiation stability [1–4]. FCM was designed to improve the fission retention capacity during accident processes; fission retention capacity may be reflected by the integrity of the silicon carbide (SiC) matrix and layers. FCM is composed of historic tri-isotropic fuel embedded in a fully dense and impermeable SiC matrix. The tristructural-isotopic (TRISO) particle consists of the fuel kernel surrounded by four successive layers [5]: the low-density carbon buffer layer, whose function is to slow down and retain the generated fission product, and the inner and outer pyroltytic graphite layers, which surround the silicon carbide (SiC) micro pressure vessel. The function of the pyrolytic carbon is severalfold, including the protection of the kernel from aggressive process gases used during TRISO processing, to protect the SiC shell from energetic fission product recoil damage, and to provide thermal–mechanical stability and toughening for this multilayer system. Historically, TRISO and its fuel forms (graphite matrix compacts in the form of the cylindrical

fuel of a prismatic high-temperature gas-cooled reactor or the spherical pebble of a pebble-bed modular high-temperature gas-cooled reactor) operate at a temperature in excess of 1000 °C. As the envisioned LWR application of the FCM fuel is at a less aggressive operating temperature for the TRISO (nominally 350–500 °C), it is anticipated that higher burn-ups and significantly improved safety benefits realized by the extraordinary fission product retention may be realized [6].

Lower fissile loading was an obvious shortcoming of FCM fuel compared with uranium dioxide (UO_2) pellets. The feasibility of FCM fuel to satisfy the reasonable fuel cycle lengths in LWRs was demonstrated by Sen et al. [7]. The effect of the UO_2 kernel size, enrichment, and type on the effective full power days (EFPD) was discussed. The results indicated that uranium nitride (UN) kernel FCM fuel can meet the fissile loading requirement of LWRs by optimizing the size of the kernel and coated layers. The sizes of the UN kernel and buffer layer were 800 μm and 100 μm, respectively, and the fraction of the FCM had to be higher than 44 vol.%. The thermal–mechanical performance of the TRISO with UO_2 kernels was simulated by PARFUM, PASTA, and other models [8]. In the CO production model, internal pressure and gap heat transfer were considered. The Recoil and Booth models were used to calculate the fission gas release. The thermal and mechanical performance of the coated layer can be calculated in the above models. The performance of the UN kernel TRISO fuel in the LWR environment was reported, and the influence of temperature and kernel size on internal pressure and the survivability of TRISO fuel was studied [9]. The tangential stress of the inner pyrocarbon (IPyC) and SiC layers was calculated using COMSOL multi-physics software (COMSOL-5.2, MERCURY LEARNING AND INFORMATION LLC, Dulles, Virginia). However, the influence of the SiC matrix on TRISO particle performance was not discussed.

The thermal–mechanical performance of FCM pellets is difficult to simulate because of its complex structure and material properties. The temperature field and thermal conductivity of FCM pellets were studied previously [10–12], but thermal and mechanical coupled simulation results are rare. The temperature of the FCM pellet used in a pressure water reactor (PWR) environment was calculated by COMSOL software in the literature [10]. Both homogeneous and heterogeneous models were used in the report, and the calculated result of the homogeneous models was in good agreement with the result calculated by RELAP. The mechanical performance of FCM was not studied. Ougouag and co-workers [13] studied the influence of the SiC matrix on the performance of TRISO fuel by adding an SiC matrix on the outer surface of a single TRISO particle model. The results indicate that the thickness of the SiC matrix has an obvious influence on the stress distribution of the SiC and IPyC layers. The structure and coated layer size can affect the stress condition of the FCM. The SiC layer stress increased upon ignoring the outer pyrocarbon (OPyC) layer or increasing the SiC matrix thickness. The stress of the SiC layer with a matrix was much higher than the single particle. Schappel [14] simulated the thermal–mechanical performance of an FCM pellet and TRISO particle separately using ABAQUS software. TRISO particles were subtracted from the FCM pellet to simplify the model and decrease the computation amount. The performance of the coated layers was not detected, and the interaction between the TRISO particle and matrix was not reflected in the literature.

There is no criterion to evaluate the integrity of the FCM pellet, and the integrity of the FCM pellet was not studied in previous work as far as we know. In this paper, the integrity of the FCM pellet was defined according to fission retention capacity. The integrity of the FCM pellet under a PWR environment was discussed by investigating the mechanical performance and failure probability of the SiC matrix and SiC layers. A two-dimensional model was established, while the buffer layer and fuel kernel were subtracted from the FCM pellet. The internal pressure of TRISO particles embedded in different locations of FCM fuel was calculated using a TRISO simulation. The interaction between the TRISO particle and the SiC matrix was investigated, and the thermal–mechanical properties of the coated layers and SiC matrix were discussed. The fission production capacity of the FCM pellet was evaluated by investigating the failure probability of SiC layers and the hoop stress of the SiC matrix.

2. Governing Equation and Material Properties

2.1. Governing Equation

COMSOL multi-physics software offered the heat transfer model for the solid materials to calculate the temperature distribution in FCM and TRISO fuel. The temperature field of FCM pellet and TRISO fuel are determined by the heat conduction equation:

$$\rho C_p \frac{\partial T}{\partial t} + \nabla \cdot q - E_f \dot{F} = 0 \tag{1}$$

where T, ρ and C_p are the temperature, density (kg/m^3) and heat capacity (J/(kg·K)) of the solid material, respectively. E_f and $\dot{F}$ are the energy released in a single fission event and volumetric fission rate, respectively. The heat flux can be written as follows:

$$q = -k\nabla T. \tag{2}$$

The stress in all coated layers and the SiC matrix was caused by the accumulation of internal pressure and the deformation of other materials. The internal pressure of TRISO fuel was caused by fission gas release. The TRISO particle located in a different part of the FCM pellet possessed a different internal pressure caused by the temperature gradient of the FCM pellet [9]. The deformation of the coated layers and SiC matrix was caused by the internal and outer pressure, thermal expansion, irradiation and creep strain. The strain tensor of FCM was written as follows:

$$\varepsilon = \varepsilon^e + \varepsilon^T + \varepsilon^i + \varepsilon^c \tag{3}$$

where ε is the strain, ε^e, ε^T, ε^i and ε^c represent the elastic strain, thermal expansion strain, irradiation strain and creep strain.

2.2. Material Properties

The properties of dense pyrolytic carbon, SiC layer, and SiC matrix were used in this simulation. The properties of dense pyrolytic carbon in PASTA code used in a high temperature gas cooled reactor have been employed to analyze the performance of the FCM pellet in an LWR environment by Idaho National Laboratory (INL), and the appropriateness of the properties of dense pyrolytic carbon have been proved in previous works [15,16]. The appropriateness of the properties of SiC ceramics described in the following part used in an LWR environment, has been reported [17,18].

2.2.1. Dense Pyrolytic Carbon (PyC) Layers

The properties of the SiC layer, SiC matrix and PyC materials are taken into account in this paper. The elastic modulus of the PyC layer is anisotropic and can be calculated by the following Equation [19]:

$$\begin{aligned} E_{PyC} = 25.5(0.384 + 0.000324\rho_{PyC})(0.481 + 0.519BAF) \\ (1 + 0.23\Phi)(0.9560275 + 0.00015T) \end{aligned} \tag{4}$$

where Φ is the neutron flux ($\times 10^{25}$ n/m^2), T is the temperature (K), and BAF is the anisotropic parameters of PyC.

The radial and tangential irradiation strain of the PyC layers are expressed by the following equations [17]:

$$\dot{\varepsilon}_r = -0.077\exp(-\Phi) + 0.031 \tag{5}$$

$$\dot{\varepsilon}_\theta = -0.036\exp(-2.1\Phi) - 0.01. \tag{6}$$

The irradiation deformation of PyC (as shown in Equations (5) and (6)) was saturated when the neutron flux reached 8.14×10^{25} n/m^2 [16].

Equation (7) is given to calculate the creep strain of the PyC layers along the radial and other directions [17].

$$\dot{\varepsilon}_{cr,r} = K_{pyc}[\sigma_r - \nu_c(\sigma_\theta + \sigma_\phi)]\dot{\Phi} \tag{7}$$

where $\dot{\Phi}$ is the fast neutron flux rate (10^{25}n·m^{-2}·s^{-1}), v_c is the Poisson ratio (v_c = 0.23), and K_{pyc} is the temperature-dependent creep coefficient.

2.2.2. SiC Layer and SiC Matrix

The elastic modulus and thermal expansion coefficient of the SiC layer are represented as in the following equations [17]:

$$E_{SiC} = 460 - 0.04T\exp\left(-\frac{962}{T}\right) \tag{8}$$

$$\alpha_{sic}(\times 10^{-6}) = \begin{cases} -1.8267 + 0.0178T - 1.5544 \\ \times 10^{-5}T^2 + 4.5246 \times 10^{-9}T^3 & T < 1273K \\ \\ 5.0 & T > 1273K \end{cases} \tag{9}$$

where E and α are the elastic modulus and thermal expansion coefficient, respectively.

The swelling model of the SiC matrix is the function of temperature and neutron flex, which can be written as follows [19]:

$$\dot{S} = k_s\gamma^{-1/3}\exp\left(-\frac{\gamma}{\gamma_{sc}}\right) \tag{10}$$

where S is the swelling rate (s^{-1}), K_s is the coefficient of the swelling rate (dpa$^{-2/3}$), γ is the neutron flux (dpa), and γ_{sc} is the characteristic dose for swelling saturation by the negative feedback mechanism (dpa). The swelling of the SiC can be obtained from the time integration of Equation (10):

$$S = S_s\left[1 - \exp\left(-\frac{\gamma}{\gamma_{sc}}\right)\right]^{2/3} \tag{11}$$

where S_s and γ_{sc} are the function of the temperature and can be expressed as follows:

$$S_s(T) = 0.05837 - 1.0089 \times 10^{-4}T + 6.9368 \times 10^{-8}T^2 - 1.8152 \times 10^{-11}T^3 \tag{12}$$

$$\gamma_{sc}(dpa) = -0.4603 + 2.6674 \times 10^{-3}T - 4.3176 \times 10^{-6}T^2 + 2.3803 \times 10^{-9}T^3. \tag{13}$$

Figure 1 shows the swelling of SiC materials as a function of temperature and dose calculated from Equation (11).

The thermal expansion coefficient of the SiC matrix is expressed as follows [20]:

$$\alpha(10^{-6}/K) = 0.7738 + 7.080 \times 10^{-3}T - 4.951 \times 10^{-6}T^2 + 1.372 \times 10^{-9}T^3. \tag{14}$$

The thermal conductivity of the SiC layer is different from that of the SiC matrix due to the differences in their fabrication and chemical components. Si and C exhibit similar electronegative properties; thus, SiC is mainly combined by C and Si with a covalent bond, according to the Principle of Electro negativity. Unirradiated SiC thermal resistance increases with temperature and defects due to an increase in phonon-phonon scattering. Because of irradiation can increase the quantity of defects, the thermal resistance of SiC increased. The thermal resistance of SiC can be simplified as Equation (15) by neglecting the contribution to the electron to the thermal conductivity at a high temperature [21]:

$$\frac{1}{k} = R_0 + R_{irr} \tag{15}$$

where R_0 and R_{irr} are the thermal resistance (K/W) of the prior- and post-irradiated SiC, respectively.

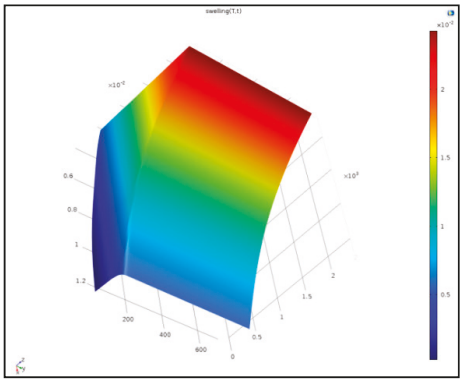

Figure 1. Variation of the swelling silicon carbide (SiC) material as functions of temperature and neutron flux.

The thermal resistance of the unirradiated SiC lay and matrix is expressed as below:

$$R_0 = \frac{1}{-3.7 \times 10^{-8} T^3 + 1.54 \times 10^{-4} T^2 - 0.214T + 153.1}. \tag{16}$$

The thermal resistance induced by the irradiation can be written:

$$R_{irr} = \frac{1}{6.08 \cdot S} \tag{17}$$

where S is the irradiation-induced volume swelling shown in Equation (11).

Failure probability of the SiC layer can be reflected by the stress distribution. The failure probability of brittleness material can be calculated by the following Equation [19]:

$$P = 1 - \exp\left[-\int_V (\sigma_p/\sigma_0)^m dV\right] \tag{18}$$

where V is the characteristic volume, m is the Weibull modulus of the SiC layer, and σ_0 is the characteristic strength, while σ_p is the true stress. The characteristic strength and the Weibull modulus of the SiC layer were 350 MPa and 5, respectively [15].

3. Geometry and Boundary Conditions

The performance of a TRISO particle with a UN kernel was simulated in our previous work [22], and the calculated internal pressure at a different temperature of TRISO was used as input parameters for the FCM pellet simulation. A 1/8 sphere unit was used to simulate the performance of the TRISO particle by defining the boundary condition. The heat source of the TRISO particle was conversed from the liner power of the FCM pellet. The surface temperature was set according to the calculated result of the FCM pellet. The symmetry boundary condition was set on the 3 side surfaces. The structure and boundary condition schematic diagram of the TRISO particle unit is shown in Figure 2. The typical size of the TRISO particle had been studied in [22], and the size of the kernel and coated layers have great influence on the performance of TRISO particles. The structural size of the TRISO particle was

similar with that of our previous work [23] and was set as follows: the diameter of the UN kernel was 800 μm, while the thickness of buffer, IPyC, SiC, and OPyC layers were 100 μm, 30 μm, 40 μm, and 30 μm, respectively.

The FCM pellet with 39.8 vol.% TRISO particle loading was simulated in this work. The diameter and height of the FCM pellet was 7 mm and 7 mm, respectively. A three-dimensional model is shown in Figure 3. In order to decrease the calculated quantity of the FCM pellet, a 2-dimensional model was used in this simulation. The 2-dimensional unit was obtained from the 3-dimensional one; the cutting pattern is shown in Figure 3.

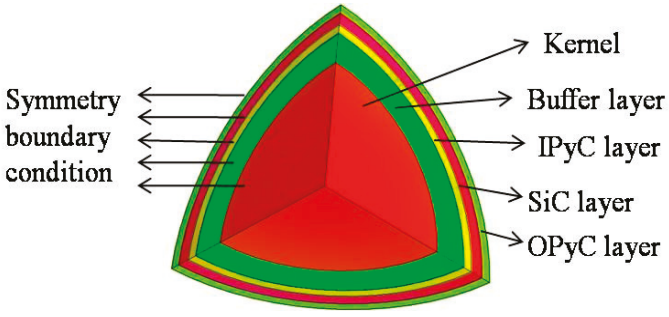

Figure 2. Schematic diagram of a tristructural-isotopic (TRISO) particle characteristic unit. IPyC, inner pyrocarbon; OPyC, outer pyrocarbon.

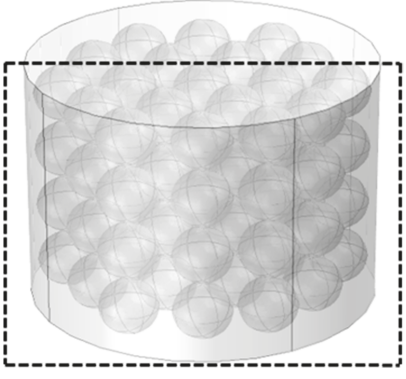

Figure 3. A three-dimensional model of a fully ceramic microencapsulated (FCM) pellet with 39.8 vol.% TRISO particle loading.

Figure 4 shows the 2-dimensional model; the structure and boundary condition was also revealed. The kernel and buffer layers were separated from the IPyC layer during the operation process and have little influence on the performance of the other coated layers and the SiC matrix; this phenomenon has been proven by previous works [19,22]. The kernel and buffer layers were subtracted from the TRISO particle, and the other coated layers, including the IPyC, SiC, and OPyC layers were reserved to reflect the SiC layer's performance and to simulate the interaction between the coated layers and the SiC matrix. The side surface temperature of the FCM pellet was set as about 800 K, which was set as a solid heat transfer boundary. Heat flux was set on the IPyC surface per particle and the value was about 3.53×10^5 W/m^2, which corresponds to an average linear power of 315 W/cm for the FCM pellet. The internal pressure has an obvious effect on the performance of the coated layers, and the internal pressure of the TRISO particle was calculated from the TRISO particle model at a different surface temperature. The bottom part of the FCM pellet was set as a spring foundation to assure

simulation convergence. The pressure on the side surface was set as a constant value (P = 2 MPa), which corresponds to the helium pressure of the fuel rod.

A schematic of the calculation flow in the COMSOL software was is shown in Figure 5, and each part of the computable flow graph was described as follows. The two-dimensional model was used to simulate the performance of the FCM pellet. Solid mechanics and heat transfer modules were selected to calculate the temperature and mechanical field of the FCM under a normal condition. The three-dimensional model of the FCM pellet was established, and the two-dimensional model was obtained from the three-dimensional ones, as shown in Figure 3. The geometric model was established by set the size of pellet and coated layers. The material model and boundary condition, as mentioned above, was input, and the grid was subdivided using the native function of COMSOL, according to the physical field. The temperature and stress field of the FCM pellet was output.

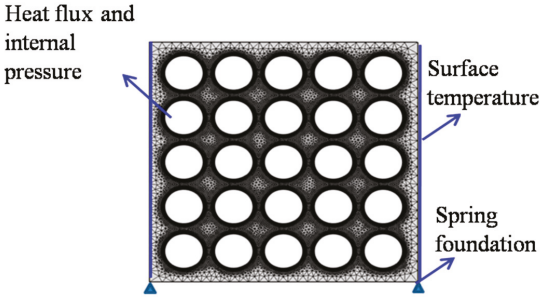

Figure 4. Two-dimensional model of the FCM pellet; the structure and boundery condition were also revealed.

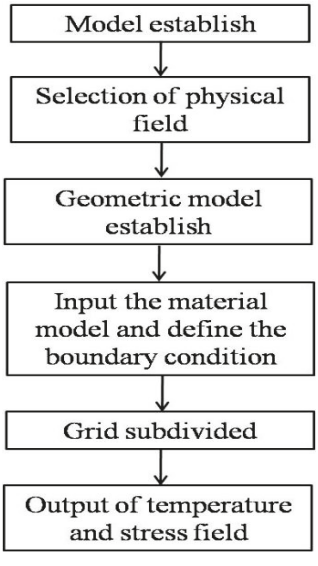

Figure 5. Computable flow graph of simulation process.

4. Results and Discussion

4.1. Temperature Distribution of FCM Pellet

The calculated temperature distribution of an FCM pellet in an LWR environment is shown in Figure 6. The highest temperature of the SiC matrix was located in the center of the FCM pellet, and the maximum temperature at the end of life was about 1390 K, which was similar with the results in the literature [14]. The maximum matrix temperature was much lower than the decomposition or molten point of SiC. The maximum temperature increased rapidly at the beginning and was followed by a slower linear increase. The swelling of the SiC matrix is the function of temperature and neutron flex, which can cause thermal conductivity degradation of SiC matrix, as discussed in the above section (shown in Equation (17)). The thermal conductivity of the SiC matrix reached an essentially steady state condition after 100 d when the SiC swelling reached saturation at about 1 dpa. The maximum temperature of the SiC matrix was much lower than that of the UO_2 pellet in the same operational environment, which was attributed to the high thermal conductivity of the SiC matrix.

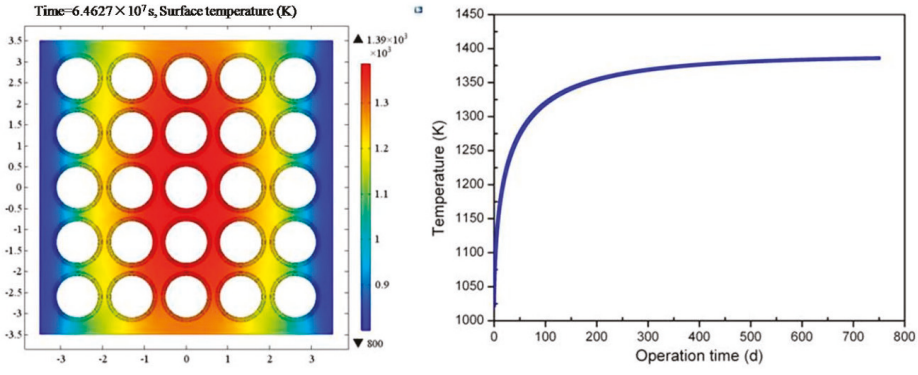

Figure 6. Matrix temperature profile at end of life (EOL) of FCM pellet and variation of the maximum matrix temperature with operation time.

4.2. Mechanical Performance of SiC Matrix

The internal pressure of TRISO particles located at different part of the FCM pellet was calculated using a 1/8 sphere unit model. Internal pressure of the TRISO particle with a different surface temperature is shown in Figure 7. The internal pressure of the TRISO particle increased with the surface temperature. No interaction occurred between the UN kernel and Buffer layers, and the internal pressure was caused by the fission gas. The calculated result was similar with the reported ones, which used UN as a TRISO kernel [23], but the internal pressure was much lower than that in the literature [14]. This result may be attributed to the different kernel, and the interaction between the UO_2 and Buffer layer may increase the internal pressure dramatically. The internal pressure increased with burn up linearly because of the increase in fission gas production. The maximum internal pressure was about 3 MPa at 1400 EFPD when the surface temperature was up to 1200 K, which was in good agreement with the literature [22]. Internal pressure has an obvious influence on the stress distribution of the TRISO particle and the FCM pellet.

Variation of hoop stress on marginal parts of the FCM pallet (non-fuel part) is shown in Figure 8. The bottom part (Parts A, B, and C) shows relatively lower stress than the side part (Parts D and E), which may be caused by the different temperature gradient. Because of the higher temperature of the inner matrix (shown in Figure 6), a higher thermal deformation was induced; thus, the hoop stress of the inner part (Parts B and C) was much higher than that of the outer part (Part A). The non-fuel part hoop stress was up to about 500 MPa at the end of life, which was confirmed by the literature [14]. Cracks may

be produced because of the high hoop stress of the SiC matrix during the running operation, but the cracks may have disappeared or been deflected when the cracks extended to the interface between the matrix and the TRISO particles [6]; the formation and extension of cracks will be investigated in our future work. The hoop stress decreased at the beginning and then increased. The variation of hoop stress may be attributed to the irradiation deformation of the PyC layers; the shrinkage of PyC at the beginning may release the stress of SiC matrix, and then the swelling of PyC may cause an increase in hoop stress.

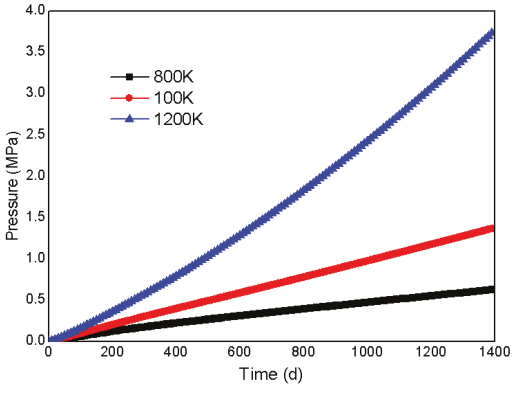

Figure 7. Fission gas pressure inside the TRISO particle throughout its life time.

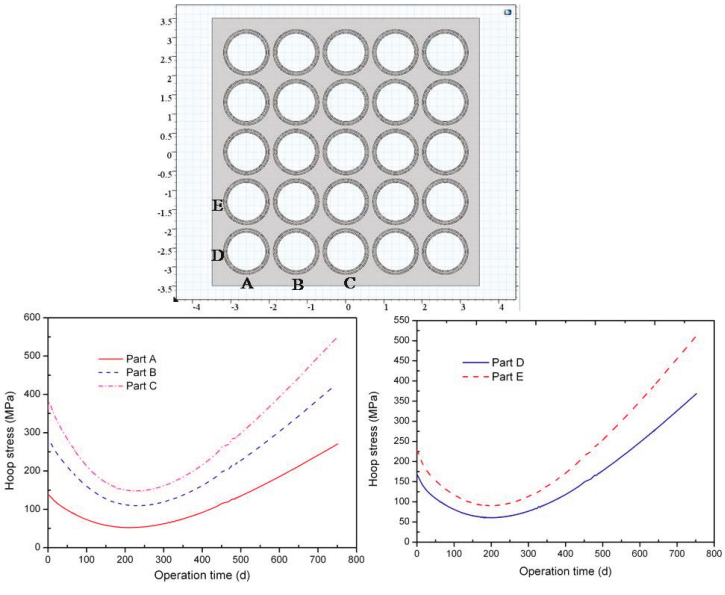

Figure 8. Variation of the hoop stress of the SiC matrix located in the marginal parts of the FCM pallet.

Figure 9 shows the hoop stress of the inner SiC matrix located between the two TRISO particles. The maximum hoop stress of the inner SiC matrix was up to 1200 MPa at the end of life, and this result was in good agreement with the literature [14] (the maximum value in the literature was about 1160 MPa). The inner SiC matrix between two TRISO particles suffered large hoop stress; the stress decreased at the beginning and then increased. This phenomenon was caused by the interaction

between the TRISO particle and the SiC matrix. The hoop stress of the SiC matrix, including the non-fuel region and the inner part, was higher than the SiC's intrinsic strength, and the SiC matrix may be broken during the operation process.

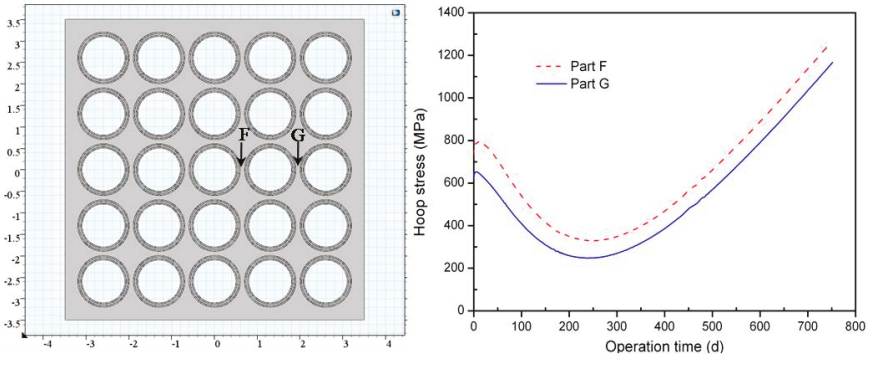

Figure 9. Variation of hoop stress of the inner SiC matrix located between two TRISO particles.

4.3. Mechanical Performance of SiC Layer

The fission product capabilities of FCM can be reflected by the structural integrity of the SiC matrix and the the SiC layers in the TRISO particles. The fission products can be effectively prevented by the SiC layers, which have been proven by an advanced gas cooled reactor [8]. The thermal-mechanical performance and failure probability of the SiC layers were important parameters to evaluate the integrity and fission product capabilities of FCM. There was no consideration of SiC layer performance on FCM pellets in previous reports as far as we know. The performance of the SiC layer located in different parts of the FCM pellet was calculated in this work.

The hoop stress of the SiC layers in TRISO particles, which embed in different parts of the FCM pellet, is shown in Figure 10, and the detected TRISO particles were labeled. SiC layers located in different parts of the FCM suffered different hoop stress. TRISO particles located in the inner part of the FCM (such as No. 1, No. 2, No. 5 and No. 8) suffered high hoop stress, which can be attributed to the high temperature gradient and thermal deformation. The maximum hoop stress of the SiC layers was about 180 MPa, which was much lower than the SiC strength (350 MPa) [15]. The maximum stress of the SiC layer was similar to the literature [19]. The hoop stress of all the SiC layers decreased at the beginning, and this result may be attributed to the irradiation deformation of the IPyC and OPyC layers, which was similar to the calculated result of the TRISO particles [22]. The irradiation deformation of the IPyC and OPyC layers can protect the SiC layers at the beginning time [19]. Then, irradiation deformation of the IPyC and OPyC layers was saturated, and the protective effect disappeared, thus the hoop stress of the SiC layer increased. The irradiation deformation of the SiC matrix may pull or push the TRISO particles located in different parts of FCM pellet, which may increase the hoop stress of the SiC layers.

The failure probability of the SiC layers located in different parts of the FCM pellet is shown in Figure 11. They are higher than the single TRISO particle with probabilities lower than 5.0×10^{-5} [22], which was confirmed by the stress distribution of the SiC layer. Similar to the single TRISO particle model, the pressure contribution to SiC failure was very limited because of the low gas release and internal pressure of the TRISO particles with the UN kernel under a PWR environment (shown in Figure 7). The maximum failure probability of the TRISO was No. 8 (showed in Figure 11), which was the inner one located on the side edge of FCM pellet. A large temperature gradient and matrix swelling deformation at a relatively low temperature (shown in Figure 1) may induce large hoop stress on the SiC layer, and the failure probability increased. As a whole, the SiC layers located in different parts of the FCM pellet suffered low stress and the integrity of the SiC layers was maintained.

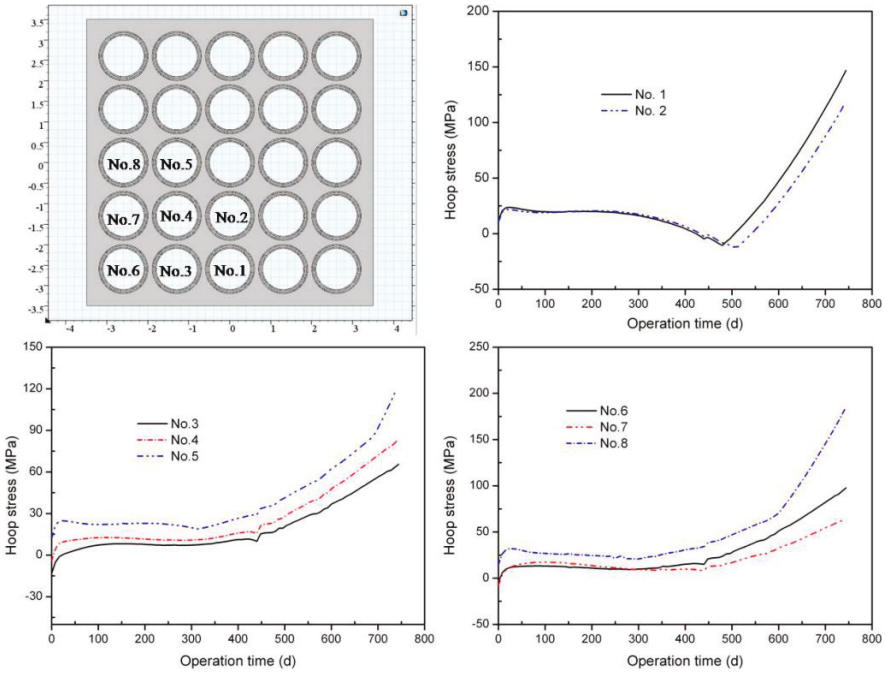

Figure 10. Variation of hoop stress on the SiC layer located in different parts in the FCM pellet.

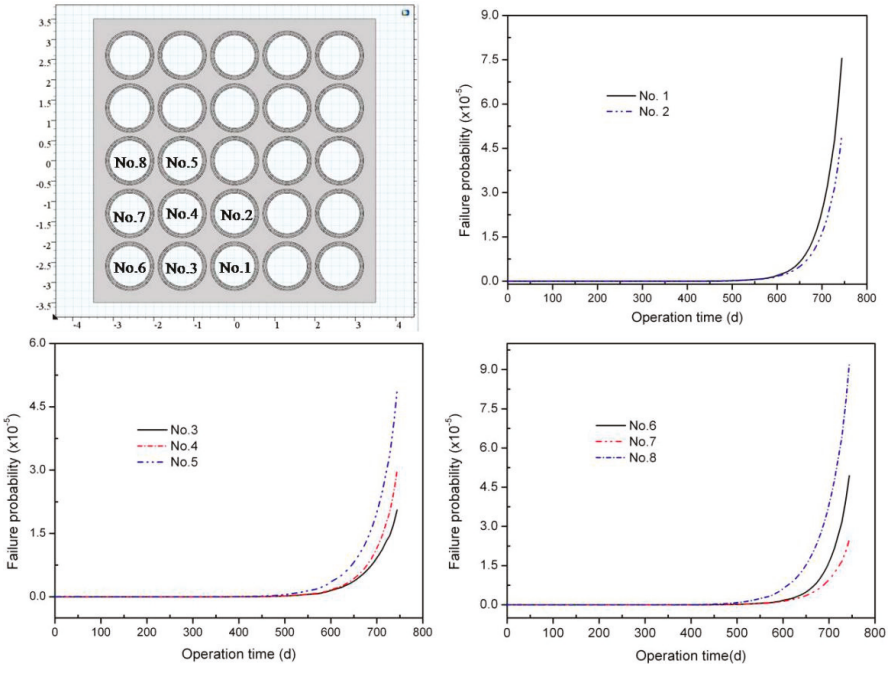

Figure 11. Failure probability of the SiC layers located in different parts of the FCM pellet.

5. Conclusions

A two-dimensional model of an FCM pellet with a homogenous distribution of TRISO particles was generated to simulate the thermal-mechanical performance of an FCM pellet. The UN kernel and buffer layers were subtracted because the kernel and buffer layer were separated from other coated layers and have little influence on the thermal-mechanical performance of the SiC layer and matrix, which has been proven by a high temperature gas cooled reactor. The interaction between the matrix and TRISO particle was considered, and the performance of SiC layer and matrix were calculated. The maximum matrix temperature increased rapidly at the beginning and was followed by a slower linear increase, which corresponded to the degradation of SiC thermal conductivity. The SiC matrix, including the non-fuel region and inner parts, suffered a large hoop, which can break the SiC matrix. The maximum hoop stress of the SiC layers located in different parts was about 180 MPa, which was much lower than the intrinsic strength of the SiC ceramics. The failure probability of the SiC layers was lower than 9×10^{-5}, which indicated that the structural integrity of the SiC layers was maintained. The integrity of the SiC layers is beneficial to the capacity of fission product retention.

Author Contributions: Conceptualization, P.C. and S.Q.; methodology, S.L.; software, S.L.; validation, Y.Z., Y.X. and S.G.; formal analysis, H.L.; investigation, X.Q.; resources, X.Q.; data curation, P.C.; writing—original draft preparation, S.L.; writing—review and editing, X.Q.; visualization, X.Q.; supervision, S.Q.; project administration, P.C.; funding acquisition, P.C.

Funding: This research received no external funding.

Conflicts of Interest: The authors declare no conflict of interest.

References

1. Chun, J.H.; Lim, S.W.; Chung, B.D. Safety evaluation of accident-tolerant FCM fueled core with SiC-coated zircalloy cladding for design-basis-accidents and beyond DBAs. *Nucl. Eng. Des.* **2015**, *289*, 287–295. [CrossRef]
2. Snead, L.L.; Terrani, K.A.; Venneri, F. Fully ceramic microencapsulated fuels: A transformational technology for present and next generation reactors-properties and fabrication of FCM fuel. *Trans. Am. Nucl. Soc.* **2011**, *104*, 668–670.
3. Snead, L.L.; Terrani, K.A.; Katoh, Y. Stability of SiC-matrix microencapsulated fuel constituents at relevant LWR conditions. *J. Nucl. Mater.* **2014**, *448*, 389–398. [CrossRef]
4. Lu, C.; Hiscox, B.D.; Terrani, K.A. Fully ceramic microencapsulated fuel in prismatic high temperature gas-cooled reactors: Analysis of reactor performance and safety Characteristics. *Ann. Nucl. Energy* **2018**, *117*, 277–287. [CrossRef]
5. Terrani, K.A.; Zinkle, S.J.; Snead, L.L. Snead, Microencapsulated fuel technology for commercial light water and advanced reactor application. *J. Nucl. Mater.* **2012**, *427*, 209–224. [CrossRef]
6. Terrani, K.A.; Kiggans, J.O.; Katoh, Y. Fabrication and characterization of fully ceramic microencapsulated fuels. *J. Nucl. Mater.* **2012**, *426*, 268–276. [CrossRef]
7. Sen, R.S.; Pope, M.A.; Ougouag, A.M. Assessment of possible cycle lengths for fully encapsulated microstructure fueled light water reactor concepts. *Nucl. Eng. Des.* **2013**, *255*, 310–320. [CrossRef]
8. Powers, J.J.; Wirth, B.D. A review of TRISO fuel performance models. *J. Nucl. Mater.* **2010**, *405*, 74–82. [CrossRef]
9. Besmann, T.M.; Ferber, M.K.; Lin, H.T. Fission product release and survivability of UN-kernel LWR TRISO fuel. *J. Nucl. Mater.* **2014**, *448*, 412–419. [CrossRef]
10. Kamalpour, S.; Salehi, A.A.; Khala, H. The potential impact of Fully Ceramic Microencapsulated (FCM) fuel on thermal hydraulic performance of SMART reactor. *Nucl. Eng. Des.* **2018**, *339*, 39–52. [CrossRef]
11. Lee, Y.; Cho, N.Z. Steady and transient-state analyses of fully ceramic microencapsulated fuel loaded reactor core via two-temperature homogenized thermal conductivity model. *Ann. Nucl. Energy* **2015**, *76*, 283–296. [CrossRef]
12. Lee, H.G.; Kim, D.; Lee, S.J. Thermal conductivity analysis of SiC ceramics and fully ceramic microencapsulated fuel composites. *Nucl. Eng. Des.* **2017**, *311*, 9–15. [CrossRef]

13. Ougouag, A.M.; Kloosterman, J.L. Investigation of bounds on particle packing in pebble-bed high temperature reactors. *Nucl. Eng. Des.* **2006**, *236*, 669–676. [CrossRef]
14. Schappel, D.; Terrani, K. *Thermo Mechanical Analysis of Fully Ceramic Microencapsulated Fuel during in-Pile Operation*; American Nuclear Society-ANS: La Grange Park, IL, USA, 2016.
15. Boer, B.; Sen, S.R.; Pope, A.M. *Material Performance of Fully-Ceramic Micro-Encapsulated Fuel under Selected LWR Design Basis Scenarios: Final Report*; INL/EXT-11-23313; Idaho National Laboratory: Idaho Falls, ID, USA, 2011.
16. Boer, B.; Ougouag, A.M. Stress analysis of coated particle fuel in graphite of High-Temperature Reactors. *Nucl. Technol.* **2008**, *162*, 276–292. [CrossRef]
17. Miller, G.K.; Petti, D.A.; Maki, J.T. *PARFUME Theory and Model Basis Report*; Idaho National Laboratory, Next Generation Nuclear Plant Project; Idaho National Laboratory: Idaho Falls, ID, USA, 2009.
18. Demancge, P.; Marian, J. TRISO fuel element thermal-mechanical performance modeling for the hybrid LIFE engine with Pu fuel blanket. *J. Nucl. Mater.* **2010**, *405*, 144–155. [CrossRef]
19. Katoh, Y.; Koyanagi, T.; Singh, G.; Terrani, K.A.; Petrie, C.M.; Snead, L.L.; Deck, C. *Irradiation-High Heat Flux Synergism in Silicon Carbide-Based Fuel Claddings for Light Water Reactors*; American Nuclear Society-ANS: La Grange Park, IL, USA, 2016.
20. Katoh, Y.; Ozawa, K.; Shih, C. Continuous SiC fiber, CVI SiC matrix composites for nuclear applications: Properties and irradiation effects. *J. Nucl. Mater.* **2014**, *448*, 448–476. [CrossRef]
21. Stone, J.G.; Schleicher, R.; Deck, C.P. Stress analysis and probalibistic assessment of multi-layer SiC-based accident tolerant nuclear fuel cladding. *J. Nucl. Mater.* **2015**, *466*, 682–697. [CrossRef]
22. Collin, B.P. Modeling and analysis of UN TRISO fuel for LWR application using the PARFUME code. *J. Nucl. Mater.* **2014**, *451*, 65–77. [CrossRef]
23. Li, W.; Wu, X.; Liu, S. Performance analysis of TRISO coated fuel particle with UN kernel. *Atom. Energy Sci. Technol.* **2018**, *52*, 283–289. (In Chinese)

© 2019 by the authors. Licensee MDPI, Basel, Switzerland. This article is an open access article distributed under the terms and conditions of the Creative Commons Attribution (CC BY) license (http://creativecommons.org/licenses/by/4.0/).

mathematics

MDPI

Article

A Numerical Study on the Crack Development Behavior of Rock-Like Material Containing Two Intersecting Flaws

Bing Dai [1], Ying Chen [1,*], Guoyan Zhao [2], Weizhang Liang [2,*] and Hao Wu [2]

[1] School of Resources Environment and Safety Engineering, University of South China, Hengyang 421000, China; daibingusc@usc.edu.cn

[2] School of Resources and Safety Engineering, Central South University, Changsha 410000, China; gyzhao@csu.edu.cn (G.Z.); hoekwu@csu.edu.cn (H.W.)

* Correspondence: csu_chenying@csu.edu.cn (Y.C.); wzlian@csu.edu.cn (W.L.); Tel.: +86-185-6906-9231 (Y.C.); +86-151-1141-9038 (W.L.)

Received: 31 October 2019; Accepted: 10 December 2019; Published: 11 December 2019

Abstract: It is quite often that rocks contain intersecting cracks. Therefore, crack behavior cannot be completely studied by only considering several isolated, single flaws. To investigate the crack behavior of rock or rock-like material containing intersecting flaws under uniaxial loading, numerical simulations were carried out using parallel bonded-particle models containing two intersecting flaws with different inclination angles (varying β) and different intersection angles (varying $\alpha\alpha$). The crack propagation processes are analyzed and two typical patterns of linkage are observed between two intersecting flaws: (1) One-tip-linkage that contains three subtypes: Coalescence position near the tip; coalescence position at the flaw, but far away from the tip; coalescence position outside the flaw at a certain distance from the tip; and (2) two-tip-linkage with two subtypes: Straight linkage and arc linkage. The geometries of flaws influence the coalescence type. Moreover, the effects of intersection angle α and inclination angle β on the peak stress, the stress of crack initiation, and the stress of crack coalescence are also investigated in detail.

Keywords: crack growth behavior; particle model; intersecting flaws; uniaxial compression

1. Introduction

Numerous discontinuities on different scales occur in rocks and rock masses, such as flaws, joints, cracks, and faults, which are induced during the formation of rock masses and successive tectonic processes. The existence of joints, cracks, or faults in rock masses has two mechanical effects [1–4]: (1) The strength and stiffness of the rock mass will be decreased; and (2) they will generate new fractures that may further develop and connect with other flaws and then may lead to the degradation of the strength and stiffness of the rock or rock mass, respectively. Therefore, the mechanism of crack propagation and coalescence is of great interest in geomechanics [5,6].

To further study the laws of cracks and the development of single cracks, physical experiments were conducted [7–18]. The observed crack patterns under uniaxial compression can be categorized as follows: (1) Wing cracks initiated at the tips of single, pre-existing flaws propagating along the direction of axial stress; and (2) secondary shear or mixed mode tensile-shear cracks initiated later from the tips of single pre-existing flaws propagating as quasi-coplanar or oblique cracks.

Crack coalescence mechanisms were studied by other researchers with rock-like materials containing two or more parallel flaws in a compression state [1,19–27]. It was observed that flaw angle, bridging angle, non-overlapping length, and frictional coefficient have significant effects on the crack initiation modes and the patterns of crack coalescence. Moreover, it was shown that the peak strength and stiffness of rocks and rock-like material depends on the number and geometry of flaws [28].

Previous work provides a good understanding of the coalescence patterns obtained from specimens with one or several single, non-intersecting flaws. However, joint patterns with more than one joint set are common in nature. Pollard and Aydin [29] defined several types of joint intersection geometries, which can be classified as orthogonal (+intersections) and non-orthogonal (X intersections). Both types can be divided into three groups according to the continuity of the joints at the intersections: (1) "all continuous joints"; (2) "continuous and discontinuous sets"; and (3) "all discontinuous sets".

Lee and Jeon [30] used three materials (PMM, Diastone and Hwangdeung granite) to study the coalescence of a horizontal flaw with an underneath lying, inclined flaw. They stated that the geometry of a double-flaw can improve the understanding of crack propagation and coalescence because echelon type of cracks can be initiated by fracture planes that are not parallel to each other. Zhang et al. also studied the crack coalescence of gypsum with two non-parallel flaws under different flaw angles and different bridge angles. Their results showed that the stress distribution in the bridge area of the non-parallel flaws is more complicated than that of the parallel flaws. This difference affects the crack initiation stress as well as the coalescence pattern. Their studies provided fundamental understanding of the coalescence of non-parallel flaws, but observations made from two non-parallel flaws can only provide a limited understanding of the complex behavior of the rock mass with several crossing discontinuities. Besides this, numerical simulation also plays an important role in crack coalescence research [1,22,31–33]. One of the popular tools nowadays is the discrete element method [18,34–40].

In the present study, numerical simulation results are shown in respect to peak strength, crack initial stress, crack coalescence stress, and coalescence patterns of rock-like material with two intersecting flaws under uniaxial compression using a bonded-particle model (BPM).

2. Numerical Simulation Procedure

We used the bonded particle model (BPM), which is one of the contact models available in the two-dimensional particle flow code (PFC2D) software for numerical simulation. Turco [41] suggested a micro-mechanical model, which completely is described by the definition of the strain energy of the interaction between two nearby grains without consideration of the dynamical effects. This model can also effectively handle large deformation processes, even if quasistatic simulations require the solution of remarkable numerical challenges because they might present instabilities and bifurcation phenomena [42]. In the present study, numerical simulation focuses on the peak strength, crack initial stress, crack coalescence stress, and coalescence patterns of rock-like material with two intersecting flaws under uniaxial compression, thus the bonded particle model (BPM) could satisfy this study.

In PFC (such as that in BPM), the model specimens are created by combining a large number of circular particles with varying diameters. These particles are interconnected using parallel bonds, as shown in Figure 1. Tensile and shear stresses acting on the parallel bonds are calculated during simulations and if the maximum tensile stress exceeds the tensile strength of the parallel bonds or the maximum shear stress exceeds the shear strength of the parallel bonds, the parallel bonds will break and a microscopic tensile or shear crack will form (Figure 1).

To resemble the real cracking processes, discrete cracks that are close enough are connected with each other by a unique technique [18]. The symbol "a" stands for the centroids' distance form a crack to the other one nearby, and the symbol "c" stands for the length of any of these two cracks (Figure 2). If a/c is less than or equal to 1, the crack, and the other one nearby, are regarded as a single continuous crack, and then the centroids of the two micro-cracks will connect with each other as a macroscopic crack trace line [18].

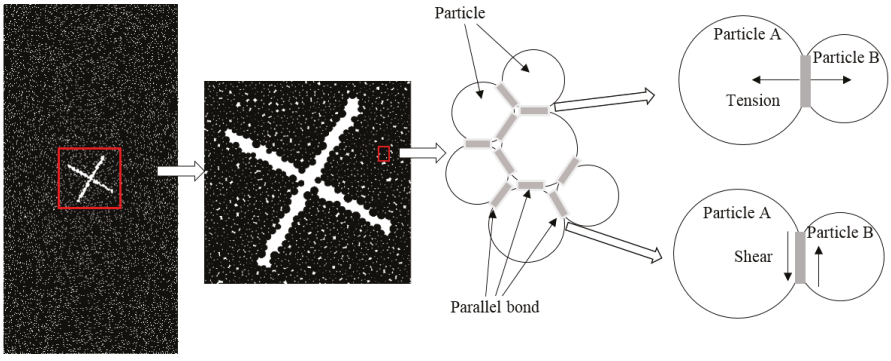

Figure 1. Illustration of the parallel bond model.

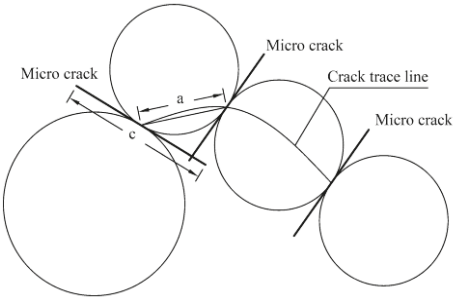

Figure 2. Constructing a macro-crack based on connecting centroids of micro-cracks [18].

The geometry and parameters of the model specimens were chosen in such a way that the model duplicates the mechanical behavior of the gypsum specimens used in the experimental investigation of Wong and his subsequent numerical simulations [43]. The model specimens were created with the dimensions 50 mm in width and 100 mm in height, which are consistent with those of the specimens used for the laboratory testing by Wong [25]. The model specimens created in this manner comprised about 19,650 particles. The porosity of the model specimens was found to be 0.01.

The simulation program consisted of two stages. First, model specimens free of pre-existing flaws (i.e., intact) were simulated. Micro-parameters for the particles were selected in order to obtain a consistent macro-scale mechanical behavior with that of the gypsum specimens used by Wong [25]. Table 1 outlines these micro parameters assigned for the particles and parallel bonds of the numerical specimens independently. The next section reports the comparison of the mechanical properties of the numerical specimens of the present study and those of the specimens used for laboratory testing by Wong [25].

The second stage of the study involved a series of numerical simulations on model specimens containing two intersecting flaws with varied geometry to explore the influence of various geometries on the mechanical behavior of model specimens; flaw length L and thickness were fixed at 20 and 1 mm for both flaws, respectively, while the intersection angle α of the two flaws varied at 90°, 60°, 45°, and 30° (Figure 3). The inclination angle of one flaw (angle β of flaw B as shown in Figure 3b) was also varied in the next stage, while α was kept unchanged. To better distinguish the crack coalescence types and for the clarity of the explanations, the bridging zone (the zone surrounding the intersection of flaws) was divided into four zones, as shown in Figure 3c (I, II, III, and IV).

Table 1. Micro-parameters used for the model specimens.

Particle Parameters	Value	Parallel Bond Parameters	Value
Ec Young's modulus of the particle	2.5 GPa	$\overline{E}$c Young's modulus of the parallel bond	2.5 GPa
kn/ks ratio of normal to shear stiffness of the particle	1	$\overline{k}$n/$\overline{k}$s ratio of normal to shear stiffness of the parallel bond	1
Grain friction coefficient,	0.01	$\overline{\sigma}$c tensile strength of the parallel bond	6 MPa
Rmax/Rmin ratio of max particle radius to min particle radius	1.66	$\overline{c}$ cohesion of the parallel bond	15 MPa
Rmin Lower bound of particle radius	0.21 mm	$\overline{\lambda}$ radius multiplier	1
ρ particle density	1.83 g/m^3	$\overline{\Phi}$ Friction angle of the parallel bond	0

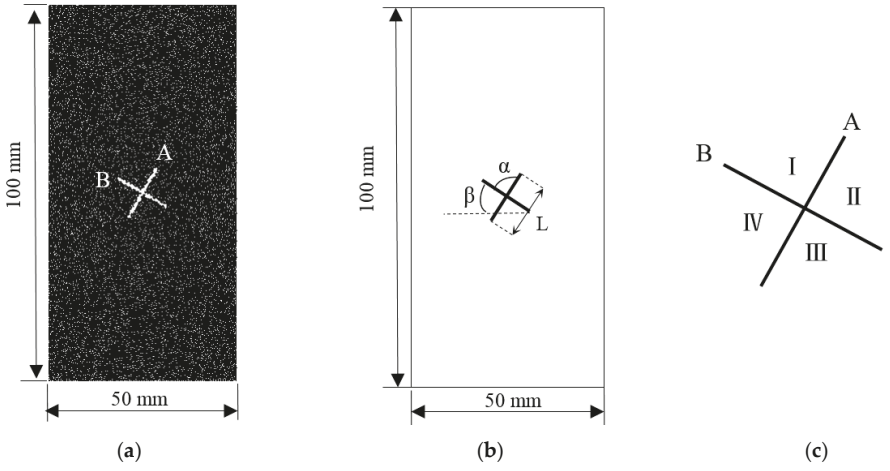

Figure 3. Geometries of the model containing two intersecting flaws: (**a**) Flaws are numbered A and B; (**b**) flaw inclination angle β, intersection angle α and flaw length L; and (**c**) four bridging zones.

For all the simulations in the present numerical study, specimens were vertically loaded in a velocity-controlled manner and no confining pressure was applied (i.e., uniaxial compression). A sufficiently low loading rate −0.05 m/s was applied to ensure that the specimens remained in a quasi-static equilibrium throughout the test.

3. Results and Discussion

3.1. Mechanical Properties of Intact Models

We first determined the macro-scale mechanical properties of the model specimens and compared them with the corresponding properties reported by Wong [43]. Table 2 and Figure 4 show this comparison. It can be seen that the numerical model has very closely reproduced the mechanical behavior of gypsum specimens used in the laboratory investigation by Wong [43]. Following this verification, we simulated the mechanical behavior of specimens containing two intersecting flaws and the forthcoming sub-sections report the results of those simulations.

Table 2. Lab test results [43] vs. numerical simulation results.

Parameter	Experimental Tests	BPM
Density (g/cm^3)	1.54	1.54
Young's modulus (GPa)	5.96	6.09
Poisson's ratio	0.15	0.15
Uniaxial compressive strength (MPa)	33.85	34.2
Tensile strength (MPa)	3.2	4.8

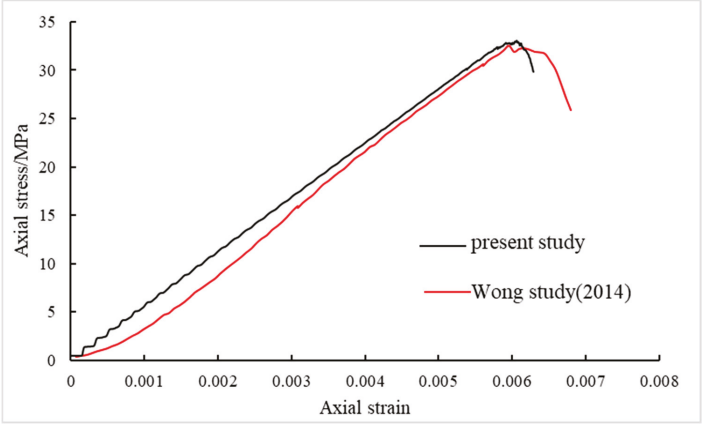

Figure 4. The stress-strain curves: Lab test vs. numerical simulation results.

3.2. Mechanical Behavior of Specimens Containing Flaws

3.2.1. Effect of the Flaw Geometries on Peak Strength

The influence of flaw geometry was investigated in regards to the strength of the sandstone samples, gypsum, and marble containing single crack, parallel cracks, or non-parallel cracks in uniaxial loading [20,21,44,45]. Their results revealed that flaw geometry has a key effect on the strength. Thus, variations of peak strength against β for different values of α are shown in Figure 5.

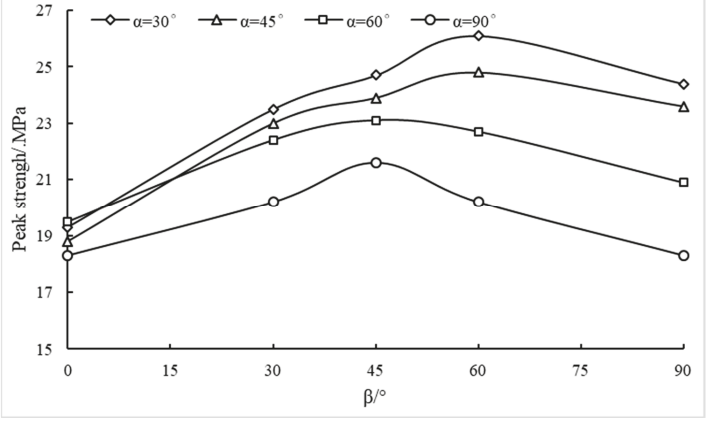

Figure 5. Variations of peak strength against β for different values of α.

From Figure 5, the following general trends can be deduced:

(1) For low values of α (below app. 50°), the peak strength first increases up to about β = 60° and then decreases.
(2) For higher values of α (above app. 50°), the peak strength first increased up to about β = 45° and then decreased.
(3) For the values of β (above app. 15°), the peak strength decreased with increasing α.

To explain this, the peak strengths of the model containing single crack against β for different initial angles are shown in Figure 6.

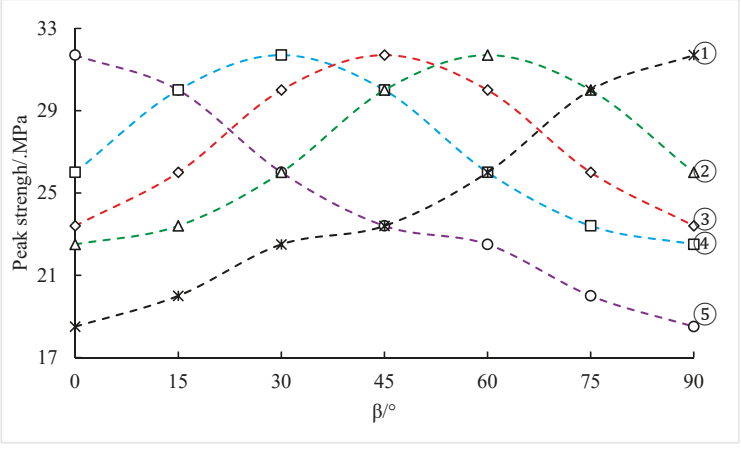

Figure 6. The peak strengths of the model containing a single flaw against β for different flaw initial inclination angles. ① ② ③ ④ ⑤ curves corresponding to five flaw initial inclination angles in Figure 7.

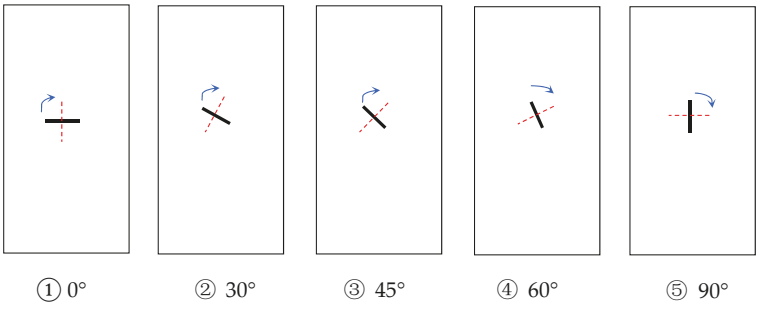

Figure 7. Five flaw initial inclination angles of the model containing a single flaw. The red dotted line represents the final state of rotation for the flaw. The blue arrow represents the direction of rotation.

The overall strength of a rock mass containing two sets of discontinues is given by the lowest strength envelope in the individual strength curves, according to Bray's suggestion [46]. It is clear from Figure 6 that the strength curves of the model containing intersect cracks had a similar trend with the lowest strength envelope in the individual strength curves. For example, the lowest strength envelope in the individual strength curves ① ⑤ show the strength of the model containing two intersect cracks (α = 90°); the peak strength first increases up to about β = 45° and then decreases with the increase of the inclination angle. It is worth noting that the lowest strength envelope in the individual strength curves ① ④ are a little bit different (when β = 60°) from the trend of α = 60° in Figure 5. One plausible explanation is that it was due to the two cracks effecting each other. Another plausible explanation is that it was due to a random distribution of particle sizes.

3.2.2. Crack Initiation and Coalescence Behavior

The crack evolution of models containing two intersecting flaws (α = 90°, 60°, 45°, and 30°) is shown in Table 3. Five stages corresponded to five points on the stress–strain curve in Figure 8: Document crack initiation, propagation, coalescence, as well as crack type at peak stress or post-peak stress level. To shorten and avoid repetition, only selected constellations of α and β are documented in detail.

Table 3. The crack evolution pattern at different stages of loading with different flaw geometry. The cracks corresponding to five points on the stress–strain curve in Figure 8. Microscopic tensile and shear cracks are shown in white and red, respectively. Original flaws are in yellow.

Flaw Geometry	Crack Evolution Pattern at Different Stages of Loading				
	(A)	(B)	I	(D)	I
α = 90° β = 30°			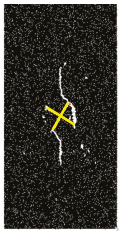	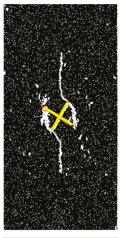	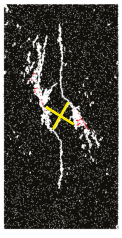
α = 60° β = 0°		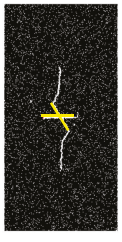	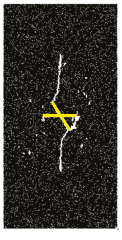	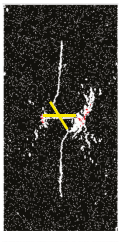	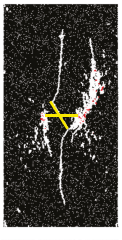
α = 45° β = 45°	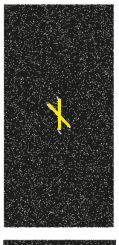	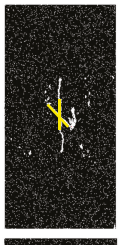	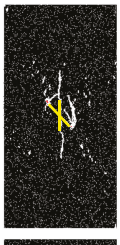	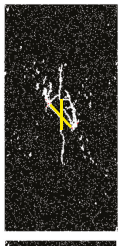	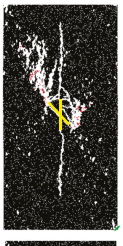
α = 30° β = 0°	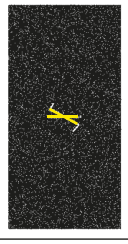	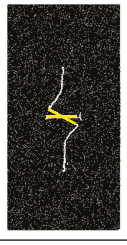	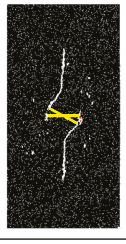	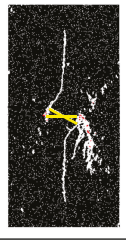	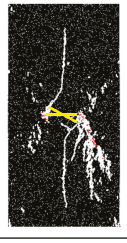

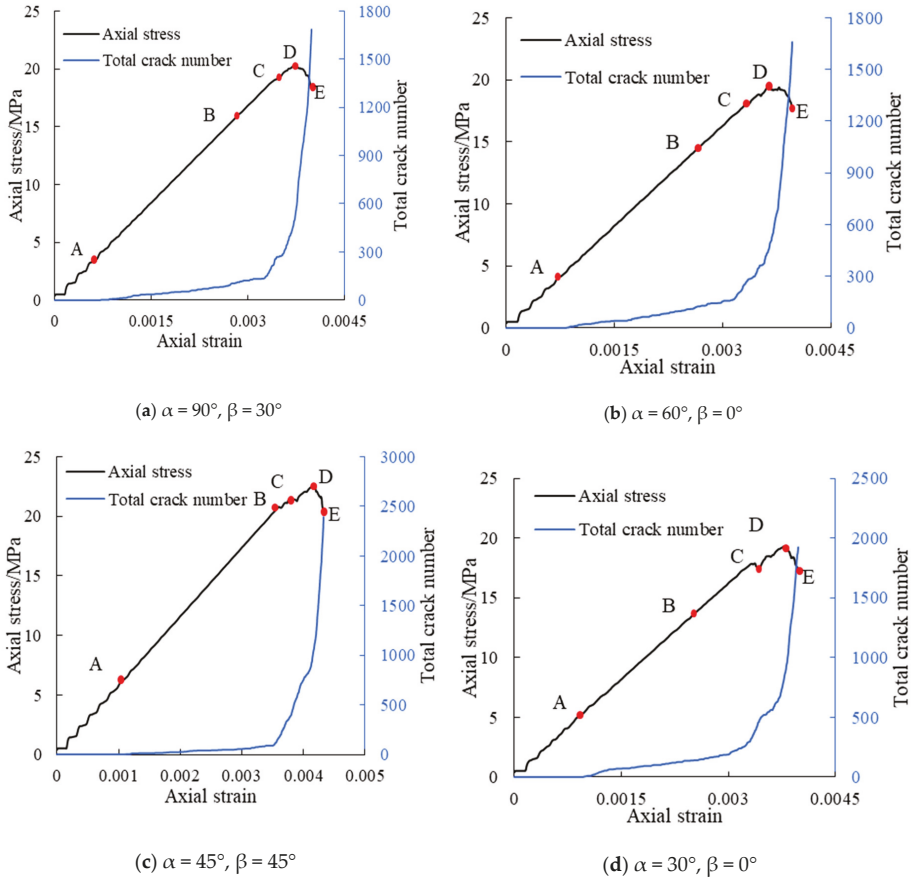

Figure 8. Axial stress (black line) and total crack number (blue line) versus axial strain with different values of α and β. Five points, A, B, C, D, and E, on the stress–strain curve are monitored to observe the crack initiation, propagation, and coalescence.

For flaw geometry with α = 90° and β = 30°, macroscopic wing cracks initiate from the tips of the A flaw. With an increasing load, the wing cracks extend, and macroscopic tensile cracks appear in the tip area of the B flaw as secondary cracks. When axial stress reaches 18.8 MPa, the first coalescence is achieved in bridge zone II by the extension of the secondary crack starting from the right tip of the B flaw. During a further load increase up to the peak strength, a downward extension of the macroscopic tensile crack, starting from the left tip of the B flaw, reaches the left tip of the A flaw, and the second coalescence occurs in bridge zone IV. The test specimen is broken by the development of cracks during the post-peak stress stage. The coalescence cracks in the bridge region become progressively wider during the cracking processes.

For flaw geometry with α = 60° and β = 0°, and when axial stress has reached 4.8 MPa, macroscopic wing cracks start to propagate from the tips of the A flaw. With a further load increase, the wing cracks extend and some microscopic cracks appear in the tip area of the B flaw (secondary cracks). At 18 MPa vertical stress, the first coalescence is achieved in bridge zone III by the extension of the secondary crack initiated from the right tip of the B flaw. At peak stress of 19.5 MPa, coalescence cracks become wider and some new microscopic tensile and shear cracks propagate downwards or upwards from the

tips of the B flaw. Beyond peak stress, some secondary cracks extend quickly towards the edge of the model, and finally the model fails.

For flaw geometry with $\alpha = 45°$ and $\beta = 45°$, macroscopic tensile cracks start from the tips of the A flaw. With an increasing load, wing cracks extend and some microscopic tensile cracks are initiated at the tips of the B flaw. With a further stress increase, secondary tensile and shear cracks propagate towards the wing crack initiated at the top tip of the A flaw. At 21.1 MPa, the first coalescence occurs in bridge zone I. At peak stress of 23.9 MPa, the secondary cracks propagate further upwards from the right tip of the B flaw towards the top tip of the A flaw. Secondary coalescence occurs in bridge zone II. Additional cracks are induced close to the B flaw tip regions in the post-peak stage.

For flaw geometry with $\alpha = 30°$ and $\beta = 0°$, at 5.4 MPa, a macroscopic wing crack starts to propagate from the tips of the A flaw. Further load increases lead to the initiation of micro tensile cracks at the right tip of the B flaw. When the axial stress increases further up to 17.6 MPa, the first coalescence is achieved in bridge zone III by the extension of a secondary crack initiated from the right tip of the B flaw. At peak strength, coalescence occurs in bridge zone I. Meanwhile, some mixed mode tensile–shear cracks appear and extend downwards near the right tips of the A and B flaws. In the post-peak region at a stress of 17.4 MPa, some secondary cracks become wider and extend to the edge of the model and the model fails.

3.3. Crack Initiation Stress

In the numerical studies performed by Zhang et al., wing cracks start to propagate simultaneously at the tips of the flaws. However, in this study, the macro-cracks initiated at the tips of the two intersecting flaws do not occur simultaneously. Therefore, the stress state when a macro-crack starts to develop from either the A flaw or B flaw is called crack initiation (CI) stress.

Specimens with different flaw geometries have different peak strengths; therefore, CI stress cannot be compared directly. Thus, the CI stress σ_{ci} is normalized by the respective peak strength σ_{cn} (see Figure 9). From Figure 9, the following general trends can be deduced:

1. The ration σ_{ci}/σ_{cn} varies between 0.2 and 0.4.
2. For the same values of α, the minimum values of σ_{ci}/σ_{cn} are observed at $\beta = 30°$, which means that the first crack initiates more easily (except $\alpha = 60°$, $\beta = 45°$). For four cases of $\beta = 90°$ and one case of $\beta = 0°$, $\alpha = 90°$ is the maximum value of σ_{ci}/σ_{cn} observed.

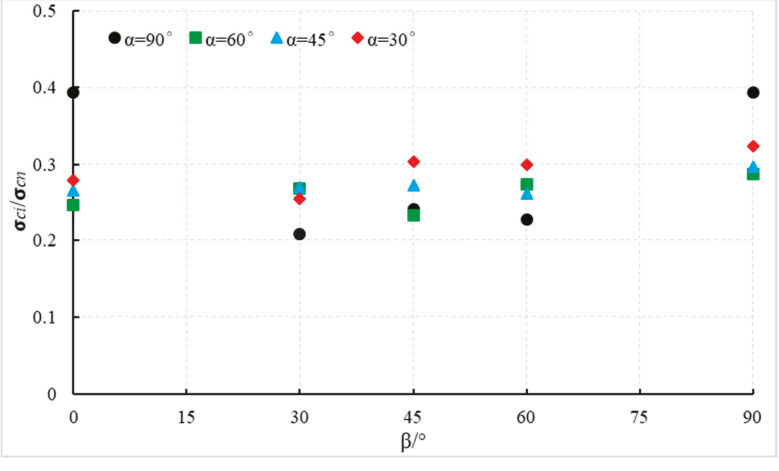

Figure 9. σ_{ci}/σ_{cn} versus flaw inclination angle β for different values of α.

To better understand the effect of α and β in the ratio σ_{ci}/σ_{cn}, the differences ($\Delta\ \sigma_{ci}/\sigma_{cn}$) between the maximum and minimum values of σ_{ci}/σ_{cn} are calculated, as shown in Figure 9. From Figure 10a, the difference of σ_{ci}/σ_{cn} is first decreased down to α = 45° and then increased with the increase of α, which indicates that the inclination angle β had less effect on the ration σ_{ci}/σ_{cn} when α = 45°.

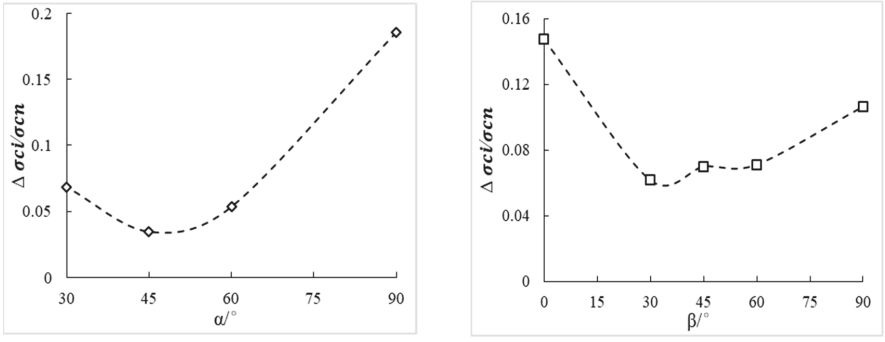

Figure 10. Variations of $\Delta\ \sigma_{ci}/\sigma_{cn}$ against α (**a**) and β (**b**).

From Figure 10b, it can be deduced that the difference of σ_{ci}/σ_{cn} also decreases down to β = 30° and then increases with the increase of β, which indicates that the intersection angle α had less of an effect on the ration σ_{ci}/σ_{cn} when β = 30°.

3.4. Crack Coalescence

Many crack coalescence types have been observed in physical experiments [1,21,26] and have been classified as seven different crack coalescence types, based on their geometry and propagation mechanism using a high-speed camera. Zhang [40] classified five types of linkages observed between two non-parallel flaws using parallel bonded-particle models. However, these crack coalescence types are based on the coalescence between two parallel or non-parallel flaws. Our study reveals that two intersect flaws show different coalescence behavior. Table 4 shows the crack coalescence patterns for two intersecting flaws with different values for α and β.

The different crack coalescence patterns observed in the case of two intersecting flaws with different geometries are shown in Figure 11 and are summarized in Table 5. Two typical patterns can be distinguished:

1. A macroscopic tensile crack initiated from the tip of one of the flaws extends upwards or downwards to the other flaw but does not reach the tip and some microscopic shear or mixed tensile-shear cracks participate at coalescence. This is classified as one-tip-linkage. According to the coalescence position, the one-tip-linkage mechanism contains three sub-types: Coalescence position near the tip (Figure 11(1),(2)), coalescence position at the flaw, but far away from the tip (Figure 11(4)), or coalescence position outside the flaw with a certain distance from the tip (Figure 11(3)).
2. A macroscopic tensile crack initiated from the tip of one flaw extends upwards or downwards to the tip of the other flaw. The coalescence occurred by the linkage of tensile cracks and is classified as two-tips-linkage. The two tips linkage has two sub-types: Straight linkage (Figure 11(5)) and arc linkage (Figure 11(6)).

Table 4. Crack coalescence patterns for two intersecting flaws with different values of α and β. Microscopic tensile and shear cracks are shown in white and red, respectively. Original flaws are in yellow.

Flaw Geometry	The Crack Coalescence Patterns of Loading				
	β = 0°	β = 30°	β = 45°	β = 60°	β = 90°
α = 90°	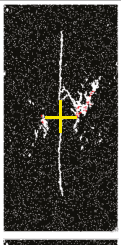	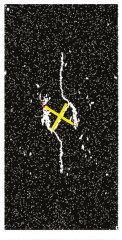	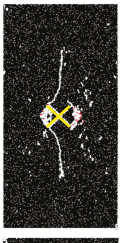	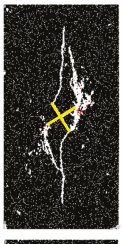	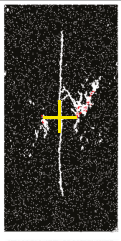
α = 60°	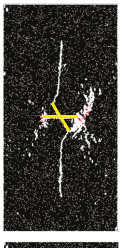	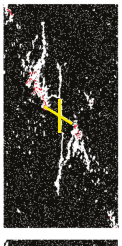	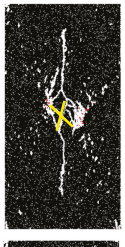	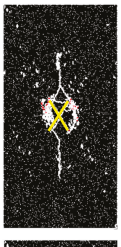	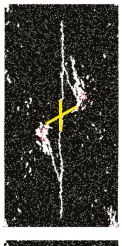
α = 45°	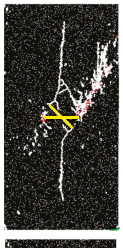	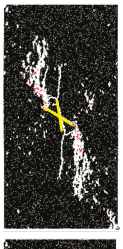	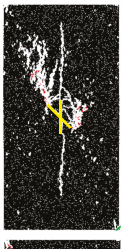	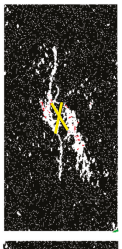	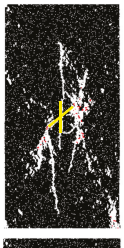
α = 30°	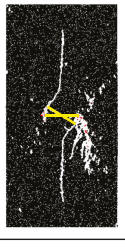	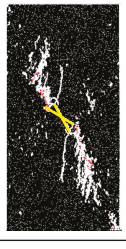	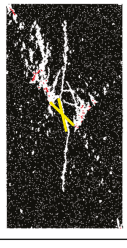	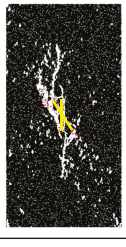	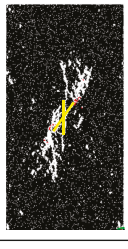

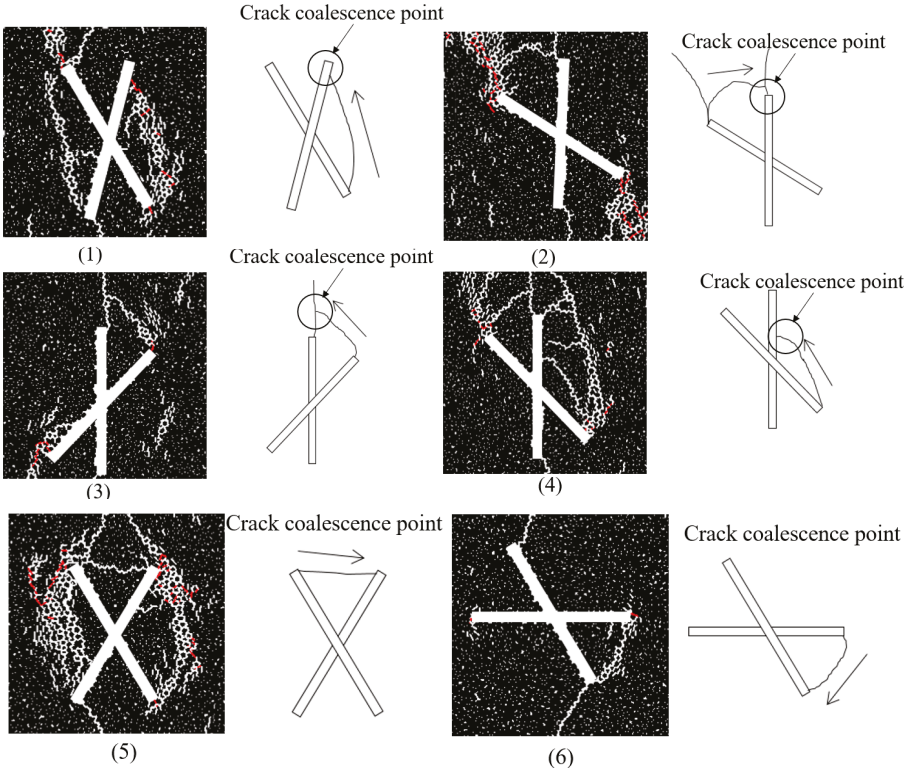

Figure 11. Observed crack coalescence patterns for two intersecting flaws (left: Simulation results, right: Simplified sketch). White and red segments represent microscopic tensile and shear cracks, respectively. The arrows represent the crack propagation direction.

Table 5. The coalescence patterns of different geometries.

Angle/°	Coalescence Types of Different Geometries									
	β = 0°		β = 30°		β = 45°		β = 60°		β = 90°	
	Type	Zone	Type	Zone	Type	Zone	Type	Zone	Type	Zone
α = 90°	(3)	II	(6)	II IV	(6)	II IV	(3) (6)	II III	(3)	II
α = 60°	(6)	III	(2) (3)	I III	(1) (2) (3) (4) (5)	I II IV	(1) (5) (6)	I II IV	(3)	I III
α = 45°	(3)	II	(2) (6)	I III	(2) (3) (4) (6)	I II	(1) (4) (6)	II IV	(3) (6)	I II
α = 30°	(5) (6)	I III	(5) (6)	I III	(2) (3)	I II	(2) (3) (4)	I III IV	(3) (4) (6)	I III

3.5. Crack Coalescence Stress

The coalescence stress σ_{co} is the vertical stress that is observed when the first coalescence of the two intersecting flaws occurs. The ratio between crack coalescence stress σ_{co} and peak strength σ_{cn} varies, as shown in Figure 12. The crack coalescence stress reaches 85%–100% of the peak stress.

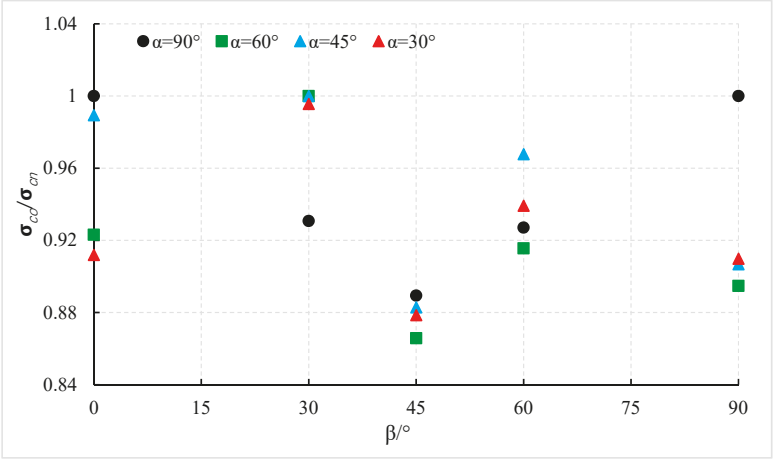

Figure 12. Ratio between coalescence stress σ_{co} and peak strength σ_{cn} for different values of α and β.

For two cases of α = 90° and one case of α = 60°, α = 45°, and α = 30°, the ratios of their cases are at or just less than 1.0, which means that their model coalesced near or at the peak stress. In contrast, for four cases of β = 45°, three cases of β = 90°, and one case of β = 0°, the ratios of their cases are significantly less than 1.0, which means that the coalescence occurs more easily. In addition, for any intersection angle α, the minimum values of σ_{co}/σ_{cn} are observed at β = 45°, which indicates that coalescence occurred more easily with that geometry.

4. Conclusions

Numerical simulations were performed on rock-like specimens containing two intersecting flaws with different inclination angle β and different intersection angle α subjected to uniaxial compressive loads. The main conclusions can be summarized as follows:

1. For any intersection angle α, the strength is increases for flaw inclination angle β, ranging from 0° to about 45°. For intersection angle α up to about 45°, the strength is further slightly increased for inclination angle β, bigger than 45°. For intersection angle α, it is bigger than about 45° and the strength is strongly decreased for inclination angle β, bigger than 45°.
2. The macro-crack initiated from the tips of two intersect flaws that did not occur simultaneously. The crack initial stress σ_ci of the first crack, obtained at the tip of flaw (A flaw or B flaw), normalized by the respective specimen peak strength σ_{cn}, which changed between 0.2 and 0.4 with different flaw geometries.
3. Two major crack coalescence patterns were observed: (a) One-tip-linkage (either near the crack tip, at the flaw but far away from the crack tip or outside the flaw at a certain distance from the tip) and (b) two-tips-linkage (straight or arc linkage). The geometry of flaws governed the coalescence type.

The ratio between coalescence stress σ_{co} and peak strength σ_{cn} varied between 0.85–1.0, which meant the first coalescence occurred near or at the peak strength. For the same values of α, the minimum values of σ_{co}/σ_{cn} were observed at β = 45°, which indicated that coalescence occurred more easily with that geometry.

Author Contributions: Conceptualization, B.D.; Methodology, Y.C.; Software, G.Z.; Validation, W.L.; Formal analysis, H.W.; Data curation, Y.C.; Writing—original draft preparation, Y.C.; Writing—review and editing, B.D.; Funding acquisition, B.D.

Funding: This study was financially supported by the national natural science foundation (51804163).

Conflicts of Interest: The authors declare no conflict of interest.

References

1. Bobet, A.; Einstein, H.H. Fracture coalescence in rock-type materials under uniaxial and biaxial compression. *Int. J. Rock Mech. Min. Sci.* **1998**, *35*, 863–888. [CrossRef]
2. Peng, K.; Zhou, J.; Zou, Q.; Yan, F. Deformation characteristics of sandstones during cyclic loading and unloading with varying lower limits of stress under different confining pressures. *Int. J. Fatigue* **2019**, *127*, 82–100. [CrossRef]
3. Hoek, E.; Martin, C.D. Fracture initiation and propagation in intact rock–a review. *J. Rock Mech. Geotech. Eng.* **2014**, *6*, 287–300. [CrossRef]
4. Peng, K.; Zhou, J.; Zou, Q.; Zhang, J.; Wu, F. Effects of stress lower limit during cyclic loading and unloading on deformation characteristics of sandstones. *Constr. Build. Mater.* **2019**, *217*, 202–215. [CrossRef]
5. Liang, W.; Zhao, G.; Wang, X.; Zhao, J.; Ma, C. Assessing the rockburst risk for deep shafts via distance-based multi-criteria decision making approaches with hesitant fuzzy information. *Eng. Geol.* **2019**, *260*, 105211. [CrossRef]
6. Wang, S.; Li, X.; Yao, J.; Gong, F.; Li, X.; Du, K.; Du, S. Experimental investigation of rock breakage by a conical pick and its application to non-explosive mechanized mining in deep hard rock. *Int. J. Rock Mech. Min. Sci.* **2019**, *122*, 104063. [CrossRef]
7. Adams, M.; Sines, G. Crack extension from flaws in a brittle material subjected to compression. *Tectonophysics* **1978**, *49*, 97–118. [CrossRef]
8. Peng, K.; Liu, Z.; Zou, Q.; Zhang, Z.; Zhou, J. Static and dynamic mechanical properties of granite from various burial depths. *Rock Mech. Rock Eng.* **2019**, *52*, 3545–3566.
9. Camones, L.A.M.; do Amaral Vargas, E.; de Figueiredo, R.P.; Velloso, R.Q. Application of the discrete element method for modeling of rock crack propagation and coalescence in the step-path failure mechanism. *Eng. Geol.* **2013**, *153*, 80–94. [CrossRef]
10. Dyskin, A.V.; Sahouryeh, E.; Jewell, R.J.; Joer, H.; Ustinov, K.B. Influence of shape and locations of initial 3-D cracks on their growth in uniaxial compression. *Eng. Fract. Mech.* **2003**, *70*, 2115–2136. [CrossRef]
11. Peng, K.; Wang, Y.; Zou, Q.; Liu, Z.; Mou, J. Effect of crack angles on energy characteristics of sandstones under a complex stress path. *Eng. Fract. Mech.* **2019**, *218*, 106577. [CrossRef]
12. Li, Y.P.; Chen, L.Z.; Wang, Y.H. Experimental research on pre-cracked marble under compression. *Int. J. Solids Struct.* **2005**, *42*, 2505–2516. [CrossRef]
13. Zhang, B.; Li, Y.; Fantuzzi, N.; Zhao, Y.; Liu, Y.-B.; Peng, B.; Chen, J. Investigation of the Flow Properties of CBM Based on Stochastic Fracture Network Modeling. *Materials* **2019**, *12*, 2387. [CrossRef]
14. Wong, L.N.Y.; Einstein, H.H. Crack coalescence in molded gypsum and Carrara marble: Part 1. Macroscopic observations and interpretation. *Rock Mech. Rock Eng.* **2009**, *42*, 475–511. [CrossRef]
15. Wong, L.N.Y.; Einstein, H.H. Crack coalescence in molded gypsum and Carrara marble: Part 2—Microscopic observations and interpretation. *Rock Mech. Rock Eng.* **2009**, *42*, 513–545. [CrossRef]
16. Wong, R.H.C.; Chau, K.T.; Tang, C.A.; Lin, P. Analysis of crack coalescence in rock-like materials containing three flaws—Part I: Experimental approach. *Int. J. Rock Mech. Min. Sci.* **2001**, *38*, 909–924. [CrossRef]
17. Yang, S.Q. Crack coalescence behavior of brittle sandstone samples containing two coplanar fissures in the process of deformation failure. *Eng. Fract. Mech.* **2011**, *78*, 3059–3081. [CrossRef]
18. Zhang, X.P.; Wong, L.N.Y. Cracking processes in rock-like material containing a single flaw under uniaxial compression: A numerical study based on parallel bonded-particle model approach. *Rock Mech. Rock Eng.* **2012**, *45*, 711–737. [CrossRef]
19. Ko, T.Y.; Einstein, H.; Kemeny, J. Crack coalescence in brittle material under cyclic loading. In Proceedings of the Golden Rocks 2006, The 41st US Symposium on Rock Mechanics (USRMS), Golden, CO, USA, 17–21 June 2006; American Rock Mechanics Association: Alexandria, VA, USA, 2006.
20. Park, C.H.; Bobet, A. Crack coalescence in specimens with open and closed flaws: A comparison. *Int. J. Rock Mech. Min. Sci.* **2009**, *46*, 819–829. [CrossRef]

21. Sagong, M.; Bobet, A. Coalescence of multiple flaws in a rock-model material in uniaxial compression. *Int. J. Rock Mech. Min. Sci.* **2002**, *39*, 229–241. [CrossRef]
22. Tang, C.A.; Lin, P.; Wong, R.H.C.; Chau, K.T. Analysis of crack coalescence in rock-like materials containing three flaws—Part II: Numerical approach. *Int. J. Rock Mech. Min. Sci.* **2001**, *38*, 925–939. [CrossRef]
23. Zhang, Z.; Cao, S.; Li, Y.; Guo, P.; Yang, H.; Yang, T. Effect of moisture content on methane adsorption- and desorption- induced deformation of tectonically deformed coal. *Adsorpt. Sci. Technol.* **2018**, *36*, 1648–1668. [CrossRef]
24. Wong, L.N.Y.; Li, H.Q. Numerical study on coalescence of two pre-existing coplanar flaws in rock. *Int. J. Solids Struct.* **2013**, *50*, 3685–3706. [CrossRef]
25. Zhao, Y.; Cao, S.; Li, Y.; Zhang, Z.; Guo, P.; Yang, H.; Zhang, S.; Pan, R. The occurrence state of moisture in coal and its influence model on pore seepage. *RSC Adv.* **2018**, *8*, 5420–5432. [CrossRef]
26. Wong, R.H.; Chau, K.T. Crack coalescence in a rock-like material containing two cracks. *Int. J. Rock Mech. Min. Sci.* **1998**, *35*, 147–164. [CrossRef]
27. Yang, S.Q.; Jing, H.W. Strength failure and crack coalescence behavior of brittle sandstone samples containing a single fissure under uniaxial compression. *Int. J. Fract.* **2011**, *168*, 227–250. [CrossRef]
28. Yang, S.Q. *Strength, Failure and Crack Evolution Behavior of Rock Material Containing Pre-Existing Fissures*; Springer: Cham, Switzerland, 2015; p. 246.
29. Pollard, D.D.; Aydin, A. Progress in understanding jointing over the past century. *GSA Bull.* **1988**, *100*, 1181–1204. [CrossRef]
30. Lee, H.; Jeon, S. An experimental and numerical study of fracture coalescence in pre-cracked specimens under uniaxial compression. *Int. J. Solids Struct.* **2011**, *48*, 979–999. [CrossRef]
31. Li, H.; Wong, L.N.Y. Influence of flaw inclination angle and loading condition on crack initiation and propagation. *Int. J. Solids Struct.* **2012**, *49*, 2482–2499. [CrossRef]
32. Ning, Y.; Yang, J.; An, X.; Ma, G. Modelling rock fracturing and blast-induced rock mass failure via advanced discretisation within the discontinuous deformation analysis framework. *Comput. Geotech.* **2011**, *38*, 40–49. [CrossRef]
33. Wu, Z.; Wong, L.N.Y. Frictional crack initiation and propagation analysis using the numerical manifold method. *Comput. Geotech.* **2012**, *39*, 38–53. [CrossRef]
34. Amarasiri, A.; Kodikara, J. Use of material interfaces in DEM to simulate soil fracture propagation in Mode I cracking. *Int. J. Geomech.* **2010**, *11*, 314–322. [CrossRef]
35. Cundall, P.A.; Strack, O.D. A discrete numerical model for granular assemblies. *Geotechnique* **1979**, *29*, 47–65. [CrossRef]
36. Chen, W.; Konietzky, H.; Tan, X.; Frühwirt, T. Pre-failure damage analysis for brittle rocks under triaxial compression. *Comput. Geotech.* **2016**, *74*, 45–55. [CrossRef]
37. Chen, W.; Konietzky, H.; Abbas, S.M. Numerical simulation of time-independent and-dependent fracturing in sandstone. *Eng. Geol.* **2015**, *193*, 118–131. [CrossRef]
38. Gui, Y.L.; Zhao, Z.Y.; Kodikara, J.; Bui, H.H.; Yang, S.Q. Numerical modelling of laboratory soil desiccation cracking using UDEC with a mix-mode cohesive fracture model. *Eng. Geol.* **2016**, *202*, 14–23. [CrossRef]
39. Gui, Y.L.; Bui, H.H.; Kodikara, J.; Zhang, Q.B.; Zhao, J.; Rabczuk, T. Modelling the dynamic failure of brittle rocks using a hybrid continuum-discrete element method with a mixed-mode cohesive fracture model. *Int. J. Impact Eng.* **2016**, *87*, 146–155. [CrossRef]
40. Zhang, X.P.; Wong, L.N.Y.; Wang, S. Effects of the ratio of flaw size to specimen size on cracking behavior. *Bull. Eng. Geol. Environ.* **2015**, *74*, 181–193. [CrossRef]
41. Turco, E. In-plane shear loading of granular membranes modeled as a Lagrangian assembly of rotating elastic particles. *Mech. Res. Commun.* **2018**, *92*, 61–66. [CrossRef]
42. Turco, E.; dell'Isola, F.; Misra, A. A nonlinear Lagrangian particle model for grains assemblies including grain relative rotations. *Int. J. Numer. Anal. Methods Geomech.* **2019**, *43*, 1051–1079. [CrossRef]
43. Wong, L.N.Y.; Zhang, X.P. Size effects on cracking behavior of flaw-containing specimens under compressive loading. *Rock Mech. Rock Eng.* **2014**, *47*, 1921–1930. [CrossRef]
44. Shen, B.; Stephansson, O.; Einstein, H.H.; Ghahreman, B. Coalescence of fractures under shear stresses in experiments. *J. Geophys. Res. Ser.* **1995**, *100*, 5975. [CrossRef]

45. Vesga, L.F.; Vallejo, L.E.; Lobo-Guerrero, S. DEM analysis of the crack propagation in brittle clays under uniaxial compression tests. *Int. J. Numer. Anal. Methods Geomech.* **2008**, *32*, 1405–1415. [CrossRef]
46. Bray, J.W. A study of jointed and fractured rock. *Rock Mech. Eng. Geol.* **1967**, *5*, 117–136.

© 2019 by the authors. Licensee MDPI, Basel, Switzerland. This article is an open access article distributed under the terms and conditions of the Creative Commons Attribution (CC BY) license (http://creativecommons.org/licenses/by/4.0/).

mathematics

MDPI

Article

Cost-Based Optimum Design of Reinforced Concrete Retaining Walls Considering Different Methods of Bearing Capacity Computation

Neda Moayyeri [1], Sadjad Gharehbaghi [1] and Vagelis Plevris [2,*]

[1] Department of Civil Engineering, Behbahan Khatam Alanbia University of Technology, Behbahan P.O. Box 6361647189, Iran; moayyeri@bkatu.ac.ir (N.M.); sgharehbaghi@bkatu.ac.ir (S.G.)
[2] Department of Civil Engineering and Energy Technology, OsloMet—Oslo Metropolitan University, 0166 Oslo, Norway
* Correspondence: vageli@oslomet.no; Tel.: +47-67238853

Received: 30 October 2019; Accepted: 8 December 2019; Published: 12 December 2019

Abstract: This paper investigates the effect of computing the bearing capacity through different methods on the optimum construction cost of reinforced concrete retaining walls (RCRWs). Three well-known methods of Meyerhof, Hansen, and Vesic are used for the computation of the bearing capacity. In order to model and design the RCRWs, a code is developed in MATLAB. To reach a design with minimum construction cost, the design procedure is structured in the framework of an optimization problem in which the initial construction cost of the RCRW is the objective function to be minimized. The design criteria (both geotechnical and structural limitations) are considered constraints of the optimization problem. The geometrical dimensions of the wall and the amount of steel reinforcement are used as the design variables. To find the optimum solution, the particle swarm optimization (PSO) algorithm is employed. Three numerical examples with different wall heights are used to capture the effect of using different methods of bearing capacity on the optimal construction cost of the RCRWs. The results demonstrate that, in most cases, the final design based on the Meyerhof method corresponds to a lower construction cost. The research findings also reveal that the difference among the optimum costs of the methods is decreased by increasing the wall height.

Keywords: reinforced concrete; retaining wall; optimization; bearing capacity; particle swarm optimization; PSO

1. Introduction

Reinforced concrete retaining walls (RCRWs) are referred to as structures that withstand the pressure resulting from the difference in the levels caused by embankments, excavations, and/or natural processes. Such situations frequently occur in the construction of several structures, such as bridges, railways, and highways. Due to the frequent application of RCRWs in civil engineering projects, minimizing the construction cost of such structures is an issue of crucial importance.

The satisfaction of both geotechnical and structural design constraints is a key component in the design of RCRWs. In most cases, primary dimensions are initially estimated based on reasonable assumptions and the experience of the designer. Then, in order to reach a cost-effective design while satisfying the design constraints, the design variables (particularly the wall dimensions) need to be revised by using a trial-and-error process, which makes it rather grueling. On the other hand, there is no guarantee that the final design will be the best possible one. To eliminate this problem, which can hinder the designer from reaching a cost-effective solution, and by considering the advances in computational technologies during the recent decades, it makes sense to express the design in the form of a formal optimization problem.

The design optimization of RCRWs has received significant attention during the last two decades. Some of the pertinent works are briefly investigated herein. As a benchmark work, Saribas and Erbatur [1] used a nonlinear programming method and investigated the sensitivity of the optimum solutions to parameters such as backfill slope, surcharge load, internal friction angle of retained soil, and yield strength of reinforcing steel. The simulated annealing (SA) algorithm has been also applied to minimize the construction cost of RCRWs [2,3]. Camp and Akin [4] developed a procedure to design cantilever RCRWs using Big Bang–Big Crunch optimization. They captured the effects of surcharge load, backfill slope, and internal friction angle of the retained soil on the values of low-cost and low-weight designs with and without a base shear key. Khajehzadeh et al. [5] used the particle swarm optimization with passive congregation (PSOPC), claiming that the proposed algorithm was able to find an optimal solution better than the original PSO and nonlinear programming. In their work, the weight, cost, and CO_2 emissions were chosen as the three objective functions to be minimized. Gandomi et al. [6] optimized RCRWs by using swarm intelligence techniques, such as accelerated particle swarm optimization (APSO), firefly algorithm (FA), and cuckoo search (CS). They concluded that the CS algorithm outperforms the other ones. They also investigated the sensitivity of the algorithms to surcharge load, base soil friction angle, and backfill slope with respect to the geometry and design parameters. Kaveh and his colleagues (e.g., [7–10]) optimized the RCRWs using nature-inspired optimization algorithms, including charged system search (CSS), ray optimization algorithm (RO), dolphin echolocation optimization (DEO), colliding bodies of optimization (CBO), vibrating particles system (VPS), enhanced colliding bodies of optimization (ECBO), and democratic particle swarm optimization (DPSO). Temur and Bekdas [11] employed the teaching–learning-based optimization (TLBO) algorithm to find the optimum design of cantilever RCRWs. They concluded that the minimum weight of the RCRWs decreases as the internal friction angle of the retained soil increases, and increases with the values of the surcharge load. Ukritchon et al. [12] presented a framework for finding the optimum design of RCRWs, considering the slope stability. Aydogdu [13] introduced a new version of a biogeography-based optimization (BBO) algorithm with levy light distribution (LFBBO) and, by using five examples, it was shown that this algorithm outperforms some other metaheuristic algorithms. In this work, the cost of the RCRWs was used as the criterion to find the optimum design. Nandha Kumar and Suribabu [14] adopted the differential evolution (DE) algorithm to solve the design optimization problem of RCRWs. The results of sensitivity analysis showed that width and thickness of the base slab and toe width increases as the height of stem increases. Gandomi et al. [15] studied the importance of different boundary constraint handling mechanisms on the performance of the interior search algorithm (ISA). Gandomi and Kashani [16] minimized the construction cost and weight of RCRWs analyzed by the pseudo-static method. They employed three evolutionary algorithms, DE, evolutionary strategy (ES), and BBO, and concluded that BBO outperforms the others in finding the optimum design of RCRWs. More recently, Mergos and Mantoglou [17] optimized concrete retaining walls by using the flower pollination algorithm, claiming that this method outperforms PSO and GA.

By taking a look at the studies so far reported, it can be noticed that there has been no work done in assessing the effect of using different available methods of determining the bearing capacity on the optimum design of the RCRWs. The current study investigates this important issue. In order to model and design the RCRWs, a code is developed in MATLAB [18]. To reach a design with minimum construction cost, an optimization problem is defined and the construction cost is considered as the single objective function to be minimized. The design criteria, including both geotechnical and structural limitations, are considered as the optimization constraints. The wall geometrical dimensions and the amount of steel reinforcement are used as the design variables. The particle swarm optimization (PSO) [19] algorithm is used to find the optimum solution.

2. Design of Retaining Walls

The design of RCRWs includes two sets of variables. The first set consists of the geometrical dimensions of the concrete wall, namely variables X_1 to X_8, that are defined as shown in Table 1

and depicted graphically in Figure 1. It can be seen that these variables fully define the geometry of the structure.

Table 1. Description of the geometric variables and their lower and upper bounds.

Geometric Variable	Description	Lower Bound	Upper Bound
X_1	Width of the base slab	$0.4H$	$0.8H$
X_2	Toe width	$0.1H$	$0.6H$
X_3	Thickness at the bottom of the stem	0.2 m	0.5 m
X_4	Thickness at the top of the stem	0.2 m	0.4 m
X_5	Thickness of the base	0.2 m	$0.3H$
X_6	Distance from the toe to the front face of the shear key	$0.5H$	$0.8H$
X_7	Width of shear key	0.2 m	0.4 m
X_8	Depth of the shear key	0.2 m	0.9 m

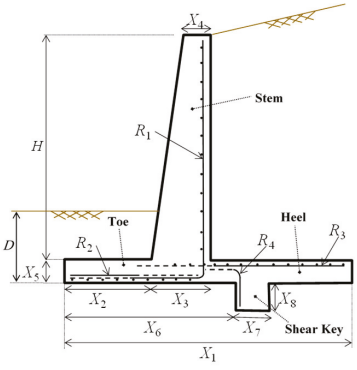

Figure 1. Design variables (X_1 to X_8 and R_1 to R_4), (redesigned based on [4]).

The second set is the amounts of steel reinforcement for four components of the wall—the stem, heel, toe, and shear key. As such, four variables, R_1 to R_4, are introduced to represent the steel reinforcement of the different components, as shown in Table 2. In this paper, a total of 223 possible reinforcement configurations were used, resulting from the combinations of using 3–28 evenly spaced bars, with varying sizes (bar diameter) from 10 to 30 mm. It is worth mentioning that the combinations used for the steel reinforcement, as listed in Table 3, are obtained such that the allowable minimum and maximum amount of steel area per unit meter length of the wall are satisfied as per ACI318-14 code [20].

Table 2. Description of the reinforcement variables.

Reinforcement Variable	Description
R_1	Vertical steel reinforcement of the stem
R_2	Horizontal steel reinforcement of the toe
R_3	Horizontal steel reinforcement of the heel
R_4	Vertical steel reinforcement of shear key

Table 3. Steel reinforcement combinations (adopted from [4]).

Index Number	Bars Quantity and Size (R)	Bars Cross-Sectional Area (cm^2) (in Ascending Order)
1	$3\phi10$	2.356 (lower bound)
2	$4\phi10$	3.141
3	$3\phi12$	3.392
4	$5\phi10$	3.926
5	$4\phi12$	4.523
.	.	.
.	.	.
221	$16\phi30$	113.097
222	$17\phi30$	120.165
223	$18\phi30$	127.234 (upper bound)

The allowable value of spacing between longitudinal bars (ds_{all}) is defined as follows [20]:

$$ds_{all} = \max\{25mm, d_{bl}, 1.33d_{max}\}, \quad (1)$$

in which d_{bl} and d_{max} are the diameter of longitudinal reinforcements and diameter of greatest aggregate of concrete, respectively. For the purposes of steel reinforcement design, ACI318-14 code [20] has been considered.

In the design of RCRWs, geotechnical stability control and the satisfaction of the structural requirements are mandatory. In geotechnical design, the stability of the structure shall be controlled against possible overturning, sliding, and bearing capacity failure modes. On the other hand, in the structural design phase, each component of the structure, including the stem, toe, heel, and shear key, shall be checked against shear and moment demands [21]. Figure 2 shows all the forces acting on the retaining wall. As shown in this figure, P_a is the resultant force of the active pressure p_a per unit length of the wall; Q_s is the resultant force of the distributed surcharge load q; W_C is the weight of all sections of the reinforced concrete wall; W_S and W_T are defined as the weight of backfill behind the retaining wall and the weight of the soil on the toe, respectively; P_p is the resultant force due to the passive pressure (p_p) on the front face of the toe and shear key per unit length of the wall; P_b is the resultant force caused by the pressure acting on the base soil; q_{max} and q_{min} are the maximum and minimum soil pressure intensity at the toe and the heel of the retaining wall, respectively. In this paper, the water level and the seismic actions were not considered in computing the forces acting on the RCRWs. The pressure distributions on the base and retaining soil have also been illustrated in Figure 2.

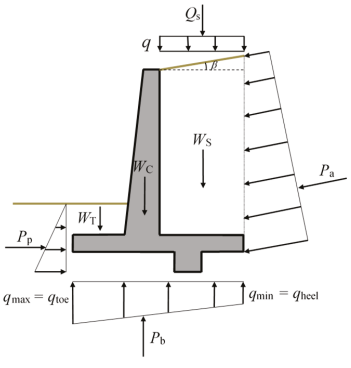

Figure 2. Forces acting on the retaining wall (redesigned based on [6]).

In this study, Rankine theory was used to evaluate the active and passive forces acting on the unit length of the retaining wall (p_a and p_p, respectively), and they are computed as follows [21]:

$$p_a = \frac{1}{2}k_a\gamma_{rs}H'^2 + k_aqH', \tag{2}$$

$$p_p = \frac{1}{2}k_p\gamma_{bs}D'^2 + 2c_{bs}\sqrt{k_p}D'^2, \tag{3}$$

where k_a and k_p are the Rankine active and passive earth pressure coefficients, respectively; D' is the buried depth of shear key; γ_{rs} is the unit weight of backfill; H' is the height of the soil located on the embedment depth of the base slab at the edge of the heel; γ_{bs} and ff_{bs} are the unit weight and the cohesion of soil in front of the toe and beneath the base slab, respectively. k_a is computed as [21]:

$$k_a = \cos\beta\frac{\cos\beta - \sqrt{\cos^2\beta - \cos^2\phi_{rs}}}{\cos\beta + \sqrt{\cos^2\beta - \cos^2\phi_{rs}}}, \tag{4}$$

in which β and ϕ_{rs} are the slope and internal friction angle of the back fill, respectively; k_p is computed as follows [21]:

$$k_p = \tan^2\left(45 + \frac{\phi_{bs}}{2}\right), \tag{5}$$

in which ϕ_{bs} (in degrees) is the internal friction angle of soil in front of the toe and beneath the base slab.

2.1. Geotechnical Stability Demands

A retaining wall may fail due to overturning about the toe, sliding along the base slab, and the loss of bearing capacity of the soil supporting the base [21]. The checks for these three failure modes are described in this section. The safety factor against overturning about the toe is defined as follows:

$$FS_O = \frac{\sum M_R}{\sum M_O}, \tag{6}$$

in which $\sum M_R$ is the sum of the moments tending to resist against overturning about the toe and $\sum M_O$ is the sum of the moments tending to overturn the wall about the toe [21]. The safety factor against sliding along the base slab is computed as follows:

$$FS_S = \frac{\sum F_R}{\sum F_D}, \tag{7}$$

where $\sum F_R$ is the sum of the resisting forces against the sliding and $\sum F_D$ is the sum of the horizontal driving forces.

The safety factor against bearing capacity failure mode is computed by:

$$FS_B = \frac{q_u}{q_{max}}, \tag{8}$$

in which q_u is the ultimate bearing capacity of the soil supporting the base slab. The ultimate bearing capacity is the load per unit area of the foundation at which shear failure occurs in the soil. For retaining walls, q_u is computed as follows [21]:

$$q_u = c_{bs}N_cF_{cs}F_{cd}F_{ci} + qN_qF_{qs}F_{qd}F_{qi} + 0.5\gamma_{bs}B'N_\gamma F_{\gamma s}F_{\gamma d}F_{\gamma i}, \tag{9}$$

where:

$$q = \gamma_{bs}D, \tag{10}$$

in which D is the embedment depth of the toe (base slab). B' is computed as:

$$B' = B - 2e, \tag{11}$$

where B is the width of the base slab. As mentioned earlier, q_{max} and q_{min}, which are the maximum and minimum stresses occurring at the end of the toe and heel of the structure, respectively, are computed as follows [21]:

$$q_{min}^{max} = \frac{\sum V}{B}\left(1 \pm \frac{6e}{B}\right), \tag{12}$$

where e is defined as the eccentricity of the resultant force, which can be computed as follows:

$$e = \frac{B}{2} - \frac{\sum M_R - \sum M_O}{\sum V}. \tag{13}$$

Note that if e becomes greater than $B/6$, then some tensile stress will be applied at the soil located under the heel section. In such a case, since the tensile strength of soil is negligible, design and calculations should be repeated.

In Equation (9), the N coefficients are used for the modification of the bearing capacity value and the F coefficients are used for the modification of the shape, depth, and inclination factors. The bearing capacity factors N_c, N_q, and N_γ are, respectively, the contributions of cohesion, surcharge, and unit weight of soil to the ultimate load-bearing capacity [21]. Some of these coefficients vary in accordance with the method used, resulting in different values for q_u. Hence, this issue could affect the final design of the RCRWs. In this paper, the effects of three methods of Meyerhof [22], Hansen [23], and Vesic [24] in computing q_u were investigated, particularly their effect on the optimized construction cost of the RCRWs. The N and F coefficients corresponding to each of the three design methods are listed in Appendix A.

2.2. Structural Requirements

The moment and shear capacity of all components of the retaining wall must be greater than their corresponding demands. The flexural strength of each component can be computed as follows [20]:

$$M_n = \phi_m A_s f_y \left(d - \frac{a}{2}\right), \tag{14}$$

in which ϕ_m is known as the nominal strength coefficient (equal to 0.9 [20]); A_s is the cross-sectional area of the steel reinforcement; f_y is the yield strength of steel; d is the effective depth of the cross section; and a is the depth of the compressive stress block. The shear strength is estimated by [20]:

$$V_n = 0.17\phi_v \sqrt{f_c} b d, \tag{15}$$

where ϕ_v is the nominal strength coefficient (equal to 0.75 [20]); f_c is the specified compressive strength of concrete; and b is the width of the cross section.

2.2.1. Flexural Moment and Shear Force Demands of Stem

As shown in Figure 2, by considering the active force acting on the unit length of the wall due to surcharge load and the weight of the backfill on the stem, the critical section for flexural moment is at the intersection of the stem with the base slab. In addition, the critical section for shear force is at a distance d_s from the intersection of the stem with the foot slab, defined as $d_s = X_3 - C_C$, where C_C is the concrete cover. The flexural moment and shear force demands of the stem at its critical section are computed by the following equations:

$$M_s = 1.6\left[\frac{1}{2}\left(\left(k_a q H^2\right) + \left(\frac{1}{3} k_a \gamma_{rs} H^3\right)\right)\right] \cos\beta, \tag{16}$$

$$V_s = 1.6\left((k_a q(H - d_s) + \frac{1}{2}k_a\gamma_{rs}(H - d_s)^2\right)\cos\beta. \tag{17}$$

2.2.2. Flexural Moment and Shear Force Demands of Toe Slab

The effective forces on the toe slab include the soil weight on the toe slab, the weight of the toe concrete slab, and the force caused by earth pressure under the toe slab. The foot of the front face of the stem is the critical section for flexural moment and the critical section for shear force is formed at a distance d_t from the front face of the stem ($d_t = X_5 - C_C$). The flexural moment and shear force demands of the toe slab at its critical section are computed by the following equations [6]:

$$M_t = \left[1.6\left(\frac{q_2}{6} + \frac{q_{max}}{3}\right) - 0.9(\gamma_c X_5 + \gamma_{bs}(D - X_5))\right]l_{toe}^2, \tag{18}$$

$$V_t = \left[1.6\left(\frac{q_{dt} + q_{max}}{2}\right) - 0.9(\gamma_c X_5 + \gamma_{bs}(D - X_5))\right].(l_{toe} - dt), \tag{19}$$

where q_2 is the soil pressure intensity at the foot of the front face of the stem; γ_c is the unit weight of concrete; l_{toe} is the length of the toe slab; and q_{dt} is the soil pressure at a distance d_t from the foot of the stem front face.

2.2.3. Flexural Moment and Shear Force Demands of Heel Slab

The forces acting on the heel section include the soil weight of top of the heel slab, the weight of the heel concrete slab, the surcharge load, and the force resulting from earth pressure under the heel slab. The foot of the stem back face is the critical section for flexural moment and the critical section for shear force is at a distance d_h from the foot of the stem back face ($d_h = X_5 - C_C$). The flexural moment and shear force demands of the heel slab at its critical section are computed by the following equations [6]:

$$M_h = \left[\left(\frac{1.6q + 1.2\gamma_c X_5 + 1.2\gamma_{rs}H}{2}\right) + \frac{1.2W_{bs}}{3} - \left(\frac{q_1 + 2q_{min}}{6}\right)\right]l_{heel}^2, \tag{20}$$

$$V_h = \left[1.6q + 1.2\gamma_c X_5 + 1.2\gamma_{rs}H + 1.2\frac{W_{bs} + W_{bsdh}}{2} - 0.9\frac{q_{dh} + q_{min}}{2}\right](l_{heel} - d_h), \tag{21}$$

in which W_{bs} is the maximum load due to triangular backfill soil weight at the top of the heel slab; q_1 is the soil pressure intensity at the foot of the stem back face; l_{heel} is the length of retaining wall heel; W_{bsdh} is the load resulting from triangular backfill soil weight; and q_{dh} is the intensity of soil pressure at a distance d_h from the stem back face.

3. Optimization Problem

3.1. Formulation

Optimization problems can be divided into two large groups in general—constrained and unconstrained problems. Because of the limitations required for the design of structures, the optimum design of RCRWs is a constrained optimization problem, which can be expressed as follows [25]:

$$\begin{gathered} \textit{Minimize } F(\boldsymbol{x}) \textit{ subjected to } g_i(\boldsymbol{x}) \le 0 \\ (i = 1, 2, \ldots, m;\ x_j \in R^d,\ j = 1, 2, \ldots, n) \end{gathered} \tag{22}$$

in which $F(\boldsymbol{x})$ is the objective function; $g_i(\boldsymbol{x})$ is the i-th constraint; m and n are the total number of constraints and design variables, respectively; R^d is a given set of discrete values from which the individual design variables x_j can take values. In this paper, an exterior penalty function method

was used to transform the constrained structural optimization problem into an unconstrained one, as follows [26]:

$$\Phi(\boldsymbol{x}, r_{\mathrm{p}}) = F(\boldsymbol{x})\left[1 + r_{\mathrm{p}}\sum_{\mathrm{r}=1}^{\mathrm{m}}\left(\max\left(\frac{g_{\mathrm{r}}}{g_{\mathrm{r,all}}} - 1, 0\right)\right)\right], \tag{23}$$

where ϕ is the pseudo (penalized) objective function; g_{r} and $g_{\mathrm{r,all}}$ are the r-th constraint and its allowable value, respectively; and r_{p} is a positive penalty parameter, which in this study was assumed to be equal to 25.

3.2. Objective Function

In this work, the initial construction cost CC_{RCRW} of the RCRW was considered the single objective function of the optimization problem, to be minimized. The objective function was defined as follows:

$$CC_{\mathrm{RCRW}} = C_{\mathrm{c}}V_{\mathrm{c}} + C_{\mathrm{st}}W_{\mathrm{st}}, \tag{24}$$

where C_{c} and C_{st} are the cost per unit volume of concrete and the cost per unit weight of steel reinforcement, respectively; V_{c} and W_{st} are the volume of concrete and weight of steel per unit length of the retaining wall, respectively. It is worth noting that the cost of the formwork, casting concrete, vibration, and generally all related labor costs were taken into consideration in the parameter C_{c}. In addition, the earthwork cost was not considered in the calculation of the total cost of the RCRWs.

3.3. Design Constraints

Two sets of constraints are considered for the optimum design of a RCRW. The first set (four constraints) is related to geotechnical requirements (wall stability). Of these, the first three are considered to provide safety factors against overturning, sliding, and bearing capacity failure modes, as shown below [21]:

$$g_1 = \frac{FS_{\mathrm{O}}}{FS_{\mathrm{O,all}}} - 1 \geq 0, \tag{25}$$

$$g_2 = \frac{FS_{\mathrm{S}}}{FS_{\mathrm{S,all}}} - 1 \geq 0, \tag{26}$$

$$g_3 = \frac{FS_{\mathrm{B}}}{FS_{\mathrm{B,all}}} - 1 \geq 0, \tag{27}$$

in which FS_{O}, FS_{S}, and FS_{B} are the safety factor demands against overturning, sliding, and bearing capacity failure modes, respectively, and $FS_{\mathrm{O,all}}$, $FS_{\mathrm{S,all}}$, and $FS_{\mathrm{B,all}}$ are their allowable values.

The fourth constraint of the first set is used to avoid the presence of tensile stresses on the base soil, as follows:

$$g_4 = q_{\min} \geq 0. \tag{28}$$

The second set of constraints is related to the structural requirements having to do with providing the required strength of wall components and reinforcement arrangements in their cross sections, in accordance with ACI318-14 [20]. To design the structural sections, the reinforcement area at each section of the retaining wall should satisfy the allowable amounts of the reinforcement area, as follows:

$$g_{5\text{–}8} = \left(\frac{A_{\mathrm{s}}}{A_{\mathrm{s,min}}}\right)_{\mathrm{st}} - 1 \geq 0, \tag{29}$$

$$g_{9\text{–}12} = \left(\frac{A_{\mathrm{s,max}}}{A_{\mathrm{s}}}\right)_{\mathrm{st}} - 1 \geq 0, \tag{30}$$

in which $A_{\mathrm{s,min}}$ and $A_{\mathrm{s,max}}$ are the minimum and maximum allowable area of steel reinforcement in accordance with the code, and A_{s} is defined as the cross-sectional area of steel reinforcement in each

section. The subscript *st* refers to all sections of the RCRW including stem, heel, toe and shear key, and similarly subscripts 5 to 8 are used for the stem, toe, heel and shear key, respectively. The same is also the case for subscripts 9 to 12.

As mentioned earlier, the moment and shear capacities of all sections of the retaining wall should be greater than the corresponding demands, namely:

$$g_{13\text{–}16} = \left(\frac{M_n}{M_d}\right)_{st} - 1 \geq 0 \tag{31}$$

$$g_{17\text{–}20} = \left(\frac{V_n}{V_d}\right)_{st} - 1 \geq 0 \tag{32}$$

In the equations above, M_n and V_n are the moment and shear nominal capacity, and M_d and V_d are the moment and shear demands, respectively. M_n and V_n are the flexural moment and shear strength formulated before. The subscripts 13 to 16 are for stem, toe, heel, and shear key. The same is true for subscripts 17 to 20.

The following geometric constraints are also applied to avoid an impossible or impracticable shape of the wall:

$$g_{21} = \frac{X_1}{X_2 + X_3} - 1 \geq 0, \tag{33}$$

$$g_{22} = \frac{X_1}{X_6 + X_7} - 1 \geq 0. \tag{34}$$

The minimum development length of the steel reinforcement bars should be considered for all the structural components. At first, the minimum basic development length l_{db} against the allowable space is checked. If the available space is not enough, a hook is added to achieve the additional development length. In this case, a minimum hook development length l_{dh} and minimum hook length of $12d_{bh}$ (d_{bh} is the diameter of the hooked bar) should be satisfied. The following limitations are considered for stem, toe, heel, and shear key in the design, respectively:

$$g_{23} = \frac{l_{db,stem}}{X_5 - C_C} - 1 \geq 0 \quad or \quad g_{23} = \frac{l_{dh,stem}}{X_5 - C_C} - 1 \geq 0, \tag{35}$$

$$g_{24} = \frac{l_{db,toe}}{X_1 - X_2 - C_C} - 1 \geq 0 \quad or \quad g_{24} = \frac{12d_{b,toe}}{X_5 - C_C} - 1 \geq 0, \tag{36}$$

$$g_{25} = \frac{l_{db,heel}}{X_2 + X_3 - C_C} - 1 \geq 0 \quad or \quad g_{25} = \frac{12d_{b,heel}}{X_5 - C_C} - 1 \geq 0, \tag{37}$$

$$g_{26} = \frac{l_{db,key}}{X_5 - C_C} - 1 \geq 0 \quad or \quad g_{26} = \frac{l_{dh,key}}{X_5 - C_C} - 1 \geq 0, \tag{38}$$

It should be noted that the inequalities g_{23} to g_{26} as described in Equations (35)–(38) were actually not considered as design constraints in the present study. In fact, during the optimization process, the required development lengths were simply considered and their role in steel cost was computed and added to the construction cost. The cost of shrinkage reinforcement was also added to the total construction cost. Another important point is that the other constraints on the arrangements of steel bars in the wall sections, such as the number of allowable bars, bar size, and bar spacing, were all considered in the optimum design, as can be seen in Table 2.

3.4. PSO Algorithm

The successful application of the particle swarm optimization (PSO) algorithm in the optimum design of RC structures has been reported in the literature (e.g., [26–33]). In this paper, the PSO algorithm was used to optimize RCRWs. The algorithm was originally developed by Kennedy and

Eberhart [19] in the mid-1990s, and was first applied to simulate the social behavior of fish schooling and bird flocking as part of a socio-cognitive research. The PSO algorithm is considered a metaheuristic algorithm that optimizes a problem by iteratively trying to improve a candidate solution. It solves a problem by having a population of candidate solutions called particles. Each particle moves through the search space and its position is updated according to (a) its local best known position, and (b) the best known position for the whole swarm in the search space. Finally, the objective function is calculated for each particle and the fitness values of the candidate solutions are assessed to discover which position in the search space is the best. The algorithm searches for the optimum by adjusting the trajectory of each particle of the swarm in the multi-dimensional design space, in terms of paths created by positional vectors in a quasi-random manner. After finding the best values of position and velocity in each iteration k, these vectors are updated using the following equations:

$$\boldsymbol{X}_{\mathrm{i,k+1}} = \boldsymbol{X}_{\mathrm{i,k}} + \boldsymbol{V}_{\mathrm{i,k+1}}, \tag{39}$$

$$\boldsymbol{V}_{\mathrm{i,k+1}} = w_{\mathrm{k}}\boldsymbol{V}_{\mathrm{i,k}} + c_1 r_1(\boldsymbol{P}_{\mathrm{i,k}} - \boldsymbol{X}_{\mathrm{i,k}}) + c_2 r_2\big(\boldsymbol{P}_{\mathrm{g,k}} - \boldsymbol{X}_{\mathrm{i,k}}\big), \tag{40}$$

in which for the i-th particle, $\boldsymbol{X}_{\mathrm{i,k}}$ and $\boldsymbol{V}_{\mathrm{i,k}}$ are the current position vector and velocity vector at iteration k, respectively; $\boldsymbol{P}_{\mathrm{i,k}}$ is the best position that the particle has visited; $\boldsymbol{P}_{\mathrm{g,k}}$ is the global best position obtained so far by all the particles in the population; r_1 and r_2 are random numbers drawn from a uniform distribution in the range of [0, 1]; c_1 and c_2 are constants, called cognitive and social scaling parameters, and are usually in the range of [0, 2]; w_{k} known as the inertia weight, has a pivotal role in updating the position and the velocity vectors. In fact, this parameter is used to stabilize the motion of the particles, making the algorithm converge more quickly. In this paper, a linear weight-updating rule was implemented as follows:

$$w_{\mathrm{k}} = w_{\max} - \frac{w_{\max} - w_{\min}}{k_{\max}} k, \tag{41}$$

in which $w_{\max}$ and $w_{\min}$ are the upper and lower bounds of the current weight w_{k}; and $k_{\max}$ is the maximum number of iterations used. Figure 3 shows a schematic view for the PSO algorithm, i.e., how a particle's position is updated from one iteration to another toward finding the global optimum.

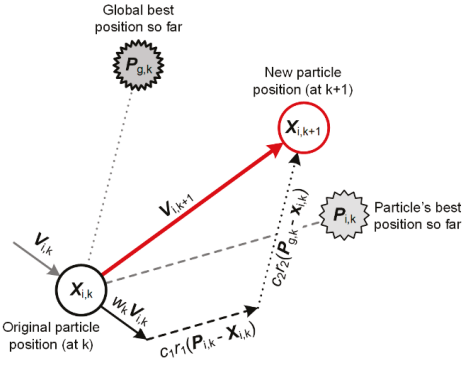

Figure 3. A schematic view for describing particle swarm optimization (PSO).

4. Methodology

As previously mentioned, although many studies have been implemented to optimize the retaining wall design, no studies have been conducted so far investigating the effect of various methods of determining the parameters of the soil ultimate bearing capacity on the design optimization of these structures. The current study deals with this issue and, in particular, the effect of using the methods developed by Meyerhof, Hansen, and Vesic (respectively abbreviated as MM, HM, and VM hereafter) on the cost of the retaining wall. For this purpose, a database containing discrete values of the

mentioned variables (X_1 to X_8 and R_1 to R_4) was generated. Then, the PSO algorithm was used to solve the optimum design problem defined above. All the process of optimum design was implemented via a code written in MATLAB [18]. The flowchart of the design optimization process is shown in Figure 4. The next section investigates the effects of the above three methods on the optimum design of RCRWs.

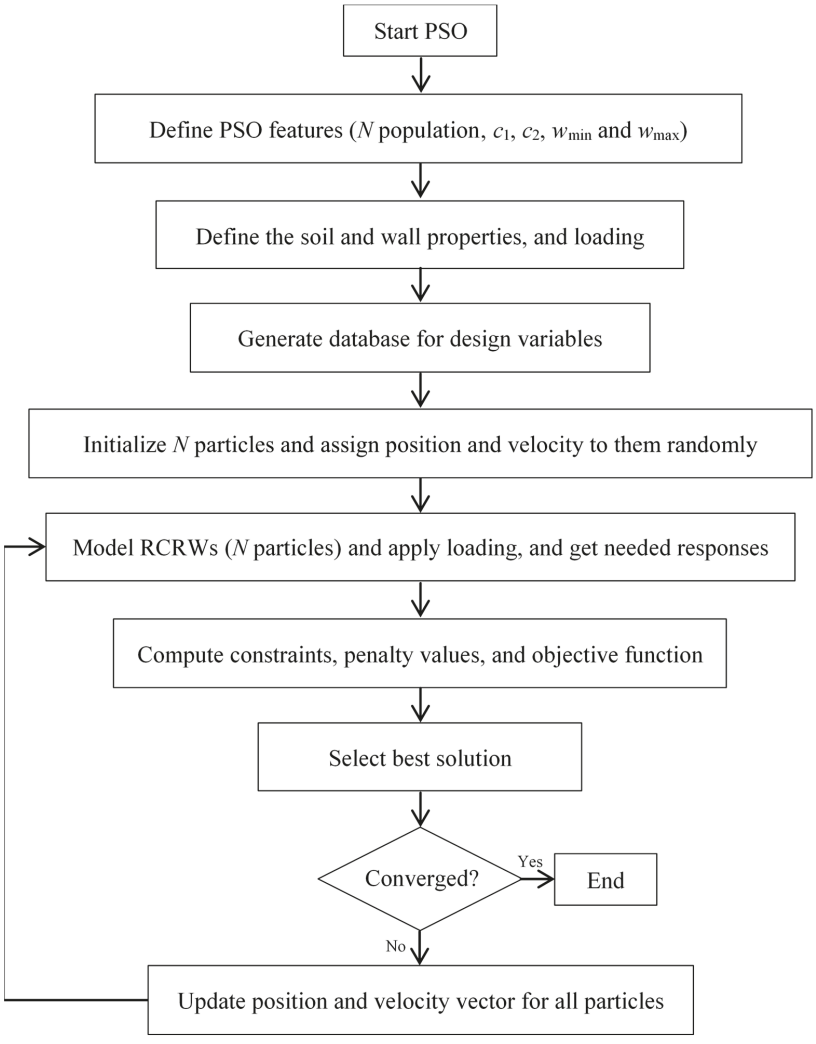

Figure 4. The flowchart of the design optimization of reinforced concrete retaining walls (RCRWs).

5. Design Examples

5.1. Assumptions

Three different RCRWs with different heights of 4.0, 5.5, and 7.0 m were considered for all three methods examined (MM, HM, and VM). A reasonable incremental step of 0.01 m was considered for the geometric variables. As shown in Table 3, a set of discrete values was considered for the steel reinforcement. It should be noted that the cross-sectional area of the steel reinforcement bars per unit length of the wall (1 m) was used during the optimization process, therefore, the number of used bars

(n_1 to n_4) needs to be obtained. All the values assumed for the modeling and design of the RCRWs are listed in Table 4.

Table 4. Values of input parameters for Examples 1, 2, and 3.

Parameter	Symbol	Value	Unit
		Examples 1–3	
Height of stem	H	4.0, 5.5, and 7.0	m
Steel yield strength	f_y	400	MPa
Shrinkage and temperature reinforcement ratio	ρ_{st}	0.002	-
Concrete compressive strength	f_c	21	MPa
Concrete cover	C_C	7	cm
Unit weight of concrete	γ_c	23.5	kN/m^3
Unit weight of steel bars	γ_s	78.5	kN/m^3
Surcharge load	q	15	kPa
Backfill slope	β	5	degrees
Internal friction angle of backfill	φ_{rs}	36	degrees
Unit weight of backfill	γ_{rs}	17.5	kN/m^3
Internal friction angle of base soil	φ_{bs}	39	degrees
Cohesion of base soil	c_{bs}	0	kPa
Unit weight of base soil	γ_{bs}	20	kN/m^3
Embedment depth of the toe	D	0.75	m
Cost of steel per unit of mass	C_{st}	0.4	\$/kg
Cost of concrete per unit of volume	C_c	40	\$/m^3

Because of the stochastic nature of the PSO algorithm, 20 independent runs were conducted for each case study corresponding to each method (MM, HM, and VM). In the PSO algorithm, the population was 20 and the maximum number of iterations was set to 6000; both c_1 and c_2 parameters were assumed to be equal to 2; w_{min} and w_{max} as the minimum and maximum value of the weight w_k, respectively, were considered to be 0.4 and 0.9.

5.2. Results and Discussion

After implementation of the optimization procedure, the best run among the 20 runs was chosen. The convergence history of all examples as Example 1 with H = 4.0 m, Example 2 with H = 5.5 m, and Example 3 with H = 7.0 m are shown in Figures 5–7, respectively. The convergence plots, which correspond to the best runs, start with a larger value of the cost, which is then minimized by the PSO algorithm at the final iteration. Note that since the optimization procedure was performed for a unit meter length of the wall, all the presented costs are per meter of length of the wall.

The optimum design variables, including the geometrical dimensions and the amounts of steel reinforcement for the three examples, are presented in Tables 5–7. As can be seen, all the results were within their allowable ranges defined in Tables 1 and 3. The last two columns of each table present the difference in the design variables for HM and VM with respect to MM as the chosen benchmark method. Based on the results, it can be noted that in general, the dimensions of X_1, X_4, X_6, X_7, and X_8 had relatively low sensitivity to the method used, while the other dimensions, namely X_2 and X_5, were quite sensitive. Concerning X_3, it seems to be sensitive to the method used merely for the case of wall height 4.0 m. The amounts of steel reinforcement (variables R_1, R_2, R_3, and R_4) were highly dependent on the method used.

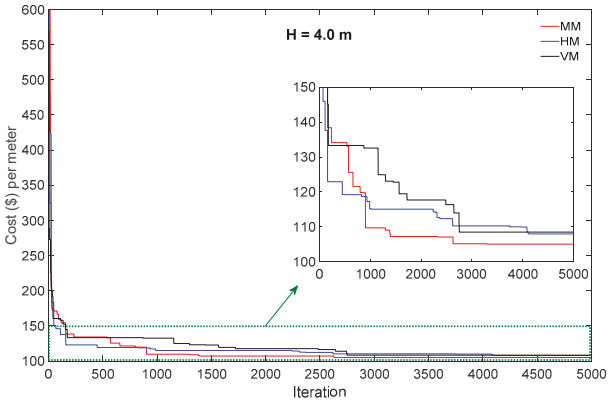

Figure 5. Convergence history of objective function—Example 1.

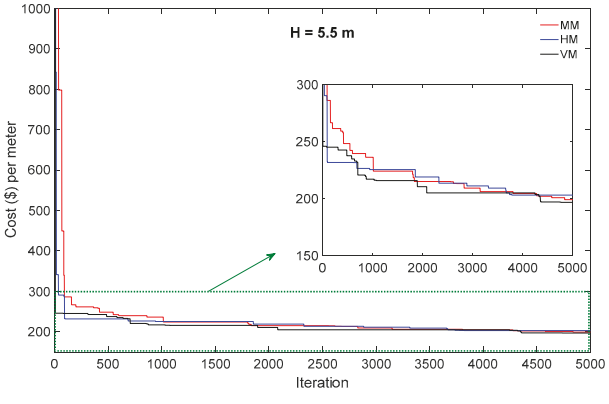

Figure 6. Convergence history of objective function—Example 2.

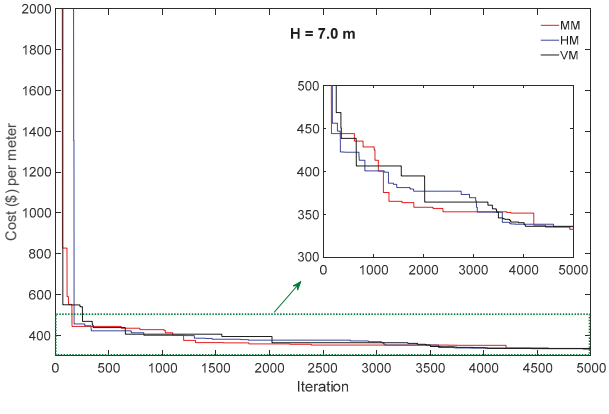

Figure 7. Convergence history of objective function—Example 3.

Table 5. Optimum design variables and comparison of the methods for Example 1—H = 4.0 m.

Variable	Method			Difference (%)	
	MM	**HM**	**VM**	**100 × (HM − MM)/MM**	**100 × (VM − MM)/MM**
X_1	2.33	2.47	2.38	6.01	2.15
X_2	0.88	1.03	1.05	17.05	19.32
X_3	0.37	0.34	0.32	−8.11	−13.51
X_4	0.20	0.20	0.20	0.00	0.00
X_5	0.24	0.25	0.27	4.17	12.50
X_6	2.01	2.01	2.05	0.00	1.99
X_7	0.26	0.27	0.28	3.85	7.69
X_8	0.23	0.22	0.24	−4.35	4.35
R_1	13ϕ12	20ϕ10	21ϕ10	6.84	12.18
R_2	13ϕ10	9ϕ12	14ϕ10	−0.31	7.69
R_3	13ϕ10	12ϕ10	9ϕ12	0.00	8.00
R_4	6ϕ12	14ϕ10	9ϕ10	62.04	4.17

Table 6. Optimum design variables and comparison of the methods for Example 2—H = 5.5 m.

Variable	Method			Difference (%)	
	MM	**HM**	**VM**	**100 × (HM − MM)/MM**	**100 × (VM − MM)/MM**
X_1	3.20	3.24	3.16	1.25	−1.25
X_2	0.99	1.19	1.33	20.20	34.34
X_3	0.47	0.48	0.46	2.13	−2.13
X_4	0.21	0.20	0.20	−4.76	−4.76
X_5	0.35	0.38	0.36	8.57	2.86
X_6	2.78	2.88	2.85	3.60	2.52
X_7	0.28	0.26	0.29	−7.14	3.57
X_8	0.23	0.20	0.25	−13.04	8.70
R_1	13ϕ16	22ϕ12	13ϕ16	−4.81	0.00
R_2	5ϕ16	5ϕ20	11ϕ14	56.25	68.44
R_3	11ϕ14	16ϕ10	7ϕ14	−25.79	−36.36
R_4	12ϕ10	7ϕ16	7ϕ12	49.33	−16.00

Table 7. Optimum design variables and comparison of the methods for Example 3—H = 7.0 m.

Variable	Method			Difference (%)	
	MM	**HM**	**VM**	**100 × (HM − MM)/MM**	**100 × (VM − MM)/MM**
X_1	4.04	3.90	3.79	−3.47	−6.19
X_2	1.34	1.51	1.76	12.69	31.34
X_3	0.49	0.48	0.48	−2.04	−2.04
X_4	0.21	0.21	0.20	0.00	−4.76
X_5	0.45	0.49	0.56	8.89	24.44
X_6	3.75	3.52	3.50	−6.13	−6.67
X_7	0.27	0.26	0.27	−3.70	0.00
X_8	0.21	0.21	0.21	0.00	0.00
R_1	19ϕ18	11ϕ24	19ϕ18	2.92	0.00
R_2	14ϕ12	16ϕ12	17ϕ12	14.29	21.43
R_3	16ϕ14	23ϕ10	22ϕ10	−26.66	−29.85
R_4	5ϕ18	22ϕ10	7ϕ12	35.80	−37.78

To show the convergence of the optimization process to the optimum solution, the best solutions in each iteration corresponding to Example 1 (with H = 4.0 m) considering the MM case are shown together in Figure 8. Based on this figure, PSO found the optimum solution in the design space very well. In addition, the optimum shapes of the three examples with consideration of the three methods of

MM, HM, and VM are shown in Figure 9. From this figure, it can be seen that the three methods resulted in different designs (geometrical dimensions) for all the optimum RCRWs with different heights.

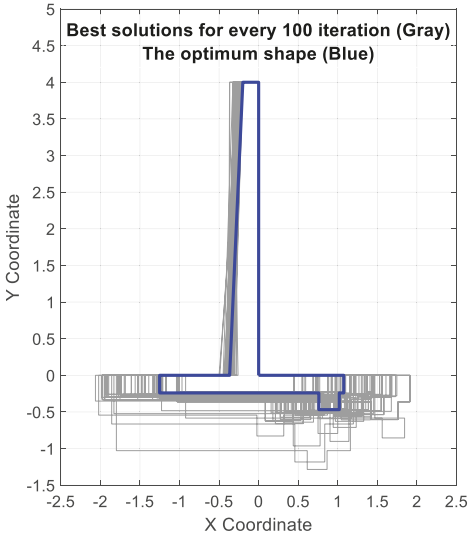

Figure 8. The candidate solutions and the final optimum shape (for H = 4.0 m, corresponding to the MM method).

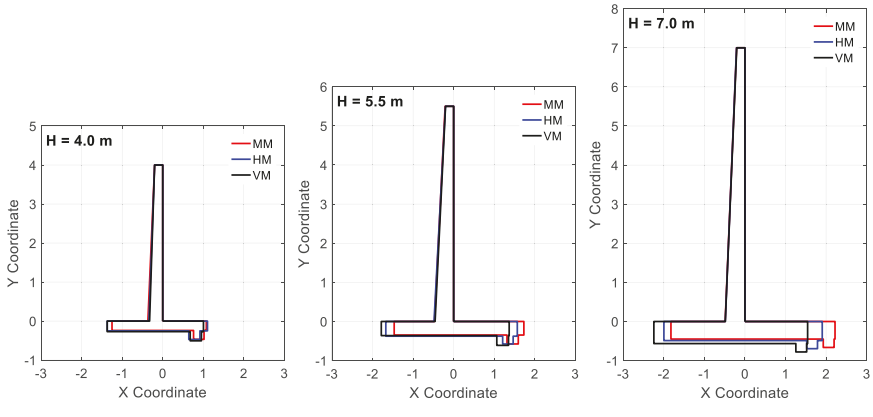

Figure 9. Optimal dimensions of the RCRWs for all examples with the three methods.

Figures 10–12 show the demand to capacity ratios of the constraints (all constraints $g_{1–3}$ and $g_{5–20}$, except for the constraint g_4 on $q_{\min}$) for the optimum solutions. As can be seen, all the corresponding values were less than 1.0, indicating that the optimum solutions have satisfied all the design constraints.

The constraint on the soil pressure intensity under the heel ($q_{\min}$), described as constraint g_4 in Equation (28), which is one of the fundamental constraints in the retaining walls design, has been excluded from the figures, yet it is examined in detail in Table 8. As described earlier, if $q_{\min}$ is negative, it means that some tensile stress is developed at the end of the heel, which is undesirable due to the negligible tensile strength of the soil. The final values for $q_{\min}$ corresponding to each example and method are listed in Table 8. As can be seen, all the values are greater than zero, indicating that no tensile stress appears beneath the heel slab of the RCRWs.

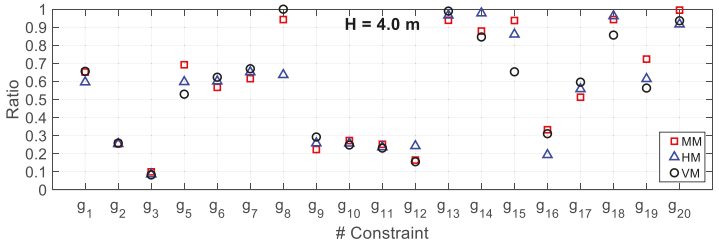

Figure 10. Demand to capacity ratio for Example 1.

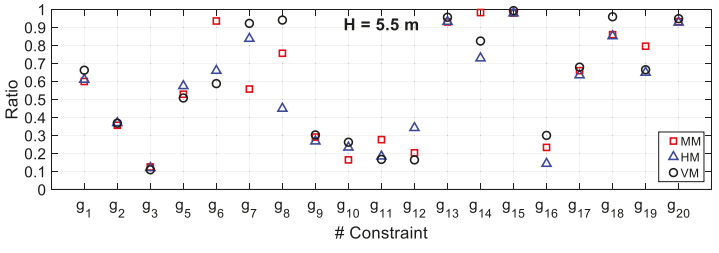

Figure 11. Demand to capacity ratio for Example 2.

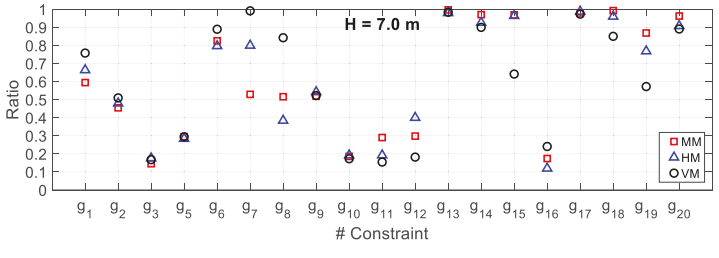

Figure 12. Demand to capacity ratio for Example 3.

Table 8. $q_{\min}$ (constraint g_4) values for all three examples and all three design methods.

Variable	Example 1—H = 4.0 m			Example 2—H = 5.5 m			Example 3—H = 7.0 m		
	MM	**HM**	**VM**	**MM**	**HM**	**VM**	**MM**	**HM**	**VM**
$q_{\min}$	16.15	26.37	17.74	29.60	31.75	23.70	40.61	27.28	9.22

Next, the construction cost of the optimum designs was examined. The concrete, steel, and total cost for all of the optimum RCRWs with different heights, considering the three methods, are listed in Table 9. As can be seen, for H = 4.0 m and H = 7.0 m, the MM resulted in the minimum cost compared with the other two methods; also, the cost for HM was less than that for VM. For H = 5.5 m, the VM had the minimum cost and the cost for MM was less than that for HM. In addition, based on the results of Table 9 and as also shown in Tables 5–7, the provided amounts of reinforcement varied depending on the method used. Moreover, it was shown that the differences among the methods decreased with increasing the height of the RCRWs.

Figure 13 reveals the variation in cost components (concrete and steel materials) to total cost ratio with respect to the RCRW heights for each method. Based on this figure, it can be concluded that the concrete cost was reduced from 65.64% 52.93% on average with increasing the height, and the steel cost was increased from 34.36% to 47.07% on average with increasing the height.

Table 9. Cost of optimum RCRWs for different heights considering the three methods.

Variable	Example 1—H = 4.0 m			Example 2—H = 5.5 m			Example 3—H = 7.0 m		
	MM	HM	VM	MM	HM	VM	MM	HM	VM
Concrete ($)	70.07	70.60	70.27	122.00	126.39	120.80	172.15	175.37	184.04
Steel ($)	34.96	37.34	38.19	77.07	76.64	75.89	160.45	160.19	152.04
Total ($)	105.04	107.94	108.46	199.08	203.03	196.68	332.61	335.56	336.08
Diff. (%) to MM for total cost	-	2.76	3.26	-	1.99	−1.20	-	0.89	1.04

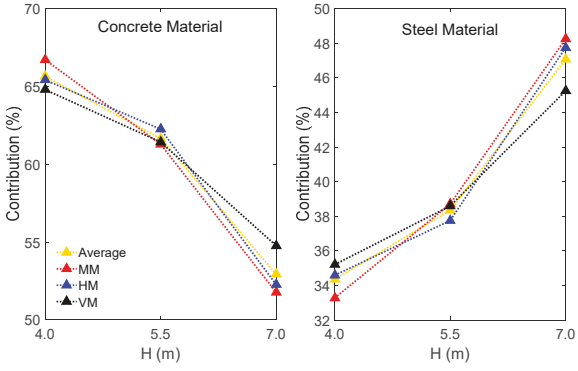

Figure 13. The contribution of concrete and steel materials in total cost for optimum RCRWs.

5.3. Comparative Study

In order to make a comparison with the literature, a specific example was chosen from the work conducted by Gandomi et al. [6] (Example 2, case 1 of the work [6] for $\beta = 0°$, see corresponding *Table 12* of *that* work). Using the methodology of the present work, all three methods of MM, HM, and VM were considered for the comparison. The results are listed in Table 10. As can be seen in this table, the results obtained for MM, HM, and VM were slightly different to those by Gandomi et al. [6], at least as far as the optimum cost is concerned. This can be attributed to the different analysis method and the different load combinations of ACI318-2014 used. Comparing the results also revealed the accuracy of the code programming used in this paper.

Table 10. Comparison of optimum cost obtained in this paper with the work by Gandomi et al. [6].

Work	Method	Cost ($/m)
Gandomi et al. [6]	-	162.37
This paper	MM	154.82
	HM	158.13
	VM	150.49

5.4. Effect of Backfill Slope

In this section, the effect of the parameter β (backfill slope) on the optimum cost of RCRWs was investigated, considering the three methods of MM, HM, and VM. Herein, this effect was assessed for Example 2—H = 5.5 m and the results are presented in Table 11. As can be seen, by increasing β, the cost was increased individually for each method. In addition, there were small differences (accounting for less than 3%) among the MM, HM, and VM methods, except for the case $\beta = 25°$, where the difference was slightly more, at 4.11%.

Table 11. Cost ($/m) of optimum RCRWs for Example 2—H = 5.5 m for different β for the three methods.

Method	β (degrees)					
	0	**5**	**10**	**15**	**20**	**25**
MM	193.52	199.08	200.78	215.98	224.86	231.04
HM	195.11	203.03	197.55	212.83	221.07	240.54
VM	191.05	196.68	202.96	209.59	220.57	234.34
HM to MM (Diff. %)	0.82	1.98	−1.61	−1.46	−1.69	4.11
VM to MM (Diff. %)	−1.28	−1.21	1.09	−2.96	−1.91	1.43

5.5. Effect of Surcharge Load

Herein, the effect of the parameter q (surcharge load) on the optimum cost of RCRWs was investigated, considering the three methods of MM, HM, and VM. Again, Example 2—H = 5.5 m was used to investigate the effect and the results are presented in Table 12. As shown, the optimum cost increased as q increased. In addition, there were small differences (accounting for less than 3%) among the MM, HM, and VM methods, except for the case that no surcharge load was applied (i.e., q = 0), which led to a difference of 4.38%.

Table 12. Cost ($/m) of optimum RCRWs for Example 2—H = 5.5 m with different q for the three methods.

Method	q (kPa)					
	0	**5**	**10**	**15**	**20**	**25**
MM	168.16	180.43	189.84	199.08	209.22	211.12
HM	172.47	180.88	186.93	203.03	203.69	213.82
VM	175.52	179.31	188.78	196.68	204.12	214.50
HM to MM (Diff. %)	2.56	0.25	−1.53	1.98	−2.64	1.28
VM to MM (Diff. %)	4.38	−0.62	−0.56	−1.21	−2.44	1.60

6. Conclusions

In the present study, three well-known methods of Meyerhof, Hansen, and Vesic were considered for the computation of the bearing capacity of RCRWs and, in particular, their influence on the optimum design of the wall. Three heights of walls were examined in the three test cases—4.0 m, 5.5 m, and 7.0 m. A code was developed in MATLAB where the PSO method was implemented for solving the constrained optimization problem. The design criteria were considered in accordance with ACI318-14 design code [20], where two sets of constraints were taken into account, the first on geotechnical requirements (wall stability) and the second on structural requirements (required strength of wall components and reinforcement arrangements). The PSO algorithm was successful in finding the optimum solutions fast and in a consistent way in all design cases, while the constraint handling mechanism was successful, managing to yield optimum solutions that satisfied the constraints in all cases.

The three methods resulted in slightly different designs for all the optimum RCRWs with different heights. In all three test examples, the MM (Meyerhof) method resulted in the design with the minimum total cost in comparison to the other two methods. It was also shown that the differences among the methods decreased with increasing the height of the RCRWs. When the height of the wall increases, the ratio of the cost of concrete to the total cost decreases, and the opposite happens with steel; the ratio of the cost of steel to the total cost increases. This observation was general and was made in all the three design methods examined. As regards the amounts of needed reinforcement, it can be concluded that the three methods give different results for the individual elements of the wall. On the other hand, as a general conclusion, it can be noted that the total cost of the wall corresponding to the three methods had only a small variation. In comparison to Meyerhof as the benchmark method, the maximum difference in the total cost was observed for the H = 4.0 m case and the VM method, and that accounted for only 3.26%. In all other cases the difference was even smaller.

In addition, the effect of the backfill slope β and the surcharge load q were examined. It was found that by increasing either the backfill slope or the surcharge load we obtained a higher total cost, but again in all cases the differences between the three methods were rather small, accounting for up to 4.5%. Finally, the results of the study were compared to results from an example of the work of Gandomi et al. [6] and were found only slightly different, which can be attributed to the different analysis method and the different load combinations used.

Author Contributions: Conceptualization, N.M. and S.G.; methodology, N.M. and S.G.; software, N.M. and S.G.; validation, V.P.; formal analysis, N.M., S.G. and V.P.; investigation, N.M., S.G. and V.P.; data curation, N.M. and S.G.; writing—original draft preparation, N.M. and S.G.; writing—review and editing, S.G. and V.P.; visualization, S.G., V.P.; supervision, S.G. and V.P.

Funding: This research received no external funding.

Conflicts of Interest: The authors declare no conflict of interest.

Appendix A

Table A1. The equations used for computing q_u based on each method.

Method	Equation	Condition
Meyerhof [22]	$N_{q,M} = e^{\pi \tan \phi_{bs}} \tan^2\left(45^\circ + \frac{\phi_{bs}}{2}\right)$	ϕ_{bs} in degrees
	$N_{c,M} = \left(N_{q,M} - 1\right) \cot \phi_{bs}$	-
	$N_{\gamma,M} = \left(N_{q,M} - 1\right) \tan(1.4\phi_{bs})$	-
	$F_{cd,M} = 1 + 0.2\sqrt{k_p}\frac{D}{B-2e}$	
	$F_{qd,M} = F_{\gamma d,M} = 1 + 0.1\sqrt{k_p}\frac{D}{B-2e}$	$\phi_{bs} > 10^\circ$
	$F_{cs,M} = F_{qs,M} = F_{\gamma s,M} = 1$	-
	$F_{ci} = F_{qi} = \left(1 - \frac{\theta}{90^\circ}\right)^2$	θ in degrees
	$F_{\gamma i} = \left(1 - \frac{\theta}{\phi_{bs}}\right)^2$	
	$\theta^\circ = \tan^{-1}\left(\frac{p_a \cos\beta}{\sum V}\right)$	for $\phi_{bs} > 0$
	θ is defined as angle of resultant measured from vertical direction	
Hansen [23]	$N_{q,H} = N_{q,M}$	-
	$N_{c,H} = N_{c,M}$	-
	$N_{\gamma,H} = 1.5\left(N_{q,H} - 1\right) \tan \phi_{bs}$	-
	$F_{cd,H} = 1 + 0.4\frac{D}{B-2e}$	$\frac{D}{B-2e} \le 1$
	$F_{cd,H} = 1 + 0.4\tan^{-1}\left(\frac{D}{B-2e}\right)$	$\frac{D}{B-2e} > 1$
	$F_{qd,H} = 1 + 2\tan\phi_{bs}\left(1 - \sin\phi_{bs}\right)^2\frac{D}{B-2e}$	$\frac{D}{B-2e} \le 1$
	$F_{qd,H} = 1 + 2\tan\phi_{bs}\left(1 - \sin\phi_{bs}\right)^2\tan^{-1}\left(\frac{D}{B-2e}\right)$	$\frac{D}{B-2e} > 1$
	$F_{\gamma d,H} = 1$	-
	$F_{cs,H} = F_{qs,H} = F_{\gamma s,H} = 1$	-
	$F_{ci,H} = F_{qi,H} - \left(\frac{1 - F_{qi,H}}{N_{q,H} - 1}\right)$	$\phi_{bs} \neq 0$
	$F_{qi,H} = \left(1 - \frac{0.5 p_a \cos\beta}{\sum V + (B-2e) c_{bs} \cot\phi_{bs}}\right)^5$	$\phi_{bs} \neq 0$
	$F_{\gamma i,H} = \left(1 - \frac{0.7 p_a \cos\beta}{\sum V + (B-2e) c_{bs} \cot\phi_{bs}}\right)^5$	$\phi_{bs} \neq 0$
Vesic [24]	$N_{q,V} = N_{q,M}$	-
	$N_{c,V} = N_{c,M}$	-
	$N_{\gamma,V} = 2\left(N_{q,V} + 1\right) \tan \phi_{bs}$	-
	$F_{cd,V} = F_{cd,H}$	-
	$F_{qd,V} = F_{qd,H}$	-
	$F_{\gamma d,V} = F_{\gamma d,H}$	-
	$F_{ci,V} = F_{ci,H}$	-
	$F_{qi,V} = \left(1 - \frac{p_a \cos\beta}{\sum V + (B-2e) c_{bs} \cot\phi_{bs}}\right)^2$	$\phi_{bs} \neq 0$
	$F_{\gamma i,V} = \left(1 - \frac{p_a \cos\beta}{\sum V + (B-2e) c_{bs} \cot\phi_{bs}}\right)^3$	$\phi_{bs} \neq 0$

References

1. Sarıbaş, A.; Erbatur, F. Optimization and sensitivity of retaining structures. *J. Geotech. Eng.* **1996**, *122*, 649–656. [CrossRef]
2. Ceranic, B.; Fryer, C.; Baines, R. An application of simulated annealing to the optimum design of reinforced concrete retaining structures. *Comput. Struct.* **2001**, *79*, 1569–1581. [CrossRef]
3. Víctor, Y.; Julian, A.; Cristian, P.; Fernando, G.-V. A parametric study of optimum earth-retaining walls by simulated annealing. *Eng. Struct.* **2008**, *30*, 821–830.
4. Camp, C.V.; Akin, A. Design of retaining walls using big bang–big crunch optimization. *J. Struct. Eng.* **2011**, *138*, 438–448. [CrossRef]
5. Khajehzadeh, M.; Taha, M.R.; El-Shafie, A.; Eslami, M. Economic design of retaining wall using particle swarm optimization with passive congregation. *Aust. J. Basic Appl. Sci.* **2010**, *4*, 5500–5507.
6. Gandomi, A.H. Optimization of retaining wall design using recent swarm intelligence techniques. *Eng. Struct.* **2015**, *103*, 72–84. [CrossRef]
7. Kaveh, A.; Khayatazad, M. Optimal design of cantilever retaining walls using ray optimization method. Iranian Journal of Science and Technology. *Trans. Civ. Eng.* **2014**, *38*, 261.
8. Kaveh, A.; Soleimani, N. CBO and DPSO for optimum design of reinforced concrete cantilever retaining walls. *Asian J. Civ. Eng.* **2015**, *16*, 751–774.
9. Kaveh, A.; Farhoudi, N. Dolphin echolocation optimization for design of cantilever retaining walls. *Asian J. Civ. Eng.* **2016**, *17*, 193–211.
10. Kaveh, A.; Laien, D.J. Optimal design of reinforced concrete cantilever retaining walls using CBO, ECBO and VPS algorithms. *Asian J. Civ. Eng.* **2017**, *18*, 657–671.
11. Temur, R.; Bekdaş, G. Teaching learning-based optimization for design of cantilever retaining walls. *Struct. Eng. Mech.* **2016**, *57*, 763–783. [CrossRef]
12. Ukritchon, B.; Chea, S.; Keawsawasvong, S. Optimal design of Reinforced Concrete Cantilever Retaining Walls considering the requirement of slope stability. *KSCE J. Civ. Eng.* **2017**, *21*, 2673–2682. [CrossRef]
13. Aydogdu, I. Cost optimization of reinforced concrete cantilever retaining walls under seismic loading using a biogeography-based optimization algorithm with Levy flights. *Eng. Optim.* **2017**, *49*, 381–400. [CrossRef]
14. Kumar, V.N.; Suribabu, C. Optimal design of cantilever retaining wall using differential evolution algorithm. *Int. J. Optim. Civ. Eng.* **2017**, *7*, 433–449.
15. Gandomi, A.; Kashani, A.; Zeighami, F. Retaining wall optimization using interior search algorithm with different bound constraint handling. *Int. J. Numer. Anal. Methods Geomech.* **2017**, *41*, 1304–1331. [CrossRef]
16. Gandomi, A.H.; Kashani, A.R. Automating pseudo-static analysis of concrete cantilever retaining wall using evolutionary algorithms. *Measurement* **2018**, *115*, 104–124. [CrossRef]
17. Mergos, P.E.; Mantoglou, F. Optimum design of reinforced concrete retaining walls with the flower pollination algorithm. *Struct. Multidiscip. Optim.* **2019**, 1–11. [CrossRef]
18. MATLAB. *The Language of Technical Computing*; Math Works Inc.: Natick, MA, USA; 2005; Volume 2018a.
19. Kennedy, J.; Eberhart, R. Particle swarm optimization (PSO). In Proceedings of the IEEE International Conference on Neural Networks, Perth, Australia, 27 November–1 December 1995.
20. ACI. *American Concrete Institute: Building Code Requirements for Structural Concrete and Commentary*; ACI: Farmington Hills, MI, USA, 2014.
21. Das, B.M. *Principles of Foundation Engineering*; Cengage Learning: Boston, MA, USA, 2015.
22. Meyerhof, G.G. Some recent research on the bearing capacity of foundations. *Can. Geotech. J.* **1963**, *1*, 16–26. [CrossRef]
23. Hansen, J.B. *A Revised and Extended Formula for Bearing Capacity*; Danish Geotechnical Institute: Lyngby, Denmark, 1970.
24. Vesic, A.S. Analysis of ultimate loads of shallow foundations. *J. Soil Mech. Found. Div.* **1973**, *99*, 45–73. [CrossRef]
25. Arora, J.S. *Introduction to Optimum Design*; Elsevier: Amsterdam, The Netherlands, 2004.
26. Gharehbaghi, S.; Khatibinia, M. Optimal seismic design of reinforced concrete structures under time-history earthquake loads using an intelligent hybrid algorithm. *Earthq. Eng. Eng. Vib.* **2015**, *14*, 97–109. [CrossRef]
27. Gholizadeh, S.; Salajegheh, E. Optimal design of structures subjected to time history loading by swarm intelligence and an advanced metamodel. *Comput. Methods Appl. Mech. Eng.* **2009**, *198*, 2936–2949. [CrossRef]

28. Plevris, V.; Papadrakakis, M. A hybrid particle swarm-gradient algorithm for global structural optimization. *Comput.-Aided Civ. Infrastruct. Eng.* **2011**, *26*, 48–68. [CrossRef]
29. Gholizadeh, S. Layout optimization of truss structures by hybridizing cellular automata and particle swarm optimization. *Comput. Struct.* **2013**, *125*, 86–99. [CrossRef]
30. Yazdani, H. Probabilistic performance-based optimum seismic design of RC structures considering soil–structure interaction effects. *ASCE-ASME J. Risk Uncertain. Eng. Syst. Part A Civ. Eng.* **2016**, *3*, G4016004. [CrossRef]
31. Gharehbaghi, S.; Moustafa, A.; Salajegheh, E. Optimum seismic design of reinforced concrete frame structures. *Comput. Concr.* **2016**, *17*, 761–786. [CrossRef]
32. Gharehbaghi, S. Damage controlled optimum seismic design of reinforced concrete framed structures. *Struct. Eng. Mech.* **2018**, *65*, 53–68.
33. Khatibinia, M.; Jalali, M.; Gharehbaghi, S. Shape optimization of U-shaped steel dampers subjected to cyclic loading using an efficient hybrid approach. *Eng. Struct.* **2019**, *197*, 108874. [CrossRef]

© 2019 by the authors. Licensee MDPI, Basel, Switzerland. This article is an open access article distributed under the terms and conditions of the Creative Commons Attribution (CC BY) license (http://creativecommons.org/licenses/by/4.0/).

MDPI
St. Alban-Anlage 66
4052 Basel
Switzerland
Tel. +41 61 683 77 34
Fax +41 61 302 89 18
www.mdpi.com

Mathematics Editorial Office
E-mail: mathematics@mdpi.com
www.mdpi.com/journal/mathematics

MDPI
St. Alban-Anlage 66
4052 Basel
Switzerland

Tel: +41 61 683 77 34
Fax: +41 61 302 89 18

www.mdpi.com

ISBN 978-3-03943-496-1